

**NASA TECHNICAL
TRANSLATION**



NASA TT F-566

2.1

NASA TT F-566



LOAN COPY: RETURN TO
AFWL (WL0L)
KIRTLAND AFB, N MEX

**ASTROMETRY AND ASTROPHYSICS, NO. 1,
PHYSICS OF THE MOON AND PLANETS**

by I. K. Koval'

"Naukova Dumka" Press, Kiev, 1968

NATIONAL AERONAUTICS AND SPACE ADMINISTRATION • WASHINGTON, D. C. • APRIL 1970



ASTROMETRY AND ASTROPHYSICS, NO. 1, PHYSICS OF THE
MOON AND PLANETS

By I. K. Koval'

Translation of "Astrometriya i Astrofizika, 1,
Fizika Luny i Planet"
"Naukova Dumka" Press, Kiev, 1968

NATIONAL AERONAUTICS AND SPACE ADMINISTRATION

For sale by the Clearinghouse for Federal Scientific and Technical Information
Springfield, Virginia 22151 - CFSTI price \$3.00

ANNOTATION

This collection contains the results of photometric investigations of the Moon, Mars and Jupiter. A large amount of the data in this collection concerns the results of a study of the lunar relief, mainly of its far side, by the photometric method; the photographs were obtained by the spacecraft "Zond-3".

The results of extensive spectrophotometric observations of Jupiter, carried out in 1964-1966 at the Main Astronomical Observatory of the Academy of Sciences of the Ukrainian S.S.R., are presented, as are calculations of the optical parameters of the Mars atmosphere and surface. The two-channel photometer measuring small light fluxes which was constructed at the Main Astronomical Observatory of the Academy of Sciences of the Ukrainian S.S.R. is described.

This collection is intended for scientific researchers, astrophysicists and geophysicists, as well as for undergraduate and graduate students in the corresponding fields.

Editorial Board:

Ye.P. Fedorov (President), Z.N. Aksent'yeva, N.P. Barabashov, A.F. Bogorodskiy (Vice President), A.A. Gorynya (Secretary), I.K. Koval', I.G. Kolinskiy, V.P. Tsesevich, A.A. Yakovkin

Editor-in-Chief

I.K. Koval'

INTRODUCTION

In 1964, the Main Astronomical Observatory of the Academy of Sciences of the Ukrainian S.S.R. began to publish inter-departmental thematic collections of the series "Astronomiya i astrofizika" (Astronomy and Astrophysics), as a result of which the "Izvestiy GAO AN USSR" stopped being published (the last issue was Vol. 5, No. 1, 1963). Articles touching on certain single divisions of astronomy were selected in each of the collections. The scientific research studies of both the workers at the Main Astronomical Observatory of the Academy of Sciences of the Ukrainian S.S.R. and the workers at other astronomical observatories and astronomy departments at institutes of higher education of the Ukrainian S.S.R. were published in the inter-departmental collections.

Up to the end of 1967, the Main Astronomical Observatory of the Academy of Sciences of the Ukrainian S.S.R. published the following inter-departmental collections in the series "Astronomiya i astrofizika":

1964. Voprosy astrometrii (Problems of Astrometry), Issledovaniya komet po programme MGSS (Studies of Comets according to the IQSY Program), Issledovaniya po fizike zvezd i diffuznoy materii (Investigations of the Physics of Stars and Diffuse Matter), Spektrofotometricheskiye issledovaniya aktivnykh obrazovaniy na Solntse (Spectrophotometric Studies of Active Formations on the Sun), Fizika Luny i planet (Physics of the Moon and Planets);

1965. Voprosy astrofiziki (Problems of Astrophysics), Figura i dvizheniye Luny (The Shape and Motion of the Moon), Fizika komet i meteorov (Physics of Comets and Meteors), Izmenyayemost' shirot (Latitude Variability);

1966. Voprosy astrometrii (Problems of Astrometry), Voprosy astrofiziki (Problems of Astrophysics), Fizika komet i meteorov (Physics of Comets and Meteors), Fizika Luny i planet (Physics of the Moon and Planets), Fizika zvezd i mezhzvezdnoy sredy (Physics of the Stars and the Interstellar Medium);

1967. Figura i dvizheniya Luny (The Shape and Motion of the Moon), Voprosy astrofiziki (Problems of Astrophysics), Izmenyayemost' shirot (Latitude Variability), Aktivnyye protsessy v kometakh (Active

Processes in Comets).

Unfortunately, no general numbering system was made for the collections of this series, and this caused difficulties in referring to them.

In order to avoid like difficulties in the future, the editorial board decided that, beginning with 1968, they would publish all the collections under the general thematic title "Astrometriya i astrofizika" (Astrometry and Astrophysics), and that they would introduce a new numbering system for the issues. In those cases when the issue is completely concerned with some single problem, the corresponding sub-title will be added.

The following issues will come out in the series "Astrometriya i astrofizika" in 1968: No. 1, Fizika Luny i planet (Physics of the Moon and Planets); No. 2, Voprosy astrometrii (Problems of Astrometry); No. 3, Voprosy astrofiziki (Problems of Astrophysics); No. 4, Fizika komet (Physics of Comets); No. 5, Voprosy atmosferno optiki (Problems of Atmospheric Optics); No. 6, Kol'tseobraznoye solnechnoye zatmeniy 20 maya 1966 g (The Annular Eclipse of the Sun on May 20, 1966).

TABLE OF CONTENTS

L. R. Lisina. A PHOTOMETRIC METHOD OF LUNAR TOPOGRAPHY.....	1
M. N. Mironova. STRUCTURAL CHARACTERISTICS OF SOME CRATERS ON THE FAR SIDE OF THE MOON.....	33
M. N. Mironova. HEIGHT PROFILES OF TWENTY-NINE CRATERS ON THE FAR SIDE OF THE MOON.....	46
I. K. Koval'. OPTICAL CHARACTERISTICS OF THE MARS ATMO- SPHERE OBTAINED ACCORDING TO CONTRAST MEASUREMENTS.....	58
I. K. Koval' and A. V. Morozhenko. THE NATURE OF THE POLAR CAPS OF MARS.....	76
I. K. Koval', A. A. Rubashevskiy and E. G. Yanovitskiy. THE EFFECT OF ATMOSPHERIC VIBRATION ON THE BRIGHTNESS DISTRIBUTION OVER THE DISK OF A PLANET.....	91
V. V. Avramchuk. THE METHANE ABSORPTION DISTRIBUTION IN THE 6190 Å BAND OVER THE DISK OF JUPITER.....	119
V. V. Avramchuk. DISTRIBUTION OF METHANE ABSORPTION IN THE 6190 Å BAND OVER THE DISK OF SATURN IN 1966.....	153
E. G. Yanovitskiy. THE PROBLEM OF DIFFUSE REFLECTION OF MONOCHROMATIC RADIATION.....	156
E. G. Yanovitskiy. BRIGHTNESS COEFFICIENTS OF A HOMOGENEOUS PLANE LAYER OF A TURBID MEDIUM.....	169
O. I. Bugayenko. COUNT RATE METER (CRM).....	178
L. A. Bugayenko, O. I. Bugayenko, V. D. Krugov and V. G. Parusimov. AN ELECTROPHOTOMETER FOR LOW LUMINOUS FLUXES.....	183

A PHOTOMETRIC METHOD OF LUNAR TOPOGRAPHY

L.R. Lisina

ABSTRACT: The photometric characteristics of the Moon scattering light are described. It is shown that, in determining the brightness of lunar details according to theoretical formulas, the macroslope must be considered. Small slopes are determined by the photometric method. The photometric method of determining the slopes for observations of the lunar surface from a spacecraft is discussed. The requisite parameters are calculated in order to determine the slopes and heights of the thalassoid Korolev on the far side of the Moon. The photographs were obtained from the Soviet spacecraft "Zond-3". The thalassoid Korolev is a basin surrounded by numerous rings with faults.

Photographing of the Moon from moving spacecraft (Ranger series), photographing of the far side from the automatic interplanetary station "Zond-3", numerous photographs obtained by stations which made a soft landing ("Luna-9", "Luna-13", Surveyor 1 and 2), and photographs taken from satellites and orbital stations: this is an incomplete list of the studies of the Moon from the space around it. The information obtained from spacecraft primarily concerns the problems of the morphology of the Moon's surface: a great deal of data has been obtained on the physical and mechanical properties of the lunar soil, and hypotheses on the microstructure of the lunar soil have been confirmed. It is now important to concentrate our attention on all the methods of lunar topography which can be applied both to photographs obtained from the Earth and to those obtained from spacecraft.

The possibilities of applying photometry to lunar topography, particularly the photometric method which was proposed by Diggelen in 1951 and further developed at the Main Astronomical Observatory of the Ukrainian S.S.R., are examined in this study. Beginning in 1962, this method was used to study an extensive region around Oceanus Procellarum and the central part of the Moon in the region of the Triesnecker crater and Hyginus rille, as well as to investigate in detail the morphology of the structure of the mounds in Mare Fecunditatis, the slopes of lighted ridges of the Archimedes

* Numbers in the margin indicate pagination in the foreign text.

crater (Fig. 1, see the insertion between pages 16 and 17). In 1966, the photometric method was modified and used to analyze close-up photographs of the far side of the Moon, taken from the "Zond-3" station.

Photometric Characteristics of the Lunar Surface

Since we will subsequently be using the conclusions obtained by a number of authors in studying the qualitative picture for the reflection of light from the lunar surface in our assumptions, let us discuss some of them here.

N.P. Barabashov [1] and then A.V. Markov [2] found that the maximum brightness of the majority of details of the Moon occurs during full moon ($i = \epsilon$). E. Opik [3] found that the appearance of the curve for the photometric function is identical for all formations, and that the brightness maximum during full moon does not depend on the position of formations of the same type on the lunar disk. These results were corroborated by A.L. Bennet [4], V.A. Fedorets [5] and van Diggelen [6]. M. Minnart [7] and V.G. Fesenkova [8] affirmed that the phase change in brightness is not latitude-dependent, but is mainly a function of the longitude. The characteristics of the microrelief of the lunar surface were established on the basis of photometric investigations. The upper layers of the lunar soil (thickness of several millimeters or centimeters) have a porous structure, and the skeleton takes up only 10% of the space, while 90% of the space is pores.

In addition to the cited studies, there were attempts at giving a quantitative description of the law of light reflection from the Moon's surface. The majority of the theoretical models were based on the assumption that there was an even surface covered with depressions or protuberances of different shapes: spherical or cylindrical depressions (N.P. Barabashov), spherical cupolas (Schoenberg), semi-ellipsoidal cavities (Bennet and Diggelen). Considering the general representations of the nature of the porosity of the lunar surface, B. Hapke [9] proposed a formula which gave a good description of the change in brightness for the regions between selenographic longitudes of $\pm 60^\circ$. It was then modified in order to represent observations in regions adjacent to the limb [10]. The formula is of the following form:

$$B(i, \epsilon, \alpha) = E_0 a d \frac{2}{3\pi} b \frac{1}{1 + \frac{\cos \epsilon}{\cos i}} \times \\ \times \frac{\sin |\alpha| + (\pi - |\alpha|) \cos \alpha}{\pi} B(\alpha, g),$$

where $E_0 a d \frac{2}{3\pi} b$ is the amount of light reflected from an area on the

Moon in the direction of the receiver in a full moon (albedo),

$\varphi(i, \varepsilon) = \frac{1}{1 + \frac{\cos \varepsilon}{\cos i}}$ is a function characterizing the law of diffuse scattering, $f(\alpha) = \frac{\sin \alpha + (\pi - |\alpha|) \cos \alpha}{\pi}$ is a phase

function, $B(\alpha, g)$ is a retrodictive function depending on the packing coefficient (g is the packing factor, $2 > g > 0.01$) and the relative density of the particles making up the surface under investigation. For the sake of simplicity in the calculations, the expression $\phi(i, \varepsilon)$ can be converted, if we assume that the lunar equator coincides with the equator of intensity in view of the smallness of the angle between them and the coincidence of the apparent center with the center of the coordinate system (zero moment of libration). Then,

$$\begin{aligned}\cos \varepsilon &= \cos \beta \cos \lambda, \\ \cos i &= \cos \beta \cos (\lambda - \alpha)\end{aligned}$$

and

$$\varphi(\lambda, \sigma) = \frac{1}{1 + \frac{\cos \lambda}{\cos (\lambda - \sigma)}}.$$

The function $\phi(i, \varepsilon, \alpha)$, or $\phi(\lambda, \alpha)$, is called a photometric one. It has information on the inclination of various formations on the Moon in the direction of the incident rays, or the so-called longitudinal component of the slope.

A.A. Akimov [11] represented this function in a somewhat different form in a formula to be used to calculate the brightness of any part of the lunar surface for different phases:

$$B(\omega, \alpha) = B_0 \varphi(\omega, \alpha) f(\alpha) \left[1 + k(\alpha) \left(\frac{B_0}{B_{0cp}} - 1 \right) \right],$$

where $B(\omega, \alpha)$ is the brightness for the given phase; B_0 is the mean brightness during full moon; B_{0cp} is the brightness of a point during full moon; $f(\alpha)$ is a phase function; $\phi(\omega, \alpha)$ is the brightness distribution over the equator of intensity, determined by the expression

$$\begin{aligned}\varphi(\omega, \alpha) &= \cos \theta_1(\alpha - \omega) \cos^{1/2} \omega, \\ \theta_1 &= \theta(-\omega) \theta(90^\circ - \alpha + \omega) + \theta(\alpha - \omega) \theta(\omega), \\ \theta_2 &= \theta(\omega - \alpha) \theta(90^\circ - \omega) + \theta(\alpha - \omega) \theta(\omega),\end{aligned}$$

while the function $\theta = 0$ for a negative value of the argument, and $\theta = 1$ for a positive value.

Correction of Theoretical Brightnesses for the Slope

The formulas of Hapke and Akimov give values of the brightnesses for a spherically uniform Moon. We compared the theoretical curves with the observational data of Fedorets and Diggelen. The comparisons were carried out for the regions of the lunar surface which are known to have no substantial macro-irregularities - regions of the maria and the floors of craters. For example, Hapke compared regions in Mare Serenitatis, Mare Nectaris, Mare Imbrium, and the centers of Ptolemaeus and Tycho.

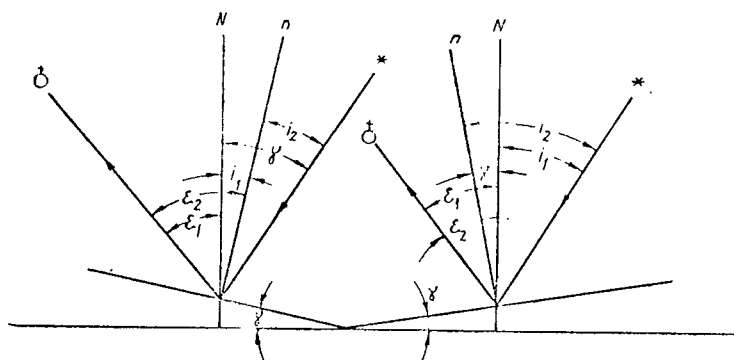


Fig. 2. Change in Values of i and ϵ with a Change in Slope.

To obtain the value for the brightness of a crater ridge which slopes toward the middle surface in a certain phase, we must make a correction for the slope. Since the slope of the surface changes the direction of the normal, the values for the angles of incidence and reflection also change (Fig. 2). Let us agree that the slope is positive if a rise is found in the direction of the incident ray. We will call the slope γ . For a positive slope, the value for the angle of incidence decreases by the value γ and is $i - \gamma$, while the value for the angle of reflection increases up to $\epsilon + \gamma$.

In order to be certain that the theoretical curves for crater ridges which have a substantial slope did not coincide with those observed, we calculated and constructed the theoretical and observational curves for the crater Theophilus. The value for the slope of the eastern ridge of the crater Theophilus was taken from [12] ($\gamma = +27^{\circ}05'$, $\beta = 11^{\circ}21'$, $\gamma_E = 46^{\circ}34'$), in which slopes of 19 craters are given. The maximum slope is given in this study, since the sliding-beam method was used. As the author shows, the value of the slope can be increased by 12° . The photometric values of the brightnesses for the phase angles from 28° before full moon to 28° after full moon were obtained in [13] for the same craters, and

segments of the phase curves (value of the diaphragm-10.8") were constructed according to them.

TABLE 1

Date	Time	Phase	B	Date	Time	Phase	B
Before Full Moon				After Full Moon			
17. 7.62	9.3	1°	1	21.4.62	8.1	15°	0.646
17. 7.62	7.1	2.5	0.955	21.4.62	10.4	16.8	0.589
15. 8.62	6.9	7.6	0.692	22.4.62	8.1	27.0	0.457
15. 8.62	9.3	6.2	0.731	22.4.62	11.8	28.6	0.501
13. 9.62	7.5	12.4	0.692	20.5.62	7.8	9.7	0.757
13. 9.62	9.2	11.5	0.724	18.6.62	9.4	5.0	1.01
9.12.62	8.6	27.8	0.534	18.7.62	7.7	11.1	0.619
10.12.62	5.8	16.0	0.751	18.7.62	9.7	12.2	0.614
10.12.62	8.2	14.7	0.711	19.7.62	7.6	24.5	0.386
9. 1.63	8.7	7.7	1.04	19.7.62	10.0	25.9	0.427
9. 1.63	9.8	7.1	0.86	14.9.62	8.9	4.6	0.802
				14.9.62	5.7	3.6	0.832
				15.9.62	5.8	15.8	0.586
				15.9.62	8.8	17.5	

TABLE 2

N	α	B obs.	B theor.	B' theor.
1	0°	1	1	1
2	5	0.89	0.866	0.892
3	10	0.78	0.735	0.783
4	15	0.68	0.626	0.691
5	20	0.61	0.537	0.625
6	25	0.55	0.461	0.568
7	30	0.51	0.393	0.521

Table 1 gives values for the brightnesses of the crater Teophilus for phases before and after full moon.

The theoretical curve was calculated according to Hapke's formula. The value g , which characterizes the microrelief, was taken as equal to 0.6, on the basis of Hapke's conclusions that the brightest details correspond to $g = 0.4$, and the floors of craters and the maria correspond to 0.8, and $g = 0.6$ for the photometrically standard Moon. The crater Theophilus can be related to the photometrically standard Moon. We then constructed a theoretical curve corrected for the slope. Table 2 gives the phase angles, the average brightnesses obtained from observations [13], the theoretical brightnesses which do not consider the slope up to $\alpha = 0$ and the theoretical brightnesses which include the slope of the ridge. The brightnesses are normalized to full moon.

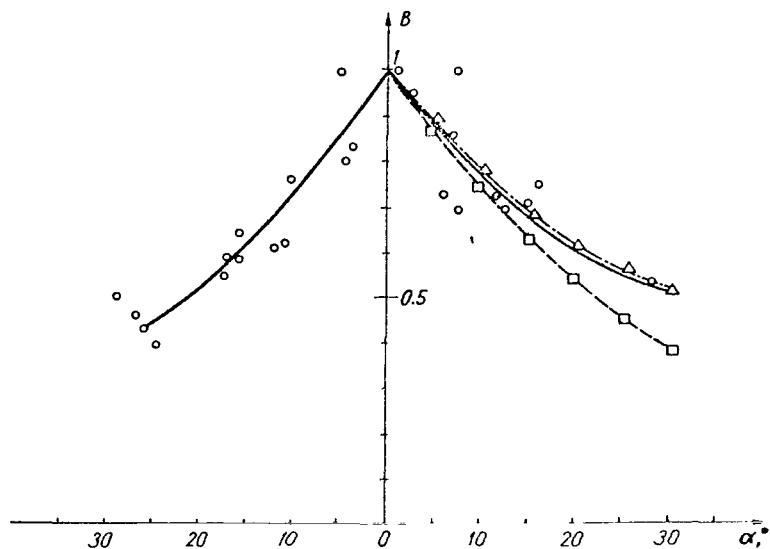


Fig. 3. Dependence of the Brightness on the Phase Angle for the Crater Theophilus (Solid Curve, Observations; Dashed Curve, Theoretical; Dot-Dashed Curve, Theoretical Corrected).

Since we are examining the inner eastern ridge, the calculations were carried out for the phases before full moon. The data of Table 2 were plotted on graphs (Fig. 3). We can see from the graph that there is complete agreement between the corrected curve and that observed. However, we must emphasize that a discrepancy between the theoretical and observational curves due to the slope should appear primarily for large phase angles.

The discrepancy between the theoretical and observational phase curves can be used in order to solve the inverse problem, i.e., that of finding the slopes. For this, we must have reliable phase curves and, moreover, we must know the characteristics of the microrelief of the given detail or its deviation from the standard Moon. The deviations in brightness from the photometrically standard Moon due to a difference in microrelief (deviation from the average value of the factor g) are given in the reports of Barabashov and Yezerskiy [14,15] for the details of the catalogue of Fedorets. This method of determining the slopes will be used only for rather steep ones, which are found mainly on the ridges of craters, particularly young craters. The authors of [13] found a dependence between the brightness and the slope for different stratigraphic classifications. Our stratigraphic classification was made according to Shoemaker [16]. The increase in brightness accompanying an increase in slope goes from formations belonging to the Proccllrum era to the era of Copernicus. The younger formations are brighter, since they have been less subjected to erosion and have

steeper slopes.

Principle of Determining the Slopes of Scarps in the Maria of the Moon

In order to study the small slopes characteristic of the scarps, furrows and banks in the regions of the maria, it is convenient to use the photometric method. The same principle of comparing the brightness of a segment of the lunar surface, which has an inclination with respect to the horizontal plane with the brightness of a segment lying in this plane, underlies this method. In connection with the fact that only the photometric function gives information on the slope, and this function gives the brightness distribution over the disk for a given phase, the slopes in a small region of the lunar surface can be studied according to one negative. Since the change in brightness over the disk is most appreciable for large angles of incidence of the solar rays, the region under investigation should be in a zone around the terminator. The reason for the change in brightness is the change in albedo and the difference in the irregularities of the macrorelief. As was shown earlier, the photometric function of any point on the disk can be represented as the function of three variables $\phi(i, \epsilon, \alpha)$, as well as the function of two variables $\phi(\lambda, \alpha)$, where λ is the selenographic longitude. The latter representation occurs for the case when the observer is on the Earth. In the general case, it is better to give the photometric function as the function of the photometric longitude and the phase $\phi(\omega, \alpha)$. This is possible because the isophotes of the lunar surface are close to the brightness meridians if the difference in albedo is considered. The angle, or the photometric longitude, characterizes the position of the brightness meridian (Fig. 4).

The photometric function $\phi(\omega, \alpha)$ was normalized so that it became equal to unity when the direction of incidence and reflection of the solar rays was perpendicular to the surface ($i = \epsilon = 0$), $\phi(0, 0, 0) = 1$, $B(\omega, \alpha) = B_0$). This allows us to determine the value of the normal albedo. Thus, the normal albedo was measured only for regions close to the center of the full Moon. However, the observations showed that the brightness of different regions during full moon does not depend on their position on the lunar disk. Therefore, the albedo at full moon should be taken as the normal albedo. The procedure of considering the difference in albedo of the measured regions is described in [17].

The photometric method of studying the slopes and heights of scarp chains in the maria of the Moon was first used by Diggelen [18], on the assumption that there was a small uniform region under the conditions of a substantial change in i and a practically unchanged ϵ near the center of the disk. The slope was then determined by the value Δi of points which had identical brightness but which occurred in planes with different slopes. In the case when the distance between the object and the observer decreases,

1

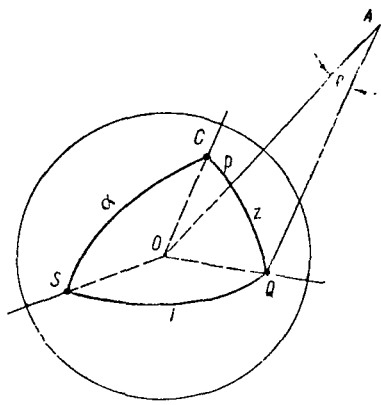


Fig. 5. Position of the Apparatus Relative to the Moon.

The position of the apparatus is characterized by the distance from the apparatus to the surface along the plumb line and the selenocentric position of the point of intersection with the surface of the line, which connects the apparatus and the center of the Moon. This determines the sub-instrumental point P (Fig. 5). We will find the point C according to the intersection of the lunar surface by the line which is parallel to the line of sight and passes through the center of the Moon. This is the apparent center of the

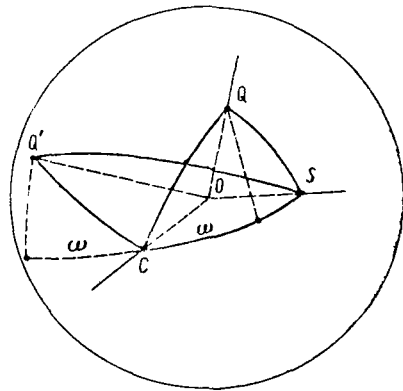


Fig. 7. Indeterminacy of the Photometric Function for Positive and Negative ω .

Moon and is called the "phase point", since it determines the phase angle and plane in which it lies. The angle COS is the phase angle. The angle of incidence of the solar rays is determined by the angle SOQ , and the angle of reflection ϵ is determined by the angle COQ ($\epsilon = p + z$). To determine the value of the slope γ , we will use the value ω . The photometric longitude ω is determined in terms of the angles i, ϵ and α . The relation between these values is represented in Figure 6. The phase angle is within the range of $-180^\circ < \alpha < +180^\circ$. However, the photometric function for the same values of i and ϵ is the same for the phases before and after full moon. This symmetry allows us to take the phase angle within the range of $0^\circ < \alpha < 180^\circ$. Moreover, because of the condition of reciprocity, the selection of i, ϵ and α for a given apparent center of the Moon determines the position of a point on the Moon ambiguously. The

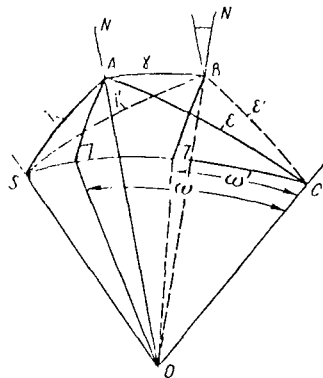


Fig. 8. Determination of the Slope in Terms of the Difference in Photometric Longitudes.

photometric function is completely unambiguous. If we define the photometric function in terms of the absolute value of ω , then its unambiguity is lost for the given interval of α . For a given α and identical ω , the values of the photometric function at the points Q and Q' differ (Fig. 7).

In order to establish unambiguity in determining ϕ , we must agree on the sign of the value ω . Since ω is read off from the point C along the intensity equator, we will consider ω to be positive if the measurements are carried out toward the terminator.

In order to determine the value of the slope in terms of the photometric function, we must have an analytical or graphic representation of the latter. Let us use the graphic representation. Since we are speaking of the photometric function of the maria and the relief of areas which are of interest from the point of view of landing and subsequently moving the apparatus along the surface, then we must assume that the slopes of the irregularities of the areas in which we are interested should be small (no more than $10-15^\circ$). The values for the angle of incidence and the angle of reflection of the solar rays change by $\pm\gamma$, compared to i and ϵ for an even surface, and the value of the phase angle remains the same. The photometric function for an even surface is $\phi(i, \epsilon, \alpha)$, and that for a sloped surface is $\phi(i \pm \gamma, \epsilon \pm \gamma, \alpha)$. For small angles of inclination, we can assume that the normal moves in the direction parallel to the intensity equator. This means that the value of ω has changed by a value of $\pm\gamma$. Figure 8 shows how the change in the normal by a value of $\Delta\omega$ indicates that the area is sloped with respect to the horizontal plane $\gamma = +\Delta\omega$. We will have the same for a negative slope. Thus, the problem of determining the slopes is reduced to that of determining the difference



Fig. 1. Photograph of the Moon Obtained at the Main Astronomical Observatory of the Academy of Sciences of the Ukrainian S.S.R. with the Aid of a 70-Centimeter Reflector on March 15-16, 1965 (IT, 21:22).

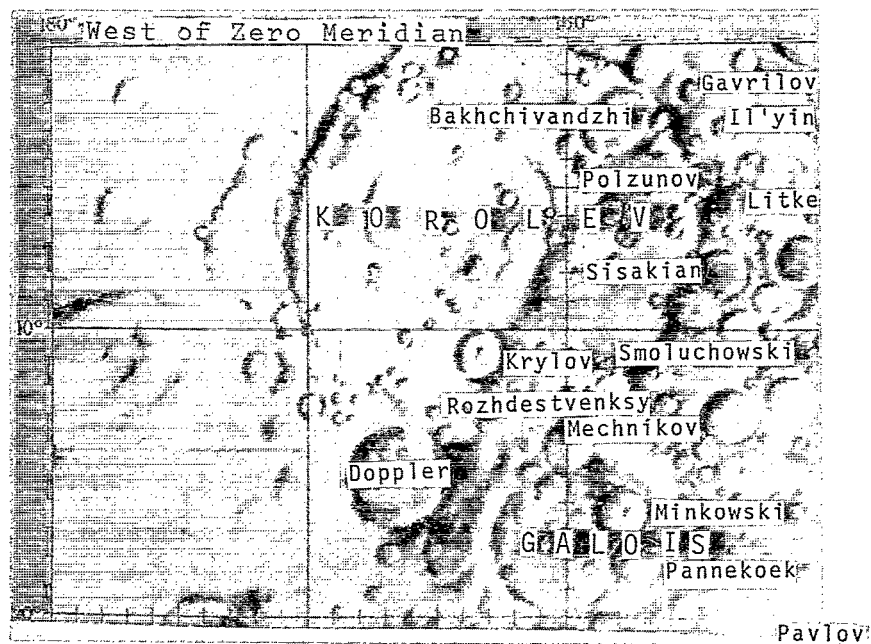


Fig. 11. The Thalassoid Korolev According to the Photographs of "Zond-3".

in brightness longitudes between the horizontal (spherical) elements of the lunar surface and those under investigation.

Let us briefly discuss the question of what the "spherical" brightness curve of the lunar surface should be. It can be a theoretical curve calculated for the case of $\gamma = 0$ for a given phase, as the function of ω according to the formulas of Hapke or Akimov. However, this type of curve is averaged over the albedo. The photometrically standard curves for different phases are given in [15]. For a region near the terminator, the law for the change in brightness is close to orthotropic; therefore, a segment of the cosine curve can be taken as the spherical curve. However, since calibrated negatives are not always available, we must often use, not the brightness distribution along the intensity equator, but the distribution of photographic density. In this case, we will obtain the spherical curve directly from measurements of the negative. We will select from all the regions those which have a smooth course for the change in density.

The light flux can be recorded both photographically and photoelectrically in ground observations. In all cases, the detail of the information will depend on the resolution of the system. The photographic material is most convenient from the point of view of analyzing the incoming information: first of all, the region of interest to us can be examined repeatedly at any moment and, secondly, the information can be read with the aid of a diaphragm corresponding to the allowance, which does not bring about a loss in information. However, substantial requirements must be imposed on the photographic material: an investigation of a detailed structure of the relief requires the presence of large-scale photographs, and the atmospheric interference under the conditions of ground observations require that the exposure be decreased, which involves an increase in the sensitivity of the photographic material, connected with an increase in grain size. For the photo-television method of transmitting information from space, it is desirable that the films have a sufficient photographic latitude, since the photometric method is used for the terminator zone of the Moon.

The photometric method has a great advantage in that it is used for monoscope photographs of the Moon obtained at any distance. In particular, this refers to the photographs of the far side of the Moon which were obtained from the automatic interplanetary station "Zond-3" on July 20, 1965.

Analysis of Photographs of the Far Side of the Moon

Calculation of Photometric Parameters. The spacecraft "Zond-3" photographed the eastern portion of the far side of the Moon, which added largely to the information on the far side which was obtained in 1959. This permitted a global survey of the morphology of the Moon's surface [19]. It was found that highlands are the predom-

ant form of the relief of the Moon.

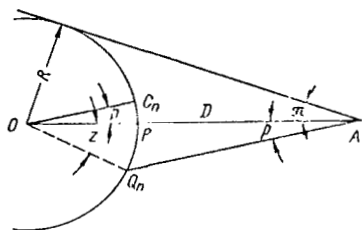


Fig. 9. Determination of the Phase Point (O is the point Representing the Center of the Lunar Sphere; Q is the Point of Intersection of the Lunar Surface with the Axis of the Camera; P is the Sub-Instrumental Point; π is the Parallax of the Moon; z is the Zenith Distance of the Point Q; p is the Angle Between the Line of Sight and the Plumb Line; R is the Radius of the Moon; D is the Distance from the Apparatus to the Center of the Moon).

10,879 km. The selenographic coordinates of the sub-instrumental point were $\lambda = 122^{\circ}55'$ and $\beta = -23^{\circ}46'$, and the coordinates of the subsolar point were $\lambda_{\odot} = -76^{\circ}57'$ and $\odot = 1^{\circ}6'36''$. The point PQ (see Fig. 5) is an orthogonal projection of the point of the Moon on the plane of the image. The image can be considered as orthogonal in the neighborhood of this point. The entire image was obtained by a diverging beam and is an external perspective projection. The position of each point in the plane of the image is determined by the value of i , ϵ and α .

In order to calculate the requisite parameters, we must determine the coordinates of the apparent disk of the Moon, i.e., the so-called phase point C (Fig. 9). The horizontal parallax was equal to $9^{\circ}11'5$. The point C is determined by the angle $z+p$. The value of the angle p is determined according to the following formula (see Fig. 9):

$$\tan p = \frac{\sin z}{\operatorname{cosec} \pi - \cos z}.$$

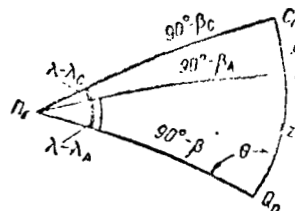


Fig. 10. Spherical Triangle for Determination of z .

In order to obtain the hypso-metric characteristics of the far side of the Moon, the Main Astronomical Observatory of the Academy of Sciences of the Ukrainian S.S.R. undertook a study of individual negatives on which the terminator zone was printed.

Let us investigate photograph No. 22, for which $UT = 2:15:16$. The distance from the apparatus to the center of the Moon was

The value of z can be obtained by an investigation of the spherical triangle QPS , where P is the pole of the Moon (Fig. 10):

$$\cos z = \sin \beta_Q \sin \beta_A + \cos \beta_Q \cos \beta_A \cos (\lambda_A - \lambda_Q).$$

Having determined the auxiliary angle θ from ΔQPA , we can find λ_C and β_C :

$$\frac{\sin \theta}{\cos \beta_A} = \frac{\sin (\lambda_A - \lambda_Q)}{\sin z},$$

$$\sin \beta_C = \sin \beta_Q \cos (z+p) + \cos \beta_Q \sin (z+p) \cos \theta,$$

$$\cos (\lambda_C - \lambda_Q) = \frac{\cos (z+p) - \sin \beta_C \sin \beta_Q}{\cos \beta_C \cos \beta_Q}.$$

Knowing the coordinates of the subsolar point and the apparent center of the disk, we will determine the phase angle thus:

$$\cos \alpha = \sin \beta_{\odot} \sin \beta_C + \cos \beta_{\odot} \cos \beta_C \cos (\lambda_C - \lambda_{\odot})$$

and the angle of incidence of the solar rays, i.e.,

$$\cos i = \sin \beta_{\odot} \sin \beta_Q + \cos \beta_{\odot} \cos \beta_Q \cos (\lambda_Q - \lambda_{\odot}).$$

The angle of reflection of the solar rays $\epsilon = z + p$.

Thus, we can determine each point on the photograph by the selenographic coordinates λ and β , in terms of i , ϵ and α . The selenographic coordinates of the details on the photographs of the Moon were determined according to a map corresponding to the photograph, which is given in [20].

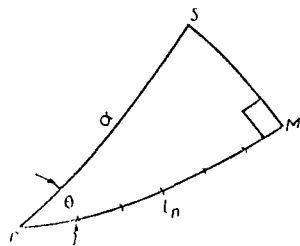
Let us derive the formula to determine the photometric longitude from the spherical triangle QCS (see Fig. 6):

$$\tan (w+\alpha) = \frac{\cos \epsilon - \cos i \cos \alpha}{\cos i \sin \alpha}.$$

This is necessary for calculating the slopes.

For the observer an infinite distance away, the phase angle for all the points on the photograph can be considered as constant. In our case, we must calculate the apparent center for each small region, which will permit us to determine α . The region under investigation (Fig. 11) occurs in the zone around the terminator and is bounded by the coordinates of λ from -155 to -170° and of β from 0 to -10° . The phase angle in the vicinity of this region

changes from $\alpha = 45^{\circ}50'$ (for the region with coordinates of the center of $\lambda = -160^{\circ}$, $\beta = 0$).



Determination of the Position of the Intensity Equator.

The entire region under investigation was divided into three parts; the value for the phase of each part was taken as constant. In addition to the two regions we have cited, we took a region with coordinates of the center of $\lambda = -160^{\circ}$, $\beta = -5^{\circ}$. For it, $\alpha = 46^{\circ}20'$. Thus, depending on the direction of the line of sight for our segment, we have three apparent centers of the Moon's disk. The direction of the cross sections should coincide with the direction of the intensity equator.

The problem is to draw a projection of the intensity equator on the photograph and to have this projection represent a large circle on the sphere, passing through the point of the apparent center and the subsolar point. For this, we must determine the coordinates of several points through which the intensity equator passes. Let us transfer the equator in our minds to the point C (Fig. 12), and let us examine the right triangle CMS , with MS as the meridian of the point S and the coordinates of the point M as $\lambda + \lambda_C$ and $\beta \odot + \beta_C$. Let us divide the line of the intensity equator into a number of intervals (for example, every 5°). We will obtain triangles similar to CMS , from which we can find the values of λ and β for all the points along the intensity equator. It can be seen from Figure 12 that

$$\cos \lambda_n = \frac{\cos l_n}{\cos \beta_n}; \quad \cos \beta_n = \sin l_n \sin \theta.$$

From ΔCMS , we find that

$$\sin \theta = \frac{\sin (\beta \odot + \beta_C)}{\sin \alpha}.$$

The coordinates of the points through which the intensity equator is plotted are $\lambda = \lambda_n + \lambda_C$ and $\beta = \beta_n + \beta_C$.

Three intensity equators were calculated.

Construction of Photometric Sections. The photograph was measured with the aid of an automatic recording microphotometer MF-2, with a record of the blackening points on the recorder tape. The scanning was carried out along the lines. The size of the window was determined by the width of the line. For an enlarge-

ment (X20), the size of the window was equal to 1 X 3 mm. The entire region over which the thalassoid Korolev (see Fig. 11) was located took up 200 lines. We recorded 166 lines. The technique of constructing the photometric sections was the following. The photograph was projected on a screen, on which the coordinate grid was then plotted and the directions of the sections along the intensity equator were determined. Forty sections were made in all. The value of the brightness was determined at the point of intersection between the line and the direction of the photometric section. The number of points on the photometric section varied from 40 to 90. This number of points allowed a complete description of the change in heights (Fig. 13). We took a curve close to a cosine one as the brightness distribution curve along a surface with no macro-irregularities (so-called spherical curve), since the region under investigation occurred in the range of angles of incidence of 80-90°. The section was connected with the spherical curve at the points of the section where $\omega + \alpha = 85^\circ$. The brightnesses along the brightness meridian $\omega + \alpha = 85^\circ$ coincided for all sections, which showed the identical orientation of this direction to the incident rays.

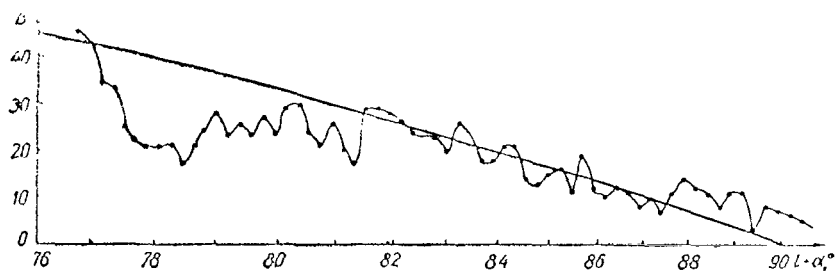


Fig. 13. Photometric Section No. 7.

In studying the relief of the far side of the Moon, we made the following assumptions: (1) the visible and far sides have an identical microstructure; (2) the floors and ridges of the thalassoid are uniform in terms of albedo.

Description of the Thalassoid Korolev. We determined the coordinates of each point λ and β for all the points on the section, as well as the inclinations toward the sphere γ and the heights h in relation to the closest point, which are given in the Appendix. We constructed the profiles for all the sections. Figure 14 gives the profiles of the heights along the sections (height scale: 1 division is 1 km). The zero-point of each section was taken as the point which had zero inclination to the sphere. These points occur on the brightness meridian of $\omega + \alpha = 85^\circ$. We will take the geometric position of the points with zero inclination as the level for all the sections. This allows us to consider all the heights as interconnected, and to construct the relative

chart of the iso-heights of the thalassoid. The relative excesses of points a distance of 5-10 km from each other were found to be equal to 200-500 km, which corresponds to deviations of 1/20. Considering the value of the change in slopes, we can assume that the inner slab of the thalassoid is surrounded by two ring-shaped faults. The radius of the inner slab is 2° in longitude, that of the first ring is 4° , and that of the second ring is 8° . The slopes of the irregularities of the inner portion of the thalassoid are in correspondence with the slopes of the scarps of the maria regions on the visible side, and occur within the range of $0-2^\circ$. The irregularities of the first ring have inclination of $2-4^\circ$, and those of the second have $3-7^\circ$. The second ring is speckled with craters. The ridges of these craters have slopes of $10-25^\circ$.

Formations similar to the thalassoid were found on the visible side after rectification of the lunar photographs [21]. These formations include [22] Mare Nectaris, Mare Humorum, Mare Imbrium, Mare Humboldtianum, Mare Orientalis, etc. Thus, ring-shaped faults and mountain chains apparently should accompany all the maria of regular shapes. It is possible that the establishment of such a characteristic of the entire surface of the Moon will show that the vast ring-shaped basins are the oldest formations, arising as a result of the deposit of the lunar crust. The ridges of sunken craters can be seen at the bottom of many maria; however, there are many fewer such ridges in maria of regular shapes than in those of irregular shape, such as Oceanus Procellarum, Mare Nubium and Mare Tranquillitatis. The existence of phantom craters indicates that the basins are filled with lava, but that the thickness of the lava varies. Considering the photographs of the far side of the Moon, the thalassoid Korolev does not show any phantom craters at the bottom or damaged craters along the edges. This characteristic is also observed in the thalassoid with coordinates of the center of $\beta = 0$, $\lambda = -131^\circ$.

The relief of the visible side of the Moon is smoother. This is possibly the result of the eruption of lava in the region of Mare Imbrium and its subsequent spreading over the entire hemisphere.

A comparison of the near and far sides of the Moon would be more complete if there were a hypsometric map of both hemispheres. This would allow us to evaluate different levels of the maria regions and similar areas, as well as the depths of craters, and it would aid in finding the principal factors affecting the origination of the morphological characteristics of the lunar relief.

REFERENCES

1. Barabashov, N.P.: Akad. Nauk, Vol. 217, No. 5, p. 207, 1922.
2. Markov, A.V.: Akad. Nauk, Vol. 221, p. 65, 1924.
3. Opik, E.: Publ. Astron. Obs. Tartu, Vol. 26, pp. 1-68, 1924.
4. Bennet, A.L.: Astrophys. J., Vol. 88, pp. 1-26, 1938.
5. Fedorets, V.A.: V kn.: Trudy Khar'kovskoy astronomicheskoy observatorii (Procedures of the Kharkov Astronomical Observatory) Vol. 2. Kharkov State University Press, 1952.
6. Diggelen, J.: Rech. Obs. Utrecht, Vol. 14, pp. 1-114, 1959.
7. Minnart, M.: Planety i sputniki (Planets and Satellites) ed. Koyper. Foreign Literature Publishing House, 1963.
8. Fesenkov, V.G.: Physics and Astronomy of the Moon, ed. Z. Kopal. Academic Press, New York, pp. 99-128, 1962.
9. Hapke, B.: J. Geophys. Res., Vol. 68, No. 15, pp. 4571-4586, 1963.
10. Hapke, B.: Astron J., Vol. 71, No. 5, pp. 333-339, 1966.
11. Akimov, A.A.: Vestnik Khar'kovsk. Universitet., Vol. 1, No. 4, pp. 43-61, 1965.
12. Pohn, H.A.: PASP, Vol. 75, p. 443, 1963.
13. Wildey, R.L., and H.A. Pohn: Astron J., Vol. 69, No. 8, pp. 619-634, 1964.
14. Barabashov, N.P., V.I. Yezerskiy and N.P. Prishlyak: Tsirkulyar KhGU (Kharkov State University Pamphlet), Vol. 25, 1962.
15. Barabashov, N.P. and V.I. Yezerskiy: Vestnik Khar'kovskogo Gosudarstv. Universitet., Vol. 4, 1965.
16. Shoemaker, E.M.: Scient. Amer., Vol. 211, No. 6, pp. 38-47, 1964.
17. Lisina, L.R.: In the Book: Fizika Luny i planet (Physics of the Moon and Planets), Kiev, "Naukova dumka", 1966.
18. Diggelen J.: B.A.N., Vol. 11, No. 423, p. 283, 1951.
19. Lipskiy, Yu.N. et al.: Kosmicheskiye Issledovaniya, Vol. 4, No. 6, pp. 912-922, 1966.
20. Atlas obratnoy storony Luny. ChII. (Atlas of the Far Side of the Moon. Part II). Moscow, "Nauka", 1967.
21. Whitaker, E.A.: ed. Rectified Lunar Atlas. Suppl. Number Two to the Photographic Lunar Atlas. The Univers. of Arizona Press, Tucson, 1963.
22. Hartmann, W.K., and G.R. Kuiper: Communs Lunar and Planetary Lab., Vol. 1, p. 12, 1962.

APPENDIX

M	λ	β	γ	h, m	M	λ	β	γ	h, m
Section 1					Section 2				
1	$-158^{\circ}50'$		$-2^{\circ}84'$	-713	1	$-158^{\circ}21'$		$-1^{\circ}50'$	-474
2	159 34	$-0^{\circ}40'$	2.60	232	2	158 50		4.92	1250
3	159 44		1.04	184	3	159 17		0.28	26
4	160 04		2.04	181	4	159 26		3.21	953
5	160 14		1.24	191	5	159 54	$-1^{\circ}04'$		10
6	160 32	0 50	3.12	1251	6	160 04			4
7	161 17		0	0	7	160 22			2
8	161 44		0.05	0	8	160 45	1 11	0.12	1
9	162 02		1.00	238	9	161 07		2.08	4
10	162 24		1.10	126	10	161 31		+0.40	+50
11	162 36	1 01	0.05	0	11	161 43	1 14	1.1	0
12	163 06		+2.35	+730	12	162 07		-0.10	-100
13	163 39		4.40	2191	13	162 41		+1.50	+322
14	164 10	1 20	3.85	868	14	163 05	1 29	3.0	40
15	164 31	1 21	+3.05	+1380	15	163 17		2.60	380
16	165 17		0	0	16	163 40	1 38	1.35	858
17	165 43		10	2468	17	164 05		1.45	170
18	166 08		6.56	1469	18	164 17		3.20	1160
19	166 31	1 24	9.56	1281	19	164 50	1 40	1.35	271
20	166 44		6.00	1156	20	165 14		12.0	2721
					21	165 38		4.30	1436
					22	166 15	1 41	1.90	930

APPENDIX (cont'd)

№	λ	β	γ	h, m	№	λ	β	γ	h, m
Section 3					23	166°05'		+3.58	+770
1	158°05'	-1°06'	-3.06	-643	24	166 29		2.16	499
2	158 30		6.79	1061	25	166 55		2.05	1110
3	158 42		5.17	1677	Section 5				
4	159 11		-1.88	-191	1	157 21		-4.72	-437
5	159 21	-1°18'	3.62	910	2	157 30	-1°43'	2.88	741
6	159 47		2.12	204	3	157 56		6.80	691
7	159 56		3.54	679	4	158 06		5.32	950
8	160 18		1.25	240	5	158 26		5.44	507
9	160 40		0.46	189	6	158 36		5.32	950
10	161 24	1 37	0.15	20	7	159 02		-3.56	-667
11	161 36		1.60	463	8	159 22	-2 07	4.44	1240
12	162 10		0	0	9	159 50		2.17	420
13	162 58		+2.15	+412	10	160 10		0	0
14	163 20	1 49	1.00	223	11	160 20		1.42	264
15	163 45		3.25	1374	12	160 40		0.36	28
16	164 21		1.74	388	13	160 48		+1.86	+623
17	164 43		5.53	657	14	161 21	2 25	-0.27	-29
18	164 55	1 58	2.95	1123	15	161 33		+0.59	+67
19	165 16		3.47	1060	16	161 46		-0.50	-10
20	166 10		0.94	326	17	162 07		+0.45	+199
21	166 45		3.79	903	18	162 55	2 35	4.10	1276
22	167 02	2 15	7.47	1393	19	163 30		-0.25	-56
Section 4					20	163 55		+6.50	+1936
1	157 52		-3.00	-514	21	164 30		-0.55	110
2	158 12	-1 32	5.57	1310	22	164 53	2 47	0.11	-32
3	158 42		5.25	854	23	165 27		+2.53	+300
4	159 00		3.25	528	24	165 40		0.79	190
5	159 20	1 43	4.25	297	25	166 05		2.21	457
6	159 30		3.79	737	26	166 26		0.84	296
7	159 50		-4.79	-1310	27	166 50	2 53	2.32	275
8	160 20		2.12	430	28	167 14		+0.80	179
9	160 42		1.88	350	29	167 30		3.74	443
10	161 02		0.71	152	30	167 42		2.9	278
11	161 22	-2 02	0	0	31	167 55		4.53	642
12	161 52		+14.0	+997	32	168 07		1.84	435
13	162 00		0.90	320	Section 6				
14	162 34		0.65	192	1	156 57		-3.12	-288
15	163 07		3.05	586	2	157 05		4.80	412
16	163 30	2 15	4.30	1534	3	157 14		3.20	749
17	164 05		1.35	120	4	157 40	-2 05	5.84	1134
18	164 17		2.68	257	5	157 57		4.60	860
19	164 40		1.16	277	6	158 14		5.52	386
20	164 53	2 23	1.74	567	7	158 22	2 15	3.48	950
21	165 27		2.47	295	8	158 49		4.04	345
22	165 40		1.79	414	9	158 58		2.92	270

APPENDIX (cont'd)

№	λ	β	γ	h, m	№	λ	β	γ	h, m
10	-159°06'		-4.24	-1154	20	-163°20'		-0.00	0
11	159 34	-2°28'	1.52	154	21	163 29		1.05	- 93
12	159 44		2.17	420	22	163 37		+1.50	+335
13	160 02		+0.22	+ 37	23	164 06		-0.79	-172
14	160 22		-1.17	-255	24	164 30		0.00	0
15	160 44		0.65	250	25	165 10	-3°32'	-0.53	-126
16	161 26	2 46	0.00	0	26	165 30		+2.16	+491
17	161 37		+0.81	+172	27	165 55		1.74	218
18	162 00		-1.62	-352	28	166 07		1.00	200
19	162 37		0.24	67	29	166 30	3 33	2.47	1116
20	162 45		+1.81	+166	30	167 10		2.06	462
21	162 55	2 55	-0.24	75	31	167 35		2.61	386
22	163 20		+2.05	+412	32	167 48		0.94	326
23	163 43		-0.26	80	33	168 35		5.00	1715
24	164 05		+0.84	+104	34	169 10		7.70	973
25	164 17		-0.16	0	Section 8				
26	-164 30	-3 04	-0.53	-95	1	-156 46	-2 33	-0.81	-143
27	165 02		+1.11	+236	2	157 03		4.46	96
28	165 25		0.63	145	3	157 12		3.46	1188
29	165 50		1.53	330	4	157 42		5.81	1036
30	166 13		1.32	156	5	157 58		1.35	220
31	166 31		3.47	800	6	158 14	-2 56	4.23	792
32	166 52	3 13	1.53	330	7	158 30		+0.42	+ 99
33	167 20		3.21	+970	8	158 52		-2.77	-517
34	167 45		1.30	377	9	159 09		0.24	73
35	168 20		3.17	708	10	159 36		1.80	113
36	168 45		4.50	1470	11	159 43	-3 10	+0.28	+ 24
Section 7					12	159 52		0.00	0
1	-156 31		+0.69	113	13	160 01		+0.37	+155
2	156 49	-2 13	-2.42	-430	14	160 45		-1.19	-111
3	157 07		4.58	756	15	160 53		0.90	190
4	157 23		5.27	940	16	161 16	-3 25	1.28	415
5	157 41		4.92	1720	17	161 50		0.24	66
6	158 18	2 37	2.35	656	18	162 18		1.43	605
7	158 48		2.88	942	19	163 11		0.38	43
8	159 22	2 47	0.41	94	20	163 24	-3 41	1.05	210
9	159 42		2.50	135	21	163 48		0.00	0
10	159 52		1.08	185	22	164 12		1.84	387
11	160 10		3.13	602	23	164 36		+1.68	+160
12	160 30		+0.62	+229	24	164 44	3 51	0.00	0
13	161 10	3 03	-0.32	-29	25	164 58		+0.21	+ 65
14	161 20		0.00	0	26	165 34		1.58	177
15	161 30		-0.82	- 84	27	165 46		0.84	277
16	161 40		+1.23	+338	28	166 20		1.68	200
17	162 15		-0.64	-117	29	166 32	3 57	3.26	386
18	162 35		+0.75	+161	30	166 45		2.47	513
19	162 58	-3 18'	-1.25	-240	31	167 12		3.83	1020
					32	167 36		3.11	413

APPENDIX (cont'd)

N ₂	λ	β	γ	h, m	N ₂	λ	β	γ	h, m
33	-167°48'		+3.94	+378	Section 10				
34	168		1.72	243	1	-155°58'		-7.04	-2085
35	168 12		2.72	341	2	156 42		3.07	311
36	168 24		2.33	244	3	156 55	-3°15'	3.75	498
37	168 36		3.78	476	4	157 19		+1.57	+270
38	168 48		3.17	1316	5	157 44		4.07	1550
39	169 30		5.22	2209	6	158 47		-1.96	-1166
Section 9					7	159 39		1.26	222
1	-155 50		-5.58	895	8	159 57	-3 53	2.83	1072
2	156 12	-2°46'	6.73	2144	9	160 33		1.48	174
3	157 01		4.42	1096	10	160 44		2.04	554
4	157 36		+0.38	+1045	11	161 05		1.28	444
5	158 10	3 13	0.00	0	12	161 50	-4 10	2.60	213
6	158 28		0.22	20	13	162 00		0.60	67
7	158 38		3.65	648	14	162 10		1.64	328
8	158 54		-1.46	-150	15	162 28		0	0
9	159 12		+0.04	+ 10	16	163 00		1.24	129
10	159 20		1.17	108	17	163 14	-4 18	0.52	54
11	159 30	3 29	-2.50	-721	18	163 28		1.32	108
12	159 58		0.50	77	19	163 40		0.60	58
13	160 16		1.29	502	20	163 54		1.20	37
14	160 56		0.00	0	21	164 30	-4 31	+0.40	+ 74
15	161 16	3 45	1.71	190	22	164 53		-0.73	- 85
16	161 29		0.83	87	23	165 05		+0.89	+386
17	161 41		1.22	108	24	165 50		3.53	755
18	161 51		0.39	48	25	166 15	-4 37	1.47	315
19	162 05		1.61	284	26	166 42		2.57	269
20	162 55		-0.93	-205	27	166 57		1.83	444
21	162 55		+0.73	+160	28	167 18		3.53	1124
22	163 17	-3 58	0.24	28	29	167 57		1.37	183
23	163 30		-1.71	-151	30	168 06		3.16	730
24	163 40		0.34	31	31	168 30		2.74	593
25	163 53		0.98	330	32	168 57		4.10	430
26	164 26		0	0	33	169 06		3.08	+690
27	164 36		-1.10	-130	34	169 30		5.54	736
28	165 00	-4 18	+0.37	+163	35	169 42		3.31	708
29	165 50		2.53	524	Section 11				
30	166 13		3.32	713	1	-155 48		0	0
31	166 36		2.37	504	2	155 53	-3 18	-4.90	-1106
32	167 03	-4 24	2.95	1051	3	156 18		+0.52	+ 44
33	167 45		5.56	1318	4	156 25	3 33	-5.93	-1709
34	168 05		1.22	252	5	156 49		7.55	1705
35	168 30		4.06	1147	6	157 11		0.62	398
36	169 00		3.61	377	7	158 25	3 58	0	0
37	169 12		5.56	1357	8	158 50		+5.86	+1546
38	169 36		4.78	460	9	159 16	4 09	-2.04	-788
39	169 48		3.67	741					

APPENDIX (cont'd)

№	λ	β	γ	h, м	№	λ	β	γ	h, м
10	—159°56'		—2.74	—525	20	—162°48'		—0.49	— 55
11	160 15		—1.56	—230	21	162 58		2.44	1028
12	160 35		2.49	538	22	163 47		1.56	480
13	160 56		2.05	426	23	164 23		0	0
14	161 20	—4°28'	3.17	730	24	164 47	—5°10'	+0.78	+087
15	161 49		1.41	268	25	165 00		—0.20	—040
16	162 13		2.20	457	26	165 23		+1.75	+335
17	162 40		1.41	488	27	165 47		0.34	35
18	163 13	4 39	1.95	303	28	166 00		1.56	297
19	163 33		1.85	384	29	166 23		1.07	95
20	163 53		0.15	15	30	166 34	5 17	0.11	28
21	164 04		1.95	360	31	167 00		1.94	172
22	164 24		1.22	142	32	167 10		1.50	257
23	164 35		0.00	0	33	167 25		4.94	1104
24	164 44	4 47	+2.44	+489	34	167 48		2.33	293
25	165 05		0.78	+175	35	168 00		4.39	653
26	165 30		0.34	103	36	168 20	5 20	3.11	595
27	166 02		1.56	330	37	168 30		2.39	251
28	166 28		0.68	608	38	168 40		4.56	605
29	166 38		1.60	552	39	168 50		2.50	279
30	167 12		1.37	440	40	169 30		4.28	960
31	167 50		3.60	805	41	169 50		3.56	790
32	168 06		2.80	313	Section 13				
33	168 20	—5 00	5.43	1289	1	—155 55		—6.46	—960
34	168 45		3.54	864	2	156 07	—4 36	4.36	1687
35	169 15		4.80	1210	3	156 50		0	0
36	169 40		3.26	341	4	157 12		+6.79	+2276
Section 12					5	158 00	4 53	—1.75	—475
1	—156 11		—8.00	—2557	6	158 17		+10.0	+1727
2	156 45		1.24	172	7	158 34		—2.62	—507
3	157 02		2.22	186	8	158 50		0.87	87
4	157 10	—4 09	0.69	217	9	159 00		2.08	211
5	157 38		+10.00	+1569	10	159 11	5 00	0.09	28
6	158 04		1.49	357	11	159 42		3.42	985
7	158 32		9.00	1615	12	160 14		1.56	113
8	158 50		—1.02	—186	13	160 23		1.83	176
9	159 10	4 33	2.42	451	14	160 34		1.48	318
10	159 31		1.50	257	15	160 58		2.28	219
11	159 53		2.67	494	16	161 10	5 21	1.05	139
12	160 12		0.46	96	17	161 22		2.38	158
13	160 32		2.71	518	18	161 32		2.14	491
14	160 50		0.75	241	19	161 55		5.24	1007
15	161 23	4 53	—2.34	—468	20	162 16		1.81	213
16	161 47		0.97	230	21	162 27		2.19	98
17	162 08		2.73	467	22	162 39		0.76	157
18	162 28		0.34	039	23	163 00	5 30	1.57	325
19	162 38	5 01	1.32	087	24	163 25		0.89	394

APPENDIX (cont'd)

No	λ	β	γ	h, μ	No	λ	β	γ	h, μ
25	-164°20'		-1.21	-115	30	-165°36'		+2.47	+252
26	164 32		+0.24	+038	31	165 46		0.79	155
27	165 09	-5°35'	0.05	0	32	166 10		2.21	510
28	165 20		0.95	169	33	166 20		0.84	265
29	165 41		-0.16	-038	34	167 12		2.42	607
30	166 02		+1.58	+130	35	167 36		2.05	197
31	166 13		0	0	36	167 48		1.32	439
32	166 33		2.58	288	37	168 20		4.95	680
33	166 41		0.89	180	38	168 30	-6°00'	+3.26	+267
34	167 05	5 42	2.00	415	39	168 40		3.84	429
35	167 30		1.53	251	40	168 50		3.37	323
36	167 45		2.63	448	41	169		1.37	273
37	168 10		4.20	970	42	169 30		4.03	2467
38	168 30		2.21	422	Section 15				
39	169 00		3.26	451	1	156 07		-2.46	-365
40	169 20		4.80	570	2	156 22		3.3	512
41	169 30		3.58	770	3	156 41	4 56	0.38	51
Section 14					4	156 57		1.61	138
1	-156 08	-4 39	-3.55	-507	5	157 13		+0.1	0
2	156 26		4.10	1498	6	157 23		1.6	+239
3	157 10		+1.55	+ 44	7	157 40		-1.79	-193
4	157 16	4 56	0	0	8	157 47	5 16	1.33	249
5	157 20		-1.69	-200	9	158 07		2.63	469
6	157 29		+0.31	+ 48	10	158 27		0.5	054
7	157 47		6.1	950	11	158 39		1.17	117
8	158 07	5 06	-1.91	-192	12	158 51		0.92	070
9	158 11		3.13	585	13	159 00		2.83	262
10	158 32		0.96	186	14	159 10		1.17	207
11	158 50		2.78	-214	15	159 28	5 31	4.04	1100
12	158 58		0.69	127	16	159 54		1.09	185
13	159 16	-5 15	4.09	393	17	160 15		1.0	139
14	159 26		2.83	272	18	160 32		3.36	470
15	159 35		3.13	415	19	160 50		4.79	1596
16	159 43		1.87	227	20	161 21	5 48	0	0
17	160 00		3.30	616	21	161 46		2	666
18	160 23	-5 26	1.04	288	22	162 20		-0.5	-103
19	160 55		3.40	699	23	162 42		0	0
20	161 16		1.30	75	24	163 05		1.62	361
21	161 25		3.65	785	25	163 29	-6 00	+1.59	+292
22	161 49	5 37	0.50	118	26	163 50		-1.66	-186
23	162 23		0.15	32	27	164 02		0.48	107
24	162 47		2.74	892	28	164 25		0.52	103
25	163 24		+3.16	+658	29	164 48		+1.33	+149
26	163 49		-1.37	-423	30	165 00		-0.67	- 64
27	164 25		0.10	19	31	165 09	6.11	+2.38	+690
28	164 48		0.68	197	32	165 42		0.2	022
29	165 13	5 53	+0.10	+ 19	33	165 51		3.19	495

APPENDIX (cont'd)

[illegible]

APPENDIX (cont'd)

N	λ	β	γ	h, m	N	λ	β	γ	h, m
42	-167°44'		+2.68	+1115	42	-167°30'		+4.32	+536
43	168 32	-7°00'	4.42	625	43	167 43		2.26	507
44	168 44		3.47	1562	44	168 10		2.37	530
45	169 25		4.42	988	45	168 30	-7°20'	4.80	1310
46	169 50		6.50	2278	46	168 50		3.42	734
Section 18					47	169 12		7.00	675
1	155 40	-5 50	-4.70	-806	48	169 24		6.26	2230
2	155 58		2.0	297	49	170 00		10.00	1262
3	156 16		1.67	142	Section 19				
4	156 26		5.11	394	1	155 52		-2.15	-349
5	156 36		3.11	266	2	156 10		0.38	95
6	156 42	6 09	5.00	1208	3	156 23	-6 16	4.53	1126
7	157 10		+0.63	+ 98	4	157 05		+4.58	+1075
8	157 28		10.0	864	5	157 33		-2.96	-274
9	157 38		4.52	387	6	157 42		1.65	524
10	157 46		7.0	601	7	158 17	6 35	+0.54	+125
11	157 56	6 22	-2.89	-851	8	158 43		-2.04	-348
12	158 32		0	0	9	159 02		1.19	92
13	158 50		2.8	523	10	159 11		3.38	290
14	159 10		2.0	185	11	159 22		2.00	185
15	159 20	6 37	3.13	530	12	159 30	6 51	4.19	749
16	159 38		1.0	186	13	159 43		2.05	208
17	159 58		2.27	230	14	160 05		3.00	304
18	160 10		1.67	338	15	160 16		2.10	393
19	160 31		2.5	271	16	160 37		4.10	796
20	160 43		1.9	163	17	160 58		2.19	461
21	160 53		4.2	426	18	161 20	7 17	1.42	150
22	161 05	6 55	1.8	345	19	161 35		2.28	658
23	161 27		4.9	986	20	162 08		+0.33	+ 74
24	161 50		0.5	58	21	162 30		-1.05	-326
25	162 02		2.1	235	22	163 05		-0.55	- 61
26	162 15		0.7	211	23	163 20	7 23	1.95	347
27	162 46		2.7	420	24	163 43		+0.95	+126
28	162 58	-7 03	1.0	80	25	163 53		-0.95	- 65
29	163 10		2.5	502	26	164 02		+0.10	+ 20
30	163 31		1.2	240	27	164 24		-0.65	- 74
31	163 51		+0.2	+ 22	28	164 38		0	0
32	164 05	-7 08	-1.15	-102	29	164 50		0	0
33	164 15		+0.35	+ 70	30	165 00		+1.65	+184
34	164 26		0	0	31	165 12	-7 35	0.55	241
35	164 37		0.15	17	32	166 06		2.06	429
36	164 50	-7 12	1.0	155	33	166 32		2.89	648
37	165 25		0.45	96	34	166 54		0.44	168
38	165 48		2.2	241	35	167 44		2.44	323
39	166 00		0.9	187	36	167 56		2.06	690
40	166 26		2.37	578	37	168 30	7 40	4.44	1876
41	166 54	-7 17	1.32	412	38	169 25		5.72	641

APPENDIX (cont'd)

N	λ	β	γ	h, m	N	λ	β	γ	h, m
Section 20					13	-159°24'	-7.30'	-3.83	-683
1	-155°54'	-6°24'	-6.69	-1406	14	159 43		4.81	-1425
2	156 19		5.37	1756	15	160 15		0.76	173
3	156 54		+2.5	+4756	16	160 40		2.43	208
4	157 10	6 42	-1.41	-408	17	160 50		1.05	220
5	157 36		0	0	18	161 12	7 47	5.90	1715
6	157 47		2.15	-184	19	161 46		0.62	65
7	157 56		0.83	71	20	161 58		1.90	551
8	158 13	6 55	0.56	49	21	162 34		0.57	118
9	158 23		0.92	314	22	162 58		2.00	164
10	158 58		+1.59	+392	23	163 17		+1.33	+140
11	159 25	7 09	-4.98	-1317	24	163 20	8 03	-0.33	-126
12	159 51		1.91	195	25	164 05		0.71	154
13	160 00		2.93	292	26	164 31		+1.33	+149
14	160 10		1.72	330	27	164 41		0	0
15	160 36		2.60	499	28	165 08		1.38	143
16	161 00		5.07	976	29	165 20	8 15	0	0
17	161 23	7 37	1.12	347	30	165 30		0.90	53
18	162 00		+3.02	+806	31	165 43		-0.19	-113
19	162 26		-0.88	-40	32	167 06		+2.66	+256
20	162 40		1.95	378	33	167 19	8 18	2.30	768
21	163 00		0.60	63	34	167 40		4.00	776
22	163 14	4 42	1.53	547	35	167 52		2.90	345
23	163 58		+0.14	+29	36	168 05		5.95	792
24	164 21		1.39	196	37	168 17		4.45	+467
25	165 21	7 56	1.61	313	38	168 30	-8 20	6.95	926
26	165 44		0	0	39	168 42		5.02	+1826
27	166 10		-0.56	-98	Section 22				
28	166 32		+1.78	+224	1	155 34	7 00	-2.18	-151
29	166 44		0.44	15	2	155 43		3.93	1314
30	167 17		2.78	330	3	156 17		+1.57	+134
31	168 15		4.67	1942	4	156 36	7 19	0	0
32	169 00	8 00	6.06	765	5	156 52		0.39	60
Section 21					6	157 10		4.36	711
1	155 19	6 36	-2.62	-507	7	157 30		-0.46	-70
2	155 38		3.52	166	8	157 38		+0.89	+131
3	155 46		2.48	443	9	157 54	7 34	0	0
4	156 11		5.83	194	10	158 14		-1.43	-90
5	156 28	6 57	1.66	285	11	158 22		+2.64	+225
6	157 04		+0.55	+124	12	158 32		8.00	1307
7	157 30		-1.41	-99	13	158 50		4.11	511
8	157 38		-0.34	26	14	159 10		-0.96	-98
9	157 46		1.66	247	15	159 20	7 49	+1.50	+385
10	158 03	7 17	0.52	40	16	159 48		-3.77	-703
11	158 12		+0.31	+92	17	160 07		2.09	389
12	158 47		1.18	368	18	160 25		4.64	761
					19	160 50		1.55	184

APPENDIX (cont'd)

[illegible]

APPENDIX (cont'd)

	λ	β	γ	h, m	No	λ	β	γ	h, m
3	—155°30'		—3°14	—268	10	—157°48'		—0°86	—140
4	155 40		3.57	305	11	158 06	—8°53'	1.21	301
5	155 50		1.61	214	12	158 34		0.61	29
6	156 08		2.46	401	13	158 44		1.32	313
7	156 25		0.68	106	14	159 13		1.18	149
8	156 40	—8°18'	+2.75	+214	15	159 36	9 13	1.49	142
9	156 51		10.00	1569	16	159 50		0.72	6
10	157 07		0.39	30	17	160 00		1.66	419
11	157 25		—1.25	—301	18	160 28		0.21	37
12	157 41		0.00	0	19	160 40	9 23		295
13	157 51		—1.41	—351	20	161 07		1.76	31
14	158 18	8 34	+0.59	+192	21	161 39		2.91	969
15	158 36		0.44	37	22	162 09		+0.72	+391
16	158 46		+1.15	+277	23	163 07	9 42	+9.72	4725
17	159 15		—1.00	—163	24	163 55		1.41	160
18	159 35	8 54	+1.22	+197	25	164 05		—0.33	—79
19	159 56		—0.70	—140	26	164 27		+3.19	+473
20	160 15		2.70	241	27	165 05		4.91	338
21	160 26		1.74	129	28	165 39	—9 53	1.81	605
22	160 35		3.17	586	29	166 02		4.12	367
23	160 57		0.87	148					
24	161 18		+0.13	+ 41					
25	161 53	9 12	—2.00	—356					
26	162 15		0.37	79					
27	162 40		+1.81	+518					
28	163 13	9 24	3.17	962	1	—155 56		—2.32	—737
29	163 50		—0.95	—113	2	156 35	—8 57	0.71	172
30	164 03		0.00	0	3	157 04		0.78	181
31	164 27		1.95	405	4	157 35		4.12	965
32	164 52		+3.05	+341	5	158 06		0.00	0
33	165 05		1.42	136	6	158 15	9 18	1.61	127
34	165 16		2.53	318	7	158 25		+0.75	+111
35	165 29	9 31	1.53	364	8	158 45		—1.14	255
36	165 52		1.05	148	9	159 09		0.83	129
37	166 05		2.89	706	10	159 30	9 36	1.88	704
38	166 27		1.79	504	11	160 13		0.83	77
					12	160 24		1.38	246
					13	160 44		0.21	63
					14	161 17	9 48	3.62	1612
					15	162 00		+1.67	+372
					16	162 22		0.00	0
					17	162 47		4.52	434
					18	162 57		7.96	1196
					19	163 09		5.48	490
					20	163 19	10 02	9.40	2467
					21	163 44		—0.61	—248
					22	164 05		+3.28	+1706
					23	164 55		1.78	211
					24	165 05	—10 11	0.28	47

APPENDIX (cont'd)

№	λ	β	γ	h, m	№	λ	β	γ	h, m
Section 28					17	159°15'		0	0
1	156°00'		-5.67	-1984	18	159°11'		-1.70	-152
2	156°39'	-9°17'	4.18	197	19	159°11'	-10°18'	0.83	136
3	156°47'		1.11	199	20	160°01'		2.05	472
4	157°04'		2.86	536	21	160°24'		0.79	61
5	157°23'		1.00	133	22	160°47'		0.72	170
6	157°40'		1.54	131	23	161°06'		0.50	66
7	157°50'		0.50	51	24	161°17'		2.78	211
8	158°06'		1.00	111	25	161°25'		0	0
9	158°16'	9°38'	1.78	277	26	161°35'	-10°30'	+1.20	1276
10	158°31'		0.21	32	27	161°36'		0	0
11	158°50'		2.31	312	28	162°15'		6.81	271
12	159°10'		1.51	278	29	162°45'		-0.28	-61
13	159°28'	9°56'	+0.59	+61	30	163°11'	10°40'	0	0
14	159°38'		-2.17	-60	Section 30				
15	160°07'		1.42	271	1	158°34'		-5.61	-392
16	160°30'		1.36	132	2	158°59'		6.71	1092
17	160°39'		2.50	214	3	156°02'		5.78	861
18	160°51'	10°04'	1.35	169	4	156°20'		2.00	747
19	161°02'		2.89	86	5	157°01'	-10°04'	1.21	102
20	161°32'		2.72	602	6	157°11'		1.32	92
21	161°44'		0.00	0	7	157°21'		2.86	316
22	162°04'		+2.00	+621	8	157°40'		4.36	719
23	162°37'		+11.07	+2817	9	157°58'		+2.14	+149
24	162°58'		1.50	313	10	158°08'		-1.96	-741
25	163°19'	-10°21'	0.67	91	11	158°52'	10°24'	0.04	0
26	163°31'		1.94	273	12	159°20'		1.74	270
27	163°43'		0	0	13	159°37'		0.78	194
28	163°55'		2.50	1910	14	160°14'		0.52	180
Section 29					15	160°50'		+0.35	+75
1	154°46'		-4.39	-922	16	161°16'	-10°45'	-1.61	-390
2	155°10'		6.07	1084	17	161°47'		0	0
3	155°30'	-9°18'	4.86	230	18	162°00'		0	0
4	155°38'		5.57	955	19	162°24'		+0.06	+14
5	155°56'		5.00	389	Section 31				
6	156°04'		7.16	955	1	155°30'	-10°00'	-4.24	-329
7	156°21'		4.33	743	2	155°40'	-10°10'	-5.96	-1813
8	156°40'		1.04	72	3	156°19'		3.28	792
9	156°48'	-9°39'	1.86	160	4	156°48'	10°20'	4.59	643
10	156°58'		0	0	5	157°06'		3.14	197
11	157°06'		1.82	155	6	157°13'		1.55	133
12	157°25'		0	0	7	157°22'		1.38	107
13	157°50'		1.50	105	8	157°35'		0.93	124
14	158°00'		2.73	640	9	157°56'		2.21	341
15	158°28'	-10°00'	0.54	593	10	158°14'		0.10	013
16	158°56'		1.65	245	11	158°31'	10°39'	2.37	495

APPENDIX (cont'd)

[illegible]

STRUCTURAL CHARACTERISTICS OF SOME CRATERS ON THE FAR SIDE OF THE MOON

M.N. Mironova

ABSTRACT: The profiles of 29 craters on the far side of the Moon are reviewed. The photographs obtained by the automatic interplanetary station Zond-3 were used. The photometric method of investigating the lunar surface was applied, and the method of obtaining the profiles of craters from lunar photographs taken from a spacecraft is described. The size and form of the lunar craters on the far side are similar to those on the near side. The depth-to-diameter ratios obtained for the craters under investigation are the same as those assumed for the eruptive craters. The older craters have greater dimensions and depths and look like a "cup". Younger craters have inner shapes in the form of the frustum of a cone. It appears that the crater formations on the far and near sides of the Moon are the same.

Annular structures are one of the most remarkable features of the lunar relief. Many years of studies on such formations on the near side of the Moon have allowed us to establish the characteristics of their structure, to find the statistical dependences between the magnitudes characterizing their form, and even to draw conclusions on the nature of the process of the arisal of ring-shaped mountains on the Moon.

The ring formations, of sizes ranging from several hundreds of kilometers to one-half a meter and smaller, cover the surface of the Moon in a solid mosaic structure. Their shape varies: cup-like formations and ones in the form of the frustum of a cone can be distinguished [1]. It is possible that the "roundness" of the form is frequently lost [2] because of ruptures and faults in the lunar crust. The inner slopes of the ridges of all the craters are steeper than the outer ones. It has been established that the curvature of the inner slope decreases with an increase in the diameter of the crater. Craters with central mountains usually have more steeply ascending ridges than craters of the same size without central peaks [1].

The "Schröter rule", according to which the internal volume of the crater is equal to the volume of masses ejected from it, is not satisfied for all objects [3].

It has been established that the ratio between the depth and the diameter of lunar craters is well represented by the dependence obtained for similar characteristics of eruptive craters [4,5]. Studies of the age sequence of the ring forms have shown that, in the majority of the cases, the younger craters are smaller in size and their bottoms are deeper [3]. The ring formations on the far side of the Moon do not differ from like objects on the near side in terms of their general nature and structure [6]. It has been of interest to obtain the quantitative characteristics which describe the shape and structure of the ring formations on the far side of the Moon, and to compare them with the known characteristics of formations on the near side.

A description of the method of obtaining these characteristics and the principal results are given in this study. Some of them were published in [11].

The height profiles of about 40 craters were constructed and such characteristics of the craters as the principal diameter, the depth, diameter of the floor, curvature of the slopes of the ridges, etc. were taken.

We used the photographs of the far side of the Moon which were obtained from the automatic interplanetary station "Zond-3". The characteristics of these photographs are given in Table 1. The negatives were measured on the automatic microphotometer MF-4 with a record of the blackenings on the recorder tape. The scanning was carried out along the lines. The size of the aperture was 0.05 x 0.15 mm.

TABLE 1

Photo-graph No.	Moment of the Photograph (UT)	Selenographic Coordinates of the Subinstrumental Point		Distance from the Spacecraft to the Lunar Surface, km
		λ_A	β_A	
22	2 ^h 15 ^m 16 ^s	-122°55'	-23°46'	10879
26	2 24 12	132 01	24 32	11211
28	2 28 40	136 22	24 42	11456

The photometric method of studying irregularities in the lunar surface was used in order to obtain the height profiles of the craters. The method selected for studying the relief allowed us to construct the height profiles of the lighted ridges and craters, according to one negative, while the shadow method would give only one characteristic in this case - the height of the ridge.

The principal theories of the photometric method are described in [7-9], where the results of its application to photographs of

the Moon obtained from the Earth are also given. A study of the negatives transmitted by the AIS "Zond-3" required a further development of the photometric method with a consideration of the characteristics of the Moon photographs obtained at close range. The method which we used is described below.

For the ground observer, the maximum difference between phase angles for regions of the lunar surface at the center and in the vicinity of the limb is within the range of 0.5° . For a photometric investigation of such a negative, this value is disregarded, and it is assumed that the direction from the observer to the center of the Moon and that from the observer to any part of the lunar surface are parallel. In this case, the image of the Moon on the negative can be considered as a perspective orthographic projection.

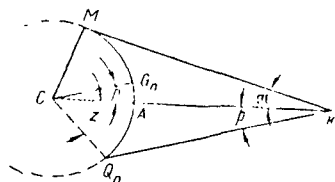


Fig. 1.

The difference between the directions to the spacecraft for the central and limb regions can be substantial on photographs of the Moon obtained from a spacecraft (at a short distance). It reaches 9° for the negatives from "Zond-3". In order to use the method developed in [7-9], those rather small regions of the lunar surface for which the image on the negative could be considered as an orthographic projection were taken for the investigation. In studying the craters, the dimensions of these regions were limited by the dimensions of the crater itself. It was necessary to find the position of the center of the Moon's disk as seen in this direction, and to construct the corresponding intensity equator for each such region projected on the negative by a parallel pencil of rays.

Let us determine the selenographic coordinates of the cited "center of the disk" according to the known coordinates of the point of the surface below the apparatus and the center of the region under investigation. The latter were taken from map No. 18 (scale 1:5000000) in [11].

Let us examine Figure 1. Let C be the center of the lunar sphere; K is the position of the spacecraft at the moment of the photographing; Q_n is the region of the lunar surface under investigation; $\angle CKO_n = p$ is the angle between the directions to the center of the lunar sphere and to the region under investigation. G_n is the center of the lunar disk seen from infinity in the direction KQ_n . From the oblique triangle KCQ_n

$$\tan p = \frac{\sin z}{\operatorname{cosec} \pi - \cos z},$$

where π is the parallax of the Moon at a distance of KC , z is the angular distance on the lunar sphere between the point on the surface below the apparatus and the center of the region under investigation.

The selenographic coordinates λ_n and β_n of the "center of the apparent disk" were calculated according to the following formulas:

$$\begin{aligned} \sin(\lambda - \lambda_n) &= \frac{\sin(\lambda - \lambda_A) \cos \beta_A \sin(z+p)}{\cos \beta_n}, \\ \sin \beta_n &= \sin \beta \cos(z+p) + \cos \beta \sin(z+p) \times \\ &\times \sqrt{1 - \left(\frac{\sin(\lambda - \lambda_A) \cos \beta_A}{\sin z} \right)^2}, \end{aligned} \quad (1)$$

where λ , β and λ_A , β_A are the selenographic coordinates of the center of the region under investigation and the point on the surface below the apparatus, respectively. The coordinates of the "center of the apparent disk" calculated according to the formulas in (1) allowed us to find the phase angles α_n for the regions of the lunar surface under investigation.

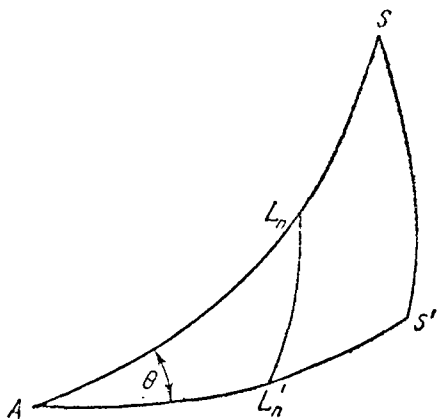


Fig. 2.

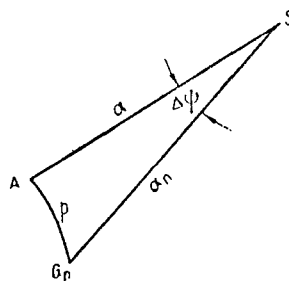


Fig. 3.

The photometric cross section of the crater passed through its center parallel to the intensity equator of the corresponding region. The positions of all the local intensity equators were determined according to their ratio with the principal intensity equator. The latter represented a halo around the Moon, passing through the sub-solar and sub-instrumental points.

In order to plot the principal intensity equator on the negative, it was necessary to know the selenographic coordinates of a number of its points. We will examine a region of the lunar sphere (Fig. 2) for this purpose. AS is the principal intensity equator, and AS' is the selenographic parallel passing through the sub-instrumental point A ; SS' is the arc of the meridian passing through the subsolar point S . Let us single out a number of points on the principal intensity equator (near the sub-instrumental point) $L_1, L_2, L_3, \dots, L_n$, with photometric coordinates of $l_1, l_2, l_3, \dots, l_n$ and $b_1 = 0, b_2 = 0, b_3 = 0, \dots, b_n = 0$, i.e., with coordinates assigned to the plane of the principal intensity equator. We can find from the right spherical triangles SAS' and L_nAL_n' that

$$\begin{aligned}\sin(\beta_n - \beta_A) &= \frac{\sin l_n \sin(\beta_S - \beta_A)}{\sin \alpha}, \\ \sin(\lambda_n - \lambda_A) &= \frac{\cos l_n}{\cos(\beta_n - \beta_A)},\end{aligned}\quad (2)$$

where l_n is the photometric longitude of the n -th point, which is read off from the subsolar point and is positive in the direction toward the sub-instrumental point. The formulas in (2) aid in determining the selenographic coordinates of a number of points of the principal equator and to plot them first on the map and then on the negative.

The positions of the local intensity equators were determined in the following way. Let us again examine a region of the lunar sphere (Fig. 3). The points S and A have the same significance as in Figure 2. G_n is the center of the apparent disk for the region under investigation, SG_n is the intensity equator of this region, and SA is the principal intensity equator. The arc $SG_n = \alpha_n$ is measured according to the phase angle of the region under investigation. It is easy to find this angle according to the known coordinates of the subsolar point S and the coordinates of the point G_n obtained according to the formulas in (2).

The angle on the sphere $\Delta\psi$ between the principal and local intensity equator of the region under investigation can be found according to the following formula, derived from the spherical triangle:

$$\cos \Delta\psi = \frac{\cos p - \cos \alpha \cos \alpha_n}{\sin \alpha \sin \alpha_n}. \quad (3)$$

Knowing the angle ψ_0 , which is constructed between the principal intensity equator and the record line on the negative (in

it is easy to calculate the angle $\psi_n = \psi_0 + \Delta\psi$ between the local intensity equator and the record line. This angle is also constructed between the record line and the corresponding photometric parallel passing through the center of the crater. The latter allows us to plot the position of the photometric cross section on the negative.

Figure 4 gives an enlarged print of part of a negative with an image of the crater Avogadro, in cross-section form. The photographic densities were taken at the points of intersection between the cross section and the record line, and the curves of density distribution along the section of the crater selected were constructed.

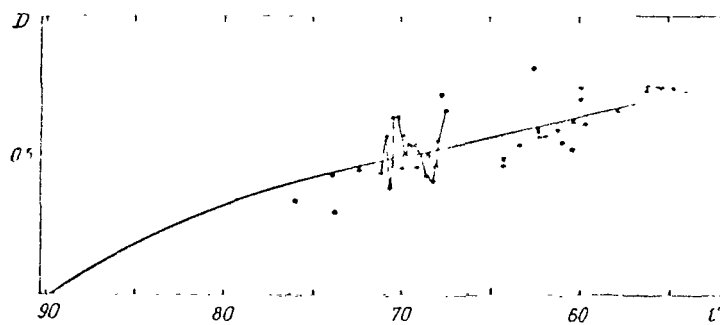


Fig. 5.

Photometric uniformity was suggested for all the regions of the lunar surface under investigation. A spherical curve representing the brightness distribution of the horizontal regions located on the intensity equator was constructed along the floors of the craters. The small difference in phase angles for all the craters studied (within the limits of 4°) showed that we could limit ourselves to one spherical curve for each negative. The spherical curve for the 22nd photograph is constructed in Figure 5 (abscissa, photometric longitude; ordinate, photographic density).

It was assumed that the regions of the lunar surface which are identically oriented have identical brightnesses and, correspondingly, identical photographic densities.

The slopes of small regions of the crater ridge (4×4 km) were determined according to their relation with the selected part of the floor of this crater. The difference in albedo between the floor and ridge of the crater, which was insignificant for highland objects, was not considered. The method of determining the slopes according to the difference in photographic densities was the same as in [9]. For an example, Figure 5 shows a superposition of a

spherical curve for the distribution of densities along a section passing through the center of the crater Avogadro. The parts of the section which occur above the spherical curve are inclined in the direction toward the Sun. Those occurring below are inclined away from the Sun. The angle of inclination of the region under investigation is measured according to the difference in longitudes of this region and the horizontal unit of the lunar surface whose photographic density is equal to the density of the unit under investigation.

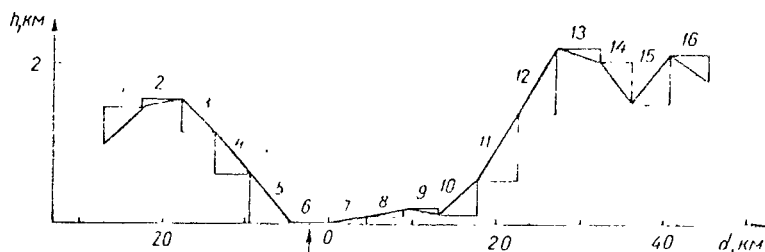


Fig. 6.

Figure 6 gives a schematic diagram of the construction of the height profile for the crater Avogadro. The relative heights are plotted along the ordinate axis, and the distances between centers of the units of the surface under study are plotted along the abscissa axis. These distances served as the bases by which we could calculate the relative heights according to the measured inclination. We took the region of the floor of the crater selected (marked off by an arrow) as the zero level for reading the heights. The slopes were determined according to their relation with the tentatively horizontal region.

Figure 7 shows a part of the map of the far side of the Moon, with an indication of the directions of the cross sections of the craters under investigation.

In the article entitled "Height Profiles of 29 Craters on the Far Side of the Moon" in this collection, the profiles of craters obtained by the method we have described are given.

An analysis of these profiles allowed us to determine the characteristics of elements in the structure of the craters being studied. These characteristics are given in Table 2, in which the index number of the crater is noted (see Fig. 7 also); the number of the figure in the Appendix; the number of the object according to the catalogue published in [11], the name of the crater from the list of suggested names in [11], the selenographic coordinates of the center of the crater λ_n , β_n , the number of the photograph N obtained from the AIS "Zond-3"; the principal diameter d , measured according to the center between crests in the ridge; the diameter

TABLE 2

No. Crater	No. Figure	No. Object [11]	Name of Crater [11]	λ	β	N
1	1	81	Gerasimovich	28.5°	-26.5°	28
2	2	9B	—	131.0	2.0	28
	3	—	—	131.0	12.0	26
3	4	82F	Lindblad	131.5	27.0	28
4	5	50	Ioffe	131.0	16.5	28
	6	—	—	131.0	16.5	26
	7	—	—	131.0	16.5	22
5	8	9A	—	132.0	11.0	26
6	9	51B	Shajn	134.0	20.0	28
	—	—	—	—	—	22
7	10	51A	—	134.0	18.5	28
	—	—	—	—	—	26
	—	—	—	—	—	22
8	11	59	Mohorovicic	135.0	23.5	28
	—	—	—	—	—	22
9	12	60	Jones	136.0	27.0	28
10	13	51J	—	136.0	17.5	28
11	14	51J	—	137.0	17.0	28
12	15	46G	Sharonov	138.5	16.5	28
	—	—	—	—	—	26
	—	—	—	—	—	22
13	16	51CE	Kimura	138.5	18.0	28
	—	—	—	—	—	26
14	17	46H	—	141.0	13.0	28
15	18	45	Michelson	142.0	12.0	28
	—	—	—	—	—	22
16	19	41H	—	142.5	18.0	28
17	20	41GH	—	143.0	17.0	28
18	21	55E	Krasovsky	143.0	25.0	28
19	22	43	Obruchev	142.5	20.0	28
20	23	42A	—	143.5	19.5	28
	—	—	—	—	—	22
21	24	55C	Helmert	145.0	26.0	28
22	25	41B	—	145.5	15.5	28
23	26	25G	Tikhov	145.5	11.5	28
24	27	41A	Avogadro	146.0	17.0	28
24	27	41A	Avogadro	146.0	17.0	26
	—	—	—	—	—	22
25	28	41BB	—	146.5	15.5	28
26	29	25	Sechenov	146.5	9.5	28
	—	—	—	—	—	26
27	30	44BB	O. Schmidt	147.0	20.0	28
	—	—	—	—	—	22
28	31	27H	—	149.0	13.0	28
29	32	20	Langemak	151.0	+ 0.5	22

TABLE 2 (cont'd)

d_1 , км	df , км	α'	h , км	H , км	β'	P
58	19	10.5°	2.5-3.5	1.6	5.0°-7.0°	I
18	5	10.5	0.8	0.2	3.0	III
27	5	3.5	0.5	0.6	4.0	III
30	8	10.5	1.1	0.2	2.0	II
85	35	8.0-16.0	5.1	1.0	4.0	I
120	40	9.0	5.0	1.0	4.0	I
85	23	8.0	3.8	1.1	5.5	I
24	4	5.5	0.7	0.4	2.5	III
49	15	15.0	2.5	—	11.0	II
49	15	6.0-7.0	2.1	—	12.0	II
55	17	10.0	2.3	—	—	I
69	26	7.0	1.8	—	—	I
60	20	3.0-10.0	1.5-2.1	—	—	I
63	28	6.0-11.0	2.0	3.0	5.0	I
67	23	5.0-11.0	2.2-3.6	3.0	6.0-12.0	I
54	14	10.0	2.6-3.0	0.6-1.0	3.0	I
46	13	15.0-20.00	4.0	—	3.0	III
17	<4	6.0	1.5-0.8	0.3	4.0	III
29	4	13.0	2.2	0.6	5.0	I
30	4	10.0	2.0	0.8	10.0	I
33	4	6.0	1.8	0.2	2.0	I
32	9	7.0	2.0	0.6	2.0	II
28	9	11.0	1.9	—	—	II
25	13	11.0	1.2	0.2	2.0	III
52	12	12.0	2.7	0.9	4.0	I
55	20	9.5	2.5	1.8	8.0	I
16	<4	11.0	1.6	0.5	3.0	III
20	<4	3.0	0.6	0.5	2.0	III
32	12	7.0	1.0	0.5	4.0	I
58	27	7.5	2.2	0.5	3.0	II
40	~10	9.0	2.2	0.2	—	III
44	~10	10.5	2.9	—	—	II
49	18	14.0-16.00	3.7	0.5	2.5	II
24	<4	7.0	1.5	0	0	III
36	<4	8.0	1.8	0.3	3.0	II
45	21	10.0	1.8	0.2	2.5	II
54	25	15.0	3.3-2.2	—	—	II
45	23	10.0	2.2-1.5	0.7	2.0	II
16	<4	7.5	1.0	0.4	4.0	III
67	29	7.0	2.3	0.8	4.0-5.0	I
65	34	15.0	4.5-3.5	—	—	I
59	15	10.0	2.7	0.7	4.0	II
52	12	11.0-15.00	2.8	—	—	II
32	6	9.5	0.9	0.2	4.0	II
100	40	15.0	5.6	~4.5	11.0	I

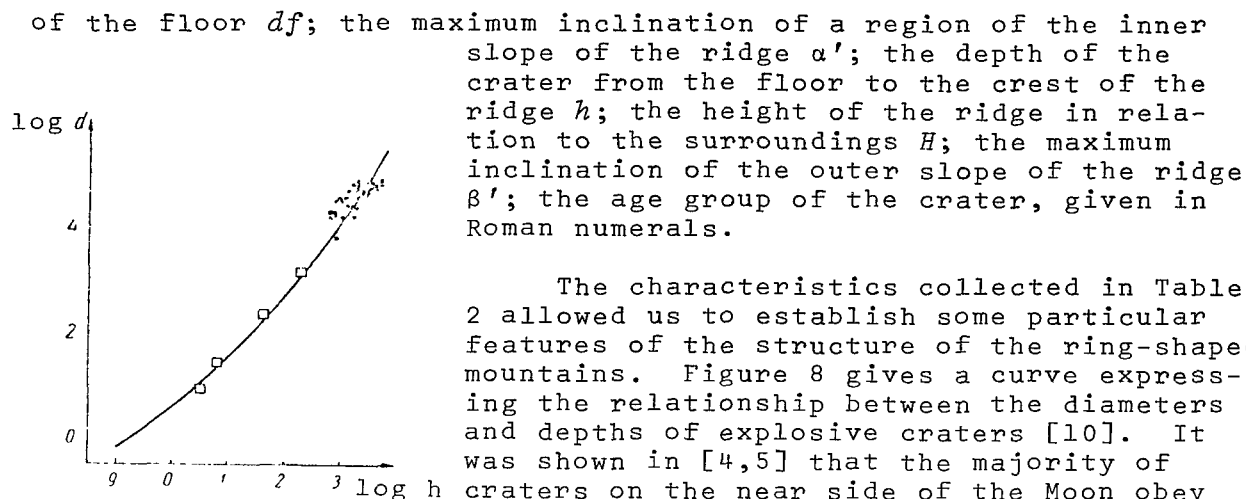


Fig. 8.

of the floor df ; the maximum inclination of a region of the inner slope of the ridge α' ; the depth of the crater from the floor to the crest of the ridge h ; the height of the ridge in relation to the surroundings H ; the maximum inclination of the outer slope of the ridge β' ; the age group of the crater, given in Roman numerals.

The characteristics collected in Table 2 allowed us to establish some particular features of the structure of the ring-shaped mountains. Figure 8 gives a curve expressing the relationship between the diameters and depths of explosive craters [10]. It was shown in [4,5] that the majority of craters on the near side of the Moon obey this dependence. The points on the figure represent ring-shaped objects on the far side of the Moon, and the small squares

designate eruptive craters. The position of the points on the graph allows us to assume that the ring-shaped mountains on the far side of the Moon also arose as the result of an eruption.

All the craters which were investigated were divided into three groups according to the degree to which they were preserved. The criterion for belonging to a certain group was the degree of preservation of the crater ridges and the overlapping of other craters.

Group I included the oldest craters studied, whose ridges and floors were damaged by younger craters which had formed at a later time. For example, of the two superposing craters Krasovsky and Helmert, the first crater should be related to group I, since its ridge was damaged by the crater Helmert, which formed later, and whose ridges were damaged by even smaller craters. The crater Helmert was included in group II, which is the intermediate group. Group III included craters whose details were well preserved.

The age division of the craters which we have described was also reflected in the characteristics of their structural elements. Group I joined together the largest craters, whose principal diameter was equal to 30-100 km, and whose depth was 2-5 km (a depth of 2.5 km predominates). The craters were shaped like a cup (for example, Ioffe, Langemak, Michelson, etc.), and the ridges and floors were broken up by smaller craters (Sechenov, Gerasimovich, Mohorovichiv). Most of them had central mountains (Michelson, Gerasimovich, etc.).

Group II includes craters with diameters of 20-50 km and depths of 1-3 km. The shape is either like a cup (Avogadro, O. Schmidt, Obruchev, etc.) or in the form of the frustum of a cone (Tikhov, 27H, etc.). As was already mentioned, this group has intermediate characteristics.

Group III includes the parasitic and individual craters with diameters of 16-40 km and depths of 0.5-4 km. Most of the craters are similar in form to the frustum of a cone (42A, 51J, 41B, 41BB, etc.). These craters have the greatest deviation in curvature of the inner slopes (2-13°).

The characteristics of the structure of craters of different ages make us think that, during the development of the lunar relief, there was one force which acted, forming ring-shaped mountains which were at first large and then smaller. The difference in shapes of the large and small craters which is observed was due to the longer effect of erosion on the older ridges of the large craters.

Thus, the characteristics contained in Table 2 and the particular features in the structure of single craters allow us to draw the following conclusions concerning the ring formations (craters) on the far side of the Moon:

1. The size and shape of the ring-shaped mountains on the far side of the Moon which we have studied are similar to those of analogous formations on the near side.

2. Just as for the near side, the curvature of the inner slopes of the ridges of the craters studied are greater than those of the outer slopes.

3. The relationships obtained between the diameters and depths of the craters obey the dependence established for eruptive craters.

4. The older craters have greater size and depth. Their shape is similar to that of a cup, while the shape of the younger craters is close to the frustum of a cone.

5. The asymmetry between the near and far hemispheres noted by the first researchers studying the far side of the Moon was not reflected in the structure of the ring-like mountains on the far side of the Moon. As investigations showed, the nature and structure of these forms of the relief are identical on the near and far sides of the Moon.

REFERENCES

1. The Moon, Meteorites and Comets. Chicago, 1963.
2. Ronca, L.B., and J.W. Salisbury: Icarus, p. 5, 1966.
3. Khabakov, A.V.: Ob osnovnykh voprosakh istorii razvitiya poverkhnosti Luny (The Principal Problems in the History of the Development of the Lunar Surface). Moscow, "Goegeografizdat", 1949.
4. Baldwin, R.B.: The Face of the Moon. Chicago, 1949.
5. Markov, A.V.: Doklady Akad. Nauk S.S.S.R., Vol. 167, No. 1, pp. 63-64, 1966.
6. Novoye o Lune (What is New on the Moon). Moscow-Leningrad, Akad. Nauk S.S.S.R., 1963.
7. Diggelen, I. van: BAN, p. 11, 1951.
8. Barabashov, N.P., V.A. Yezerskaya and V.I. Yezerskiy: Uchenyye Zapiski Khar-kovsk. Gosudarstv. Universit. Trudy AO, No. 14, pp. 1-7, 1962.
9. Lisina, L.R.: In the Book: Fizika Luny i planet (Physics of the Moon and Planets). Kiev, "Naukova dumka", 1966.
10. Stanyukovich, K.P. and V.A. Bronshten: In the Book: Luna (The Moon). Moscow, "Fizmatgiz", p. 304, 1960.
11. Atlas obratnoy storony Luny (Atlas of the Far Side of the Moon), Part II. Moscow, "Nauka", 1967.

HEIGHT PROFILES OF TWENTY-NINE CRATERS ON THE FAR SIDE OF THE MOON

M.N. Mironova

ABSTRACT: The profiles of 29 craters on the far side of the Moon are shown. The method used in obtaining these crater profiles and an analysis of the results obtained are given in the preceding article by the same author.

The height profiles of 29 craters on the far side of the Moon are given in this study. Three photographs of the far side of the Moon, obtained from the spacecraft "Zond-3", were used in order to construct these profiles. The method of constructing them according to photometric sections of the craters and the characteristics of the materials used are discussed in the preceding article. That article also analyzes the results obtained and contains Table 2, in which the data characterizing the different structural elements of the craters under investigation are collected.

The numeration for the figures corresponds to the numeration of the craters in Table 2 of the preceding article.

Since the directions of the photometric cross sections of the craters did not coincide on different photographs, different graphic representations were introduced for the height profiles obtained according to the different photographs (the solid line designates the 28th photograph; the dotted line represents the 22th; the dashed line designates the 26th photograph).

On the figures, one division along the abscissa axis corresponds to 10 km, and one division along the ordinate axis corresponds to 1 km. The shaded regions of the crater ridges are marked off by a thick dotted line.

In order to depict the outer slope of the eastern (shaded) ridge, it was suggested that, in some cases, its height be made equal to the height measured for the opposite ridge.

The profile of each crater was drawn twice: on the lower part of the figure, the scale along the abscissa axis is ten times less than the scale along the ordinate axis, and, on the upper part, the scale is identical along both axes, which makes a clear representation of the curvature of the ridges.

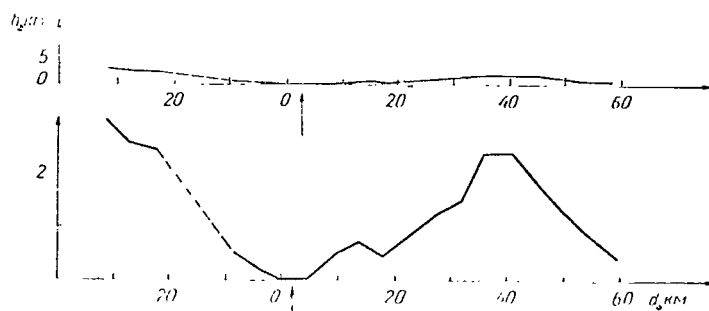


Fig. 1.

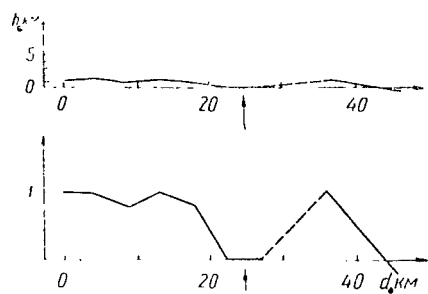


Fig. 2.

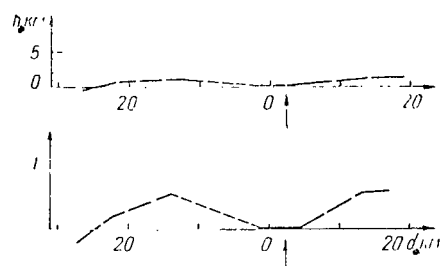


Fig. 3.

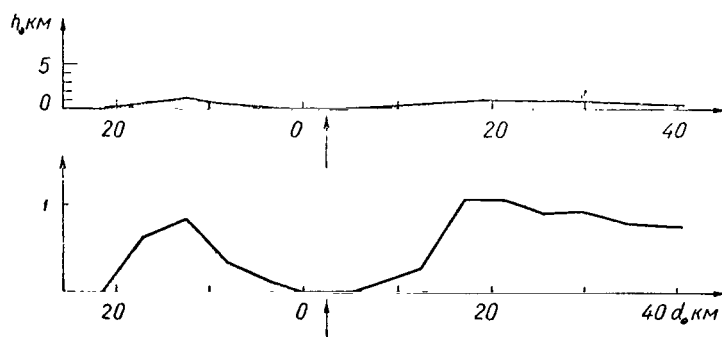


Fig. 4.

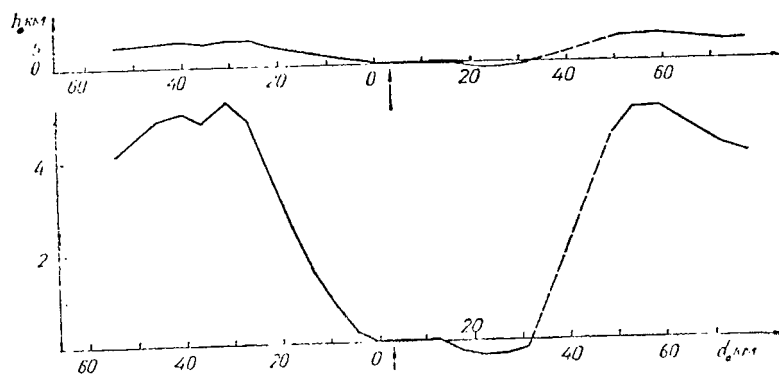


Fig. 5.

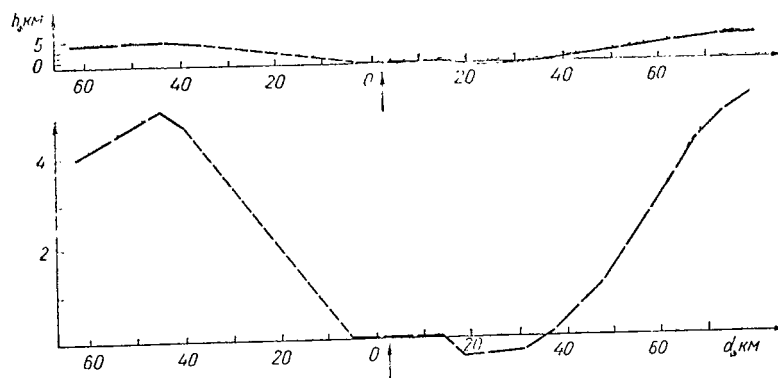


Fig. 6.

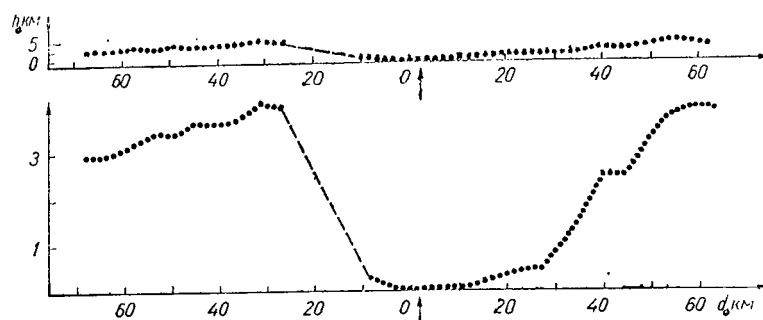


Fig. 7.

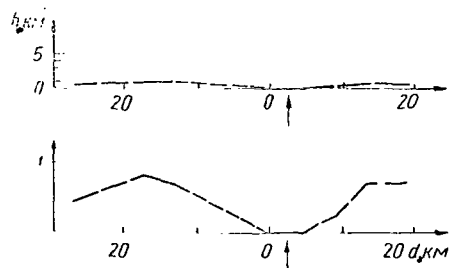


Fig. 8.

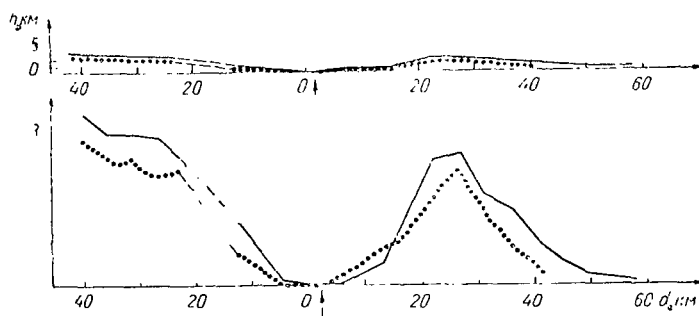


Fig. 9.

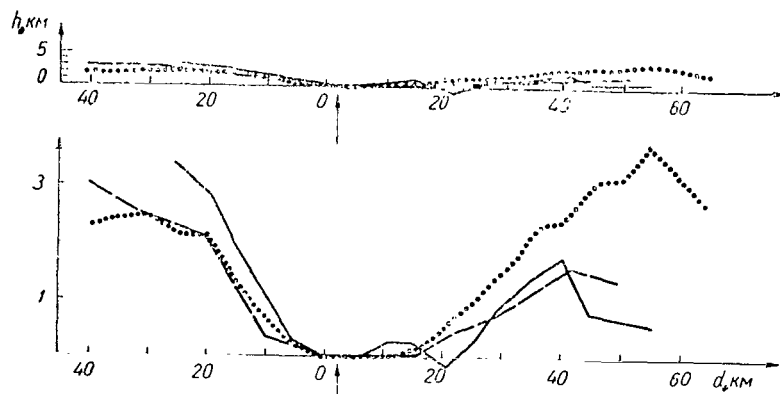


Fig. 10.

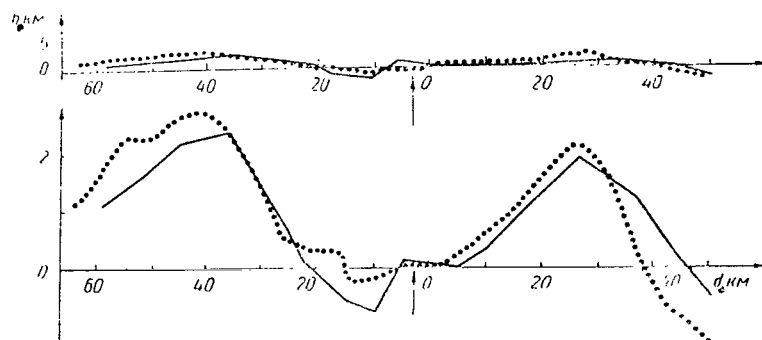


Fig. 11.

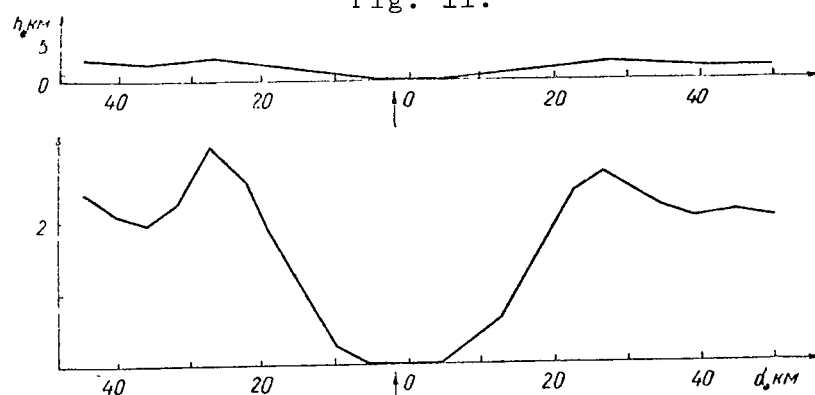


Fig. 12.

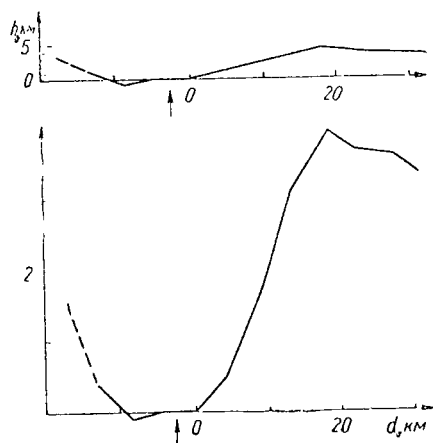


Fig. 13.

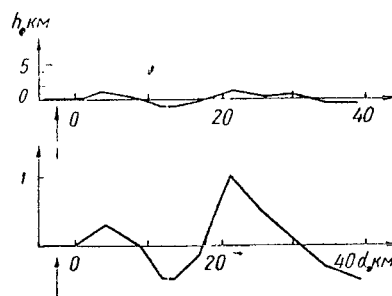


Fig. 14.

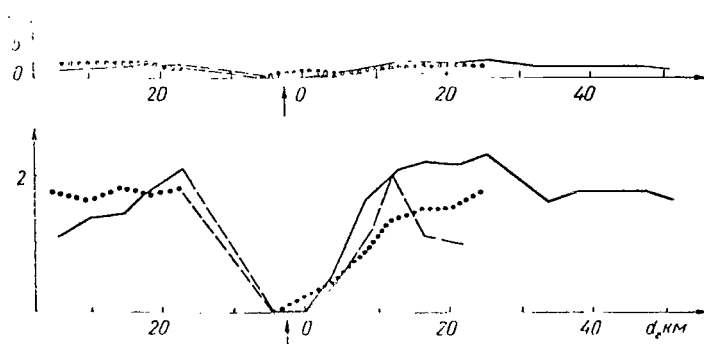


Fig. 15.

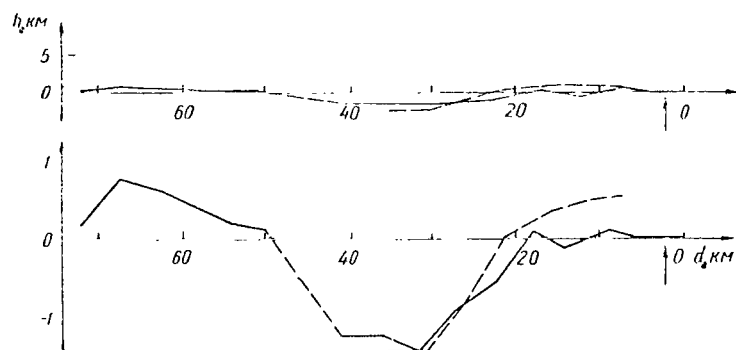


Fig. 16.

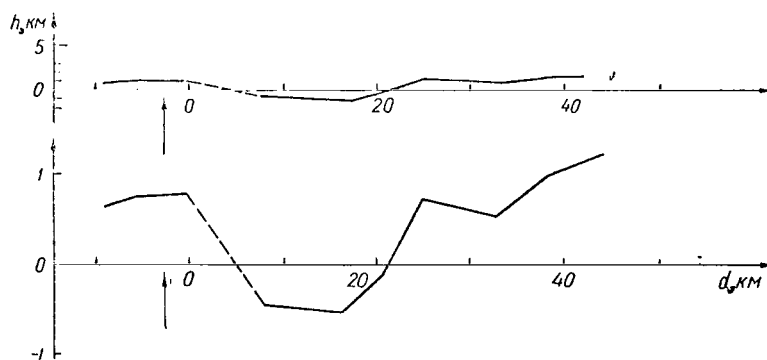


Fig. 17.

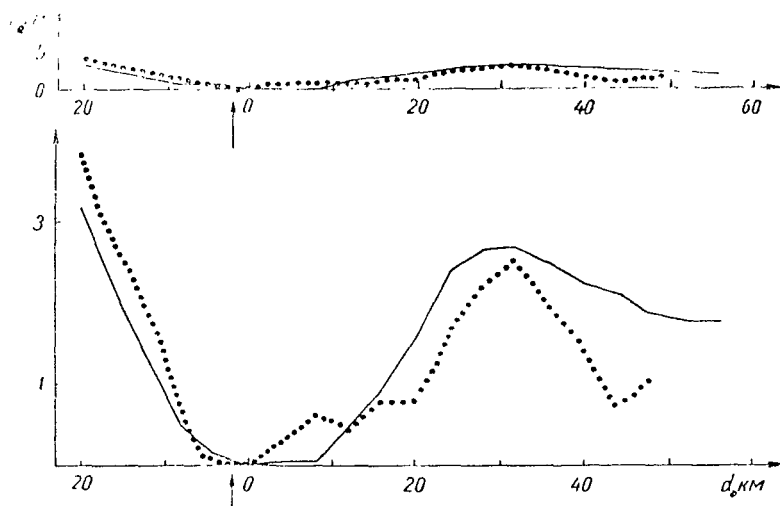


Fig. 18.

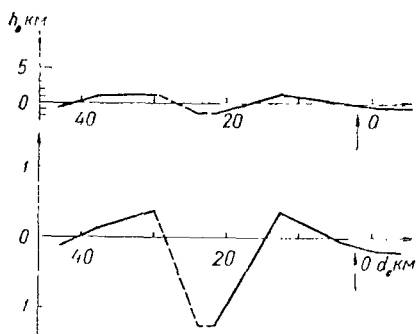


Fig. 19.

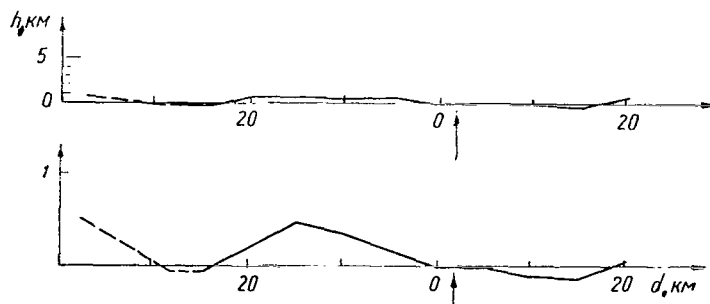


Fig. 20.

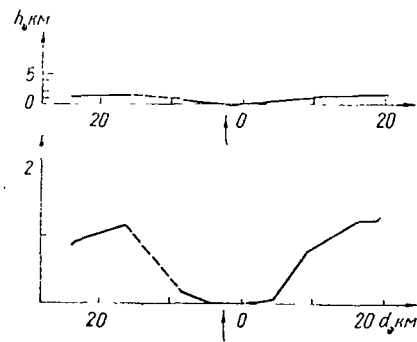


Fig. 21.

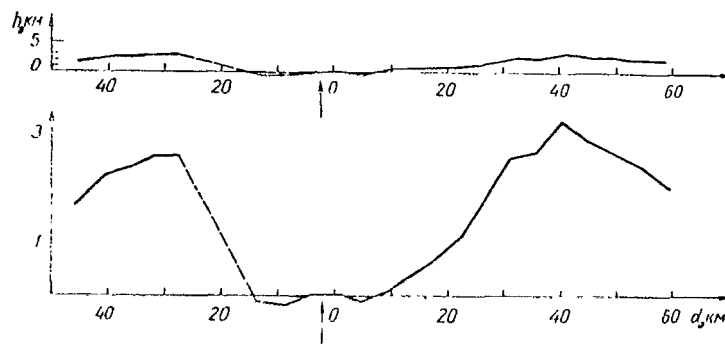


Fig. 22.

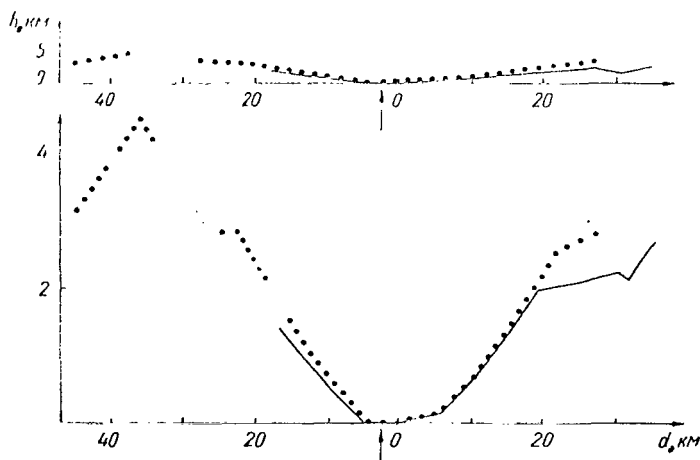


Fig. 23.

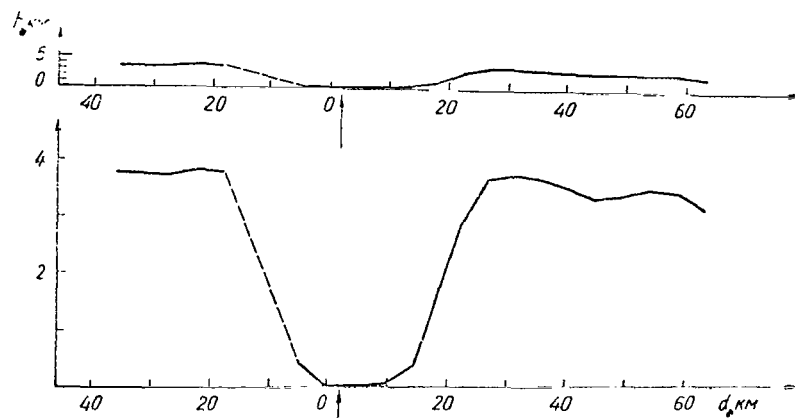


Fig. 24.

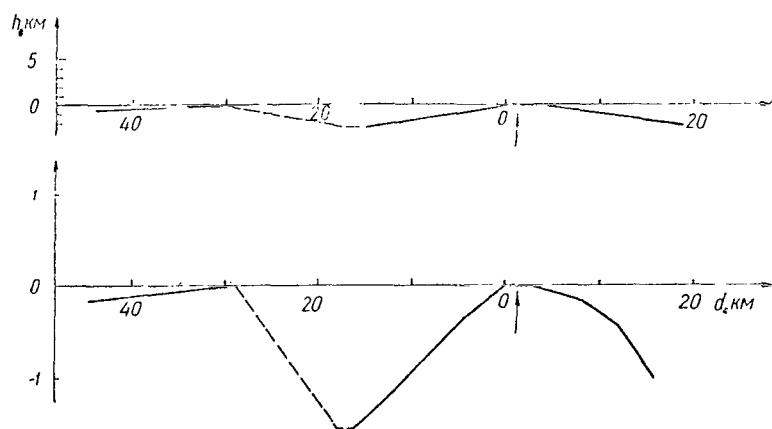


Fig. 25.

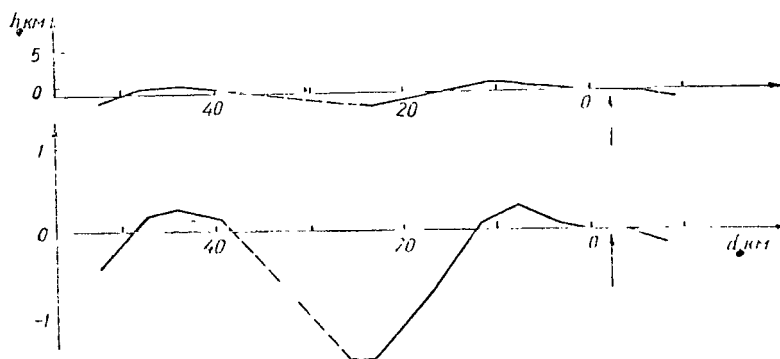


Fig. 26.

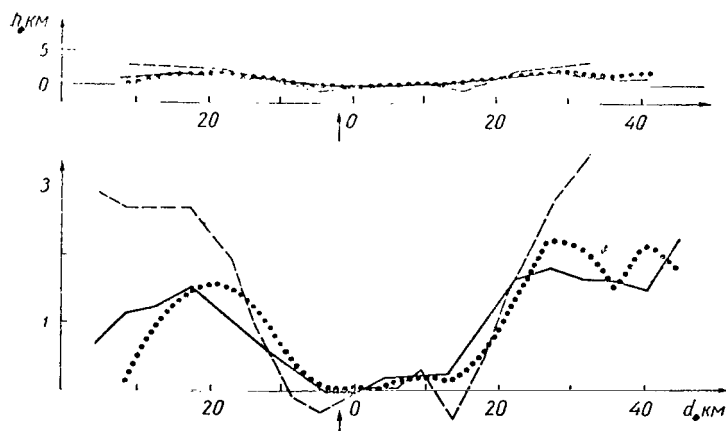


Fig. 27.

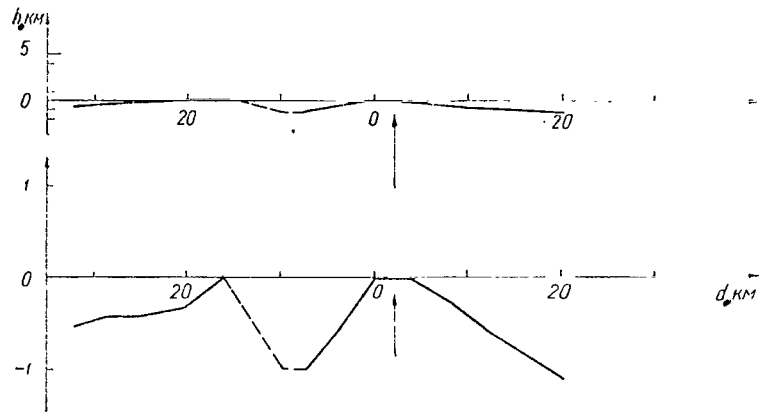


Fig. 28.

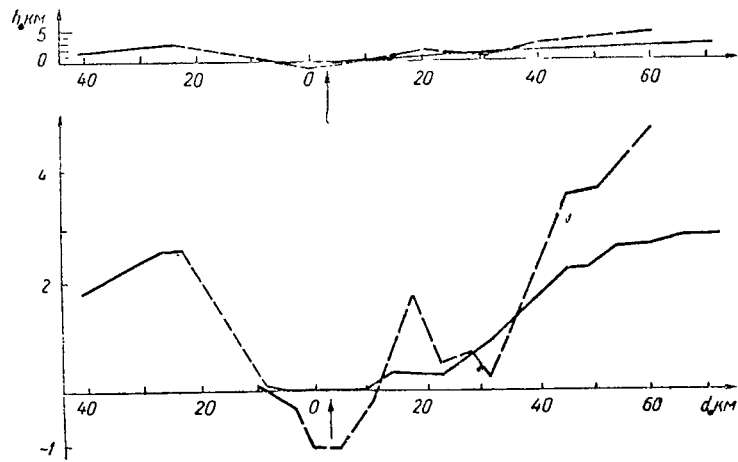


Fig. 29.

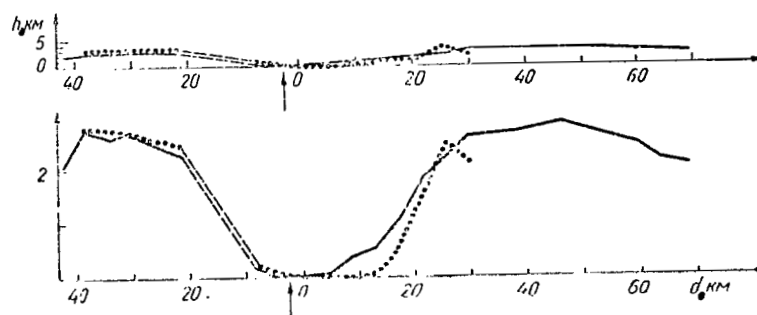


Fig. 30.

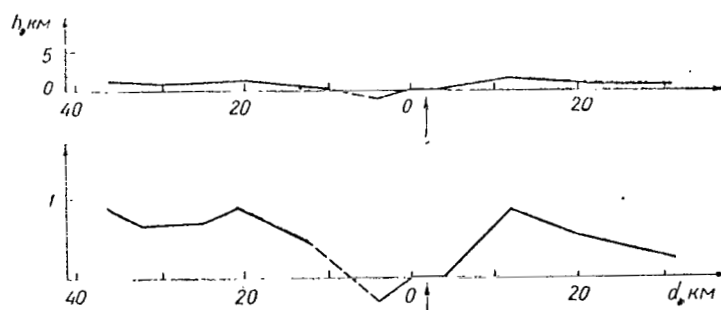


Fig. 31.

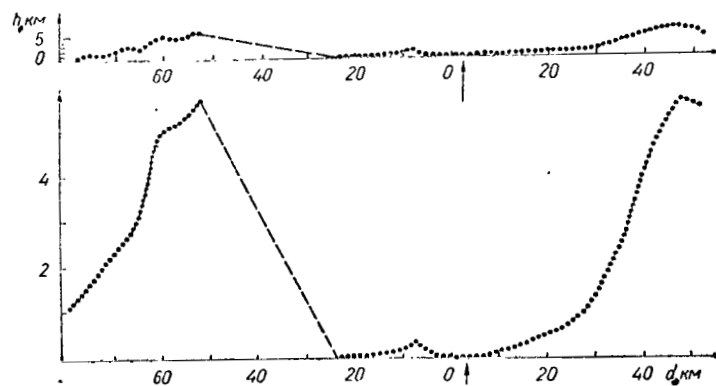


Fig. 32.

OPTICAL CHARACTERISTICS OF THE MARS ATMOSPHERE OBTAINED ACCORDING TO CONTRAST MEASUREMENTS

I.K. Koval'

ABSTRACT: Photometric data on the contrasts between the highlands and maria of Mars, measured in different spectral regions, are analyzed. The optical parameters of the Mars atmosphere are determined. Some assumptions on the behavior of the true contrast over the spectrum are made. The results show that the model of the scattering atmosphere with optical thickness of approximately 0.2 at 0.43μ is in good agreement with the observations.

After the polar caps, the dark regions of the Mars maria are the most remarkable details of the planetary disk. As a rule, any photograph of Mars obtained on lines with wavelength greater than 0.5μ contains regions of rather large maria. Many years of observations have shown that the contrast between the Mars maria and the neighboring highland regions is not identical for different maria. The maria of aerographic longitudes of $280-60^\circ$ have the greatest contrast, and those of the longitude interval of $80-240^\circ$ have lowest contrasts. We will discuss the reasons for these changes below.

Thus, systematic observations carried out during a total apparent revolution of Mars (around 40 days) can give a complete aerographic-longitude sweep of the highland-mare contrast. A recycling of the measurements, which is achieved by observations during the course of several oppositions or by prolonged observations during the period of one opposition, can serve as the basis in clarifying the changes on the planet connected both with the maria themselves and with the Mars atmosphere.

The problem of the optical properties of the Mars atmosphere is discussed in this study on the basis of photometric data concerning the highland-mare contrasts, obtained recently by the author and other observers. This way of studying the Mars atmosphere was also used earlier in [1,2]. The calculations presented were of a preliminary nature, and showed that the contrast method of investigating the Mars atmosphere deserves attention.

Photometric Data. The very first photographs of Mars, which were obtained by G.A. Tikhov and then by Sleifer, Wright and Ross, showed that the highland-mare contrast decreases smoothly toward

the violet end of the spectrum and, as a rule, disappears completely around 0.4μ . Some observers are particularly occupied with the establishment of a spectral limit to the disappearance of the highland-mare contrast, and, meanwhile, we can mention only the wavelength interval in which this boundary is included for a normal state of the Mars atmosphere (absence of so-called violet trans-illuminations). When the limit for detecting a contrast is equal to 0.05, this interval is limited to wavelengths of $0.43, 0.47 \mu$ for photometric observations. However, as photometric observations during several oppositions of Mars showed, the highland-mare contrast can be reliably measured during certain periods even around 0.43μ , where it sometimes reaches 30% of the value near 0.7μ . Finally, the contrast in the violet rays can reach 80% of the value in the red in rare cases. These instances were called the moments of the illuminations in the violet layer of the Mars atmosphere.

The fact of such illuminations is very important in itself, since, being connected with atmospheric extinction, it allows us to draw definite conclusions on the course of the true contrast over the spectrum, as well as the variations in optical thickness of the Mars atmosphere, which sheds light on the nature of the so-called violet layer.

However, not every report of a rather clearly visible Mars mare in the violet lines should be taken as an indication that the transmissivity of the Mars atmosphere is increased.

The fact is that the highland-mare contrast in the red region of the spectrum changes very strongly according to aerographic longitude. For example, as our measurements [2] at all aerographic longitudes showed (the measurements were taken near the center of the planetary disk), the contrast changes in June-August of 1956 from 0.14 to 0.41 for 0.65μ . Naturally, when the transmissivity of the Mars atmosphere is unchanged, the darker maria in the red lines can involve an increase in the corresponding contrast in the violet lines. Thus, if the observations are carried out during a time interval which does not exceed the period of an apparent complete revolution of Mars, i.e., without repeated observation of the same details, it is very difficult to draw any reliable conclusion on the illumination of the Mars atmosphere.

A clear illustration of what we have said can be found in the longitudinal contrast scan constructed according to visual measurements in 1956 by V.V. Sharanov (Fig. 1) [3]. The period of these observations encompasses all the aerographic longitudes with slight superposition in the longitude range of $L = 110-150^\circ$. The overwhelming majority of observers have noted that, in September of 1956, a dust storm arose in the southern hemisphere of Mars and greatly decreased the observed contrasts. Our measurements [4] confirmed this by numerous determinations of the contrast in the red lines, with a double overlapping of aerographic longitudes.

One such factor, which always effects a decrease (blurring) of the real contrast values is the atmospheric vibration of the image. If during visual observations we can almost always catch a moment when the image of the planet becomes rather clear, then, in photometric observations, particularly with small telescopes and light filters requiring a recording time of several seconds, the result of the contrast measurements depends very strongly on the turbulent state of the Earth's atmosphere.

As our photoelectric observations in 1963 [7] and 1965 [8] showed, the width of the profile of the diffuse image of the star, which is generally well approximated by a function of the type $\exp(-x^2/2\sigma^2)$, undergoes substantial oscillations ($\sigma = 1-2''$) for satisfactory steadiness of the image over visual evaluations. All the data which have presently been obtained on the contrasts on Mars are based on measurements either with a visual photometer or according to photographic material. In both cases, the recording time greatly exceeds the rate of vibration of the image, which must necessarily lead to a blurring of the real contrast.

For an example, we calculated the contrasts K arising as a result of the effect of a Gaussian contour with different values of the parameter σ on a large detail differing in contrast K_0 and size Δr_0 located at the center of a Lambert sphere. The calculations were carried out for values of K_0 equal to 0.1, 0.3 and 0.5 and for a diameter of the detail of $\Delta r_0 = 0.05, 0.1, 0.2, 0.3R_\sigma$ with values of $\sigma = 0.02, 0.05, 0.10$ and $0.30 R_\sigma$.

Table 1 gives values of the ratio K/K_0 ($0.1 \leq K_0 \leq 0.5$), which was found to be practically independent of K_0 for the set of values of this parameter which we selected.

As can be seen from this table, the "observed" contrast for a detail with diameter of $0.2R_\sigma$ and preliminary contrast of 0.1-0.5 decreases by 30% at $\sigma = 0.1 R_\sigma$ and almost by a factor of three at $\sigma = 0.15 R_\sigma$. For a radius of Mars equal to $10''$, this example corresponds to $\sigma = 1''$ and $1.5''$, which is close to the actual observational conditions. Under these conditions, for example at $\sigma = 1''$, the diameter of the detail should be no less than $3.5''$ to achieve accuracy in measuring the contrast of no less than 10% on a disk with radius of $10''$.

TABLE 1

Δr_0	σ				
	0.0	0.05	0.10	0.15	0.30
0.30	1.00	0.99	0.92	0.58	0.05
0.20	0.99	0.98	0.73	0.32	0.02
0.10	0.96	0.66	0.36	0.12	0.01
0.05	0.50	0.25	0.12	0.02	0.00

Thus, the value of the contrast measured on the planet depends to a great extent on the turbulent state of the Earth's atmosphere (on σ); therefore, observations of this type should be accompanied by supplementary observations which can give certain necessary criteria for subsequent analysis of the data obtained. Without such a control, the measured variations in contrasts could be deceptive.

In addition to the cited blurring of the contrasts, the atmospheric vibration brings about a broadening of the detail, which can be seen clearly in Figure 2, showing the change in rectangular profile of the detail at the center of the Lambert sphere for different K_0 , Δr_0 and σ . At $\Delta r_0 < \sigma$, the detail becomes practically imperceptible for the K_0 under investigation.

Unfortunately, we still do not have sufficient observational data on the change in the parameter σ characterizing the "astrospheric contour". The minimum value of σ measured according to images of the stars on the 70-cm reflector of the Main Astronomical Observatory of the Academy of Sciences of the Ukrainian S.S.R. was obtained on April 6/7, 1965, and was equal to 1.1" for a zenith distance of the star close to 50°. Considering that the observations are sometimes carried out at shorter zenith distances, while the angular dimension of the planet changes from 14 to 25" for different oppositions, we can take the value $\sigma = 1''$ as an average. Then, for conditions close to the real ones ($0.1 \leq K_0 \leq 0.5$ and $\Delta r_0 \approx 0.3 R_\oplus$), the contrast blurring is up to 10-40%. We can use the data of Table 1 under specific observational conditions in order to evaluate the possible errors. For example, in 1965, when the zenith distance was close to 50°, while the angular diameter was equal to 14", the values obtained for σ were equal to 1.7" (March 23/24) and 1.1" (April 6/7), which shows that the contrast for a detail with $\Delta r_0 = 0.3 R_\oplus$ decreases by 80 and 40%, respectively.

All these calculations confirm that there is need for a more rigorous approach to an evaluation of the results of photometric observations, particularly if it is a matter of measuring the contrasts in order to investigate different types of changes on Mars. This does not mean at all that the vast amount of photographic materials obtained to the present and those conclusions which were obtained as a result of their analysis do not deserve recognition. Many of the Mars maria are large enough for reliable data to be obtained on their contrast with the adjacent highlands. The fact of temporal changes in the transmissivity of the Mars atmosphere also raises no doubts; however, the periods of violet transilluminations apparently occur very rarely.

In 1956, during the great opposition, the transmissivity of the Mars atmosphere in the violet lines undoubtedly changed at times. The observation program stipulated that, together with the

photographic observations, there must be parallel visual observations for a subsequent comparison between the sketches and the

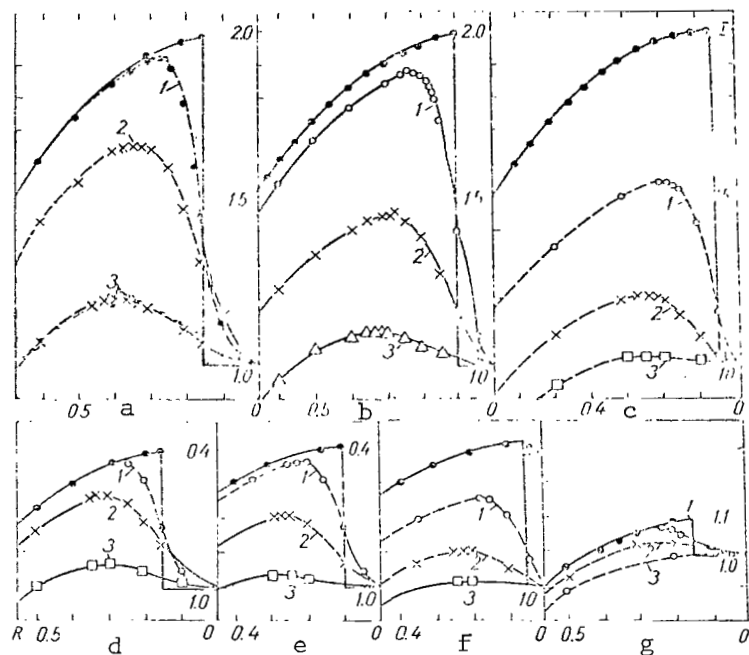


Fig. 2. Distortion of the Given Contrasts by the Function $\exp(-x^2/\sigma^2)$ for $\sigma = 0.05$ (1); 0.10 (2) and $0.20 R\sigma$ (3); $K_0 = 0.5$ and $\Delta r_0 = 0.3$ (a); 0.2 (b) and $0.1 R\sigma$ (c); $K_0 = 0.3$ and the same Δr_0 (d,e,f); $K_0 = 0.1$ and $\Delta r_0 = 0.3 R\sigma$ (g).

photographic images (Astronomical Observatory of the Khar'kov State University, reflector, $10.25''$). During the period from July 7 to October 21, 1956, N.P. Barabashov made hundreds of sketches of the planetary disk, using red, green and blue light filters [4]. On September 27, and then October 21, there was more or less clear visibility in the blue lines of the maria near aerographic longitudes of 70 and 200° . As we mentioned earlier, these maria have low contrast in the red lines. At the same time, one of the darkest maria of Mars - Syrtis Major - was not observed once during the entire period of observations on the blue line.

On April 21, 1967, five days after the opposition, the maria located in the longitude range of $340-60^\circ$ were clearly seen visually with a blue filter ($\lambda_{\max} = 0.45 \mu$) and hardly perceptible with a violet filter ($\lambda_{\max} = 0.4 \mu$). These observations were carried out on the 70-centimeter reflector of the Main Astronomical Observatory of the Academy of Sciences of the Ukrainian S.S.R.

by L.A. Bugayenko, A.V. Morozhenko and the author, in the breaks between the series of programmed photoelectric observations. Obviously, the Mars atmosphere during this period differed by its relatively high transmissivity over the entire visible spectral region.

However, all the variations noticed visually in the contrasts on Mars can remain unnoticed in photometric studies, except for those which are based on photographic materials obtained with exposures of hundredths of a second.

Let us turn to a brief analysis of the photometric data on the contrasts which are based on photographic observations, and let us attempt to use these materials in order to discuss the degree of transmissivity of the Mars atmosphere.

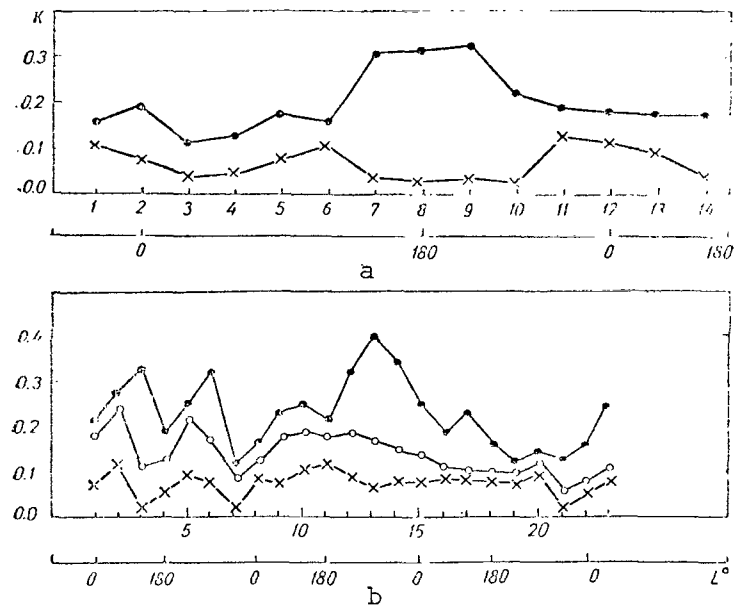


Fig. 3. Contrast Distribution over the Longitude in 1956 (a) and 1958 (b), Found According to Photographs (● - Red Filter, ○ - Green, + Blue)

Figure 3 gives the contrasts measured for filters with transmission maxima of 0.43, 0.53, 0.65 and 0.75 μ , obtained in June-October of 1956, and 0.47 and 0.68 μ in 1958 [9]. The aerographic longitude of the detail L (lower scale) is plotted along the abscissa axis, and the numbers of the points, the values of the measured contrasts of which are given in Table 2, are written out.

We will carry out our principal calculations according to the

observations of 1956. Therefore, Table 2 does not contain the data for 1958. When necessary, we will use the data of Figure 3.

Since no data was obtained during the entire observational period relative to the changes in the brightness coefficient of the highlands of Mars at the center of the disk, the optical properties of the Mars atmosphere are determined completely according to the ratio between the measured and the true contrast.

TABLE 2

N	L, °	0.43 μ		0.53 μ		0.65 μ		0.75 μ
		κ	$\kappa:\kappa_{rk}$	κ	$\kappa:\kappa_{rk}$	κ	$\kappa:\kappa_{rk}$	κ
1	0	0.07	0.29	0.18	0.75	0.21	0.89	0.24
2		0.12	0.33	0.24	0.67	0.34	0.95	0.36
3		0.02	0.06	0.11	0.33	0.33	1.00	0.33
4	180	0.06	0.29	0.13	0.62	0.19	0.90	0.24
5		0.10	0.34	0.22	0.76	0.26	0.90	0.27
6		0.08	0.21	0.17	0.45	0.33	0.87	0.33
7		0.02	0.12	0.09	0.33	0.12	0.70	0.17
8	0	0.09	0.53	0.13	0.77	0.17	1.00	0.17
9		0.08	0.26	0.18	0.40	0.21	0.75	0.31
10		0.11	0.39	0.19	0.68	0.25	0.90	0.35
11	180	0.12	0.57	0.15	0.86	0.21	1.00	0.21
12		0.09	0.53	0.19	0.50	0.32	1.00	0.32
13		0.06	0.16	0.17	0.45	0.38	1.00	0.38
14		0.08	0.22	0.15	0.42	0.35	0.97	0.36
15	0	0.08	0.27	0.14	0.47	0.25	0.83	0.30
16		0.09	0.41	0.11	0.50	0.18	0.82	0.22
17		0.09	0.35	0.10	0.38	0.24	0.92	0.26
18	180	0.08	0.42	0.10	0.53	0.17	0.89	0.19
19		0.09	0.64	0.10	0.71	0.13	0.93	0.14
20		0.11	0.79	0.13	0.93	0.14	1.00	0.14
21		0.02	0.11	0.05	0.28	0.13	0.72	0.18
22	0	0.06	0.29	0.07	0.33	0.17	0.81	0.21
23		0.10	0.34	0.11	0.38	0.26	0.90	0.29
Average		0.08	0.33	0.14	0.56	0.23	0.90	0.26
1—8		0.07	0.26	0.17	0.63	0.24	0.90	0.27
9—14		0.09	0.30	0.18	0.60	0.29	0.94	0.31
15—23		0.08	0.39	0.10	0.50	0.19	0.90	0.21

Let us call ρ_1 , A_1 and ρ_2 , A_2 the brightness coefficients and albedo of the highland and mare, respectively, near the apparent center of the planet, and let us call ρ_0 the brightness coefficient of the Mars atmosphere. As is well known [10], the brightness coefficient ρ is determined according to the following formula for the Lambert law of reflection from the surface:

$$\rho = \rho_0 + \frac{A}{1-AC} M^2.$$

Since, ordinarily, $AC \ll 1$, we can write the following:

$$\rho = \rho_0 + AM^2.$$

Using this formula, we find that

$$\rho_0 = \rho_1 \left(1 - \frac{K}{K_0} \right)$$

and

$$M^2 = \frac{\rho_1}{A_1} \cdot \frac{K}{K_0},$$

where

$$K = \frac{\rho_1 - \rho_2}{\delta_1} \text{ and } K_0 = \frac{A_1 - A_2}{A_1}.$$

For the true contrast, we can take the contrast measured for 0.75μ , where the effect of the Mars atmosphere is obviously negligibly small, with a certain wavelength-dependent coefficient $- \frac{1}{c(\lambda)}$, and we can use the following formulas:

$$\rho_0 = \rho_1 \left[1 - c(\lambda) \frac{K}{K_{rk}} \right] \quad (1)$$

$$M^2 = c(\lambda) \frac{\rho_1}{A_1} \cdot \frac{K}{K_{rk}}. \quad (2)$$

As we mentioned above, the degree of blurring of the contrasts in the range of 0.1-0.5 remains the same. If we assume (the assumption is not too rough) that the true contrasts on Mars for all the wavelengths under investigation do not exceed 0.5, then the ratios of interest to us K_λ / K_{rk} are found to be free of any effect of atmospheric vibration, since σ is not a selective value in this spectral range. Thus, the error in the contrast ratio is determined by the error in the photometric method. In measuring these contrast values, the method of photographic photometry yields a relative error equal to 20%.

Table 2 also contains the ratios K/K_{rk} and the average values of K and K/K_{rk} for three periods, each of which encompasses the entire longitudinal belt of Mars. Table 3 gives data of the contrasts measured in 1954 [11] according to photographic materials obtained by the author on the 20-centimeter refractor of the Astrophysical Observatory of Khar'kov State University. Eighteen maria were subjected to investigations according to these data [12]. However, in order to use the contrasts to study the Mars atmosphere, we selected six of the maria, which had been observed reliably two

or three times near the central meridian after a complete revolution of the planet. The aerographic coordinates of the measured region are given for each mare. We should mention that the observations of 1954 were carried out also with the aid of green and yellow light filters; however, we will use the contrast ratio for the blue light filter for our purposes, since the values for the contrasts are rather high and, at the same time, the transmission maximum for this filter occurs in the spectral region in which the Mars atmosphere appears rather clearly.

TABLE 3

Period of Observations	0.49 μ			0.61 μ			$K_C:K_K$
	av	ρ_T	K_C	av	ρ_T	K_K	
Margaritifer Sinus ($\varphi = -12^\circ$, $L = 24^\circ$)							
1-6 June	0.14	0.14	0.21	0.24	0.18	0.26	0.81
6-15 July	0.14	0.14	0.21	0.24	0.17	0.29	0.72
12-21 August	0.14	0.11	0.21	0.24	0.15	0.38	0.56
Aurorae Sinus ($\varphi = 15^\circ$, $L = 55^\circ$)							
30 June-10 July	0.13	0.11	0.15	0.22	0.19	0.31	0.71
7-15 August	0.14	0.11	0.21	0.24	0.16	0.39	0.72
Syrtis Major ($\varphi = -10^\circ$, $L = 28^\circ$)							
9-15 June	0.14	0.12	0.15	0.24	0.17	0.26	0.55
16-25 July	0.14	0.11	0.21	0.24	0.14	0.32	0.59
24 August-2 Sept.	0.14	0.11	0.21	0.24	0.13	0.46	0.46
Mare Erythraeum ($\varphi = 20^\circ$, $L = 40^\circ$)							
30 June-10 July	0.13	0.11	0.15	0.22	0.15	0.32	0.47
7-15 August	0.13	0.11	0.15	0.20	0.13	0.35	0.43
Sabaeus Sinus ($\varphi = -5^\circ$, $L = 350^\circ$)							
1-8 June	0.14	0.11	0.21	0.24	0.18	0.25	0.84
8-18 July	0.14	0.11	0.21	0.23	0.17	0.26	0.81
15-23 August	0.13	0.10	0.23	0.24	0.16	0.33	0.70
Mare Cimmerium ($\varphi = -25^\circ$, $L = 210^\circ$)							
21 June	0.14	0.11	0.21	0.24	0.18	0.25	0.84
25 July-3 August	0.13	0.10	0.23	0.21	0.15	0.29	0.73
29 August-3 Sept.	0.13	0.10	0.23	0.23	0.15	0.35	0.67

Optical Characteristics of the Atmosphere. It was mentioned in [1,2] that the ratio K/K_{Rk} for the Mars observations in 1956 undergoes substantial oscillations for day to day, and is close to unity for certain maria in all the spectral regions.

Let us examine two possible cases connected with this.

1. The true highland-mare contrast is not wavelength-dependent and is equal to its value measured at 0.75μ . In this case, all the variations observed in the ratio K/K_{Rk} should be attributed

to the oscillations in transmissivity of the atmosphere. It follows from Table 2 that the weakest change in contrast ratio over the spectrum is observed for the point with number 20, which corresponds to the aerographic longitude of $L \approx 280^\circ$. In the assumption we made, this moment of observations corresponds to the highest transmissivity of the Mars atmosphere.

TABLE 4

№	0.43 μ				0.53 μ				0.63 μ			
	$\rho_1 = 0.055,$ $A_1 = 0.653$		$\rho_2 = 0.120,$ $A_2 = 0.102$		$\rho_1 = 0.121,$ $A_1 = 0.115$		$\rho_2 = 0.170,$ $A_2 = 0.169$		$\rho_1 = A_1 = 0.270,$ $\rho_2 = A_2 = 0.278$			
	$\rho_0^{(1)}$	M_1	$\rho_0^{(2)}$	M_2	$\rho_0^{(1)}$	M_1	$\rho_0^{(2)}$	M_2	$\rho_0^{(1)}$	M_1	$\rho_0^{(2)}$	M_2
1	0.046	0.59	0.085	0.58	0.030	0.89	0.041	0.88	0.031	0.91	0.025	0.94
2	0.041	0.64	0.090	0.67	0.030	0.84	0.053	0.84	0.014	0.97	0.010	0.97
3	0.060	0.56	0.113	0.27	0.081	0.59	0.117	0.58	0.060	1.09	0.080	1.09
4	0.046	0.60	0.085	0.58	0.046	0.81	0.067	0.80	0.028	0.95	0.021	0.95
5	0.043	0.65	0.079	0.63	0.079	0.86	0.042	0.89	0.028	0.95	0.023	0.95
6	0.051	0.51	0.085	0.50	0.067	0.70	0.093	0.69	0.036	0.93	0.030	0.93
7	0.057	0.39	0.106	0.37	0.057	0.75	0.082	0.74	0.083	0.84	0.069	0.84
8	0.031	0.81	0.056	0.79	0.028	0.90	0.040	0.89	0.000	1.00	0.006	1.09
9	0.048	0.57	0.089	0.56	0.048	0.79	0.070	0.79	0.061	0.88	0.051	0.88
10	0.049	0.69	0.070	0.68	0.039	0.84	0.056	0.89	0.028	0.95	0.023	0.95
11	0.028	0.84	0.052	0.82	0.017	0.95	0.025	0.94	0.014	0.98	0.012	0.98
12	0.017	0.58	0.086	0.57	0.061	0.73	0.088	0.72	0.002	1.00	0.000	1.00
13	0.055	0.45	0.101	0.44	0.067	0.69	0.096	0.70	0.014	0.98	0.012	0.98
14	0.051	0.52	0.094	0.51	0.070	0.66	0.102	0.66	0.008	0.99	0.007	0.99
15	0.047	0.57	0.088	0.57	0.064	0.70	0.093	0.70	0.017	0.91	0.039	0.91
16	0.036	0.71	0.067	0.69	0.068	0.73	0.098	0.72	0.050	0.91	0.011	0.91
17	0.042	0.66	0.078	0.64	0.075	0.63	0.109	0.63	0.022	0.96	0.018	0.96
18	0.038	0.72	0.070	0.71	0.057	0.75	0.082	0.74	0.031	0.94	0.025	0.94
19	0.023	0.89	0.043	0.87	0.035	0.87	0.051	0.86	0.019	0.96	0.016	0.96
20	0.014	0.98	0.025	0.96	0.008	0.99	0.012	0.99	0.000	1.00	0.000	1.00
21	0.058	0.37	0.107	0.36	0.087	0.54	0.126	0.54	0.078	0.85	0.064	0.85
22	0.046	0.60	0.085	0.58	0.081	0.59	0.117	0.58	0.053	0.90	0.044	0.90
23	0.043	0.65	0.079	0.63	0.075	0.63	0.109	0.63	0.028	0.95	0.023	0.95
Average	0.043	0.62	0.080	0.61	0.053	0.75	0.077	0.76	0.029	0.94	0.024	0.94

Assuming that $\sigma(\lambda) = 1$ (1), we will determine ρ_0 for this moment. Using the tables of [13], and assuming that there is pure scattering and a spherical index according to the value of ρ_0 found, let us find τ . Knowing τ and using (2), we will determine A_1 according to the tables in [14]. The values of A_1 thus found are given in Table 4. They were used subsequently in calculations of the function M according to (2) and for other observation periods. Figure 4 shows the dependence of the brightness factor on the wavelength for a Mars highland at the center of the disk. As can be seen from the figure, the energy distribution in the Mars spectrum which was found according to the method of photographic photometry with filters differs substantially from the spectral and photoelectric data. Without analyzing the reasons for this deviation, we used both values of ρ in the subsequent calculations.

The final data for ρ_0 are given in Table 4. Table 5 shows the values for the optical thickness τ and the probabilities of quantum survival ω for three values of the first coefficient is an expansion of the scattering index into a series by Legendre polynomials x_1 . In determining them, we used the average values of ρ_0 and M given in Table 4, as well as the tables of [13,14]. We then calculated

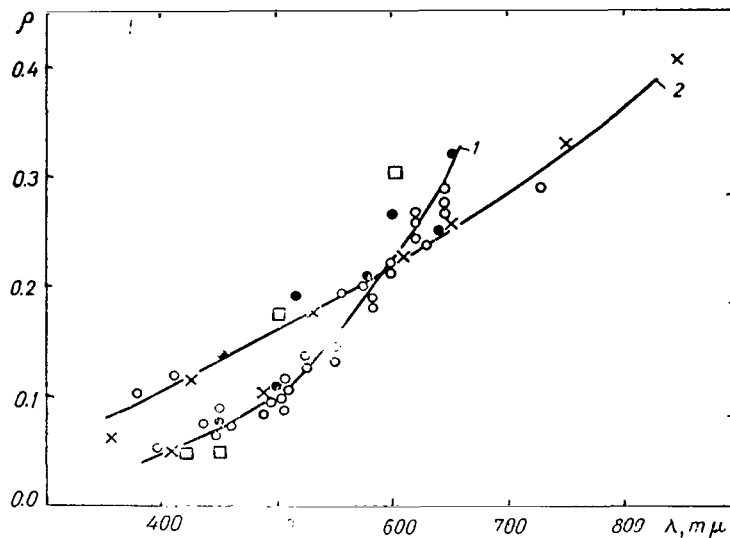


Fig. 4. Function of the Brightness Coefficient with the Wavelength for the Mars Highlands (1 - Spectral and Photoelectric Data; 2 - Data of Photographic Photometry).

the values of the brightness coefficient of the limb of the Mars disk ρ_r ($r = 0.85 R_{\oplus}$) according to the values found for τ and ω , and we presented them in Table 6. The observed values of ρ_r at the edge of the disk and the final values for the parameters A_1 , x_1 , ω and τ are given in Table 7 (the subscripts correspond to Table 4).

TABLE 5

x_1	0.43 μ				0.53 μ				0.65 μ			
	$\rho_1=0.065$		$\rho_2=0.120$		$\rho_1=0.120$		$\rho_2=0.175$		$\rho_1=0.230$		$\rho_2=0.278$	
	τ	ω	τ	ω	τ	ω	τ	ω	τ	ω	τ	ω
0.0	0.57	0.44	0.67	0.63	0.39	0.61	0.41	0.78	0.11	0.99	0.10	1.00
1.0	0.72	0.57	0.88	0.73	0.53	0.74	0.63	0.84	0.17	0.95	0.19	1.00
1.5	0.90	0.68	1.14	0.81	0.72	0.82	0.85	0.90	0.26	0.97	0.30	1.00

TABLE 6

x_1	0.43 μ		0.53 μ		0.65 μ	
	ρ_1	ρ_2	ρ_1	ρ_2	ρ_1	ρ_2
0.0	0.063	0.109	0.099	0.142	0.138	0.161
1.0	0.059	0.093	0.086	0.118	0.130	0.155
1.5	0.045	0.071	0.058	0.093	0.112	0.140

TABLE 7

Optical Parameters	0.43 μ		0.53 μ		0.65 μ	
	1	2	1	2	1	2
ρ_{11}	0.065	0.120	0.120	0.175	0.230	0.278
ρ_r	0.019	0.092	0.084	0.115	0.128	0.152
A_1	0.053	0.102	0.115	0.169	0.230	0.278
x_1	1.3	1.1	1.1	1.1	1.1	1.1
ω	0.65	0.76	0.76	0.85	0.96	1.00
τ	0.76	1.05	0.55	0.68	0.19	0.21

2. Aside from rare exceptions, the Mars atmosphere has a transmissivity factor which does not change in time over the entire interval $\lambda\lambda$ under investigation. Thus, for the overwhelming majority of maria, we have $c(\lambda) = 1$. In other words, the true highland-mare contrast changes over the spectrum.

In this case, the observed oscillations of K/K_{rk} indicate that the energy distribution in the spectrum of each single mare is different. As in the first case, the mare with number 20 is characterized by the smallest decrease in observed contrast near the violet end of the spectrum. We will attribute the small difference between spectral values for the contrast of this mare to the blurring effect of the Mars atmosphere, and we will assume that $c(\lambda) = 1$. Then, in the case of pure scattering and a spherical index, for values of the albedo of the highland as given in Table 4, we will find the following values according to the ρ_0 and μ found for this mare (Table 4) for the Mars atmosphere:

λ_μ	0.43	0.53	0.65
τ_1	0.035	0.029	0.008
τ_2	0.072	0.033	0.013

Just as in the first case, we used the tables of [13,14] for these calculations, and we made the computed values of ρ_r agree with those

observed.

The optical parameters found in this case for the Mars atmosphere allow us to determine the average behavior of the real contrast over the spectrum over all the maria, within the framework of the assumptions made. Omitting the simple calculations based on (1) let us present the final result for the coefficient $\frac{1}{c(\lambda)}$:

λ_{μ}	0.43	0.53	0.65	0.75
$\frac{1}{c(\lambda)}$	0.64	0.75	0.96	1.00

Analysis of the Results and Conclusions. We have examined two possible causes for the observed oscillations in contrasts on Mars in the visible spectral region. In the first variation, the data of the observations correspond to substantial disordered oscillations in the transmissivity of the Mars atmosphere, and, in the second case, they correspond to a certain difference in the energy distribution in the spectrum of individual maria for constant transmissivity of the atmosphere. In the first case, the Mars atmosphere should have an optical thickness close to unity in the violet lines, as well as substantial true absorption. The scattering of light occurs mainly in aerosols ($x_1 \approx 1$). In the second case, the Mars atmosphere has an optical thickness which is one order less than in the first case, for pure scattering and a spherical index.

Let us turn to Table 2, where the contrasts are given, as well as their ratios, representing the average value for each complete revolution of Mars. As can be seen from the table, the ratios K/K remained practically unchanged for all the three observation periods, which can be considered as an indication that the transmissivity of the Mars atmosphere was constant during the entire period of observations in 1956. We should mention, however, that the data of the last row in Table 2 refer to the period of a dust storm on Mars, which caused a decrease in contrast in all the spectral regions under investigation, except for the violet (0.43 μ), where this change could remain unnoticeable, since the measurement accuracy was not great in small contrast measurements in these lines.

Thus, this fact, that the ratio K/K_{rk} kept its value during the period of the dust storm, corroborates that variation according to which the Mars atmosphere in its ordinary state (in the absence of abrupt anomalous phenomena) has a low optical thickness which is constant in time. Finally, having revised the data of Table 3 (last column), we can see that, except for rare cases, all the Mars maria observed in 1954 with double superposition of longitudes show constancy (within the limits of the errors) in the ratio K_c/K_k for the entire period of observations. The monotonous decrease observed in the contrast at the end of the period of observations

(near the beginning of summer in the southern hemisphere of Mars) was apparently due to a true decrease in surface contrasts.

The above shows, in our opinion, that the observed oscillations in the ratio examined for the highland-mare contrasts were due mainly to some difference in the change of albedo over the spectrum for individual maria of Mars, as well as to the substantial effect of the measurement errors. Some of the observed changes in the contrasts themselves should not be considered, since they may be found to be deceptive when there is no strict control over the turbulent state of the Earth's atmosphere and there are substantial measurement errors.

TABLE 8

x_1	0.43 μ			0.53 μ			0.65 μ		
	τ	ω	ρ_r	τ	ω	ρ_r	τ	ω	ρ_r
0.0	0.17	0.77	0.08	0.14	0.85	0.10	0.01	1.00	0.14
1.0	0.27	0.83	0.07	0.23	0.85	0.09	0.07	1.00	0.13
1.5	0.45	0.90	0.06	0.33	0.95	0.08	0.12	0.98	0.12

TABLE 9

Optical Parameters	λ, μ			
	0.43 μ	0.53 μ	0.65 μ	0.75 μ
K_{app}	0.12	0.17	0.26	0.28
K_{real}	0.18	0.21	0.27	0.28
A_1	0.08	0.14	0.25	0.30
c	0.09	0.15	0.25	0.30
ρ_r	0.07	0.10	0.14	0.16
ρ_0	0.032	0.028	0.010	0
τ	0.25	0.17	0.05	0
ω	0.80	0.85	1	—

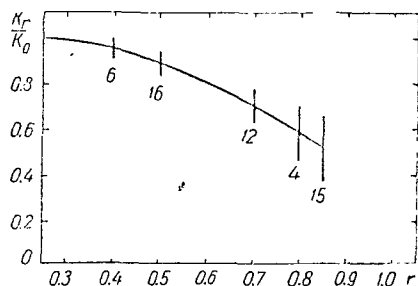


Fig. 5. Change in Highland-Mare Contrast at the Limb of the Mars Disk (1954, 1956).

We will definitely assume that the change in true contrast over the spectrum is characterized by the average values of the parameter $1/c(\lambda)$ discussed in Section 2 of the preceding division. Then, taking the average values of the ratio K/K_{rk} (Table 2) without a consideration of the values of $K \leq 0.05$ for

0.43 μ and using the formulas in (1) and (2) and the tables of [13, 14], we will obtain the data presented in Table 8. This table also contains values of ρ_p calculated according to those found for τ and ω , which were compared to those observed. In these calculations, we used the average values of ρ_1 and ρ_2 given in Table 4 for the brightness coefficient of the highlands at the center of the disk, since it is still difficult to give preference to any single result included in Figure 4.

The final results for τ and ω at $0 \leq x_1 \leq 1$ are given in Table 9, together with other optical characteristics of Mars.

Finally, let us formulate the conclusions which can be drawn from an analysis of the observed contrasts between the highlands and maria of Mars and the calculations presented above.

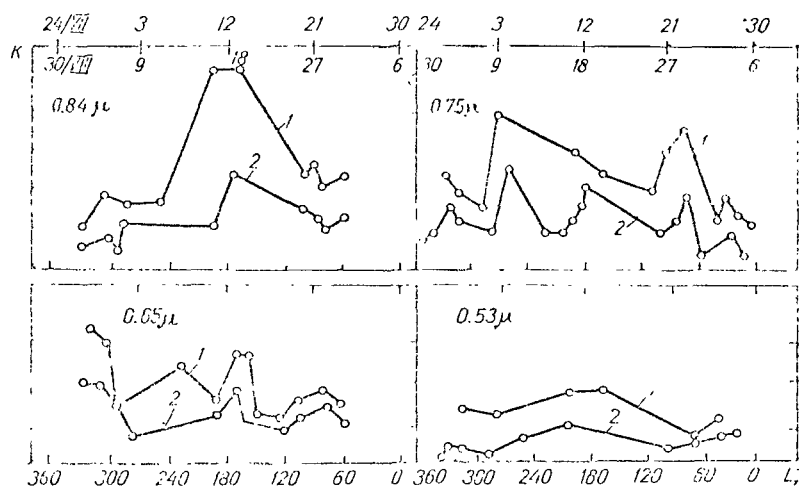


Fig. 6. Decrease in Highland-Mare Contrast on Mars Due to the Dust Storm in 1956 (1 - July, 2 - August-September).

(1) The photometric data on the highland-mare contrasts obtained in different spectral regions can serve as the basis for determining the optical parameters of the Mars atmosphere. The oscillations in the transmissivity of the Mars atmosphere can be detected only when there are contrasts measured for the same maria.

(2) A study of the measured variations in the contrast ratio K/K_{rk} shows that this phenomenon can be explained mainly by the differences in the behavior of the albedo over the spectrum for individual maria, as well as the measurement errors.

(3) The Mars atmosphere has invariable transmissivity, except

for rare cases. The observations which we carried out in 1954, 1956 and 1958 according to the method of photographic photometry did not show any so-called violet transilluminations. At the same time, these illuminations were sometimes observed in visual observations. In order to obtain quantitative data on the transilluminations, there must be photographic observations with exposures of hundredths of a second, which partially eliminate the distorting effect of the Earth's atmosphere, bringing about substantial blurring of the true contrasts. In photometric observations requiring several seconds of recording time, there must be strict control over the state of the Earth's atmosphere. The decrease we obtained earlier [12] in the red lines of the highland-mare contrast at the edge of the Mars disk (Fig. 5) also may be deceptive, since the distorting effect of the Earth's atmosphere increases in the same direction;

(4) The Mars atmosphere has an optical thickness which is one order greater than follows from spectral data according to measurements of the CO_2 bands, and is characterized by a certain true absorption in the violet spectral region. If we assume that the values of the parameter τ given in Table 9 are due completely to aerosols, and if we divide the scattering component according to the values obtained for ω , then we will find a radius of aerosol particles on the order of 10^{-5} cm and a quantity of particles of 10^{10} cm^{-2} . The contrasts found according to the 1956 observations for the same maria before and after the dust storm (Fig. 6) gave dimensions of the dust particles of $r \approx 1.5 \mu$ [6]. Approximating calculations show that the quantity of these particles is equal to 10^6 - 10^7 cm^{-2} .

REFERENCES

1. Koval', I.K.: Izvest. Komissii po Fizike Planet, Vol. 3, pp. 76-84, 1961.
2. Barabashov, N.P. and I.K. Koval': Astron. Zhur., Vol. 37, No. 2, 1960.
3. Sharonov, V.V.: In the Book: Rezul'taty nablyudeniya Marsa vo vremya velikogo protivostoyaniya 1956 g. v SSSR (Results of Mars Observations During the Great Opposition of 1956 in the U.S.S.R.). Moscow, Akad. Nauk S.S.S.R., pp. 155-164, 1959.
4. Barabashov, N.P. and I.K. Koval': Fotograficheskaya fotometriya so svetofil'trami v 1956 (Photographic Photometry with Light Filters in 1956). Khar'kov, Khar'kov State University Press, 1959.
5. Sytinskaya, N.N.: In the Book: Rezul'taty nablyudeniya Marsa vo vremya velikogo protivostoyaniya 1956 g. v SSSR (Results of Mars Observations during the Great Opposition of 1956 in the U.S.S.R.). Moscow, Akad. Nauk S.S.S.R., pp. 166-171, 1959.
6. Koval', I.K. and A.V. Morozhenko: Astron. Zhur., Vol. 39, p. 65, 1962.
7. Bugayenko, L.A., O.I. Bugayenko, I.K. Koval' and A.V. Morozhenko: In the Book: Fizika Lunny i planet (Physics of the Moon and Planets). Kiev, "Naukova dumka", 1964.
8. Bugayenko, L.A., O.I. Bugayenko, I.K. Koval' and A.V. Morozhenko: In the Book: Fizika Lunny i planet (Physics of the Moon and Planets). Kiev, "Naukova dumka", 1966.
9. Barabashov, N.P., I.K. Koval' and A.T. Chekirda: Izvest. Komissii po Fizike Planet, Vol. 2, pp. 36-40, 1960.
10. Sobolev, V.V.: Kurs teoreticheskoy astrofiziki (Course in Theoretical Astrophysics). Moscow, "Nauka", pp. 239-255, 1967.
11. Koval', I.K.: Astron. Tsirk Khar'kov. Astron. Observ., Vol. 15, 1956.
12. Koval', I.K.: Astron. Zhur., Vol. 34, pp. 412-418, 1957.
13. Morozhenko, A.V. and E.G. Yanovitskiy: In the Book: Voprosy astrofiziki (Problems of Astrophysics). Kiev, "Naukova dumka", 1965.
14. Morozhenko, A.V. and Ye.G. Yanovits'kiy: Tablitsi dlya rozrakhunku intensivnostey viprominyuvannya atmosfer planet (Tables for Calculating the Radiation Intensities of the Atmospheres of Planets). Kiev, "Naukova dumka", 1964.

THE NATURE OF THE POLAR CAPS OF MARS

I.K. Koval' and A.V. Morozhenko

ABSTRACT: Data are given on the change in size of the polar caps of Mars with the heliocentric longitude, according to photographic and visual observations (Fig. 2). The structure and nature of the polar caps are discussed on the basis of long-term photometric investigations. The amount of water on Mars is estimated. The substance forming the polar caps is assumed to be concentrated on the Mars surface, and seems to be a discontinuous layer of snow with neutral albedo equal to 0.8. This assumes that the layer of snow occupies approximately 25% of the area of the cap. Using a value of 2 cm for the thickness of the snow layer, the amount of precipitable water is found to be equal to 0.005-0.05 g/cm².

The monochromatic albedo of the polar regions of Mars has been determined repeatedly, and it can presently be held that the contrast produced by the polar caps with the neighboring Mars surface increases rapidly around the violet end of the spectrum and averages 40-50% around 0.4 μ , against the 20% around 0.65 μ . At the same time, the brightness factor of the caps, which is obtained directly from observations, has the reverse behavior over the spectrum and averages 0.25 and 0.45 μ for the same wavelengths.

The spectral values for the albedoes of the caps change substantially in dependence on the season in the given hemisphere of the planet; however, the path of the albedo over the spectrum remains practically unchanged.

We could mention a number of periods when the polar cap was at the limit of detection (contrast of about 0.05) in the long-wave spectral region, while it was rather bright in the blue lines. For example, we could mention the opposition of 1961, as well as 1965 (after the middle of September).

During other periods, for example is June-August of 1956, the polar cap was clearly distinguishable against the planetary disk over all the spectral regions of the interval 0.36-0.84 μ .

These observational facts should underlie any hypothesis concerning the nature of the polar caps of Mars.

Information on the change in size of the polar caps of Mars in dependence on the heliocentric longitude of the planet is given in this study. The data were based mainly on years of photographic observations. Our work also discusses the photometric characteristics of the caps obtained for a number of oppositions. The problem of the possible nature of the caps of Mars is examined on the basis of the latter, with some assumptions relative to their structure.

Change in Size of the Polar Caps. The polar caps of Mars are the most accessible for observations of details of the planetary disk because of their relatively large size. For many years, observers using micrometric measurements directly with a telescope or photographic images have accumulated a vast amount of data which indicate the change in size of the polar caps of Mars during the course of a practically complete cycle of seasons for all the heliocentric longitudes of the planet.

Since the observational period is limited to a few months during one opposition of the planet, and it allows for measurements only in a small range of heliocentric longitudes, the complete cycle of changes in size of the caps of Mars can be traced only according to many years of observations carried out by various observers with different observational instruments for different states of the Earth's atmosphere. This leads to a substantial discrepancy in the points on summary tables of the change in size of the polar caps.

As a rule, the change in size of the Martian caps is given in the form of a graph of the change in latitude of the average boundary of the cap in dependence on the heliocentric longitude of Mars.

The contrast between the polar cap and the neighboring highland regions of the planet in the visible spectral region is usually 30-40%, and visual measurements of the apparent height of the cap can be carried out with error of about 1", which is equivalent to an error in the latitude of the cap boundary of about 4° for a latitude of 60° in zero areocentric inclination of the Earth at the moment of a great opposition ($d \odot = 25''$), and about 6° for a latitude of 70°. It is obvious that these errors increase in correspondence with an increase of the Earth-to-Mars distance and, for example, are equal to 5 and 8° for $d \odot = 15''$ for the same values of the aerographic latitude.

However, the size of a polar cap is usually determined during periods when the corresponding pole is inclined toward the Earth at several degrees; therefore, the error in measurements is actually less than the cited values.

In measuring the dimensions of the polar caps according to

photographic images, the error in the value of the latitude determined is made by photographic irradiation arising as a result of a substantial cap-highland contrast, as well as the shaking of the image due to the instability of the Earth's atmosphere.

In order to evaluate the error contributed by the photographic irradiation, we carried out the following experiment. Two adjacent bands coated with substances with different degrees of selected reflectivity were photographed so that their total image did not exceed 2 mm in width (which is close to the diameter of the image of Mars), while the photographic-density differential was close to

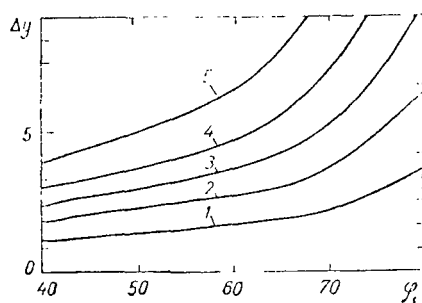


Fig. 1. Errors in Determining the Apparent Latitude ϕ of a Polar Cap for Linear Diffusion of the Real Boundary Δy Due to Photographic Irradiation and Shaking of the Image [$\Delta y = 0.01$ (1); 0.03 (2); 0.05 (3); 0.07 (4); 0.10 (5)].

planet from the Earth and, with the scale of the image ordinarily unchanged during the course of the entire observational period during an opposition, together with the shaking of the image, it can bring about substantial errors in determining the boundary of a Mars cap.

Figure 1 contains graphs which illustrate the values of the error in determining the position of the boundary of a polar cap with apparent latitude of ψ_1 for different linear values of the spread Δy of the true boundary ϕ_2 , expressed in percentages of the radius of the planet. The calculations were carried out according to the following formula:

$$\sin \varphi_2 = \frac{\Delta y}{2} + \sin \varphi_1.$$

the differential between the cap and the highlands surrounding it. It was found that the increase in width of the lighter band imitating the polar cap of Mars was about 5% of the scaled width of the model for normal photographic density (1.2), for the emulsion Agfa ISS. For a diameter of the image of Mars equal to 2 mm obtained at the moment of the great opposition, this increase is by 1.2" and is comparable to the error introduced by the shaking of the image for a satisfactory turbulent state of the atmosphere of the Earth.

Thus, the photographic irradiation, just as the image shaking, brings about a systematic decrease in the latitude of the boundary of the polar caps of Mars determined according to photographic images. This decrease progresses with an increase in the distance of the

To determine ϕ_2 of the polar caps of Mars during the oppositions of 1950, 1952, 1954, 1956, 1958 and 1960-1961, we used the photographic data obtained by N.P. Barabashov and others on the 20-centimeter refractor and the 27-centimeter reflector of the Astronomical Observatory of Khar'kov State University. The exception was the period of 1960-1961, when the measurements were carried out according to data obtained at the Main Astronomical Observatory of the Academy of Sciences of the Ukrainian S.S.R. with the aid of a 70-centimeter reflector. All the micrometric measurements were carried out for the blue and green spectral regions. The data of the Astronomical Observatory of Khar'kov State University were used by us in 1965. The "heights" of the polar caps measured were roughly corrected for the cited effects with values of $\Delta y = 0.05-0.08 R \odot$, in dependence on the Earth-Mars distance and for $\Delta y = 0.05 R \odot$ for the moment of a great opposition. This value corresponds to the spread of the boundary of the cap by 1.2" and, in our opinion, is close to the true value. The measurement results obtained are given in Table 1 and they agree well with the observations of other authors.

TABLE 1

1950		1954			1956		1958			1958		
τ_1	N	τ_1	S	N	τ_1	S	τ_1	S	N	τ_1	S	N
200	82	264	66	69	285	57	16	69	69	38		68
207	83	285	69	67	290	58	17		68	39	78	68
216	82	305	72	61	300	59	19		69	40		71
220	81	321	76	61	310	62	21		70	41		70
227	81	1960-1961			320	70	25		68	44	80	71
229	82	85	69	67	330	77	26		69	45	77	69
236	84	108	68	70	340	83	28	74	71	49	76	69
238	78	135	62	76	350		29	74	71	53	77	70
1952					0	75	32	76	67			
208	80				10	71	35	73	73			
216	80				20	81	36	79	73			
221	78				30	78	37		70			

Figure 2 shows a complete cycle of the change in dimensions of both polar caps of Mars, which was obtained both according to our measurements and according to the data published by other observers [1,2,3, etc.]. We should mention that the data concerning a determination of the dimensions of polar caps which are based on visual observations and published in the literature are not very great, and it is impossible to plot all the measurements on the summary graphs; therefore, Figure 2 gives only those points which characterize the average change in ϕ_2 over the entire range of heliocentric longitudes.

It follows from Figure 2 that the southern cap of Mars occupies an area at the maximum which is 1.5 times larger than that of the northern cap. The maximum rate of melting (increase) of the south-

ern cap $\frac{d\phi}{d\eta}$ corresponds to 0.35, while it is equal to 0.25 for the northern cap.

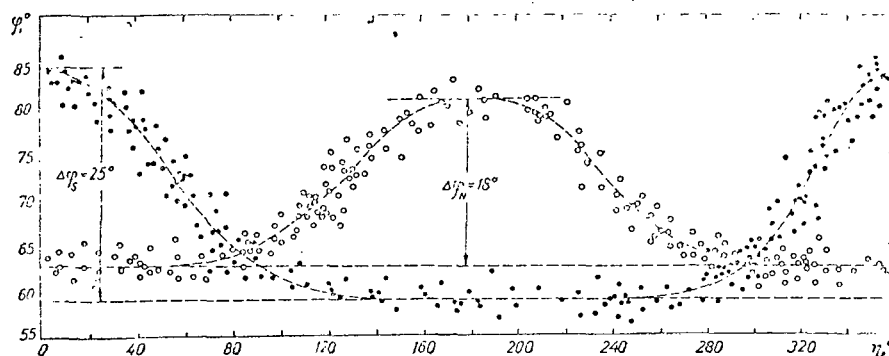


Fig. 2. Change in Dimensions of the Polar Caps of Mars in Dependence on the Heliocentric Longitude η (Summary Graphs) (ϕ is the Aerographic Latitude of the Cap Boundary, \bullet - S, \circ - N).

The summary graphs of the change in dimensions of the polar caps of Mars with the heliocentric longitude given in Figure 2, together with the data on the temperature phase on the planet, can be used for different types of calculations of the amount of the yearly water cycle on Mars. Some calculations on this then are found in [4,5].

Structure and Possible Nature of the Polar Caps. Photometric data show that the cap-highland contrast increases monotonously around the violet end of the spectrum. Absolute measurements leave no doubt that the brightness coefficients of the caps decrease in the same direction. Only in isolated cases does the spectral course of the brightness factor for the polar caps in the range of 0.4-0.65 μ come close to the neutral one. It is possible that the polar caps consist of only one atmospheric component during these periods, and the brightness coefficient in the red part of the measurement spectrum relates to the surface of Mars.

The question of the structure of polar caps during different seasons has long been discussed in the literature. The infrared spectra of the caps [6,7], as well as polarization observations [8], indicate that the polar region has the nature of water (hoarfrost or a thin layer of snow). This is also indicated in the photographic observations which show the reality of a shaded margin around the cap boundary which is clearly visible in the green and red lines during the period of the maximum rate of melting. The observations which were carried out for four months in 1956 [9] showed the existence of a shaded ridge around the boundary of the southern polar cap only during the period from July 30 to

August 20, which corresponds to a heliocentric longitude of Mars of about 330° and maximum rate of melting of the southern polar cap.

The extensive visual observations of the polar caps indicate that not only their dimensions change, but also their color and brightness. Previous photographic observations with light filters [10] showed that the polar caps have greater dimensions during certain periods in the violet lines than in the red. Wright states justifiably that this effect may be due to the existence of an atmospheric component around the polar cap, although the photographic irradiation and shaking of the image could play a substantial role here, and their effect could bring about a false increase in the photographic size of the cap in the violet lines, in which the contrast between the cap and the surrounding highlands is close to 0.5, against the 0.2 in the red lines. A stronger argument in favor of the existence of atmospheric haze over the polar regions of Mars, scattering the violet rays, is the varying brightness of the polar cap noticed by several observers during visual observations in the period preceding its melting, and during the melting period. For example, in 1956, the brightness of the southern polar cap of Mars during the melting period (July, August increased substantially in comparison with the other seasons and was clearly seen in the blue and infrared lines (0.43) and 0.84 [11]). The photometric analyses of the photographs obtained showed that all the observational data relating to the polar cap during this period could be explained completely if we assumed that the polar substance was propagated completely over the surface of the planet and was observed through a Mars atmosphere which was uniform for the entire visible hemisphere. During the second half of September of 1956, and later, after an almost total disappearance of the southern polar cap over the entire spectral range of $0.36 - 0.84 \mu$, a bright spot again arose over the polar region, but this time with other spectral values of the albedo.

The brightness factors of the southern polar cap of Mars which were obtained in June-October of 1956 with light filters of 0.36, 0.43, 0.53, 0.65 and 0.75μ transmission maxima are given in Figure 3.

Figure 4 shows the dependence of the brightness coefficient of the southern polar cap of Mars on the heliocentric longitude according to observations in 1954 [12] and 1956 [9]. During these two oppositions, there were absolute photometric observations which were most suitable for comparing the brightness of the cap in the red and blue lines. The observations were carried out with broad-band filters with several transmission maxima; therefore, the brightness coefficients obtained in 1956 were reduced preliminarily to the wavelengths for 1954 according to the average course of the brightness of the cap depicted in Table 2 in relation to the wavelength. The data given in Figure 4 relate to wavelengths of 0.46 and 0.65μ . The horizontal lines show the values of the brightness

coefficients for the red and blue lines, referring to regions of the planet at a distance of $0.8 R \odot$ from the center (the measurements were carried out during the period of the opposition).

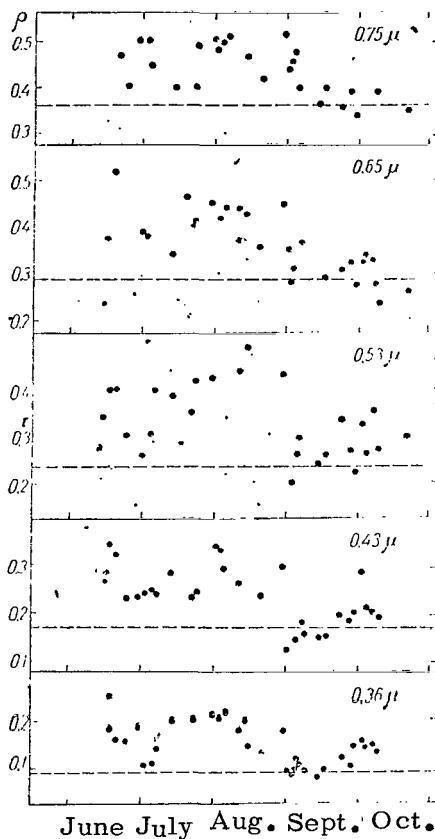


Fig. 3. Brightness Factors ρ for the Southern Polar Cap of Mars According to the Observations of 1956.

As can be seen from the figure, for a value of $\eta = 330^\circ$ for a general substantial deviation in the measured points, which can be explained mainly by the measurement errors and the nonuniform brightness of the cap at different aerographic longitudes, the brightness of the cap remained constant in both spectral regions.

This result can be explained by the fact that, during the Martian autumn and the beginning of the summer in the southern hemisphere of Mars, up to the period of the abrupt decrease in dimensions of the cap in the blue and red lines, there was only one formation observed, and that was located most probably over the surface of the planet. The more or less smooth decrease in brightness of the cap in the range of the maximum rate of its melting ($\eta = 340^\circ$) hardly corresponds to reality. Most probably, the effect of the atmospheric vibration of the image,

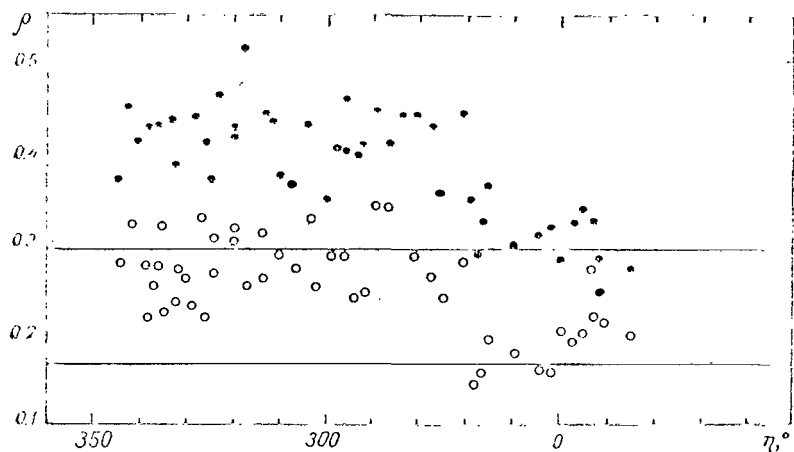


Fig. 4. Change in Brightness Coefficient for the Southern Polar Cap of Mars According to Observations in 1954 [12] and 1956 [9] (● - 0.65μ ; ○ = 0.46μ).

blurring a small polar spot during this period and decreasing its surface brightness, appears here to a significant extent.

Starting in the middle of September in 1965 ($\eta = 15^\circ$), the polar cap which again appeared in the blue lines almost reached the previous brightness (brightness factor averaging 0.2, instead of 0.28 before the disappearance of the cap) and made a contrast of 0.2 with the brightness of the surrounding surface. The brightness coefficient of the cap in the red lines decreases from 0.42 to 0.31, while the contrast decreases to 0.08 around the detection limit of 0.05.

TABLE 2

λ_μ	Spectral Values of the Cap- Highland Contrast			
	1950-1961 (average)		1956, June - Aug.	1960 - 1961 (average)
	S	N	S	S and N
0.36	0.41	0.42	0.52	
0.40	0.41	0.40	0.43	0.45
0.45	0.37	0.35	0.39	0.35
0.50	0.32	0.29	0.36	0.27
0.55	0.28	0.24	0.33	0.20
0.60	0.22	0.19	0.31	0.07
0.65	0.18	0.15	0.28	0.07
0.70	0.15	0.12	0.25	
0.75	0.11	0.09	0.22	
0.80	0.10		0.19	
0.84	0.09		0.17	

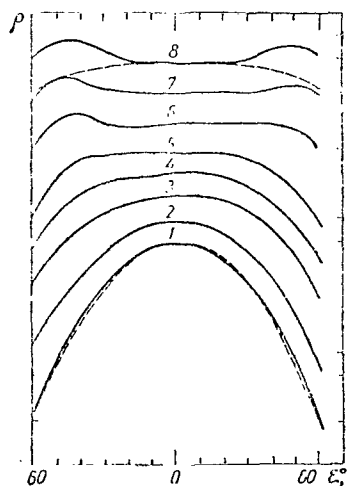


Fig. 5. Brightness Distribution along the Central Meridian of Mars According to Observations on January 6-7, 1961 ($\Delta p = 0.02$; ϵ is the Angle of Reflection: 1 - 0.65; 2 - 0.60; 3 - 0.57; 4 - 0.55; 5 - 0.54; 6 - 0.49; 7 - 0.45; 8 - 0.42 μ). The Brightness Distribution Along the Intensity Equator on the Highlands is Represented by the Dashed Line.

During the opposition of 1961, the spectrophotometric observations of Mars carried out at the Main Astronomical Observatory of the Academy of Sciences of the Ukrainian S.S.S. [13]

for orientation of the slit of the spectrograph along the central meridian of the planet, led to the same result. The photometric sections of the spectrum (Fig. 5) show that the cap-highland contrast for both polar caps decreases smoothly from 0.45 (0.4 μ) to 0.07 (0.65 μ). The photographs of Mars obtained with light filters during this period also do not show the polar caps in the red lines, while they are clearly visible in the blue.

This period of observations corresponds to equinox on Mars. The polar regions were in symmetrical seasonal stages; the southern cap underwent the process of formation, while the northern cap was on the eve of the melting process. The photometric characteristic of the polar caps of Mars mentioned above refers to definite periods of their evolution; during these periods, the polar caps are mainly atmospheric formations similar in terms of optical properties to the Wright clouds sometimes observed on the morning and evening limbs.

Let us examine the problem of the structure and nature of the polar caps when they are located on the surface of the planet. Several hypotheses relative to the substance forming the polar cap have been proposed. One of them, the ice hypothesis, won popularity in its time because of the specific reflectivities of ice. Ice is transparent in the long-wave spectral range; therefore, the brightness of the polar regions in these lines is determined mainly by the reflectivity of the true Mars surface. When the wavelength decreases, the reflectivity of ice increases and reaches 53% near 0.43 [14]. However, this hypothesis does not agree with the fact that the polar caps during single periods are seen very clearly over the entire spectral range under investigation. In this case, to explain the nature of the caps, we must have a substance with a more neutral reflection coefficient. This substance is snow or hoarfrost. The hypothesis that there is a continuous snow cover is confronted with the problem that the reflection coefficient of snow is almost wavelength-independent and is close to 80%. The fact that the observed brightness coefficient of the polar cap is always much less than 0.8 is explained by some authors either in terms of a diminishing of the brightness of the polar cap by the Mars atmosphere, or with the concept that the snow layer is not continuous.

The polarization observations of the polar cap and the laboratory measurements of the polarization properties of hoarfrost carried out by Dollfus [8], as well as the calculations carried out by Lebedenskiy and Salova [5], show that the substance covering the polar regions of Mars is hoarfrost or a discontinuous layer of snow.

In our opinion, the hypothesis of the discontinuous snow layer or hoarfrost is likely and can explain the spectral properties of the polar cap. The presence or absence of a cap in the long-wave

spectral region can be determined completely by the ratio between the areas of the regions covered with snow and those without snow.

Let us attempt to confirm this by calculations.

We will assume in a rough approximation that there is no atmosphere on Mars. We will call the area of the polar region which is covered with snow β . The brightness coefficient of the cap ρ_c can then be expressed in terms of the brightness coefficients of the highland ρ_h and snow ρ_s in the following way:

$$\rho_c = (1-\beta)\rho_h + \beta\rho_s. \quad (1)$$

For the contrast highland-cap,

$$K'_0 = \frac{\rho_h - \rho_c}{\rho_h}. \quad (2)$$

For the sake of convenience, we will use the highland-cap contrast in the following way, as opposed to the ratio usually used:

$$K_0 = \frac{\rho_c - \rho_h}{\rho_h} = \beta \left(\frac{\rho_s}{\rho_h} - 1 \right). \quad (3)$$

Since ρ_s is close to 0.8 in the range of 0.36-0.84 μ , while β is also wavelength-independent, the change in contrast with the wavelength will be wholly determined by the spectral path of the brightness coefficient of the highland. Table 3 gives the computed values for the contrast, for several values of β , in dependence on the wavelength. The brightness coefficients of the highland were taken from the catalogue in [9].

TABLE 3

β	λ, μ					
	840	750	647	530	429	360
0.03	0.028	0.013	0.065	0.107	0.188	0.358
0.10	0.095	0.142	0.218	0.357	0.627	1.190
0.30	0.280	0.430	0.650	1.070	1.880	3.580

As can be seen from this table, the contrast in the long-wave spectral region for low β is very low, and can be imperceptible, a circumstance attributable to measurement errors for the existing

accuracy of photographic photometry. For example, this is affirmed in [13], where it is shown that the curves for the brightness distribution along the intensity equator and the central meridian coincide, although, as we will see later, the contrast reached 7% around 0.64μ on January 6-7, 1961.

These calculations can explain the spectral properties of the polar caps qualitatively; therefore, we will attempt to determine the values of β in the example of the Mars observations in 1956 and 1960-61.

For the planets enveloped by an atmosphere, the measured contrast K_m is connected with the real contrast K_0 by the following expression:

$$K_m = K_0 \left(1 - \frac{\rho}{\rho_h} \right), \quad (4)$$

where ρ is the brightness coefficient of the atmospheric column over the polar cap. For approximative calculations, we will not consider the effect of the Mars atmosphere. This approximation is not too rough if it is true that the Mars atmosphere in the spectral regions usually observed is optically thin ($\tau \leq 0.1$). In this case, (4) is converted into (3).

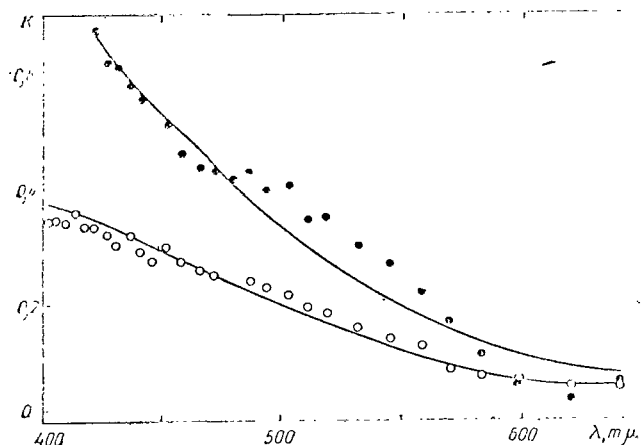


Fig. 6. Dependence of the Contrast of the Polar Caps of Mars on the Wavelength (● - December 5-6, 1960; ○ - January 6-7, 1961). The Solid Curves Designate the Contrast Calculated for $\beta = 0.061$ (upper) and 0.038 (lower).

Figure 6 shows the highland-cap contrast with the wavelengths for the observations during the opposition of 1960-1961. The

average values of the contrast obtained from observations of the southern and northern polar caps are given for both dates. Average values of β equal to 0.061 ± 0.005 and 0.038 ± 0.002 , respectively, were obtained for these two observation dates. The solid curves on Figure 6 represent the contrast calculated according to the values of β obtained as a function of the wavelength. As can be seen, the disagreement between the calculated and observed contrasts are insignificant and can be explained by the errors in observations and the fogging effect of the Mars atmosphere.

TABLE 4

λ $m\mu$	K_m	ΔK	β	K_0	τ	K'_m
750	0.29	0.03	0.24	0.30	(0.019)	0.29
647	0.41	0.01	0.25	0.44	(0.026)	0.42
530	0.59	0.07	0.25	0.59	(0.040)	0.51
429	0.75	0.06	0.19	0.96	0.060	0.75
330	0.89	0.09	0.11	1.97	0.090	0.89

For 1956, we used the average values of the contrast for the southern polar cap according to observations in June-August. The value of the contrast K_m , the root-mean-square deviation in the contrast ΔK and the values of β are given in Table 4. The data of this table show that the value of β in the long-wave spectral region ($0.53 - 0.75 \mu$) is almost wavelength-independent, while it decreases around the ultraviolet end of the spectrum. This decrease may be due to the fogging effect of the Mars atmosphere. Therefore, the values of β were taken as equal to 0.25 for an average, and the true highland-polar cap contrast K_0 was calculated with these values (see Table 4). Knowing K_m and K_0 , the optical thickness τ of the Mars atmosphere was evaluated according to (4) as 0.36 and 0.43μ . We should mention that the values found can be considered as the lower limit, since we took values for the observed brightness coefficients which may be much greater than the reflection coefficient of the Mars surface in calculating K_0 for the reflection coefficient of the highlands in the short-wave spectral region. Assuming pure scattering and a spherical scattering index, the optical thickness was found to be equal to 0.09 and 0.06 for 0.36 and 0.43μ respectively. Assuming that the function of the optical thickness with the wavelength obeys the same law for the red spectral region as in the region of $0.36 - 0.43 \mu$, we found the values of τ over all the spectral regions and roughly estimated which one should be the measured contrast K'_m if the true one were the same as in the column K_0 (the values of τ and K_m are given in Table 4). As can be seen, the fogging effect of the Mars atmosphere in the long-wave spectral region is small and is within the limits of the errors in determining the average value of the contrast.

Now let us attempt a rough estimation of that amount of water M which is necessary for the formation of a polar cap. The value we took for the reflection coefficient of snow, equal to 0.8, can be a layer of any thickness but, obviously, no less than several centimeters. To evaluate the lower limit to the amount of water forming the polar cap, we took the thickness of the snow layer as equal to 2 cm, while the density of the snow was $\bar{d} = 0.1 - 0.001$ g/cm³. The data obtained for the two values of β are given in Table 5. Data on the amount of water on Mars found according to the rate of melting of the polar cap [5] and according to observations [15] are given in the last two rows for the sake of a comparison. As can be seen, the model we have investigated for the polar caps does not contradict the spectroscopic determinations of the amount of water in the Mars atmosphere.

TABLE 5

β	α	$M, \text{ g/km}^2$
0.04	10^{-1}	0.008
	10^{-2}	0.0008
0.25	10^{-1}	0.050
	10^{-2}	0.005
		0.010
		0.0614

Thus, the calculations above show that the polar cap of Mars is a discontinuous layer of snow occupying up to 25% of the total area in the model we have assumed.

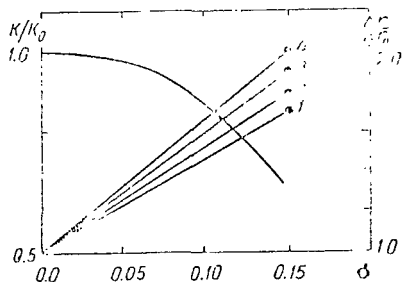


Fig. 7. Dependence of the Values $\Delta r/\Delta r_0$ on σ and on K_0 ($1 - K_0 = 0.5$; 2 - $K_0 = 1.0$; 3 - $K_0 = 1.5$; 4 - $K_0 = 2.0$).

As was shown in [16,17], the turbulent vibration of the image distorts the real brightness distribution over the disk of the planet. It is obvious that the highland-cap contrast will also undergo distortions of this type. Since we used the observed (distorted) values of the contrast in the calculations, we considered the effect of the image shaking in order to determine the possible error in β for blurring of the highland-cap contrast. The calculations were carried out for values of the contrast of 0.5, 1.0, 1.5, 2.0, for dimensions of the polar cap of $\Delta r_0 = 0.3R_0$ and for values of the parameter σ ,

characterizing the turbulent state of the Earth's atmosphere, of 0.05, 0.075, 0.10 and 0.15. Since these calculations are of an especially evaluative nature, we assumed that there was no limb darkening along the central meridian, while the polar cap was

represented by a rectangle.

The calculations showed the following: (1) for the same values of σ , the ratio between the distorted contrast and the true one K_m/K_0 does not depend on K_0 ; (2) the turbulent vibration of the image, in addition to the blurring of the contrast, increases the dimensions of the cap, while the value of $\Delta r/\Delta r_0$ depends both on σ and on K_0 (Fig. 7). For the boundary of the polar cap, we took a point at which the measured contrast was equal to 5% in determining its distorted dimensions.

Since the value of β is proportional to K , the values of β given in Table 4 should be considered as the lower limit. As can be seen from Figure 7, the measured contrast and, consequently β , is 0.67 of the actual values even at $\sigma = 0.15R \odot$.

REFERENCES

1. Antoniadi: La planète Mars (The Planet Mars). Paris, 1930.
2. Miyamoto, S.: Contribs. Inst. Astrophys. and Kwasan Observ. Univ. Kyoto, pp. 124-125, 1963.
3. Bronshten, V.A.: Rezul'taty nablyudeniy Marsa vo vremya velikogo protivostoyaniya 1956 g. v SSSR (Results of Mars Observations During the Great Opposition of 1956 in the U.S.S.R.). Moscow, Akad. Nauk S.S.S.R., 1959.
4. Geneslay, E.: Astronomie, p. 73, 1959.
5. Lebedinskiy, A.I. and G.I. Salova: Astron. Zhur., Vol. 39, p. 2, 1962.
6. Atmosfery Zemli i planet (The Atmospheres of the Earth and Planets), Collection ed. by D.P. Kayper. Moscow, Foreign Literature Publishing House, 1951.
7. Moroz, V.I.: Fizika planet (Physics of the Planets). Moscow, "Nauka", 1967.
8. Dollfus, A.: An. d'Astrophys., Suppl. p. 4, 1957.
9. Barabashov, N.P. and I.K. Koval': Fotograficheskaya fotometriya Marsa so svetofil'trami v 1956 g. (Photographic Photometry of Mars with Light Filters in 1956). Khar'kov State University Press, 1959.
10. Wright, W.H.: Lick Observ. Bull., p. 366, 1925.
11. Barabashov, N.P. and I.K. Koval': Astron. Zhur., Vol. 36, p. 3, 1958.
12. Koval', I.K.: Astron. Zhur., Vol. 34, p. 3, 1957.
13. Didychenko, Ye.I., I.K. Koval' and A.V. Morozhenko: Izvest. Glavnoy Astron. Observ. Akad. Nauk Ukr. S.S.R., Vol. 5, p. 1, 1963.
14. Sharonov, V.V.: Tsirkulyar GAO v Pulkovo (Circular of the Main Astronomical Observatory in Pulkovo). p. 32, 1941.
15. Kaplan, L.D., D. Munch and G. Spinard H.: Ap. J., Vol. 139, p. 1, 1964.
16. Bugayenko, L.A., O.I. Bugayenko, I.K. Koval' and A.V. Morozhenko: In the Book: Fizika Luny i planet (Physics of the Moon and

- Planets). Kiev, "Naukova dumka", 1964.
17. Bugayenko, L.A., O.K. Bugayenko, I.K. Koval' and A.V. Morozhenko: In the Book: Fizika Luny i planet (Physics of the Moon and Planets). Kiev, "Naukova dumka", 1966.

THE EFFECT OF ATMOSPHERIC VIBRATION ON THE BRIGHTNESS DISTRIBUTION OVER THE DISK OF A PLANET

I.K. Koval', A.A. Rubashevskiy and E.G. Yanovitskiy

ABSTRACT: The problem of making corrections for the distortions in the brightness distribution observed along the disk of the planet because of atmospheric vibration is discussed. The effect of the width of the slit used in determining the vibrational disk on the atmospheric vibration (instrumental function) is estimated for the case when the latter is a Gaussian function. It is shown that a rather narrow slit does not effect the instrumental function. It is discussed whether or not the distortions involved are stationary. Detailed tables are given for the brightness distribution observed when the true distribution is known.

In order to obtain reliable values for the physical parameters of the atmosphere and the surface of a planet from the observed brightness distribution over its disk, it is necessary, first of all, to eliminate the effect of the Earth's atmosphere.

The principal factor causing a distortion of the true brightness distribution over the disk of the planet is the atmospheric vibration, which brings about a situation where (1) the observed brightness distribution seems to be "smeared" compared to the real one because of the energy "transfer" beyond the limits of the disk of the planet, so that the brightness of the planet directly behind the limb of the ephemeris disk is not equal to zero, or (2) if the intensity of the light reflected by the planet decreases from the center to the limb, then the atmospheric vibration leads to a decrease in the observed intensity in the central part of the disk. If there is an increase in brightness around the limb, then an increase in brightness will be observed in the central regions of the disk. Generally speaking, this distortion should be considered in carrying out observations by the methods of absolute photometry.

Until very recently, parallel investigations which might correct the observed brightness distribution for atmospheric vibration to some extent had not been carried out for observations of planets. The first such study was carried out at the Main Astronomical Observatory of the Academy of Sciences of the Ukrainian S.S.R. during the Mars observations in 1965 [1]. Using these observations, I.K. Koval' [2] attempted to make a rough correction of the bright-

ness distribution observed over the disk of Mars.

The principal equations used to determine the true brightness distribution over the disk of a planet according to the observed distribution are presented in this study. The effect of the width of the slit used, in obtaining a photometric section of the turbulent disk of a star, on the function of the atmospheric distortion (instrumental function), if the latter represents a Gaussian curve, is evaluated; a review is given of the methods used for an accurate solution to the principal equation, and detailed tables are given for the brightness distribution observed when the real distribution is given

PRINCIPAL EQUATIONS

Let the true brightness distribution over the disk of a planet be determined by the function $F(r)$, where r is the radius vector of the point on the disk of the planet which has coordinates of x, y . The apparent brightness distribution $f(r)$ is then determined by the following relationship [1]:

$$f(r) = \int_{-\infty}^{+\infty} \int_{-\infty}^{+\infty} F(r') K(r-r') dx' dy', \quad (1)$$

where

$$r' = \sqrt{x'^2 + y'^2}. \quad (2)$$

Equation (1) is an integral Fredholm equation of the first kind. The kernel of this equation $K(r)$ is the instrumental function. It includes both the atmospheric distortion and the distortions introduced by the instrument.

In the one-dimensional case, we obviously have the following, instead of (1):

$$f(x) = \int_{-\infty}^{+\infty} F(y) K(x-y) dy. \quad (3)$$

This equation is usually used in this form in correcting the observed spectral line of the Sun for the instrumental contour [3]. In such a case, the contour of an infinitely narrow spectral line, i.e., the instrumental contour, should be taken as $K(x)$. However, in observations of planets, the appearance of the function $K(r)$ is determined primarily by the atmospheric vibration [1]. Therefore,

we must establish the form of the function $K(r)$ for a further investigation of (1).

INSTRUMENTAL FUNCTION AND ACCURACY IN FINDING IT FROM THE EXPERIMENT

The distorting effect of the atmosphere is due primarily to deflections of the beam of light, which are of a random nature. Therefore, it is natural to assume that the instrumental function has (in the one-dimensional case) the following form:

$$K(x) = e^{-\frac{x^2}{2\sigma^2}}. \quad (4)$$

Actually, as Meinel noted [4], the profile of the disk for the oscillation of a star when the transmissivity of the Earth's atmosphere is good is approximated rather well by a Gaussian curve. At the Main Astronomical Observatory of the Academy of Sciences of the Ukrainian S.S.R., I.G. Kolchinskiy [5] found from many years of investigations that the distribution of the vibration amplitudes of a star is Gaussian, while it was shown in [6] that, if the turbulence in the atmosphere is considered to be uniform, the amplitudes of vibration of a point source beyond the boundaries of the atmosphere are distributed according to (4).

Let us now turn to the method which was used at the Main Astronomical Observatory of the Academy of Sciences of the Ukrainian S.S.R. [1] to find the instrumental function. Photoelectric scanning of the star image with a slit whose height greatly exceeded the effective diameter of the turbulent disk of the star was carried out to determine this function. Let us assume that the true brightness distribution over the turbulent disk obeys the Gauss law. We mean the following. Let the image of the star be scanned by a round diaphragm¹ of radius d (so small that $d \ll \sqrt{2}\sigma$). Let it be found as a result that the energy measured changes according to the following law along the radius r of the image²:

$$E(r) = I_0 e^{-a^2 r^2}, \quad (5)$$

¹ The specific shape of the diaphragm is not of significance in this case. It is important only that the diaphragm be so small that the brightness of the turbulent disk within its limits can be considered as constant in any of its parts.

² It is assumed that the energy distribution over the disk does not depend on the azimuth.

where I_0 is the amount of energy over the area πd^2 when the center of the diaphragm coincides with the center of the image;

$$a^2 = \frac{1}{2\sigma^2}. \quad (6)$$

The question arises: will the brightness distribution over the turbulent disk of the image of the same star change according to the law in (5) with the same parameter a , if the brightness distribution is measured by means of a slit of infinite length, i.e., to what degree does the brightness distribution depend on the shape of the diaphragm? We will not consider the phenomenon of diffraction on the slit.

The amount of energy incident on a unit area at a point with coordinates (z, y) (Fig. 1) is

$$dE(z, y) = \frac{I_0}{\pi d^2} e^{-a^2 r^2} dx dy, \quad (7)$$

The total amount of energy recorded from the entire slit of width $2d$ is then written thus:

$$\begin{aligned} E(z) &= \frac{2I_0}{\pi d^2} \int_0^\infty dy \int_{z-d}^{z+d} e^{-a^2(x^2+y^2)} dx = \frac{I_0}{\sqrt{\pi} a d^2} \int_{z-d}^{z+d} e^{-a^2 x^2} dx = \\ &= \frac{2I_0}{\sqrt{\pi} a d^2} e^{-a^2 z^2} \int_0^d e^{-a^2 x^2} \operatorname{ch}(2a^2 x z) dx, \end{aligned} \quad (8)$$

Thus, we ultimately find that

$$E(z) = \frac{2I_0 e^{-a^2 z^2}}{\sqrt{\pi} a^2 d^2} \int_0^{ad} e^{-x^2} \operatorname{ch}(2axz) dx. \quad (9)$$

We can select the halfwidth of the slit as so small that the dimensionless value ad satisfies the following condition:

$$ad \ll 1. \quad (10)$$

Let us represent the integral in (9) in the following way:

$$\int_0^{ad} e^{-x^2} \operatorname{ch}(2axz) dx = ad [1 + \alpha(z)]. \quad (11)$$

However,

$$\int_0^{ad} e^{-x^2} \operatorname{ch}(2axz) dx \leq \int_0^{ad} \operatorname{ch}(2axz) dx = \frac{\operatorname{sh}(2a^2dz)}{2az},$$

from which we find that

$$\alpha(z) \leq \frac{\operatorname{sh}(2a^2dz)}{2a^2dz} - 1. \quad (11a)$$

Consequently, we ultimately find from (9) and (11) that

$$E(z) = \frac{2I_0}{\sqrt{\pi}ad} e^{-a^2z^2} [1 + \alpha(z)]. \quad (12)$$

Thus, if the brightness distribution over the turbulent disk of the star is measured with the aid of a rather narrow slit [narrow in the sense of fulfilling the condition in (10)], then, as follows from (12), the distribution found is almost identical to the true one. In other words, if we assume that the observed brightness distribution is given by the formula

$$E(z) = \frac{2I_0}{\sqrt{\pi}ad} e^{-a^2z^2},$$

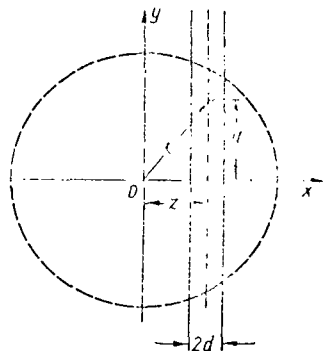


Fig. 1.

then, in this case, the relative error determined by (11a) is allowed.

The profiles of the image of the star which are given in [1], are approximated well by a Gaussian curve. Some discrepancy is sometimes observed in the limbs. However, this can be eliminated if the instrumental function is represented in the form of the sum of two Gaussian curves, i.e.,

$$K(x) = I_1 e^{-\frac{x^2}{2\sigma_1^2}} + I_2 e^{-\frac{x^2}{2\sigma_2^2}}. \quad (13)$$

This representation does not introduce any basic additional difficulties in solving (3).

In all appearances, the brightness distribution is not iso-

tropic. It is natural to assume that the flickering disk has a shape close to the form of an ellipse. Then, instead of (4), we have the following:

$$K(x, y) = e^{-\left(\frac{x^2}{2\sigma_1^2} + \frac{y^2}{2\sigma_2^2}\right)} \quad (14)$$

In this case, the solution to (1) is made more complex. Therefore, it is important, generally speaking, to find out when we can disregard the anisotropy in the brightness distribution over the vibrational disk. This disregard is most probably possible for rather short zenith distances. However, for a reliable answer to the question raised, there must be special observations.

Finally, there is one more important question. Since there is some time interval between the moments of observing the planet and the contour of the star, can the cited time interval change the brightness distribution over the wavering disk of the star substantially?

Let us turn to the study of I.G. Kolchinskiy [5] on this topic; he carried out an investigation of the wavering of images of stars at the Main Astronomical Observatory of the Academy of Sciences of the Ukrainian S.S.R. The so-called trails of star images were obtained for this purpose on photoplates, with fixed clockwise. The average length of a trail was found to be equal to 14 cm, which corresponds to a time interval of about 6 minutes for a star with inclination of $\delta = 0^\circ$. The correlation analysis of the observation results carried out by the author showed the approximate stationarity of the random process of the vibration of the stellar images in the cited time interval.

Since the program of Mars observations [1] was structured so that, immediately after Mars, the image of the star was followed with the same filter, then the time interval between the scans of Mars and the star did not exceed 10 minutes. Since this time interval is comparable to the cited "delay" time of the stars [5], then we can apparently assume that, in the time interval between the observations of Mars and the star, the brightness distribution over the disk of the latter did not change substantially.

Let us mention one more circumstance. The star for which the study of its vibration disk is carried out for the purpose of determining the instrumental function should be selected at azimuths and zenith distances close to the planet, as was done in the Mars observations of [1], or, as was shown theoretically in [8] and confirmed experimentally in [5], the root-mean-square amplitudes of the vibration of the star images in the telescope increase in proportion with the value \sqrt{M} , where M is the air mass.

PRECISE METHODS OF SOLVING THE PRINCIPAL EQUATION

If we assume that the instrumental function has the form of (14), then the principal equation in (1) can be written in the following way:

$$f(x, y) = \frac{1}{2\pi\sigma_1\sigma_2} \int_{-\infty}^{+\infty} \int_{-\infty}^{+\infty} F(x', y') e^{-\left[\frac{(x-x')^2}{2\sigma_1^2} + \frac{(y-y')^2}{2\sigma_2^2}\right]} dx' dy'. \quad (15)$$

The constant factor in front of the integral is found from the condition that the total energy of emission going from the planet through the Earth's atmosphere does not change, i.e., there is no absorption in the Earth's atmosphere for the wavelengths of light under investigation. Obviously, this condition has the following form:

$$\int_{-\infty}^{+\infty} \int_{-\infty}^{+\infty} f(x, y) dx dy = \int_{-\infty}^{+\infty} \int_{-\infty}^{+\infty} F(x, y) dx dy. \quad (16)$$

In the general case described by (15), to determine $F(x, y)$ we must find values of the function $f(x, y)$ at many points of the observed image, which raises fundamental difficulties in practice. Therefore, let us examine the following, simpler cases.

1. If we disregard the brightness gradient in the direction y , then, instead of (15), we find the following:

$$f(x) = \frac{1}{\sqrt{2\pi}\sigma} \int_{-\infty}^{+\infty} F(y) e^{-\frac{(x-y)^2}{2\sigma^2}} dy. \quad (17)$$

Obviously, this approximation is justified for a rather low σ and near the zenith. We will give some estimates of the accuracy of the approximation under examination below.

2. If $\sigma_2 \rightarrow 0$, then we find from (15) that

$$f(x, y) = \frac{1}{\sqrt{2\pi}\sigma} \int_{-\infty}^{+\infty} F(x', y) e^{-\frac{(x-x')^2}{2\sigma^2}} dx', \quad (18)$$

i.e., the dependence on the second coordinate y is purely parametric. It is obvious that (17) is a particular case of (18).

3. Let the brightness distribution over the disk of the planet have central symmetry and let $\sigma_1 = \sigma_2 = \sigma$. Let us turn to the

spherical system of coordinates r, ϕ . Then, if the coordinates of the points M and M' are x, y and x', y' respectively (Fig. 2), whereas the positions of these points are defined, in addition, by the radius vectors r and r' , respectively, the angle between which is equal to ϕ , then the projections of the segment MM' on the axes x and y are $AA' = x' - x$ and $BB' = y - y'$. Consequently,

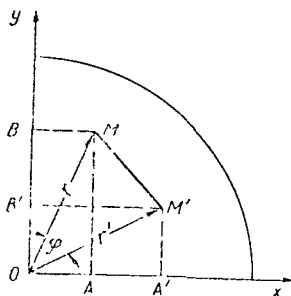


Fig. 2.

$$(x-x')^2 + (y-y')^2 = r^2 + r'^2 - 2rr' \cos \phi. \quad (19)$$

In this case, instead of (15), we obtain the following:

$$f(r) = \frac{e^{-\frac{r^2}{2\sigma^2}}}{2\pi\sigma^2} \int_0^{2\pi} e^{\frac{rr'}{\sigma^2} \cos \varphi} d\varphi \int_0^\infty F(r') e^{-\frac{r'^2}{2\sigma^2}} r' dr'. \quad (20)$$

The Bessel function of the purely imaginary argument of zero order is determined by the formula

$$I_0(x) = \frac{1}{\pi} \int_0^\pi e^{x \cos \varphi} d\varphi. \quad (21)$$

Consequently, instead of (20), we ultimately find

$$f(x) = \frac{e^{-\frac{x^2}{2\sigma^2}}}{\sigma^2} \int_0^\infty F(y) e^{-\frac{y^2}{2\sigma^2}} I_0\left(\frac{xy}{\sigma^2}\right) y dy. \quad (22)$$

The principal equation (15) under investigation [as well as its particular forms in (17), (18) and (22)] is an integral Fredholm equation of the first kind. As is well known, the problems described by an equation of this type belong to the class of so-called incorrectly formulated problems. This means that an indirect solution to this equation, for example by the method of numerical inversion of a Fourier transformation or by converting to a system of linear algebraic equations, does not pass here; small errors in the functions found from the experiment will yield arbitrarily large errors in the result.

A general formulation of the problem of regularization of incorrectly formulated problems, specific regularization methods, and an investigation of the stability of the result of inversion are given in the works of A.N. Tikhonov [9-12].

We will not discuss the application of Tikhonov's method to a solution for the problem under investigation. We will be concerned only with methods used for a precise solution to the principal equations, i.e., solutions to the problem on the assumption that the functions found from the experiment are known absolutely precisely. As was already mentioned, these solutions are not correct and, consequently, they cannot be used in practice. However, an analysis of the solution written out in explicit form can aid in a number of cases in finding the characteristics of the behavior of the solution, which can then be considered in regularization of the incorrect problem under examination.

It is obvious that the solution to (17) can be obtained by inversion of the Fourier transformation. The application of the method of Fourier transformation to a solution for (17) was discussed in [7]. We will therefore not discuss this method any further.

Let us examine the method of orthogonal series for a solution to (17). Since the kernel of this equation is Hermitian, it is completely natural to look for the function $F(x)$ in the form of a series by Hermite polynomials.

Let us assume that

$$F(y) = \sum_{n=0}^{\infty} c_n H_n(y), \quad (23)$$

where $H_n(y)$ is a Hermite polynomial of order n , while c_n are coefficients to be determined. Then, substituting (23) into (17), we find the following for $0 \leq \sigma^2 < 1/2$ [13, p. 852]:

$$f(x) = \sum_{n=0}^{\infty} c_n (1-2\sigma^2)^{n/2} H_n \left[\frac{x}{(1-2\sigma^2)^{1/2}} \right]. \quad (24)$$

Considering the property of orthogonality of the Hermite polynomials, we find that

$$c_n = \frac{\gamma_n}{2^n n! (1-\sigma^2)^{n/2}}, \quad (25)$$

where

$$\gamma_n = [\pi(1-2\sigma^2)]^{-1/2} \int_{-\infty}^{+\infty} f(x) e^{-\frac{x^2}{1-2\sigma^2}} H_n \left[\frac{x}{(1-2\sigma^2)^{1/2}} \right] dx. \quad (26)$$

If the function $F(x)$ is of even parity, then

$$\gamma_{2n+1} = 0 \quad (n = 0, 1, 2, \dots)$$

and

$$H_{2n}(x) = (-1)^n 2^n n! L_n^{-1/2}(x^2),$$

where $L_n^{-1/2}(x)$ is a Laguerre polynomial.

Substituting (27) into (23) and (26), we find the following after conversions:

$$\dot{F}(x) = \sum_{n=0}^{\infty} \bar{c}_n L_n^{-1/2}(x^2), \quad (28)$$

where

$$\bar{c}_n = \frac{\gamma_n n! 2^n}{(2n-1)!! (1-2\sigma^2)^n}, \quad (29)$$

while

$$\gamma_n = 2[\pi(1-2\sigma^2)]^{1/2} \int_0^{\infty} f(x) e^{-\frac{x^2}{1-2\sigma^2}} L_n^{-1/2}\left(\frac{x^2}{1-2\sigma^2}\right) dx. \quad (30)$$

Using the formulas below

$$\frac{dH_n(x)}{dx} = 2nH_{n-1}(x), \quad (31)$$

$$H_{n+1}(x) = 2xH_n(x) - 2nH_{n-1}(x) \quad (32)$$

and expanding $F(x)$ into a series by σ^2 , we find

$$F(x) = f(x) - \frac{\sigma^2}{2} \cdot \frac{d^2 f(x)}{dx^2} + \frac{\sigma^4}{2^2 \cdot 2!} \cdot \frac{d^4 f(x)}{dx^4} - \frac{\sigma^6}{2^3 \cdot 3!} \cdot \frac{d^6 f(x)}{dx^6} + \dots \quad (33)$$

It can be seen from (17) and (33) that, if the function $f(x)$ is rather smooth, while σ is rather low, then the solution to the problem of reproduction does not present any particular difficulty. However, in the case of a planet, the smoothness $F(x)$ is lost near its limb and, consequently, even for low σ , a reproduction near the edge of the planet's disk presents fundamental difficulties. It is appropriate to mention in this regard that the

correction of the spectral line observed for the instrumental contour given in [3] did not present any fundamental difficulties and was carried out by the method of successive approximations, since the distorted contour does not represent a sufficiently smooth function.

Using (23), which gives a precise solution to the idealized problem, let us estimate the error $\Delta F(x)$ in solving (17), if the function $f(x)$ is given with a *constant* absolute error Δf , while the value of σ is determined with absolute error of $\Delta\sigma$. We find from (23) and (25) that

$$\Delta F(x) = \sum_{n=0}^{\infty} \Delta c_n I_n(x), \quad (34)$$

$$\Delta c_n = \frac{\Delta \gamma_n}{2^n n! (1-2\sigma^2)^{n/2}} + \frac{2\gamma_n (n+1) \sigma \Delta\sigma}{2^n n! (1-2\sigma^2)^{\frac{n+1}{2}}}. \quad (35)$$

We find the following from (26), considering (31) and (32):

$$\Delta \gamma_0 = \Delta f; \quad (36)$$

$$\Delta \gamma_n = - \frac{\sigma \Delta\sigma}{(1-2\sigma^2)^{n/2}} [\gamma_{n+2} + 2(n+1)\gamma_n] \quad (n \geq 1). \quad (37)$$

Substituting (36) and (37) into (35) and considering (23) and (24), we ultimately find that

$$\Delta F(x) = \Delta f - \sigma \Delta\sigma \frac{d^2 F(x)}{dx^2}. \quad (38)$$

It can be clearly seen from this formula that, even for an arbitrarily small error in determining σ , we can obtain an arbitrarily large absolute error in determining the function $F(x)$, if the latter is not sufficiently smooth.

We can also find a precise solution to (22) in a similar way. Let us assume that

$$F(y) = \sum_{n=0}^{\infty} l_n L_n(y^2), \quad (39)$$

where $L_n(x)$ is a Laguerre polynomial of order n ; the l_n are coefficients to be determined.

Substituting (39) into (22), we find that

$$f(x) = \frac{e^{-\frac{x^2}{2\sigma^2}}}{\sigma^2} \sum_{n=0}^{\infty} l_n \int_0^{\infty} e^{-\frac{y^2}{2\sigma^2}} L_n(y^2) I_n\left(\frac{xy}{\sigma^2}\right) y dy, \quad (40)$$

but for $0 \leq \sigma^2 < 1/2$ [13, p. 861],

$$\int_0^{\infty} e^{-\frac{y^2}{2\sigma^2}} L_n(y^2) I_0\left(\frac{xy}{\sigma^2}\right) y dy = \sigma^2 (1-2\sigma^2)^n e^{-\frac{x^2}{2\sigma^2}} L_n\left(\frac{x^2}{1-2\sigma^2}\right),$$

i.e.,

$$f(x) = \sum_{n=0}^{\infty} l_n (1-2\sigma^2)^n L_n\left(\frac{x^2}{1-2\sigma^2}\right). \quad (41)$$

Considering the property of orthogonality of the Laguerre polynomials, we find that

$$l_n = \frac{2}{(1-2\sigma^2)^{n+1}} \int_0^{\infty} f(x) L_n\left(\frac{x^2}{1-2\sigma^2}\right) e^{-\frac{x^2}{1-2\sigma^2}} x dx. \quad (42)$$

We can also find the solution to the more general equation in (15) in a similar way.

SOME RESULTS OF THE CALCULATIONS

In order to have a quantitative representation of the degree to which the atmosphere affects the brightness distribution over the disk of the planet, we will assume that

$$F(x) = \begin{cases} (1-x^2)^v, & |x| \leq 1, \\ 0, & |x| > 1. \end{cases} \quad (43)$$

This formula was obtained empirically by N.N. Sytinskaya for rough surfaces. The parameter v is connected with the smoothness factor q introduced by N.N. Sytinskaya by the ratio $v = q/2$.

For the law of (43), instead of (17), we find that

$$f(x) = \frac{1}{\sqrt{2\pi}\sigma} \int_{-1}^{+1} (1-y^2)^v e^{-\frac{(x-y)^2}{2\sigma^2}} dy, \quad (44)$$

and, instead of (22),

$$f_c(x) = e^{-\frac{x^2}{2\sigma^2}} \int_0^1 (1-y^2)^v e^{-\frac{xy^2}{2\sigma^2}} I_0\left(\frac{xy^2}{\sigma^2}\right) y dy. \quad (45)$$

The tables for the functions $f(x)$ and $f_c(x)$ were calculated according to (44) and (45) on the digital computer "Minsk-22" for $v = 0.0-1.0$ (every 0.10) and $\sigma = 0.05-0.40$ (every 0.05) and are given in the Appendix.

The calculations according to (44) did not cause any difficulties. As for (45), it was found to be more suitable to transform it somewhat for $\sigma \geq 0.20$. Using the expression for the generating function of the Laguerre polynomials [13, p. 1052], i.e.,

$$I_0(2\sqrt{xz})e^{-z} = \sum_{n=0}^{\infty} L_n(x) \frac{(-1)^n z^n}{n!} \quad (46)$$

formula (45) is converted into the following:

$$f_c(x) = \frac{e^{-\frac{x^2}{2\sigma^2}}}{2\sigma^2} \Gamma(v+1) \sum_{n=0}^{\infty} \frac{(-1)^n L_n\left(\frac{x^2}{2\sigma^2}\right)}{2^n \sigma^{2n} \Gamma(v+n+2)}. \quad (47)$$

This expression was also used for $f_c(x)$ for the calculations with $\sigma \geq 0.20$.

The following formulas are useful for controlling the accuracy of the producible calculations. For $v = 0$, we have the expression written below from (44):

$$f(x) = \frac{1}{2} \left[\Phi\left(\frac{1-x}{\sqrt{2}\sigma}\right) + \Phi\left(\frac{1+x}{\sqrt{2}\sigma}\right) \right], \quad (48)$$

where $\Phi(x)$ is the probability integral, while we find from (45) [13, p. 731] that

$$f_c(1) = \frac{1}{2} [1 - e^{-1/2\sigma^2} I_0(1/\sigma^2)]. \quad (49)$$

Let us turn to some conclusions which can be drawn from an analysis of the numerical results given in the tables of the Appendix. First of all, let us evaluate the difference in the results of calculations according to (44) and (45) for identical

ν and σ . For this, the table contains the value

$$\Delta f = \left| 1 - \frac{f(0.95)f_c(0)}{f(0)f_c(0.95)} \right| 100\%,$$

calculated for $\nu = 0.0$ and 0.5 and different values of σ .

σ	ν	Δf
0.05	0.0	0.71
	0.5	1.1
0.10	0.0	2.7
	0.5	3.9
0.15	0.0	5.0
	0.5	6.1
0.20	0.0	7.3
	0.5	8.3
0.25	0.0	9.6
	0.5	9.8
0.30	0.0	12.0
	0.5	11.0
0.35	0.0	13.6
	0.5	11.5
0.40	0.0	14.2
	0.5	11.0

It follows from the table that the use of the simpler equation (44) instead of (45) for $\sigma \leq 0.25$ yields an error which does not exceed 10% for $x \leq 0.95$. However, we must keep in mind that, for $x \leq 1$ (i.e., beyond the edge of the disk), this error increases somewhat. For example, the value $\Delta f = 19\%$ for $\sigma = 0.30$ at $x = 1.25$ with $\nu = 0$, and $\Delta f = 18\%$ for $\nu = 0.5$.

Let us also mention that, in the case of the Lambert law ($\nu = 0.5$) for $\sigma = 0.20$, the decrease in brightness of the center of the disk of the planet due to the atmospheric vibration is roughly 4%. However, even at $\sigma = 0.40$ this decrease is equal to 20%. Thus, we can disregard the effect of vibrations on the absolute value of the brightness at the center of the disk only for rather low σ (i.e., for $\sigma < 0.20$), when we are measuring the brightness according to the method of absolute photometry. The estimates given for the errors refer only to the case of the Lambert law, and for $\nu = 0$ they will be much less.

Let us discuss the use of the tables given in the Appendix. If we assume that the planet reflects light according to (43), then we can make a rough estimate of the value σ from a comparison between the brightness distribution obtained for observations

and the results of calculations for a given v , i.e., we can basically solve the inverse problem. I.K. Koval' attempted to find v for Mars in this way in [2]. However, the error in the value of v found was not evaluated in that study. Therefore, the result is not reliable.

In continuing our study, it is suggested that the value of v be found in the following way. The value of v is first roughly estimated from a comparison between the observed values for the brightness distribution over the Mars disk during an opposition [1] and the results of calculations according to (45). The values of the errors Δv and $\Delta \sigma$ in the rough values of v and σ are then found according to the least-square method by (45); and, finally, the probable error in finding the latter is evaluated. This method of solving the principal problem is correct if the assumption that the Mars surface reflects light according to the law in (43) is valid.

REFERENCES

1. Bugayenko, L.A., O.I. Buyayenko, I.K. Koval' and A.V. Morozhenko: In the Book: Fizika Luny i planet (Physics of the Moon and Planets). Kiev, "Naukova dumka", 1966.
2. Koval', I.K.: Astron. Tsink., p. 319, 1965.
3. Gurtovenko, E.A.: Astron. Zhur., Vol. 43, No. 3, p. 659, 1966.
4. Meinel, A.B.: In the Book: Teleskopy (Telescopes). Moscow, Foreign Literature Publishing House, pp. 196-206, 1963.
5. Kolchinskiy, I.G.: Astron. Zhur., Vol. 34, No. 4, p. 638, 1957.
6. Duntley, S.Q., W.H. Culver, F. Ricuey and R.W. Priesendorfer: J. Opt. Soc. Amer., Vol. 53, No. 3, p. 351, 1963.
7. Barabashov, N.P., V.I. Garazha and V.N. Dudinov: Astron. Zhur., No. 1, p. 144, 1966.
8. Krasil'nikov, V.A.: Doklady Akad. Nauk S.S.S.R., Vol. 65, No. 3, p. 241, 1949.
9. Tikhonov, A.N.: Doklady Akad. Nauk S.S.S.R., Vol. 39, No. 5, p. 198, 1943.
10. Tikhonov, A.N.: Doklady Akad. Nauk S.S.S.R., Vol. 151, No. 3, p. 501, 1963.
11. Tikhonov, A.N.: Doklady Akad. Nauk S.S.S.R., Vol. 153, No. 1, p. 49, 1963.
12. Tikhonov, A.N. and V.B. Glasko: Zhurn. Vychisl. Matem. i Matem. Fiz., Vol. 4, No. 2, p. 564, 1964.
13. Gradshteyn, I.S. and I.M. Ryzhik: Tablitsy integralov, summ, ryadov i proizvedeniy (Tables of Integrals, Sums, Series and Products). Moscow, "Fizmatgiz", 1962.

APPENDIX

ν	0.0		0.1		0.2		0.3		0.4	
	f	f_c	f	f_c	f	f_c	f	f_c	f	f_c
$\sigma=0.05$										
0.00	1.000	1.000	1.000	1.000	1.000	1.000	0.999	0.999	0.999	0.998
0.05	1.000	1.000	1.000	1.000	1.000	1.000	0.999	0.998	0.999	0.998
0.10	1.000	1.000	0.999	0.999	0.998	0.998	0.996	0.995	0.995	0.994
0.15	1.000	1.000	0.997	0.997	0.995	0.995	0.992	0.991	0.990	0.989
0.20	1.000	1.000	0.996	0.996	0.991	0.991	0.987	0.986	0.983	0.982
0.25	1.000	1.000	0.993	0.993	0.987	0.987	0.980	0.979	0.973	0.972
0.30	1.000	1.000	0.990	0.990	0.981	0.981	0.971	0.970	0.962	0.961
0.35	1.000	1.000	0.987	0.987	0.974	0.974	0.961	0.960	0.948	0.947
0.40	1.000	1.000	0.982	0.982	0.965	0.965	0.948	0.947	0.931	0.930
0.45	1.000	1.000	0.977	0.977	0.955	0.955	0.933	0.932	0.912	0.911
0.50	1.000	1.000	0.971	0.971	0.943	0.943	0.916	0.915	0.890	0.888
0.55	1.000	1.000	0.964	0.964	0.929	0.929	0.896	0.895	0.864	0.863
0.60	1.000	1.000	0.956	0.955	0.913	0.912	0.873	0.872	0.834	0.833
0.65	1.000	1.000	0.946	0.945	0.894	0.893	0.846	0.845	0.800	0.799
0.70	1.000	1.000	0.934	0.933	0.872	0.871	0.815	0.813	0.761	0.759
0.75	1.000	1.000	0.919	0.918	0.844	0.844	0.776	0.775	0.714	0.712
0.80	1.000	1.000	0.900	0.900	0.810	0.809	0.730	0.729	0.658	0.657
0.85	0.999	0.998	0.873	0.872	0.764	0.763	0.670	0.668	0.588	0.586
0.90	0.977	0.976	0.848	0.846	0.687	0.685	0.580	0.577	0.491	0.488
0.95	0.841	0.835	0.666	0.660	0.530	0.526	0.426	0.422	0.344	0.340
1.00	0.500	0.490	0.374	0.365	0.282	0.276	0.215	0.210	0.165	0.161
1.05	0.159	0.153	0.113	0.107	0.082	0.078	0.059	0.056	0.043	0.042
1.10	0.023	0.022	0.015	0.014	0.009	0.009	0.007	0.007	0.004	0.004
1.15	0.001	0.001	0.000	0.000	0.000	0.000	0.000	0.000	0.000	0.000
1.20	0.000	0.000	0.000							
$\sigma=0.10$										
0.00	1.000	1.000	0.999	0.998	0.998	0.996	0.997	0.994	0.996	0.992
0.05	1.000	1.000	0.999	0.998	0.997	0.995	0.996	0.993	0.995	0.991
0.10	1.000	1.000	0.998	0.997	0.996	0.994	0.994	0.991	0.992	0.988
0.15	1.000	1.000	0.997	0.996	0.993	0.991	0.990	0.987	0.987	0.982
0.20	1.000	1.000	0.995	0.994	0.990	0.988	0.985	0.981	0.979	0.975
0.25	1.000	1.000	0.992	0.991	0.985	0.983	0.977	0.974	0.970	0.966
0.30	1.000	1.000	0.989	0.988	0.979	0.976	0.968	0.965	0.958	0.954
0.35	1.000	1.000	0.986	0.984	0.971	0.969	0.958	0.954	0.944	0.939
0.40	1.000	1.000	0.981	0.980	0.963	0.960	0.945	0.941	0.927	0.922
0.45	1.000	1.000	0.976	0.974	0.952	0.949	0.929	0.926	0.907	0.902
0.50	1.000	1.000	0.969	0.968	0.940	0.937	0.912	0.908	0.884	0.879
0.55	1.000	1.000	0.962	0.960	0.926	0.923	0.891	0.887	0.858	0.853
0.60	1.000	1.000	0.953	0.951	0.909	0.906	0.867	0.862	0.827	0.822
0.65	1.000	1.000	0.942	0.940	0.888	0.885	0.838	0.833	0.791	0.785
0.70	0.999	0.998	0.928	0.925	0.863	0.859	0.803	0.798	0.749	0.742
0.75	0.994	0.993	0.907	0.904	0.829	0.824	0.760	0.753	0.697	0.690
0.80	0.977	0.974	0.872	0.867	0.782	0.774	0.702	0.694	0.632	0.623
0.85	0.933	0.926	0.812	0.803	0.710	0.700	0.623	0.613	0.549	0.539
0.90	0.841	0.828	0.712	0.698	0.606	0.593	0.519	0.506	0.447	0.435
0.95	0.691	0.673	0.568	0.552	0.471	0.456	0.394	0.380	0.331	0.318

APPENDIX (cont'd)

		0.6		0.7		0.8		0.9		1.0	
f	f_c	f	f_c	f	f_c	f	f_c	f	f_c	f	f_c
0.999	0.998	0.999	0.997	0.998	0.996	0.998	0.996	0.998	0.996	0.998	0.995
0.998	0.997	0.998	0.996	0.997	0.995	0.997	0.995	0.996	0.994	0.996	0.994
0.991	0.993	0.993	0.991	0.991	0.990	0.990	0.988	0.989	0.987	0.988	0.985
0.987	0.986	0.985	0.983	0.982	0.980	0.980	0.978	0.977	0.975	0.975	0.972
0.978	0.977	0.974	0.972	0.970	0.968	0.966	0.964	0.962	0.959	0.958	0.955
0.967	0.966	0.960	0.959	0.954	0.952	0.948	0.946	0.941	0.939	0.935	0.932
0.952	0.952	0.943	0.942	0.934	0.932	0.925	0.923	0.916	0.914	0.908	0.904
0.935	0.934	0.923	0.921	0.911	0.909	0.901	0.897	0.887	0.884	0.875	0.869
0.915	0.914	0.899	0.897	0.883	0.881	0.863	0.856	0.852	0.850	0.842	0.835
0.891	0.890	0.871	0.870	0.851	0.849	0.832	0.830	0.813	0.811	0.795	0.787
0.864	0.863	0.839	0.838	0.815	0.813	0.792	0.789	0.769	0.767	0.743	0.735
0.833	0.832	0.803	0.802	0.775	0.773	0.747	0.745	0.721	0.718	0.695	0.683
0.798	0.796	0.762	0.761	0.729	0.727	0.697	0.695	0.667	0.664	0.637	0.625
0.757	0.755	0.717	0.714	0.678	0.676	0.642	0.639	0.608	0.605	0.575	0.562
0.711	0.709	0.665	0.662	0.621	0.619	0.581	0.578	0.543	0.540	0.508	0.495
0.657	0.655	0.605	0.603	0.557	0.554	0.513	0.510	0.472	0.470	0.435	0.423
0.594	0.592	0.536	0.534	0.484	0.482	0.437	0.435	0.395	0.393	0.358	0.345
0.517	0.514	0.455	0.452	0.400	0.398	0.353	0.350	0.311	0.309	0.275	0.264
0.416	0.413	0.351	0.351	0.301	0.298	0.257	0.254	0.220	0.217	0.188	0.186
0.278	0.275	0.227	0.223	0.186	0.183	0.152	0.150	0.129	0.123	0.104	0.102
0.128	0.125	0.099	0.097	0.077	0.075	0.061	0.059	0.049	0.047	0.039	0.037
0.032	0.031	0.023	0.023	0.017	0.017	0.013	0.013	0.010	0.010	0.008	0.008
0.002	0.002	0.002	0.002	0.001	0.001	0.001	0.001	0.001	0.001	0.001	0.001
0.000	0.000	0.000	0.000	0.000	0.000	0.000	0.000	0.000	0.000	0.000	0.000
0.995	0.990	0.991	0.988	0.993	0.986	0.992	0.984	0.991	0.982	0.990	0.980
0.994	0.989	0.992	0.986	0.994	0.984	0.990	0.982	0.989	0.980	0.987	0.977
0.990	0.985	0.988	0.982	0.986	0.979	0.981	0.976	0.982	0.973	0.980	0.970
0.983	0.978	0.980	0.974	0.977	0.970	0.974	0.966	0.971	0.962	0.968	0.958
0.974	0.969	0.969	0.963	0.965	0.957	0.960	0.952	0.955	0.946	0.950	0.940
0.963	0.957	0.955	0.949	0.948	0.941	0.941	0.933	0.934	0.925	0.928	0.918
0.948	0.942	0.938	0.932	0.928	0.921	0.919	0.911	0.909	0.900	0.900	0.890
0.931	0.925	0.917	0.911	0.905	0.897	0.892	0.884	0.880	0.870	0.868	0.858
0.910	0.904	0.893	0.886	0.877	0.869	0.861	0.852	0.845	0.836	0.830	0.820
0.896	0.880	0.865	0.858	0.845	0.837	0.825	0.817	0.806	0.797	0.788	0.778
0.878	0.852	0.833	0.826	0.808	0.801	0.785	0.776	0.762	0.753	0.740	0.730
0.826	0.820	0.796	0.789	0.767	0.759	0.739	0.731	0.713	0.703	0.688	0.677
0.790	0.783	0.754	0.747	0.721	0.712	0.689	0.680	0.659	0.649	0.630	0.620
0.748	0.741	0.707	0.699	0.668	0.660	0.633	0.624	0.599	0.589	0.568	0.558
0.699	0.691	0.652	0.644	0.610	0.601	0.570	0.561	0.534	0.524	0.500	0.490
0.641	0.633	0.590	0.581	0.543	0.534	0.501	0.491	0.463	0.453	0.428	0.418
0.571	0.561	0.516	0.506	0.468	0.458	0.425	0.415	0.386	0.376	0.352	0.342
0.486	0.475	0.431	0.420	0.383	0.373	0.342	0.332	0.305	0.296	0.274	0.264
0.387	0.375	0.336	0.325	0.293	0.282	0.256	0.246	0.224	0.216	0.197	0.189
0.280	0.268	0.238	0.225	0.203	0.193	0.174	0.165	0.150	0.142	0.129	0.122

APPENDIX (cont'd)

v x	0.0		0.1		0.2		0.3		0.4	
	f	f _c	f	f _c	f	f _c	f	f _c	f	f _c
1.00	0.500	0.180	0.400	0.383	0.323	0.309	0.254	0.251	0.216	0.206
1.05	0.309	0.292	0.211	0.227	0.153	0.179	0.134	0.142	0.112	0.114
1.10	0.159	0.147	0.121	0.112	0.094	0.086	0.073	0.067	0.053	0.053
1.15	0.067	0.061	0.050	0.045	0.038	0.034	0.029	0.026	0.022	0.020
1.20	0.023	0.020	0.017	0.015	0.012	0.011	0.009	0.008	0.007	0.006
1.25	0.006	0.006	0.004	0.003	0.003	0.002	0.002	0.002	0.002	0.001
1.30	0.001	0.001	0.001	0.001	0.000	0.000	0.000	0.000	0.000	0.000
1.35	0.000	0.000	0.000	0.000						
σ = 0.1										
0.00	1.000	1.000	0.998	0.995	0.995	0.990	0.993	0.997	0.991	0.994
0.05	1.000	1.000	0.997	0.994	0.995	0.990	0.992	0.996	0.995	0.990
0.10	1.000	1.000	0.997	0.993	0.993	0.989	0.990	0.983	0.987	0.977
0.15	1.000	1.000	0.995	0.992	0.991	0.986	0.986	0.979	0.984	0.974
0.20	1.000	1.000	0.993	0.990	0.987	0.982	0.980	0.973	0.974	0.964
0.25	1.000	1.000	0.991	0.988	0.982	0.977	0.973	0.965	0.964	0.954
0.30	1.000	1.000	0.988	0.985	0.975	0.970	0.964	0.956	0.952	0.942
0.35	1.000	1.000	0.981	0.981	0.968	0.963	0.952	0.944	0.937	0.926
0.40	1.000	1.000	0.979	0.976	0.958	0.953	0.939	0.930	0.920	0.909
0.45	1.000	1.000	0.973	0.970	0.947	0.941	0.923	0.914	0.899	0.888
0.50	1.000	0.999	0.966	0.962	0.934	0.928	0.904	0.894	0.875	0.863
0.55	0.999	0.998	0.957	0.952	0.918	0.910	0.881	0.870	0.846	0.833
0.60	0.996	0.995	0.945	0.940	0.897	0.889	0.853	0.842	0.813	0.799
0.65	0.990	0.987	0.928	0.921	0.871	0.864	0.820	0.807	0.772	0.757
0.70	0.977	0.972	0.903	0.894	0.837	0.824	0.777	0.762	0.724	0.707
0.75	0.952	0.943	0.866	0.853	0.791	0.775	0.724	0.707	0.666	0.647
0.80	0.909	0.894	0.812	0.795	0.730	0.711	0.658	0.638	0.597	0.576
0.85	0.841	0.821	0.738	0.716	0.652	0.630	0.579	0.557	0.517	0.495
0.90	0.748	0.722	0.644	0.618	0.559	0.534	0.488	0.465	0.429	0.407
0.95	0.631	0.604	0.533	0.506	0.455	0.430	0.391	0.368	0.339	0.317
1.00	0.500	0.470	0.416	0.388	0.349	0.325	0.295	0.274	0.252	0.232
1.05	0.369	0.342	0.302	0.278	0.250	0.229	0.208	0.190	0.175	0.159
1.10	0.252	0.230	0.203	0.184	0.166	0.149	0.136	0.123	0.113	0.101
1.15	0.159	0.142	0.126	0.112	0.101	0.090	0.082	0.073	0.067	0.059
1.20	0.091	0.080	0.071	0.063	0.057	0.050	0.045	0.039	0.037	0.032
1.25	0.048	0.041	0.037	0.032	0.029	0.025	0.023	0.020	0.018	0.016
1.30	0.023	0.019	0.017	0.015	0.013	0.011	0.011	0.009	0.008	0.007
1.35	0.010	0.008	0.007	0.006	0.006	0.005	0.004	0.003	0.003	0.003
1.40	0.004	0.003	0.003	0.002	0.002	0.002	0.002	0.001	0.001	0.001
1.45	0.001	0.001	0.001	0.001	0.001	0.000	0.001	0.000	0.000	0.000
1.50	0.000	0.000	0.000	0.000	0.000	0.000	0.000			
σ = 0.20										
0.00	1.000	1.000	0.996	0.991	0.992	0.983	0.987	0.974	0.983	0.966
0.05	1.000	1.000	0.995	0.991	0.991	0.982	0.987	0.974	0.982	0.965
0.10	1.000	1.000	0.995	0.990	0.989	0.980	0.984	0.971	0.979	0.962
0.15	1.000	1.000	0.993	0.989	0.986	0.977	0.980	0.967	0.973	0.956

APPENDIX (cont'd)

		0.6		0.7		0.8		0.9		1.0	
I	I_c	I	I_c	I	I_c	I	I_c	I	I_c	I	I_c
0.179	0.170	0.149	0.141	0.124	0.117	0.105	0.098	0.088	0.083	0.077	0.070
0.099	0.092	0.080	0.075	0.066	0.061	0.054	0.050	0.045	0.041	0.037	0.033
0.046	0.042	0.037	0.033	0.029	0.027	0.024	0.022	0.019	0.018	0.016	0.014
0.018	0.016	0.014	0.012	0.011	0.010	0.009	0.008	0.007	0.006	0.005	0.004
0.005	0.005	0.004	0.004	0.003	0.003	0.003	0.002	0.002	0.002	0.001	0.001
0.001	0.001	0.001	0.001	0.001	0.001	0.001	0.000	0.000	0.000	0.000	0.000
0.000	0.000	0.000	0.000	0.000	0.000						
0.989	0.978	0.966	0.972	0.961	0.968	0.952	0.961	0.950	0.959	0.978	0.975
0.987	0.975	0.965	0.971	0.962	0.966	0.953	0.962	0.977	0.975	0.975	0.972
0.983	0.971	0.960	0.966	0.977	0.961	0.971	0.975	0.971	0.970	0.967	0.965
0.977	0.965	0.972	0.958	0.968	0.969	0.961	0.946	0.959	0.948	0.955	0.953
0.968	0.956	0.961	0.947	0.955	0.939	0.949	0.931	0.943	0.923	0.938	0.945
0.956	0.943	0.947	0.933	0.939	0.912	0.931	0.912	0.923	0.902	0.915	0.902
0.941	0.928	0.929	0.915	0.919	0.902	0.908	0.889	0.898	0.877	0.888	0.875
0.923	0.910	0.908	0.893	0.891	0.877	0.881	0.862	0.868	0.848	0.855	0.842
0.901	0.888	0.883	0.868	0.866	0.849	0.849	0.830	0.833	0.812	0.818	0.795
0.876	0.862	0.851	0.838	0.833	0.815	0.813	0.794	0.794	0.773	0.775	0.752
0.847	0.833	0.821	0.805	0.796	0.778	0.772	0.753	0.749	0.728	0.728	0.705
0.814	0.798	0.783	0.766	0.751	0.735	0.726	0.706	0.700	0.678	0.675	0.652
0.774	0.759	0.739	0.721	0.706	0.687	0.675	0.651	0.645	0.621	0.618	0.595
0.729	0.712	0.689	0.670	0.652	0.632	0.618	0.597	0.586	0.561	0.556	0.531
0.676	0.657	0.632	0.612	0.591	0.571	0.555	0.531	0.521	0.500	0.490	0.464
0.613	0.594	0.567	0.546	0.525	0.504	0.487	0.466	0.452	0.431	0.421	0.390
0.542	0.521	0.495	0.473	0.452	0.431	0.415	0.391	0.374	0.351	0.341	0.311
0.463	0.441	0.417	0.396	0.376	0.356	0.334	0.321	0.309	0.290	0.282	0.263
0.379	0.358	0.336	0.316	0.300	0.281	0.268	0.250	0.236	0.223	0.216	0.200
0.295	0.275	0.258	0.240	0.227	0.210	0.200	0.185	0.177	0.163	0.158	0.145
0.216	0.199	0.186	0.171	0.162	0.148	0.141	0.128	0.123	0.112	0.108	0.098
0.138	0.134	0.126	0.114	0.108	0.097	0.093	0.084	0.080	0.072	0.070	0.062
0.094	0.084	0.079	0.071	0.067	0.060	0.057	0.051	0.049	0.043	0.042	0.037
0.055	0.049	0.046	0.040	0.038	0.034	0.032	0.028	0.027	0.021	0.023	0.020
0.030	0.026	0.025	0.021	0.020	0.017	0.017	0.015	0.014	0.012	0.012	0.010
0.015	0.013	0.012	0.010	0.010	0.008	0.008	0.007	0.007	0.006	0.006	0.005
0.007	0.005	0.005	0.004	0.004	0.004	0.004	0.003	0.003	0.002	0.002	0.002
0.003	0.002	0.002	0.002	0.002	0.001	0.001	0.001	0.001	0.001	0.001	0.001
0.001	0.001	0.001	0.001	0.001	0.000	0.000	0.000	0.000	0.000	0.000	0.000
0.000	0.000	0.000	0.000	0.000	0.000						
0.979	0.958	0.975	0.950	0.971	0.942	0.968	0.935	0.964	0.927	0.960	0.930
0.978	0.957	0.974	0.949	0.970	0.941	0.966	0.933	0.961	0.925	0.958	0.917
0.974	0.953	0.969	0.941	0.964	0.935	0.959	0.927	0.955	0.918	0.959	0.910
0.967	0.946	0.961	0.936	0.955	0.926	0.949	0.916	0.943	0.907	0.938	0.897

APPENDIX (cont'd)

$\begin{array}{c} y \\ \backslash \\ x \end{array}$	0.0		0.1		0.2		0.3		0.4	
	f	f_c	f	f_c	f	f_c	f	f_c	f	f_c
0.20	1.000	1.000	0.991	0.986	0.982	0.973	0.974	0.960	0.966	0.948
0.25	1.000	1.000	0.988	0.983	0.977	0.967	0.966	0.952	0.955	0.937
0.30	1.000	1.000	0.985	0.979	0.970	0.960	0.956	0.942	0.942	0.924
0.35	0.999	0.999	0.980	0.974	0.961	0.951	0.944	0.929	0.927	0.907
0.40	0.999	0.998	0.974	0.968	0.951	0.940	0.929	0.913	0.903	0.883
0.45	0.997	0.995	0.966	0.959	0.938	0.925	0.911	0.894	0.885	0.864
0.50	0.994	0.991	0.960	0.947	0.921	0.907	0.889	0.870	0.873	0.856
0.55	0.989	0.983	0.942	0.931	0.900	0.884	0.862	0.841	0.847	0.830
0.60	0.977	0.969	0.923	0.909	0.871	0.855	0.830	0.807	0.829	0.813
0.65	0.960	0.948	0.897	0.879	0.841	0.819	0.799	0.769	0.785	0.770
0.70	0.933	0.916	0.861	0.840	0.799	0.773	0.743	0.715	0.691	0.663
0.75	0.891	0.872	0.815	0.789	0.747	0.718	0.687	0.656	0.631	0.602
0.80	0.841	0.813	0.757	0.726	0.685	0.652	0.623	0.599	0.570	0.536
0.85	0.773	0.739	0.686	0.651	0.614	0.578	0.552	0.517	0.499	0.464
0.90	0.691	0.653	0.606	0.568	0.535	0.498	0.475	0.449	0.425	0.391
0.95	0.599	0.558	0.518	0.479	0.451	0.416	0.396	0.363	0.351	0.319
1.00	0.500	0.460	0.427	0.390	0.368	0.334	0.319	0.289	0.279	0.251
1.05	0.401	0.364	0.338	0.305	0.288	0.258	0.248	0.221	0.214	0.190
1.10	0.309	0.276	0.257	0.228	0.217	0.192	0.184	0.162	0.158	0.138
1.15	0.227	0.199	0.187	0.164	0.156	0.136	0.131	0.114	0.111	0.096
1.20	0.159	0.137	0.129	0.112	0.107	0.092	0.089	0.076	0.075	0.061
1.25	0.106	0.090	0.085	0.073	0.070	0.059	0.058	0.049	0.048	0.040
1.30	0.067	0.056	0.053	0.045	0.043	0.036	0.035	0.029	0.029	0.021
1.35	0.040	0.033	0.032	0.026	0.026	0.021	0.021	0.017	0.017	0.014
1.40	0.023	0.019	0.018	0.015	0.014	0.012	0.011	0.009	0.009	0.008
1.45	0.012	0.010	0.010	0.008	0.008	0.006	0.006	0.005	0.005	0.004
1.50	0.006	0.005	0.005	0.004	0.004	0.003	0.003	0.002	0.002	0.002
1.55	0.003	0.002	0.002	0.002	0.002	0.001	0.001	0.001	0.001	0.001
1.60	0.001	0.001	0.001	0.001	0.001	0.001	0.001	0.000	0.000	0.000
1.65	0.001	0.000	0.000	0.000	0.000	0.000	0.000	0.000	0.000	0.000
1.70	0.000									

$\sigma=0.25$										
0.00	1.000	1.000	0.993	0.985	0.986	0.971	0.980	0.958	0.973	0.945
0.05	1.000	1.000	0.993	0.985	0.986	0.971	0.979	0.957	0.972	0.944
0.10	1.000	0.999	0.992	0.984	0.984	0.969	0.976	0.954	0.969	0.940
0.15	1.000	0.999	0.990	0.982	0.980	0.965	0.971	0.949	0.963	0.934
0.20	0.999	0.998	0.987	0.978	0.976	0.960	0.965	0.942	0.954	0.924
0.25	0.999	0.997	0.984	0.974	0.969	0.952	0.956	0.932	0.943	0.912
0.30	0.997	0.995	0.979	0.968	0.961	0.943	0.945	0.919	0.929	0.897
0.35	0.995	0.992	0.972	0.960	0.951	0.931	0.930	0.904	0.911	0.878
0.40	0.992	0.986	0.964	0.950	0.937	0.916	0.913	0.885	0.890	0.856
0.45	0.986	0.978	0.952	0.935	0.921	0.897	0.892	0.861	0.865	0.829
0.50	0.977	0.966	0.937	0.917	0.900	0.873	0.867	0.834	0.836	0.797
0.55	0.964	0.949	0.917	0.893	0.875	0.844	0.836	0.800	0.802	0.761
0.60	0.945	0.925	0.891	0.863	0.843	0.810	0.800	0.762	0.762	0.719
0.65	0.919	0.893	0.859	0.826	0.806	0.768	0.759	0.717	0.717	0.672

APPENDIX (cont'd)

0.5		0.6		0.7		0.8		0.9		1.0	
f	f_c	f	f_c	f	f_c	f	f_c	f	f_c	f	f_c
0.958	0.936	0.950	0.924	0.942	0.913	0.935	0.901	0.927	0.891	0.920	0.880
0.945	0.923	0.935	0.909	0.925	0.896	0.916	0.882	0.907	0.870	0.898	0.858
0.929	0.907	0.917	0.890	0.905	0.874	0.893	0.859	0.881	0.844	0.870	0.830
0.910	0.887	0.895	0.868	0.880	0.849	0.865	0.831	0.851	0.814	0.838	0.798
0.888	0.864	0.869	0.841	0.850	0.819	0.833	0.799	0.816	0.779	0.800	0.760
0.861	0.836	0.838	0.810	0.817	0.785	0.796	0.762	0.777	0.739	0.758	0.718
0.830	0.804	0.803	0.774	0.778	0.746	0.755	0.719	0.732	0.695	0.711	0.671
0.794	0.766	0.763	0.732	0.735	0.701	0.708	0.672	0.683	0.645	0.659	0.620
0.752	0.722	0.718	0.686	0.686	0.652	0.656	0.621	0.629	0.592	0.604	0.565
0.704	0.673	0.666	0.634	0.632	0.598	0.600	0.565	0.571	0.535	0.544	0.507
0.649	0.617	0.609	0.576	0.573	0.538	0.540	0.505	0.510	0.474	0.483	0.446
0.589	0.555	0.547	0.513	0.510	0.476	0.477	0.442	0.447	0.412	0.419	0.385
0.523	0.489	0.481	0.447	0.445	0.411	0.412	0.379	0.383	0.350	0.356	0.324
0.453	0.419	0.413	0.380	0.378	0.346	0.347	0.316	0.320	0.290	0.295	0.266
0.382	0.350	0.345	0.314	0.312	0.283	0.284	0.256	0.259	0.233	0.237	0.212
0.312	0.282	0.279	0.251	0.250	0.224	0.225	0.201	0.204	0.181	0.185	0.164
0.246	0.220	0.218	0.194	0.194	0.171	0.173	0.152	0.155	0.136	0.140	0.122
0.187	0.165	0.164	0.144	0.144	0.126	0.128	0.111	0.114	0.098	0.101	0.088
0.136	0.119	0.118	0.103	0.103	0.089	0.091	0.078	0.080	0.068	0.071	0.060
0.095	0.082	0.082	0.070	0.071	0.060	0.062	0.052	0.054	0.046	0.047	0.040
0.063	0.054	0.054	0.046	0.046	0.039	0.040	0.034	0.035	0.029	0.030	0.025
0.040	0.034	0.034	0.028	0.029	0.024	0.025	0.021	0.021	0.018	0.019	0.015
0.024	0.020	0.020	0.017	0.017	0.014	0.015	0.012	0.013	0.010	0.011	0.009
0.014	0.011	0.012	0.009	0.010	0.008	0.008	0.007	0.007	0.006	0.006	0.005
0.008	0.006	0.006	0.005	0.005	0.004	0.004	0.004	0.004	0.003	0.003	0.002
0.004	0.003	0.003	0.003	0.003	0.002	0.002	0.002	0.002	0.001	0.002	0.001
0.002	0.002	0.002	0.001	0.001	0.001	0.001	0.001	0.001	0.001	0.001	0.001
0.001	0.001	0.001	0.001	0.001	0.000	0.000	0.000	0.000	0.000	0.000	0.000
0.000	0.000	0.000	0.000	0.000							
0.967	0.932	0.961	0.920	0.955	0.908	0.949	0.897	0.943	0.886	0.938	0.875
0.966	0.931	0.959	0.918	0.953	0.906	0.947	0.895	0.941	0.884	0.935	0.873
0.961	0.926	0.954	0.913	0.947	0.901	0.941	0.888	0.934	0.877	0.928	0.865
0.954	0.919	0.946	0.905	0.938	0.891	0.930	0.878	0.922	0.865	0.915	0.853
0.944	0.908	0.934	0.892	0.924	0.877	0.915	0.863	0.906	0.849	0.898	0.835
0.930	0.894	0.919	0.876	0.907	0.859	0.896	0.843	0.885	0.828	0.875	0.813
0.914	0.876	0.899	0.856	0.886	0.837	0.873	0.819	0.860	0.802	0.848	0.786
0.893	0.855	0.876	0.832	0.860	0.811	0.845	0.791	0.830	0.772	0.816	0.754
0.869	0.829	0.849	0.804	0.830	0.780	0.812	0.758	0.795	0.737	0.779	0.718
0.841	0.799	0.817	0.771	0.796	0.745	0.775	0.721	0.756	0.698	0.738	0.677
0.808	0.764	0.781	0.734	0.757	0.706	0.734	0.679	0.712	0.655	0.692	0.632
0.770	0.725	0.740	0.692	0.713	0.662	0.688	0.634	0.665	0.608	0.643	0.584
0.727	0.680	0.695	0.646	0.665	0.614	0.638	0.585	0.613	0.558	0.590	0.533
0.679	0.631	0.645	0.595	0.614	0.562	0.585	0.532	0.559	0.505	0.535	0.480

APPENDIX (cont'd)

λ	$\sigma=0.1$		$\sigma=0.2$		$\sigma=0.3$		$\sigma=0.4$	
	I	I_c	I	I_c	I	I_c	I	I_c
0.70	0.885	0.853	0.819	0.782	0.761	0.720	0.711	0.667
0.75	0.841	0.803	0.774	0.729	0.710	0.666	0.657	0.611
0.80	0.788	0.745	0.714	0.669	0.652	0.605	0.593	0.551
0.85	0.726	0.678	0.651	0.603	0.589	0.540	0.535	0.498
0.90	0.655	0.605	0.582	0.533	0.521	0.473	0.470	0.435
0.95	0.579	0.528	0.509	0.460	0.452	0.405	0.403	0.359
1.00	0.500	0.450	0.435	0.389	0.382	0.339	0.339	0.298
1.05	0.421	0.373	0.363	0.320	0.316	0.276	0.277	0.241
1.10	0.345	0.301	0.294	0.256	0.254	0.219	0.221	0.190
1.15	0.274	0.237	0.232	0.199	0.199	0.169	0.172	0.145
1.20	0.212	0.180	0.178	0.150	0.151	0.127	0.129	0.103
1.25	0.159	0.133	0.132	0.110	0.111	0.092	0.095	0.078
1.30	0.115	0.095	0.095	0.078	0.080	0.065	0.067	0.055
1.35	0.081	0.066	0.066	0.054	0.055	0.044	0.046	0.039
1.40	0.055	0.041	0.041	0.035	0.037	0.029	0.031	0.026
1.45	0.036	0.028	0.029	0.023	0.024	0.019	0.020	0.015
1.50	0.023	0.018	0.018	0.014	0.015	0.012	0.012	0.010
1.55	0.014	0.011	0.011	0.009	0.009	0.007	0.007	0.006
1.60	0.008	0.006	0.006	0.005	0.005	0.004	0.004	0.003
1.65	0.005	0.003	0.003	0.003	0.003	0.002	0.002	0.002
1.70	0.003	0.002	0.002	0.001	0.002	0.001	0.001	0.001
1.75	0.001	0.001	0.001	0.001	0.001	0.001	0.001	0.000
1.80	0.001	0.000	0.001	0.000	0.000	0.000	0.000	0.000
1.85	0.000		0.000					

$\sigma=0.30$								
0.00	0.999	0.996	0.989	0.974	0.979	0.953	0.969	0.934
0.05	0.999	0.996	0.988	0.971	0.978	0.952	0.968	0.933
0.10	0.999	0.995	0.987	0.972	0.975	0.950	0.965	0.929
0.15	0.993	0.993	0.984	0.968	0.971	0.945	0.959	0.923
0.20	0.986	0.990	0.980	0.963	0.966	0.938	0.952	0.914
0.25	0.974	0.986	0.975	0.956	0.958	0.928	0.941	0.902
0.30	0.960	0.980	0.968	0.946	0.947	0.916	0.928	0.887
0.35	0.985	0.972	0.958	0.934	0.934	0.900	0.912	0.869
0.40	0.977	0.961	0.946	0.919	0.918	0.881	0.892	0.846
0.45	0.967	0.946	0.930	0.899	0.898	0.857	0.868	0.820
0.50	0.952	0.927	0.911	0.875	0.874	0.830	0.841	0.789
0.55	0.933	0.902	0.887	0.846	0.845	0.798	0.808	0.754
0.60	0.909	0.872	0.857	0.812	0.812	0.760	0.772	0.715
0.65	0.878	0.836	0.822	0.773	0.773	0.718	0.730	0.671
0.70	0.841	0.793	0.781	0.728	0.729	0.672	0.684	0.623
0.75	0.798	0.744	0.735	0.678	0.681	0.621	0.634	0.573
0.80	0.748	0.690	0.683	0.623	0.628	0.567	0.581	0.519
0.85	0.691	0.631	0.626	0.566	0.572	0.511	0.525	0.464
0.90	0.631	0.568	0.567	0.506	0.513	0.453	0.468	0.409
0.95	0.566	0.504	0.505	0.445	0.454	0.396	0.411	0.355
1.00	0.500	0.439	0.442	0.385	0.394	0.340	0.355	0.303

APPENDIX (cont'd)

		0.6		0.7		0.8		0.9		1.0	
f	f_c	f	f_c	f	f_c	f	f_c	f	f_c	f	f_c
0.427	0.573	0.591	0.541	0.559	0.508	0.530	0.478	0.503	0.451	0.479	0.426
0.470	0.522	0.534	0.485	0.501	0.452	0.472	0.423	0.446	0.396	0.421	0.373
0.511	0.463	0.475	0.427	0.443	0.396	0.414	0.367	0.388	0.342	0.365	0.329
0.449	0.403	0.415	0.369	0.384	0.340	0.356	0.313	0.332	0.290	0.310	0.269
0.488	0.345	0.355	0.313	0.326	0.286	0.301	0.262	0.278	0.241	0.258	0.222
0.328	0.288	0.298	0.260	0.272	0.235	0.249	0.214	0.229	0.196	0.211	0.184
0.271	0.235	0.244	0.210	0.221	0.189	0.201	0.171	0.184	0.156	0.168	0.143
0.218	0.187	0.195	0.166	0.176	0.149	0.159	0.134	0.144	0.121	0.131	0.109
0.171	0.145	0.152	0.128	0.136	0.113	0.122	0.102	0.115	0.094	0.104	0.084
0.134	0.115	0.116	0.096	0.102	0.085	0.094	0.075	0.082	0.064	0.074	0.059
0.107	0.090	0.095	0.070	0.075	0.061	0.066	0.054	0.059	0.049	0.053	0.043
0.079	0.067	0.064	0.050	0.054	0.043	0.047	0.038	0.042	0.034	0.037	0.030
0.049	0.040	0.042	0.034	0.037	0.029	0.032	0.026	0.028	0.022	0.025	0.020
0.023	0.026	0.029	0.023	0.025	0.019	0.021	0.017	0.019	0.015	0.016	0.013
0.002	0.017	0.019	0.015	0.016	0.012	0.014	0.011	0.012	0.009	0.011	0.008
0.014	0.011	0.012	0.009	0.010	0.008	0.009	0.007	0.007	0.006	0.007	0.005
0.008	0.007	0.007	0.005	0.006	0.005	0.005	0.004	0.004	0.003	0.004	0.003
0.005	0.004	0.004	0.003	0.004	0.003	0.003	0.002	0.003	0.002	0.002	0.002
0.003	0.002	0.002	0.002	0.002	0.002	0.002	0.001	0.001	0.001	0.001	0.001
0.002	0.001	0.001	0.001	0.001	0.001	0.001	0.001	0.001	0.001	0.001	0.001
0.001	0.001	0.001	0.001	0.001	0.000	0.000	0.000	0.000	0.000	0.000	0.000
0.000	0.000	0.000	0.000	0.000							
0.951	0.858	0.912	0.884	0.934	0.865	0.926	0.859	0.918	0.835	0.910	0.824
0.919	0.806	0.910	0.879	0.932	0.863	0.923	0.847	0.915	0.833	0.908	0.818
0.945	0.891	0.935	0.874	0.926	0.857	0.917	0.841	0.909	0.826	0.900	0.811
0.937	0.883	0.926	0.864	0.916	0.847	0.906	0.830	0.897	0.814	0.888	0.799
0.926	0.871	0.914	0.851	0.902	0.832	0.891	0.815	0.881	0.798	0.871	0.782
0.911	0.855	0.898	0.834	0.885	0.814	0.872	0.795	0.860	0.777	0.849	0.760
0.893	0.836	0.878	0.813	0.863	0.792	0.848	0.772	0.835	0.752	0.822	0.734
0.872	0.813	0.854	0.788	0.837	0.765	0.821	0.744	0.805	0.723	0.791	0.704
0.856	0.786	0.826	0.759	0.806	0.735	0.788	0.712	0.772	0.690	0.756	0.679
0.847	0.755	0.794	0.726	0.772	0.700	0.752	0.676	0.734	0.653	0.716	0.632
0.783	0.720	0.757	0.690	0.734	0.662	0.712	0.637	0.692	0.613	0.673	0.591
0.745	0.681	0.717	0.649	0.692	0.620	0.669	0.594	0.647	0.570	0.627	0.548
0.703	0.638	0.674	0.606	0.647	0.576	0.622	0.549	0.600	0.524	0.579	0.502
0.658	0.592	0.627	0.559	0.599	0.529	0.573	0.502	0.550	0.478	0.528	0.455
0.609	0.544	0.577	0.510	0.548	0.481	0.522	0.454	0.498	0.430	0.477	0.408
0.557	0.493	0.525	0.461	0.496	0.431	0.470	0.405	0.447	0.382	0.425	0.361
0.504	0.442	0.472	0.410	0.443	0.382	0.418	0.357	0.395	0.335	0.374	0.315
0.449	0.390	0.418	0.360	0.391	0.334	0.367	0.311	0.345	0.290	0.325	0.271
0.395	0.340	0.366	0.312	0.340	0.287	0.317	0.266	0.297	0.247	0.278	0.230
0.342	0.291	0.315	0.266	0.291	0.244	0.270	0.224	0.251	0.207	0.234	0.192
0.292	0.245	0.267	0.223	0.245	0.203	0.226	0.186	0.209	0.171	0.194	0.158

APPENDIX (cont'd)

$\begin{array}{c} v \\ \diagdown \\ x \end{array}$	0.0		0.1		0.2		0.3		0.4	
	f	f_c	f	f_c	f	f_c	f	f_c	f	f_c
1.05	0.434	0.376	0.381	0.327	0.337	0.287	0.301	0.254	0.270	0.227
1.10	0.369	0.316	0.322	0.273	0.283	0.238	0.251	0.209	0.224	0.186
1.15	0.309	0.261	0.267	0.223	0.233	0.194	0.205	0.169	0.182	0.149
1.20	0.252	0.210	0.217	0.179	0.188	0.154	0.164	0.134	0.145	0.117
1.25	0.202	0.166	0.172	0.141	0.149	0.120	0.129	0.101	0.113	0.090
1.30	0.159	0.129	0.134	0.108	0.115	0.092	0.099	0.079	0.087	0.068
1.35	0.122	0.097	0.102	0.081	0.087	0.069	0.075	0.059	0.065	0.051
1.40	0.091	0.072	0.076	0.060	0.065	0.050	0.055	0.043	0.048	0.037
1.45	0.067	0.052	0.056	0.042	0.047	0.036	0.040	0.030	0.034	0.026
1.50	0.048	0.037	0.040	0.030	0.033	0.025	0.028	0.021	0.024	0.018
1.55	0.033	0.025	0.027	0.021	0.023	0.017	0.019	0.014	0.016	0.012
1.60	0.023	0.017	0.019	0.014	0.015	0.011	0.013	0.010	0.011	0.008
1.65	0.015	0.011	0.012	0.009	0.010	0.007	0.008	0.006	0.007	0.005
1.70	0.010	0.007	0.008	0.006	0.006	0.005	0.005	0.004	0.005	0.003
1.75	0.006	0.004	0.005	0.004	0.004	0.003	0.003	0.002	0.003	0.002
1.80	0.004	0.003	0.003	0.002	0.002	0.002	0.002	0.001	0.002	0.001
1.85	0.002	0.002	0.002	0.001	0.001	0.001	0.001	0.001	0.001	0.001
1.90	0.001	0.001	0.001	0.001	0.001	0.001	0.001	0.000	0.001	0.000
1.95	0.001	0.001	0.001	0.000	0.000	0.000	0.000	0.000	0.000	
2.00	0.000	0.000	0.000							
$\sigma = 0.35$										
0.00	0.996	0.983	0.981	0.953	0.967	0.925	0.954	0.899	0.942	0.875
0.05	0.995	0.982	0.980	0.952	0.966	0.924	0.953	0.898	0.940	0.874
0.10	0.994	0.980	0.978	0.949	0.963	0.920	0.949	0.893	0.936	0.869
0.15	0.992	0.976	0.974	0.944	0.958	0.914	0.943	0.886	0.929	0.861
0.20	0.989	0.971	0.969	0.936	0.954	0.905	0.941	0.876	0.918	0.849
0.25	0.984	0.963	0.961	0.926	0.941	0.893	0.922	0.862	0.905	0.834
0.30	0.977	0.953	0.952	0.913	0.929	0.878	0.907	0.845	0.888	0.816
0.35	0.968	0.940	0.939	0.897	0.913	0.859	0.889	0.825	0.867	0.794
0.40	0.957	0.924	0.924	0.878	0.894	0.837	0.868	0.801	0.843	0.768
0.45	0.942	0.904	0.905	0.855	0.872	0.812	0.843	0.773	0.816	0.739
0.50	0.923	0.880	0.882	0.828	0.846	0.782	0.814	0.742	0.785	0.706
0.55	0.901	0.852	0.856	0.797	0.816	0.749	0.781	0.707	0.750	0.670
0.60	0.873	0.819	0.825	0.762	0.782	0.712	0.745	0.669	0.712	0.631
0.65	0.841	0.782	0.789	0.723	0.745	0.672	0.705	0.628	0.670	0.590
0.70	0.804	0.740	0.750	0.680	0.703	0.629	0.662	0.585	0.626	0.546
0.75	0.762	0.694	0.706	0.634	0.658	0.583	0.616	0.539	0.580	0.501
0.80	0.716	0.645	0.659	0.585	0.610	0.535	0.568	0.492	0.532	0.455
0.85	0.666	0.593	0.608	0.534	0.560	0.486	0.518	0.445	0.482	0.409
0.90	0.612	0.539	0.556	0.483	0.508	0.436	0.468	0.397	0.433	0.364
0.95	0.557	0.484	0.502	0.431	0.456	0.387	0.417	0.350	0.384	0.319
1.00	0.500	0.429	0.448	0.380	0.404	0.339	0.368	0.306	0.337	0.277
1.05	0.443	0.376	0.394	0.331	0.354	0.294	0.320	0.263	0.292	0.237
1.10	0.388	0.324	0.343	0.284	0.306	0.251	0.275	0.223	0.249	0.200
1.15	0.334	0.276	0.294	0.240	0.260	0.211	0.233	0.187	0.210	0.167
1.20	0.284	0.232	0.248	0.200	0.219	0.175	0.195	0.154	0.174	0.137

APPENDIX (cont'd)

0.5		0.6		0.7		0.8		0.9		1.0	
f	f _c	f	f _c	f	f _c	f	f _c	f	f _c	f	f _c
0.245	0.203	0.222	0.184	0.203	0.166	0.186	0.152	0.171	0.139	0.158	0.127
0.201	0.165	0.182	0.148	0.165	0.134	0.151	0.121	0.138	0.110	0.127	0.101
0.163	0.132	0.146	0.118	0.132	0.106	0.120	0.095	0.109	0.086	0.100	0.078
0.129	0.103	0.115	0.092	0.103	0.082	0.093	0.073	0.085	0.066	0.077	0.060
0.100	0.079	0.089	0.070	0.079	0.062	0.071	0.056	0.064	0.050	0.058	0.045
0.076	0.060	0.067	0.052	0.060	0.046	0.053	0.041	0.048	0.037	0.043	0.033
0.057	0.044	0.050	0.038	0.044	0.034	0.039	0.030	0.035	0.026	0.031	0.024
0.041	0.032	0.036	0.027	0.032	0.024	0.028	0.021	0.025	0.019	0.022	0.017
0.029	0.022	0.026	0.019	0.022	0.017	0.020	0.015	0.017	0.013	0.016	0.011
0.020	0.015	0.018	0.013	0.015	0.011	0.014	0.010	0.012	0.009	0.011	0.008
0.014	0.010	0.012	0.009	0.010	0.008	0.009	0.007	0.008	0.006	0.007	0.005
0.009	0.007	0.008	0.006	0.007	0.005	0.006	0.004	0.005	0.004	0.005	0.003
0.006	0.004	0.005	0.004	0.004	0.003	0.004	0.003	0.003	0.002	0.003	0.002
0.004	0.003	0.003	0.002	0.003	0.002	0.002	0.002	0.002	0.001	0.002	0.001
0.002	0.002	0.002	0.001	0.002	0.001	0.001	0.001	0.001	0.001	0.001	0.001
0.001	0.001	0.001	0.001	0.001	0.001	0.001	0.001	0.001	0.001	0.001	0.000
0.001	0.001	0.001	0.000	0.001	0.000	0.001	0.000	0.000	0.000	0.000	0.000
0.000	0.000	0.000	0.000	0.000	0.000	0.000	0.000				
0.930	0.853	0.919	0.832	0.908	0.812	0.898	0.794	0.888	0.776	0.878	0.759
0.928	0.851	0.917	0.830	0.906	0.810	0.896	0.791	0.886	0.774	0.876	0.757
0.923	0.846	0.911	0.824	0.900	0.804	0.889	0.785	0.879	0.767	0.869	0.750
0.915	0.837	0.902	0.815	0.890	0.794	0.879	0.774	0.868	0.756	0.857	0.739
0.903	0.824	0.889	0.801	0.876	0.780	0.864	0.760	0.852	0.741	0.841	0.723
0.888	0.808	0.873	0.784	0.858	0.762	0.845	0.741	0.832	0.722	0.820	0.703
0.870	0.788	0.853	0.763	0.837	0.740	0.822	0.718	0.808	0.698	0.794	0.679
0.847	0.765	0.828	0.739	0.811	0.715	0.795	0.692	0.779	0.671	0.765	0.652
0.821	0.738	0.801	0.711	0.781	0.685	0.764	0.662	0.747	0.641	0.731	0.621
0.792	0.708	0.769	0.679	0.748	0.653	0.729	0.629	0.711	0.607	0.695	0.587
0.758	0.674	0.734	0.645	0.712	0.618	0.692	0.593	0.673	0.571	0.655	0.550
0.722	0.637	0.696	0.607	0.673	0.580	0.651	0.555	0.631	0.533	0.613	0.512
0.682	0.598	0.655	0.567	0.630	0.540	0.608	0.515	0.587	0.492	0.568	0.472
0.639	0.556	0.611	0.526	0.586	0.498	0.563	0.474	0.542	0.451	0.523	0.431
0.594	0.513	0.566	0.482	0.540	0.456	0.517	0.431	0.495	0.410	0.476	0.390
0.547	0.468	0.519	0.439	0.493	0.413	0.470	0.389	0.449	0.368	0.430	0.349
0.499	0.423	0.471	0.395	0.446	0.370	0.423	0.347	0.402	0.327	0.384	0.309
0.451	0.378	0.423	0.352	0.399	0.328	0.377	0.307	0.357	0.288	0.339	0.271
0.403	0.335	0.376	0.309	0.353	0.287	0.332	0.268	0.313	0.250	0.296	0.235
0.356	0.292	0.330	0.269	0.308	0.249	0.289	0.231	0.271	0.215	0.256	0.201
0.310	0.252	0.287	0.231	0.266	0.213	0.248	0.197	0.232	0.182	0.218	0.170
0.267	0.215	0.246	0.196	0.227	0.180	0.211	0.165	0.196	0.153	0.184	0.142
0.227	0.181	0.208	0.164	0.191	0.150	0.177	0.137	0.164	0.126	0.153	0.117
0.190	0.150	0.173	0.136	0.159	0.123	0.146	0.112	0.135	0.103	0.125	0.095
0.157	0.123	0.143	0.110	0.130	0.100	0.119	0.091	0.110	0.083	0.101	0.076

APPENDIX (cont'd)

v x	0.0		0.1		0.2		0.3		0.4	
	f	f _c	f	f _c	f	f _c	f	f _c	f	f _c
1.25	0.238	0.191	0.206	0.165	0.181	0.143	0.160	0.126	0.143	0.111
1.30	0.196	0.156	0.169	0.133	0.147	0.115	0.130	0.101	0.115	0.089
1.35	0.159	0.125	0.136	0.106	0.118	0.091	0.104	0.079	0.091	0.069
1.40	0.127	0.098	0.108	0.083	0.093	0.071	0.081	0.062	0.071	0.054
1.45	0.099	0.076	0.084	0.064	0.072	0.055	0.063	0.047	0.055	0.041
1.50	0.077	0.058	0.065	0.049	0.055	0.041	0.048	0.035	0.042	0.031
1.55	0.058	0.043	0.049	0.036	0.042	0.031	0.036	0.026	0.031	0.022
1.60	0.043	0.032	0.036	0.027	0.031	0.022	0.026	0.019	0.023	0.016
1.65	0.032	0.023	0.026	0.019	0.022	0.016	0.019	0.014	0.016	0.012
1.70	0.023	0.016	0.019	0.014	0.016	0.011	0.013	0.010	0.012	0.008
1.75	0.016	0.011	0.013	0.009	0.011	0.008	0.009	0.007	0.008	0.006
1.80	0.011	0.008	0.009	0.006	0.008	0.005	0.006	0.004	0.005	0.004
1.85	0.008	0.005	0.006	0.004	0.005	0.004	0.004	0.003	0.004	0.002
1.90	0.005	0.003	0.004	0.003	0.003	0.002	0.003	0.002	0.002	0.002
1.95	0.003	0.002	0.003	0.002	0.002	0.002	0.002	0.001	0.002	0.001
2.00	0.002	0.001	0.002	0.001	0.001	0.001	0.001	0.001	0.001	0.001
2.05	0.001	0.001	0.001	0.001	0.001	0.001	0.001	0.000	0.001	0.000
2.10	0.001	0.001	0.001	0.000	0.001	0.000	0.000		0.000	
2.15	0.001	0.000	0.000		0.000					
2.20	0.000									
$\sigma = 0.40$										
0.00	0.988	0.956	0.968	0.918	0.951	0.884	0.934	0.853	0.919	0.825
0.05	0.987	0.955	0.967	0.917	0.950	0.883	0.933	0.852	0.918	0.824
0.10	0.985	0.952	0.965	0.913	0.946	0.879	0.929	0.847	0.913	0.818
0.15	0.981	0.946	0.960	0.907	0.940	0.871	0.922	0.839	0.905	0.810
0.20	0.976	0.938	0.953	0.897	0.931	0.861	0.912	0.828	0.894	0.798
0.25	0.969	0.928	0.943	0.885	0.920	0.848	0.899	0.814	0.880	0.783
0.30	0.959	0.915	0.931	0.870	0.906	0.831	0.883	0.796	0.862	0.765
0.35	0.948	0.898	0.917	0.852	0.889	0.812	0.864	0.775	0.842	0.743
0.40	0.933	0.879	0.899	0.831	0.869	0.789	0.842	0.752	0.818	0.718
0.45	0.915	0.856	0.878	0.806	0.846	0.763	0.817	0.724	0.791	0.690
0.50	0.894	0.830	0.854	0.779	0.819	0.734	0.788	0.694	0.760	0.660
0.55	0.870	0.801	0.827	0.748	0.789	0.702	0.756	0.662	0.727	0.626
0.60	0.841	0.768	0.796	0.714	0.756	0.667	0.722	0.626	0.691	0.591
0.65	0.809	0.732	0.761	0.677	0.720	0.630	0.684	0.589	0.652	0.554
0.70	0.773	0.692	0.724	0.637	0.681	0.590	0.644	0.550	0.611	0.515
0.75	0.734	0.650	0.683	0.595	0.640	0.549	0.602	0.509	0.569	0.475
0.80	0.691	0.606	0.640	0.552	0.596	0.507	0.558	0.468	0.526	0.435
0.85	0.646	0.560	0.595	0.508	0.551	0.464	0.514	0.426	0.481	0.394
0.90	0.599	0.513	0.548	0.463	0.505	0.421	0.469	0.385	0.437	0.355
0.95	0.550	0.466	0.500	0.418	0.459	0.378	0.424	0.345	0.393	0.316
1.00	0.500	0.418	0.453	0.374	0.413	0.337	0.379	0.306	0.351	0.279
1.05	0.450	0.372	0.405	0.331	0.368	0.297	0.336	0.268	0.310	0.244
1.10	0.401	0.328	0.359	0.290	0.324	0.259	0.295	0.233	0.270	0.211
1.15	0.354	0.286	0.315	0.251	0.283	0.223	0.256	0.200	0.234	0.181
1.20	0.309	0.246	0.273	0.216	0.244	0.191	0.220	0.170	0.200	0.153

APPENDIX (cont'd)

0.5		0.6		0.7		0.8		0.9		1.0	
f	f_c	f	f_c	f	f_c	f	f_c	f	f_c	f	f_c
0.128	0.099	0.116	0.089	0.105	0.080	0.096	0.072	0.088	0.066	0.081	0.060
0.103	0.078	0.092	0.070	0.084	0.063	0.076	0.057	0.069	0.051	0.063	0.047
0.081	0.061	0.073	0.054	0.065	0.049	0.059	0.044	0.054	0.039	0.049	0.036
0.063	0.047	0.056	0.042	0.051	0.037	0.045	0.033	0.041	0.030	0.037	0.027
0.048	0.036	0.043	0.032	0.038	0.028	0.034	0.025	0.031	0.022	0.028	0.020
0.036	0.027	0.032	0.023	0.029	0.021	0.026	0.018	0.023	0.016	0.021	0.015
0.027	0.020	0.024	0.017	0.021	0.015	0.019	0.013	0.017	0.012	0.015	0.010
0.020	0.014	0.017	0.012	0.015	0.011	0.013	0.009	0.012	0.008	0.011	0.007
0.014	0.010	0.012	0.009	0.011	0.008	0.010	0.007	0.008	0.006	0.008	0.005
0.010	0.007	0.009	0.006	0.008	0.005	0.007	0.005	0.006	0.004	0.005	0.004
0.007	0.005	0.006	0.004	0.005	0.004	0.005	0.003	0.004	0.003	0.004	0.002
0.005	0.003	0.004	0.003	0.004	0.003	0.004	0.002	0.003	0.002	0.003	0.002
0.003	0.002	0.003	0.002	0.002	0.002	0.002	0.001	0.002	0.001	0.002	0.001
0.002	0.001	0.002	0.001	0.002	0.001	0.001	0.001	0.001	0.001	0.001	0.001
0.001	0.001	0.001	0.001	0.001	0.001	0.001	0.001	0.001	0.001	0.001	0.000
0.001	0.001	0.001	0.000	0.001	0.000	0.000	0.000	0.000	0.000	0.000	
0.001	0.000	0.000		0.000							
0.000											
0.905	0.799	0.891	0.775	0.878	0.753	0.866	0.732	0.855	0.712	0.844	0.694
0.903	0.797	0.889	0.773	0.876	0.751	0.864	0.730	0.852	0.710	0.841	0.692
0.898	0.792	0.884	0.768	0.871	0.745	0.858	0.724	0.846	0.704	0.835	0.686
0.889	0.783	0.875	0.759	0.861	0.736	0.848	0.714	0.835	0.694	0.823	0.676
0.877	0.771	0.862	0.746	0.847	0.722	0.833	0.701	0.820	0.681	0.808	0.662
0.862	0.755	0.845	0.729	0.830	0.706	0.815	0.684	0.801	0.663	0.788	0.644
0.843	0.736	0.825	0.710	0.809	0.685	0.793	0.663	0.779	0.642	0.765	0.623
0.821	0.713	0.802	0.687	0.784	0.662	0.768	0.639	0.752	0.618	0.738	0.599
0.795	0.688	0.775	0.660	0.756	0.636	0.739	0.613	0.722	0.591	0.707	0.572
0.767	0.659	0.745	0.632	0.725	0.606	0.707	0.583	0.689	0.562	0.674	0.542
0.735	0.628	0.712	0.600	0.691	0.575	0.672	0.551	0.654	0.530	0.637	0.510
0.700	0.595	0.676	0.566	0.654	0.541	0.634	0.518	0.616	0.496	0.599	0.477
0.663	0.559	0.638	0.531	0.616	0.506	0.595	0.483	0.576	0.462	0.559	0.442
0.624	0.522	0.598	0.494	0.575	0.469	0.554	0.446	0.535	0.426	0.517	0.407
0.583	0.484	0.557	0.456	0.533	0.432	0.512	0.410	0.493	0.390	0.475	0.372
0.540	0.445	0.514	0.418	0.491	0.394	0.470	0.373	0.451	0.354	0.433	0.336
0.497	0.406	0.471	0.380	0.448	0.357	0.427	0.337	0.409	0.318	0.392	0.302
0.453	0.366	0.428	0.342	0.406	0.320	0.386	0.301	0.367	0.284	0.351	0.269
0.410	0.328	0.385	0.305	0.364	0.285	0.345	0.267	0.327	0.251	0.312	0.237
0.367	0.292	0.344	0.270	0.324	0.251	0.305	0.235	0.289	0.220	0.274	0.207
0.326	0.256	0.304	0.237	0.285	0.219	0.268	0.204	0.253	0.191	0.239	0.179
0.286	0.223	0.266	0.205	0.248	0.190	0.233	0.176	0.219	0.164	0.206	0.153
0.249	0.192	0.231	0.176	0.215	0.162	0.200	0.150	0.188	0.139	0.176	0.130
0.215	0.164	0.198	0.150	0.183	0.137	0.170	0.126	0.159	0.117	0.149	0.109
0.183	0.138	0.168	0.126	0.155	0.115	0.144	0.106	0.134	0.097	0.125	0.090

APPENDIX (cont'd)

v x	0.0		0.1		0.2		0.3		0.4	
	f	f _c	f	f _c	f	f _c	f	f _c	f	f _c

1.25	0.266	0.210	0.234	0.183	0.209	0.161	0.187	0.143	0.169	0.128
1.30	0.227	0.176	0.199	0.153	0.176	0.134	0.157	0.119	0.142	0.106
1.35	0.191	0.147	0.166	0.127	0.147	0.111	0.131	0.098	0.117	0.087
1.40	0.159	0.121	0.138	0.104	0.121	0.090	0.107	0.079	0.096	0.070
1.45	0.130	0.098	0.113	0.084	0.098	0.073	0.087	0.063	0.077	0.056
1.50	0.106	0.078	0.091	0.067	0.079	0.058	0.070	0.050	0.062	0.044
1.55	0.085	0.062	0.072	0.053	0.063	0.045	0.055	0.039	0.048	0.034
1.60	0.067	0.048	0.057	0.041	0.049	0.035	0.043	0.030	0.038	0.026
1.65	0.052	0.037	0.044	0.032	0.038	0.027	0.033	0.023	0.029	0.020
1.70	0.040	0.028	0.034	0.024	0.029	0.020	0.025	0.017	0.022	0.015
1.75	0.030	0.021	0.026	0.018	0.022	0.015	0.019	0.013	0.016	0.011
1.80	0.023	0.016	0.019	0.013	0.016	0.011	0.014	0.009	0.012	0.008
1.85	0.017	0.012	0.014	0.010	0.012	0.008	0.010	0.007	0.009	0.006
1.90	0.012	0.008	0.010	0.007	0.009	0.006	0.007	0.005	0.006	0.004
1.95	0.009	0.006	0.007	0.005	0.006	0.004	0.005	0.003	0.004	0.003
2.00	0.006	0.004	0.005	0.003	0.004	0.003	0.004	0.002	0.003	0.002
2.05	0.004	0.003	0.004	0.002	0.003	0.002	0.003	0.002	0.002	0.001
2.10	0.003	0.002	0.002	0.002	0.002	0.001	0.002	0.001	0.001	0.001
2.15	0.002	0.001	0.002	0.001	0.001	0.001	0.001	0.001	0.001	0.001
2.20	0.001	0.001	0.001	0.001	0.001	0.001	0.001	0.000	0.001	0.000
2.25	0.001	0.001	0.001	0.000	0.001	0.000	0.000		0.000	
2.30	0.001	0.000	0.000		0.000					
2.35	0.000									

0.5		0.6		0.7		0.8		0.9		1.0	
f	f _c	f	f _c	f	f _c	f	f _c	f	f _c	f	f _c

0.154	0.115	0.141	0.104	0.130	0.095	0.120	0.087	0.111	0.080	0.103	0.074
0.128	0.095	0.117	0.086	0.107	0.078	0.099	0.071	0.091	0.065	0.084	0.060
0.106	0.077	0.096	0.070	0.088	0.063	0.080	0.057	0.074	0.052	0.068	0.048
0.086	0.062	0.078	0.056	0.071	0.050	0.065	0.046	0.059	0.042	0.055	0.038
0.069	0.050	0.062	0.044	0.056	0.040	0.051	0.036	0.047	0.033	0.043	0.030
0.055	0.039	0.049	0.035	0.044	0.031	0.040	0.028	0.037	0.025	0.034	0.023
0.043	0.030	0.038	0.027	0.035	0.024	0.031	0.022	0.028	0.019	0.026	0.018
0.033	0.023	0.030	0.021	0.027	0.018	0.024	0.016	0.022	0.015	0.020	0.013
0.025	0.018	0.023	0.016	0.020	0.014	0.018	0.012	0.016	0.011	0.015	0.010
0.019	0.013	0.017	0.012	0.015	0.010	0.014	0.009	0.012	0.008	0.011	0.007
0.014	0.010	0.013	0.009	0.011	0.008	0.010	0.007	0.009	0.006	0.008	0.005
0.011	0.007	0.009	0.006	0.008	0.005	0.007	0.005	0.007	0.004	0.006	0.004
0.008	0.005	0.007	0.004	0.006	0.004	0.005	0.003	0.005	0.003	0.004	0.003
0.005	0.004	0.005	0.003	0.004	0.003	0.004	0.002	0.003	0.002	0.003	0.002
0.004	0.003	0.003	0.002	0.003	0.002	0.003	0.002	0.002	0.001	0.002	0.001
0.003	0.002	0.002	0.001	0.002	0.001	0.002	0.001	0.002	0.001	0.001	0.001
0.002	0.001	0.002	0.001	0.001	0.001	0.001	0.001	0.001	0.001	0.001	0.001
0.001	0.001	0.001	0.001	0.001	0.001	0.001	0.001	0.001	0.000	0.001	0.000
0.001	0.001	0.001	0.000	0.001	0.000	0.001	0.000	0.000		0.000	
0.001	0.000	0.000		0.000		0.000					
0.000											

THE METHANE ABSORPTION DISTRIBUTION IN THE 6190 Å BAND OVER THE DISK OF JUPITER

V.V. Avramchuk

ABSTRACT: The results of measurements of the methane absorption in the 6190 Å band along the disk of Jupiter are given. The data were taken from 52 spectrograms, which were obtained in 1964-66 with the aid of a 70-cm reflector ($F_{\text{eff}} = 30 \text{ m}$) with a diffraction spectrograph attached (dispersion of 30 Å/mm). It is shown that the value of the methane absorption for the center of the disk of Jupiter changed during different periods of observations. The greatest variations in intensity of absorption are found for longitudes of 190-320° (System 1). The equivalent widths W_p and depths R_p of the 6190 Å band are smaller for the edge zones of the Jupiter disk than for the center. The difference between the equivalent widths is 5-6 Å. The variations change substantially from the edges to the center.

One of the possible methods of investigating the structure and optical properties of the cloud cover of Jupiter is to study the variations in absorption in the methane bands over the disk of the planet and with respect to time. In the visible spectral region, the studies are carried out in the 6190 Å methane absorption band, and many authors have measured the intensity of this band. A large-scale study on the methane absorption over the disk of Jupiter was carried out recently at the Astrophysics Institute of the Academy of Sciences of the Kazakh S.S.R. It was shown in [1,2] that the intensity of the 6190 Å methane absorption band remained practically constant over the disk during all the observation periods, and only in the dark bands of Jupiter could a small increase in the equivalent widths of the 6190 Å CH_4 band be detected. One of the important earlier studies was that of Hess [3]. By Jupiter observations carried out in October of 1949, Hess found some variations in the latitudinal distribution of methane absorption, which he attributed to the changes in relative altitude of the cloud cover at different jovicentric latitudes. It follows that, in order to establish the real changes in the structure of the cloud cover of Jupiter, there must be more complete and, if possible, more accurate observational data on the distribution of molecular absorption over the disk of Jupiter. Observations of this type were carried out at the Main Astronomical Observatory of the Academy of Sciences of the Ukrainian SSR from 1964 to 1966.

OBSERVATIONS

Fifty-two spectrograms of Jupiter were obtained during the period from November of 1963 to August of 1966. The observations were carried out on the 70-cm reflector with Cassegrainian focus ($F_{\text{eff}} = 30$ m) with the aid of the diffraction spectrograph ASP-21 (dispersion of 30 Å/mm). The slit of the spectrograph was oriented along the central meridian and the equator of the planet. Moreover, a number of spectrograms of the south and north pole regions, as well as the east and west limbs, were obtained. The general characteristics of the observational data are given in the Appendix (Tables 1-3). The spectral width of the spectrograph slit was usually 4 Å. Many spectrograms were also obtained with a spectral width of the slit of 1 Å. It was suggested that these spectrograms be used not only to study the 6190 Å methane band, but also to measure the intensity of the ammonia band near 6450 Å. All the spectrograms were obtained on Kodak OaF photoplates. The type of emulsion of these plates is characterized by a high and rather uniform spectral sensitivity in a broad spectral region.

An important advantage of the Kodak plates is the extremely high uniformity of the background. An insignificant decrease in sensitivity near 6100-6200 Å was considered in analyzing the spectrograms. The exposures were for 7-10 minutes for spectral resolution of 4 Å, and 80-100 minutes for resolution of 1 Å.

To develop the plates, we used the D-19b developer and we achieved with it a negative contrast on the order of 1.5-2.0, while the linear segments of the characteristic curves encompassed a range of blackenings from 0.3 to 1.6-1.8.

The negatives were calibrated with the aid of the a nine-stage reducer. Particular attention was given to the equality of the exposures when obtaining the spectrograms of Jupiter and applying the reducer.

METHOD OF ANALYZING THE SPECTROGRAMS

The microphotometer MF-4 was used to analyze the spectrograms. The receiving slit of the microphotometer guaranteed both the requisite spectral resolution and resolution of details on the disk of the planet. Ordinarily the height of the slit allowed us to cut a detail on Jupiter into dimensions of 1.5".

Since we were interested in a detailed distribution of the equivalent widths of the 6190 Å band along the equator and central meridian of the planet, the photometric scanning of the spectrogram was carried out in such a way that a continuous change in the intensity of this band was obtained. For this, the slit of the microphotometer was moved along the equator and central meridian by the value of the height of the aperture of the microphotometer.

Depending on the angular dimensions of the planet disk, we obtained from 25 to 17 changes in the equivalent width and central intensity of the 6190 Å. The plates used in the range of the methane absorption band under study are characterized by some inconstancy in spectral sensitivity. This effect was considered in the following way. While recording the spectrograms of the planets, we also recorded the spectrograms of the electric bulb which was used for calibration and which also served as the standard for "tie-in" of the spectrograms of Jupiter. We then obtained the ratios $\frac{I_{\lambda_1 2t}}{I_{\lambda_1 st}}$,

where $I_{\lambda_1 2t}$ is the intensity at a certain wavelength of the

Jupiter spectrogram and $I_{\lambda_1 st}$ is the corresponding intensity of the standard. The intensities thus corrected could be used in order to construct the band contour and to determine its equivalent width W_b ; in this case, the possible decrease of the continuous spectrum due to the "crowding" of the spectral (Fraunhofer) lines was not considered. Moreover, we obtained an incorrect picture for the general intensity distribution in the range from 6000-6500 Å, since the maximum in the energy distribution in the spectrum of the bulb moved with respect to the maximum in the spectrum of the Sun.

In August of 1964 and October of 1966, we carried out a special study on the "tie-in" of our standards to the center of the solar disk. As would be expected, the curve expressing the development of the ratio I_{st}/I_{\odot} coincides with the wavelength for both periods, since the regime for supplying the bulbs remained unchanged. As a

result, the ratios $\frac{I_{\lambda_1 2t}}{I_{\lambda_1 st}}$ can be converted into the ratios $\frac{I_{\lambda_1 2t}}{I_{\lambda_1 \odot}}$,

and then the contours may be constructed and the equivalent width determined.

A comparison of the equivalent width of the 6190 Å band obtained for "tie-in" to the standard and to the Sun shows a systematic difference of 2-2.5 Å, where the equivalent widths were found to be smaller in the second case. They were also used as the final data.

The equivalent width and central intensities were calculated on the electronic computer "Primin".

EVALUATION OF ACCURACY OF THE RESULTS

The problem of evaluating the accuracy in determining the equivalent width of the molecular band is rather complex.

The fact is that, strictly speaking, the spectrograms obtained at different moments are not comparable for any given target. The changes in intensity of the band on several spectrograms for the same points on the disk may be due to actual processes, and not only to measurement errors. Moreover, substantial variations may also

occur in the distribution of molecular absorption on the disk itself. Nevertheless, we are compelled to use the spectrograms re-

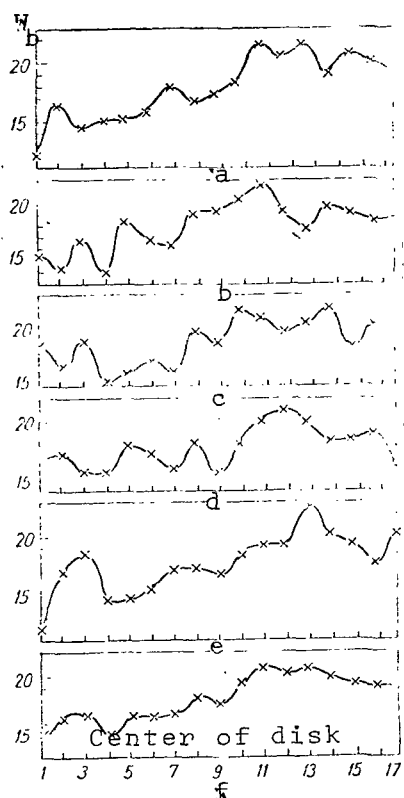


Fig. 1. Methane Absorption Distribution in the 6190 Å Band Along the Central Meridian on March 23-24, 1966. (a) UT 17^h13^m; (b) UT 17^h24^m; (c) UT 17^h38^m; (d) UT 17^h49^m; (e) UT 17^h58^m; (f) Average for the 5 Times).

each of the spectrograms. In this case, the calculations yield $\sigma = \pm 1.4 \text{ Å}$, which also characterizes the intrinsic accuracy of our results.

We should mention that some differences in the distribution of methane absorption along the central meridian are possible and realistic for the cited moments of observation. In any case, there are certain differences in the distribution of light and dark details on the disk of the planet, although the entire process of observation took around 50 min.

lating to different methods of observations of the same region of Jupiter in order to estimate the accuracy of the results. The spectrograms which are most suitable from this point of view are those obtained directly one after another, with short exposures. We use this method to evaluate the accuracy of our results.

In March of 1966, we obtained a number of spectrograms of Jupiter with short exposures ($t = 7 \text{ min}$) for orientation of the spectrograph slits along the central meridian. After analyzing them, we obtained the equivalent width W_b of the 6190 Å, and constructed the dependences of W_b on the jovicentric latitudes. The results are given in Figure 1. It is easy to see that the general nature of the distribution of W_b is identical for all the cited moments of observation. This permitted us to construct the averaged distribution curves for W_b along the central meridian, for a given period of observations, and to estimate the errors. The root-mean-square error in a single measurements of W_b was calculated according to the following formula:

$$\sigma^2 = \frac{\sum |v_i|^2}{\sum n_i - N},$$

where $|v_i|$ is the modulus of the deviation from the arithmetical mean, $\sum n_i$ is the total number of measurements of

It can be seen from Figure 1 that the northern latitudes are

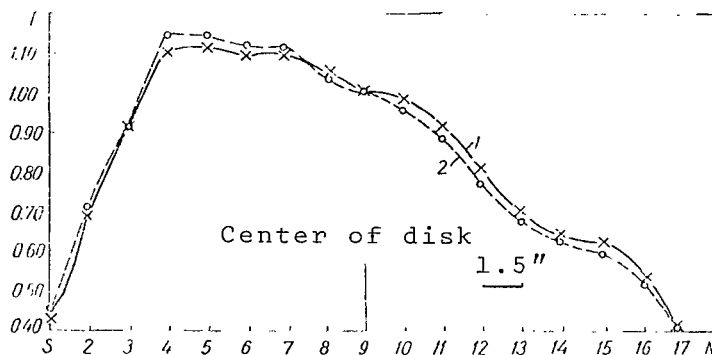


Fig. 2. Brightness Distribution Along the Central Meridian on March 23-24, 1966. (1) At the Center of the 6190 Å Band; (2) Outside the 6050 Å Band.

characterized during the given observation period by stronger absorption than are the southern latitudes. The difference in absorption is 3-4 Å for the cited latitudes. It is important that the northern part of the disk is much darker than the south (Fig. 2). This indicates that there is a direct relationship between the distribution of the dark substance and the intensity of the methane absorption band: the dark regions are characterized by stronger absorption.

The difference in brightness distribution along the central meridian at the center of the absorption band (6190 Å) and outside the bands (6050 Å) is represented in Figure 2.

RESULTS OF THE OBSERVATIONS

The equivalent widths W_D and depths R_D of the 6190 Å methane absorption band which were obtained from an analysis of the spectrograms of Jupiter are given in this study (Tables 1, 2 of the Appendix). The spectrograms were obtained for orientation of the spectrograph slit both along the central meridian and along the equator of the planets. Moreover, a number of spectrograms of the limb zones of the Jupiter disk was obtained. The results of an analysis of these spectrograms are given in Table 3 of the Appendix.

Numerous light and dark details are observed on the spectrograms obtained for orientation of the spectrograph slit along the central meridian. A description is given in Table 1 of the Appendix. Some of these details were identified as "continuous" light zones and dark bands of the visible surface of Jupiter, but this identification may not be accurate in some cases, since we could not obtain direct photographs of the entire disk of the planet in a parallel manner.

In the case of orientation of the slit along the equator of Jupiter, a description of the individual details is not given. This can be explained by the fact that, although the equatorial zone has a complex structure in individual cases, it nevertheless generally has much fewer details than the direction along the central meridian.

Let us discuss the characteristics of the results obtained in more detail.

First of all, let us mention that the value for the methane absorption for the central part of the Jupiter disk shows substantial changes from one observation period to another. Thus, the equivalent width W_b of the 6190 Å band was 17-19 Å in February and August 1964, in March and August of 1966 and during certain other observation periods. An increase in the methane absorption was observed in January and February 1965. The equivalent width of the 6190 Å band for the central part of the Jupiter disk was 23-25 Å during this period. The changes in intensity of the methane band were insignificant for closely-spaced observation times (from day to day), 1-2 Å in equivalent width.

We have still not found a mechanism which might explain the changes observed in the values for methane absorption. However, we can mention a number of causes which might bring about this effect. As was indicated in [1], one of them could be a change in linear thickness of the purely gaseous layer above the clouds due to a change in the effective upper boundary of the cloud layer of Jupiter.

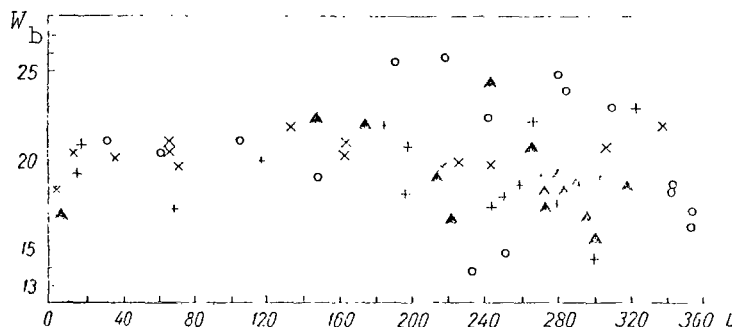


Fig. 3. Longitudinal Distribution of Methane Absorption for the Center of the Jupiter Disk. (+) Observations of 1960 (Data Taken from [1]); (X) Observations of 1964; (O) Observations of 1965; (Δ) Observations of 1966.

The vertical movements of the boundary layer of the cloud may be due to the level of convection, i.e., the maximum level to which the ascending motions of the gas can penetrate for a certain region

of the planet. In other words, the circulation processes in the Jupiter atmosphere may be caused by certain local sources distributed by longitude which have definite activity. Therefore, we must determine whether the oscillations observed in the intensity of methane absorption are characteristic of all the longitudes or if they occur more frequently for completely defined regions of the planet. To answer this question, we constructed the longitudinal distribution of methane absorption and its change for different observation periods.

As can be seen from Figure 3, this distribution shows a number of interesting characteristics. The greatest variations in intensity of methane absorption are observed in the range of longitudes of $190-320^\circ$ (system 1). During single observation periods, the equivalent width of the 6190 \AA band changed at the longitudes from $14-15$ to $25-26 \text{ \AA}$. Other longitudes are characterized by much smaller variations in intensity of methane absorption during the entire observation periods.

It can be assumed that these differences may be explained in terms of the varying intensity of the circulation processes in the Jupiter atmosphere at different longitudes.

The intensity distribution of the 6190 \AA methane band over the disk of Jupiter has been studied by many authors. A review of the early studies can be found in [3] of Hess. It is indicated in all these studies that there are no CH_4 variations. Although his observations were not numerous, Hess himself found that the 6190 \AA methane band is somewhat diminished around the west and east limbs near the equatorial region and much more diminished during a transition from the equatorial regions to the middle latitudes.

V.G. Teyfel' [1] did not find a substantial change in the 6190 \AA band along the equator with his much greater number of spectra but narrower dispersion than that of Hess. Although the latitudinal distributions showed some particular characteristics, the deviations were smaller than those which Hess found. However, Munch and Younkin [4] found, with the aid of a photoelectric spectrometer, that the 6190 \AA band somewhat decreases in intensity along the equator from the center to the edge. It is difficult to establish a quantitative agreement between these results and those of other authors, since the authors cited did not publish numerical results for their measurements.

Thus, there are discrepancies in the results of individual authors. A detailed study of the distribution of methane absorption in the 6190 \AA band along the central meridian and the equator of the planet was therefore carried out according to all the spectrograms obtained (see the Appendix).

Considering our results, it can be assumed that the nature of

an absorption distribution in the 6190 Å band both along the central meridian and along the equator changes substantially from one observation period to another. Almost all of the observations which were carried out in January-February of 1965 show a gradual decrease in equivalent width of the 6190 Å band around the edges of the planet disk (Fig. 4). Other observation periods are characterized by a less pronounced decrease in intensity of methane absorption around the edges of the Jupiter disk, but the values of W_b of the 6190 Å band are lower for the edge zone than for the center of the disk of the planet in this case, as a rule. The final average data for the central and edge zones are given in the Tables.

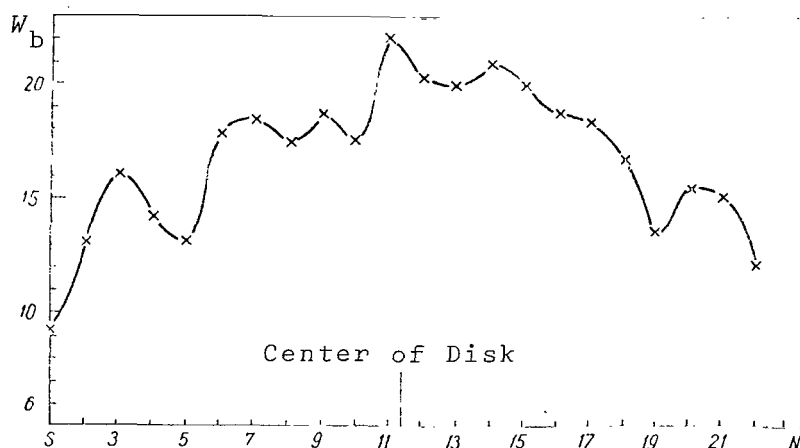


Fig. 4. Absorption Distribution in the 6190 Å Methane Band Along the Central Meridian on January 16-17, 1965. (UT18^h25^m).

Zone	W_b , Å	R_b	No. of Measurements
S-polar region	14.8	0.163	50
S-tropical dark band	20.9	0.221	46
Equatorial light zone	20.3	0.211	45
N-tropical dark band	19.2	0.202	51
N-polar regions	15.7	0.171	55
Western Limb	14.8	0.162	28
Eastern Limb	16.4	0.176	32

The photographic edge effects obviously do not play a significant role in determining the equivalent widths of outer bands, since the spectrograms obtained especially for the edge zones of the Jupiter disk with normal densities also gives less equivalent widths, compared to the center of the disk.

The variations from center to edge are shown in Figures 5 and 6 for all the observation periods.

Since a quantitative interpretation of the results obtained will be given in a separate study, we will discuss only some general concepts.

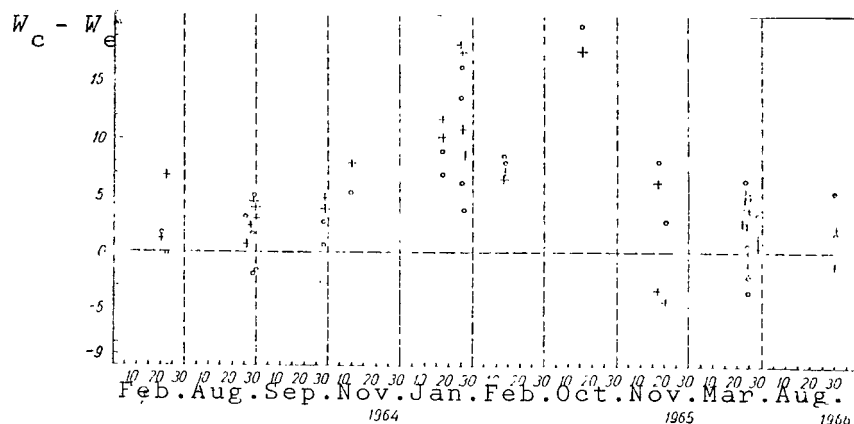


Fig. 5. Variations of $W_c - W_e$. (+) Center, S-Polar Region; o - Center, N-Polar Region.

Several hypotheses have been suggested to explain the small variations between the center and the edges. We have already mentioned one of them, proposed by Hess [3]. V.G. Teyfel' [2] suggested the following hypothesis in order to explain the constancy in intensity of the CH_4 absorption band on the disk of Jupiter: the real methane absorption occurs not only in the purely gaseous layer of the Jupiter atmosphere above the cloud cover, but also in the cloud layer itself.

However, as our observations show, the variations from center to edge are of a much more complex nature for the absorption in the 6190 Å band than was assumed before. The value of $W_c - W_e$ can change from one observation period to another.

It seems to us that the hypothesis of multiple scattering proposed by V.V. Sharonov [5] is the most natural explanation for our results. According to this hypothesis, the absorption lines are formed in the cloud layer during multiple scattering. In this case, the depths to which the quanta penetrate near the edge of the disk is less than for perpendicular incidence, which brings about a decrease of the absorption bands. Moreover, the upper boundary of the cloud layer may have a complex "relief", which should have a substantial effect on the observed variations from the center to the edge.

As can be seen from the table, differences have not been established in the value for methane absorption for the light equatorial

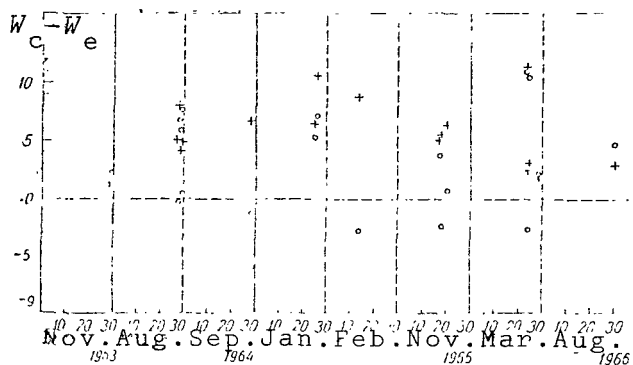


Fig. 6. Variations of $W_C - W_e$. (+ -Center, Western Limb; O -Center, Eastern Limb).

band and the dark tropical band. Obviously, there is reason to speak only of a connection between the intensity of methane absorption and the general distribution of dark matter over the disk of the planet.

REFERENCES

1. Teyfel', V.G. and N.V. Priboyeva: Izvest. Akad. Nauk Kaz. S.S.R., seriya Fiz.-Mat. Nauk, Vol. 1, 1963.
2. Teyfel', V.G.: Astron. Tsirk., Vol. 296, 1964.
3. Hess, S.L. Astrophys. J., Vol. 118, No. 1, 1953.
4. Munch, G. and R.L. Younkin: Astron. J., Vol. 69, p. 553, 1964.
5. Sharonov, V.V.: In the book: Priroda planet (The Nature of the Planets). Moscow, "Fizmatgiz", 1958.

APPENDIX

TABLE 1 DISTRIBUTION OF METHANE ABSORPTION IN THE 6190 Å BAND ALONG THE CENTRAL MERIDIAN

No.	Characteristics of Details	Identification with "Constant" Formations	$W_D, \text{\AA}$	R_D
1964 February 20-21, UT 17 ^h 53 ^m ($L_I = 280.6^\circ$, $L_{II} = 120.3^\circ$)				
1.	S-Polar Region		16.4	0.180
2.	Dark Region		17.1	0.169
3.	Dark Region		12.0	0.170
4.	Light Band		11.8	0.139
5.	Light Band		14.6	0.173
6.	Light Band		14.8	0.152
7.	Light Band		14.9	0.175
8.	Dark Detail of Preceding Light Band		16.1	0.175
9.	Light Band		15.7	0.180
10.	Dark Band			
11.	Dark Band	S Tropical Dark Band	16.5	0.185
12.	Dark, Clearly Distinguishable Band		17.7	0.185
			18.5	0.180
13.	Light Band. Very Weak	Equatorial Zone	15.5	0.162
14.	Dark Band. Small Duplication with Preceding Light Band		17.9	0.185
15.	Dark Band (Darkness on Disk)	N Tropical Dark Band	16.8	0.182
16.	Light, Clearly Distinguishable Band		14.7	0.163
17.	Same		12.3	0.159
18.	Dark Region		12.8	0.162
19.	Dark Region		14.2	0.155
20.	Polar Region		13.5	0.160
21.	N-Polar Region		16.3	0.200
February 21-22 UT 16 ^h 15 ^m ($L_I = 18.5^\circ$, $L_{II} = 211.4^\circ$)				
1.	S-Polar Region		14.2	0.179
2.	Dark, Clearly Distinguishable band		17.3	0.188
3.	Light Detail		18.0	0.200
4.	Light Region		18.5	0.229
5.	Darker Detail of Light Region		20.2	0.238
6.	Beginning of Wide Light Band		17.0	0.222
7.	Light Band		16.5	0.230
8.	Darker Detail of Light Band		18.1	0.239
9.	Light Band		18.0	0.228
10.	Light Band		18.7	0.200

CONTINUATION OF TABLE 1

No.	Characteristics of Details	Identification with "Constant" Formations	$W_D, \text{\AA}$	R_D
11.	Beginning of Wide Dark Region		19.2	0.242
12.	Dark Region		20.9	0.232
13.	Same		19.2	0.231
14.	Light Sharp Band		19.9	0.229
15.	Light Sharp Band		15.8	0.181
16.	Dark Band		18.2	0.179
17.	Light Sharp Band		16.2	0.180
18.	Dark Region		16.8	0.202
19.	Dark Region		16.2	0.210
20.	Dark Region		17.5	0.203
21.	N-Polar Region		17.1	0.198
22.	N-Polar Region		14.8	0.199
23.	N-Polar Region		21.0	0.241

August 26-27 UT 23h15m ($L_I = 250.2^\circ$, $L_{II} = 94.0^\circ$)

1.	S-Polar Region		17.3	0.209
2.	Light Band		20.1	0.205
3.	Light Band		22.3	0.208
4.	Dark Band		20.3	0.219
5.	Superposition of Dark and Following Light Bands		19.2	0.220
6.	Light Sharp Band		19.3	0.199
7.	Superposition of Preceding Band and Following Dark Wide Bands	S Tropical Dark Band	18.7	0.205
8.	Dark Band		17.6	0.212
9.	Light Band Hinted		22.1	0.222
10.	Light Band (Center)		17.9	0.213
11.	Darker Segment of Preceding Light Band	Equatorial Light Zone	18.1	0.185
12.	Dark Band		19.9	0.218
13.	Dark Band	N Tropical Dark Band	19.3	0.205
14.	Dark Band		18.8	0.211
15.	Light Sharp Band		18.2	0.202
16.	Darker Segment of Preceding Band		18.8	0.215
17.	Dark Region		17.9	0.212
18.	Lighter Detail in Dark Regions		19.5	0.199
19.	Dark Region		19.4	0.205
20.	N-Polar Region		17.8	0.182
21.	N-Polar Region		14.9	0.159

August 28-29 UT 00h17m ($L_I = 243.7^\circ$, $L_{II} = 72.0^\circ$)

1.	S-Polar Region
----	----------------

CONTINUATION OF TABLE 1

No.	Characteristics of Details	Identification with "Constant" Formations	$W_b, \text{\AA}$	R_b
2.	Dark Region		14.8	0.195
3.	Dark Region		17.6	0.182
4.	Light Band		18.3	0.192
5.	Dark Detail in Light Band		17.2	0.204
6.	Light Band		17.6	0.185
7.	Light Band		16.6	0.198
8.	Light Band	S Tropical	18.2	0.196
9.	Dark Band	Dark Band	16.4	0.202
10.	Light Band in Wide Dark Region	Equatorial Light Zone	16.8	0.192
11.	Same		17.6	0.208
12.	Superposition of Previous Light Band and Dark Region	N Tropical Dark Band	16.7	0.186
13.	Dark Band		17.4	0.194
14.	Light Sharp Band		16.7	0.196
15.	Same		16.0	0.179
16.	Dark Region		14.1	0.184
17.	Dark Region		15.2	0.180
18.	Light Detail		17.5	0.186
19.	Dark Band		18.1	0.193
20.	Superposition of Light Band and Following Dark Region		18.6	0.188
			19.3	0.185
21.	N-Polar Region			
22.	N-Polar Region			

August 28-29 UT 01^h02^m ($L_I = 271.2^\circ$, $L_{II} = 99.2^\circ$)

1.	S-Polar Region		14.6	0.160
2.	Light Band in Polar Region		15.8	0.166
3.	Dark Detail		16.8	0.182
4.	Light Sharp Band		15.6	0.176
5.	Same		17.2	0.200
6.	Dark Band		17.1	0.194
7.	Light, Clearly Distinguishable Band		19.8	0.188
8.	Lightest Detail on Disk		16.4	0.184
9.	Light Band		16.9	0.200
10.	Dark Band		18.6	0.196
11.	Center of Dark Band	S Tropical Dark Band	19.1	0.204
12.	Dark Band		18.0	0.172
13.	Light, Clearly Distinguishable Band	Equatorial Light Zone	19.2	0.212
14.	Superposition of Preceding Light and Following Dark Bands	N Tropical Dark Band	18.8	0.197
15.	Dark Band		17.2	0.177
16.	Dark Band (Its Darkest Segments)		19.2	0.196

CONTINUATION OF TABLE 1

No.	Characteristics of Details	Identification with "Constant" Formations	$W_b, \text{\AA}$	R_b
17.	Very Light Band		18.3	0.193
18.	Light Band		16.1	0.178
19.	Dark Region		17.6	0.180
20.	Dark Region		17.5	0.196
21.	Dark Region		15.8	0.178
22.	Dark Region		17.5	0.188
23.	Superposition of Light Band and Following Light Region		15.5	0.178
24.	N-Polar Region		19.1	0.192
25.	N-Polar Region		17.5	0.180

August 29-30 UT 23^h33^m ($L_I = 14.9^\circ$, $L = 195.7^\circ$)

1.	S-Polar		16.3	0.177
2.	S-Polar Region		17.2	0.193
3.	Dark Region		19.2	0.190
4.	Light Band		17.7	0.195
5.	Darker Region		17.4	0.198
6.	Same		18.0	0.200
7.	Same		18.8	0.198
8.	Light, Clearly Distinguishable Band		19.8	0.204
9.	Light, Clearly Distinguishable Band		20.8	0.209
10.	Dark Band	}	19.4	0.205
11.	Dark Band		22.7	0.216
12.	Light Band	}	20.0	0.216
13.	Superposition of Light and Following Dark Bands		19.3	0.208
14.	Dark Band		21.0	0.229
15.	Light Band		18.8	0.203
16.	Dark Detail in Light Band		18.8	0.204
17.	Light Band		17.3	0.194
18.	Light Band		18.3	0.202
19.	Light Band		17.5	0.183
20.	Dark Region		18.7	0.202
21.	Dark Region		20.0	0.259
22.	Dark Region		18.2	0.206
23.	Dark Region		19.5	0.202
24.--	(defect)			
25.	N-Polar Region		14.6	0.168

August 20-30 UT 01^h02^m ($L_I = 69.1$, $L = 249.5$)

1.	S-Polar Region		13.1	0.141
----	----------------	--	------	-------

CONTINUATION OF TABLE 1

No.	Characteristics of Details	Identification with "Constant" Formations	$W_D, \text{\AA}$	R_D
2.	Dark Region		14.6	0.175
3.	Dark Region		18.1	0.191
4.	Dark Region		15.3	0.186
5.	Light Band		15.4	0.186
6.	Dark Band		15.4	0.176
7.	Light Band		16.3	0.182
8.	Dark Detail in Light Band		15.3	0.185
9.	Light Band		14.7	0.171
10.	Dark Band		14.6	0.190
11.	Dark Band (Insignificant Overlapping with Following Light Band)	S Tropical Dark Band	18.2	0.198
12.	Light Band		15.9	0.184
13.	Light Band	Equatorial Light Zone	17.3	0.189
14.	Dark Band	N Tropical	17.4	0.191
15.	Overlapping of Dark and Light Bands	Dark Band	15.2	0.174
16.	Lightest Band on Disk		16.9	0.188
17.	Same		14.4	0.161
18.	Somewhat Darker Site Than Preceding Light Band		13.2	0.180
19.	Same		14.0	0.177
20.	Same		16.8	0.192
21.	Dark Band		19.4	0.200
22.	Light Detail		17.5	0.194
23.	Dark Region		18.9	0.183
24.	-		-	-
25.	N-Polar Region		-	-

September 27-28 UT 21^h04^m ($L_I = 184.8^\circ$, $L_{II} = 145.1$)

1.	S-Polar Region		17.2	0.205
2.	Dark Region		16.2	0.182
3.	Light Band		16.5	0.175
4.	Light Band (Somewhat Lighter)		18.7	0.206
5.	Dark Detail in Light Band		16.9	0.194
6.	Light Band		18.1	0.199
7.	Lightest Detail on Disk, Con- sisting of Two Component Details		21.1	0.210
8.	Light Band		21.7	0.215
9.	Dark Band		21.2	0.208
10.	Dark Band	S Tropical Dark Band	21.8	0.226
11.	Light Band		22.0	0.217
12.	Light Band (Lightest Segment)	Equatorial Light Zone	20.7	0.220

CONTINUATION OF TABLE 1

No.	Characteristics of Details	Identification with "Constant" Formations	$W_D, \text{\AA}$	R_D
13.	Dark Band (Insignificant Overlapping with Preceding Detail) }	N Tropical Dark Band	21.0	0.209
14.	Dark Band		17.2	0.202
15.	Light Band		17.4	0.185
16.	-		-	0.180
17.	Light Region		17.9	0.174
18.	Light Region		15.9	0.180
19.	Dark Region		16.6	0.210
20.	N-Polar Region		21.3	0.227
21.	N-Polar Region		-	-

September 27-28 UT 23^h19^m ($L_I = 267.1^\circ$, $L_{II} = 225.7^\circ$)

1.	S-Polar Region		18.3	0.188
2.	S-Polar Region		17.0	0.211
3.	Light Region		17.6	0.184
4.	Light Band		18.5	0.198
5.	Dark Detail in Light Band		19.4	0.199
6.	Light Band		20.1	0.213
7.	Lightest Detail on Disk		21.3	0.206
8.	Light Band		21.5	0.221
9.	Dark Band		21.2	0.226
10.	Dark Band		23.0	0.210
11.	Overlapping of Dark Band and Trace of Light Band }	S Tropical Dark Band	21.7	0.218
12.	Light Band		22.7	0.214
13.	Light Band (Darker Segment) }	Equatorial Light Zone	17.6	0.212
14.	Dark Band		20.0	0.206
15.	Dark Band	N Tropical Dark Band	19.9	0.214
16.	Light Band		17.2	0.193
17.	Light, Clearly Distinguishable Band		18.2	0.198
18.	Light Band (Darker Segment)		18.0	0.191
19.	Dark Region		19.1	0.210
20.	N-Polar Region		19.4	0.207

November 8-9 UT 18^h35^m ($L_I = 260.1^\circ$, $L_{II} = 251.7^\circ$)

1.	S-Polar Region		10.8	0.130
2.			12.0	0.145
3.			14.0	0.161
4.			14.5	0.182
5.			14.7	0.180
6.			17.1	0.188

CONTINUATION OF TABLE 1

No.	Characteristics of Details	Identification with "Constant Formations	$W_{b,A}$	R_b
7.			16.1	0.180
8.			16.8	0.182
9.			17.2	0.188
10.			19.1	0.211
11.			19.0	0.208
12.	Dark Wide Band	} S Tropical	18.9	0.209
13.	Dark Wide Band		18.4	0.216
14.	Light Band	} Equatorial	[illegible]	
15.	Light Band (Center)		18.6	0.208
16.	Light Band	} Light Band	19.0	0.198
17.	Dark Band		17.3	0.182
18.	Dark Band	} N Tropical	15.8	0.178
19.	Dark Band		13.0	0.155
20.	Light Band		14.6	0.154
21.	Light Band		14.7	0.162
22.	Dark Region		13.0	0.168
23.	N-Polar Region		13.5	0.177
24.	N-Polar Region		13.4	0.167

January 16-17 UT 18^h25^m ($L_I = 342.8$, $L_{II} = 177.0^\circ$)

1.	S-Polar Region		8.2	0.102
2.	S-Polar Region		14.7	0.150
3.	Light Band		15.9	0.176
4.	Light Band		12.5	0.168
5.	Dark Detail		17.9	0.198
6.	Light Band		19.3	0.200
7.	Overlapping of Dark and Following		17.9	0.196
	Dark Bands	} S Tropical		
8.	Dark Band		18.0	0.184
9.	Dark Band	} Dark Band	16.4	0.183
10.	Light Band		20.8	0.190
11.	Light Band	} Equatorial	17.1	0.185
12.	Dark Region		12.7	0.182
13.	Dark Region	} N Tropical	16.1	0.171
14.	Dark Region		13.8	0.1148
15.	Light Band		12.6	0.142
16.	Light Band		11.9	0.126
17.	N-Polar Region		11.2	0.120
18.	N-Polar Region		11.5	0.114

January 16-17 UT 19^h44^m ($L_I = 31.0^\circ$, $L_{II} = 177.0^\circ$)

1.	S-Polar Region	9.2	0.090
2.	S-Polar Region	13.0	0.138

CONTINUATION OF TABLE 1

No.	Characteristics of Details	Identification with "Constant" Formations	$W_B, \text{\AA}$	R_B
3.	Light Band		16.0	0.174
4.	Light Band		14.2	0.166
5.	Light Band		13.0	0.170
6.	Dark Detail in Light Band		17.8	0.181
7.	Light Band		18.4	0.185
8.	Light Band		17.4	0.180
9.	Dark Band		18.7	0.200
10.	Dark Band	S Tropical Dark Band	17.5	0.194
11.	Dark Band (Overlapping with Following Light Band)		22.0	0.212
12.	Light Band	Equatorial Light Zone	20.2	0.204
13.	Light Band (Overlapping with Following Dark Band)		19.9	0.198
14.	Dark Band	N Tropical Dark Band	20.8	0.204
15.	Dark Band		19.8	0.208
16.	Dark Band		18.7	0.184
17.	Overlapping of Dark and Following Light Bands		18.3	0.190
18.	Light Band		16.6	0.168
19.	Light Band		13.4	0.146
20.	N-Polar Region		15.4	0.150
21.	N-Polar Region		15.0	0.148
22.	N-Polar Region		12.0	0.115

January 24-25 UT 16^h47^m ($L_I = 105.2^\circ$, $L_{II} = 239.0^\circ$)

1.	S-Polar Region		8.1	0.116
2.	S-Polar Region		12.7	0.157
3.	S-Polar Region		15.5	0.186
4.	Light Band		17.2	0.182
5.	Dark Band (Overlapping with Preceding Light Band)		22.4	0.204
6.	Light Band		21.8	0.224
7.	Dark Band		26.7	0.248
8.	Light Band		28.0	0.262
9.	Light Band (Overlapping Somewhat with Following Dark Band)		23.4	0.248
10.	Dark Band	S Tropical Dark Band	17.4	0.250
11.	Dark Band		22.1	0.220
12.	Overlapping of Dark and Following Light Bands		20.8	0.193
13.	Light Band	Equatorial Light Zone	18.5	0.196
14.	Light Band (Overlapping with Following Dark Band)		19.8	0.206

CONTINUATION OF TABLE 1

No.	Characteristics of Details	Identification with "Constant" Formations	$W_b, \text{\AA}$	R_b
15.	Dark Band	} N Tropical Dark Band	18.2	0.200
16.	Dark Band		21.9	0.207
17.	Dark Band		19.0	0.203
18.	Light Band		16.3	0.187
19.	Light Band		13.1	0.166
20.	Overlapping of Light and Following Dark Band		14.1	0.162
21.	Dark Band		15.8	0.168
22.	Light Band		11.5	0.149
23.	N-Polar Region		9.3	0.140

January 24-25 UT 17^h55^m ($L_I = 146.7$, $L_{II} = 280.1^\circ$)

1.	S-Polar Region		9.1	0.121
2.	S-Polar Region		11.8	0.126
3.	Overlapping of Dark and Light Bands		13.8	0.168
4.	Light Band		15.8	0.172
5.	Dark Detail in Light Band		15.6	0.172
6.	Same		18.4	0.179
7.	Light Band		23.2	0.200
8.	Overlapping of Dark and Following Light Bands		20.4	0.203
9.	Light Band		20.6	0.210
10.	Dark Detail Seems to be Hinted at.		19.5	0.186
11.	Light Band		21.3	0.204
12.	Light Band		17.1	0.182
13.	Overlapping of Light and Following Dark (Wide) Band		15.9	0.178
14.	Dark Band	} N Tropical Dark Band	17.5	0.190
15.	Dark Band		14.6	0.180
16.	Dark Band		15.2	0.180
17.	Overlapping of Dark and Following Light Bands		13.9	0.152
18.	Light Band		15.0	0.168
19.	Dark Band		14.0	0.146
20.	Light Band		11.5	0.135
21.	N-Polar Region		11.2	0.154
22.	N-Polar Region		12.9	0.144

January 24-25 UT 19^h06^m ($L_I = 190.0^\circ$, $L_{II} = 322.7^\circ$)

1.	S-Polar Region		7.6	0.108
2.	S-Polar Region		12.8	0.142
3.	Light Band		14.8	0.166
4.	Light Band		16.9	0.176

CONTINUATION OF TABLE 1

No.	Characteristics of Details	Identification with "Constant" Formations	$W_b, \text{\AA}$	R_b
5.	Dark Detail in Light Band		20.9	0.202
6.	Dark Band		24.2	0.236
7.	Dark Band		28.7	0.261
8.	Light Sharp Band		25.5	0.256
9.	Dark Band		26.6	0.250
10.	Dark Band	S Tropical Dark Band	27.9	0.274
11.	Dark Band		27.9	0.270
12.	Dark Band (Overlapping with Following Light Band)			
13.	Light Band	Equatorial Light Band	25.5	0.236
14.	Light Band		27.0	0.251
15.	Overlapping of Light and Following Dark Bands)		24.2	0.224
16.	Dark Band	N Tropical Dark Band	17.0	0.191
17.	Dark Band		16.9	0.190
18.	Overlapping of Dark and Following Light Bands		17.9	0.203
19.	Light Band		15.1	0.188
20.	Light Band (Overlapping with Following Dark Band)		14.8	0.172
21.	Dark Band		14.4	0.171
22.	Dark Band		14.7	0.158
23.	N-Polar Region		13.8	0.174
24.	N-Polar Region		11.3	0.134
25.	N-Polar Region		11.9	0.144

January 25-26 UT 19^h14^m ($L_I = 352.6$, $L_{II} = 118.0^\circ$)

1.	S-Polar Region		7.8	0.101
2.	S-Polar Region		10.2	0.133
3.	S-Polar Region		11.0	0.122
4.	Light Band		16.6	0.146
5.	Light Band		16.4	0.168
6.	Dark Detail in Light Band		16.7	0.174
7.	Light Band		17.9	0.177
8.	Light Band		19.6	0.192
9.	Dark Band		19.8	0.188
10.	Dark Band	S Tropical Dark Band	17.8	0.180
11.	Overlapping of Dark and Following Light Bands		16.8	0.182
12.	Light Band		16.1	0.178
13.	Light Band (Overlapping with Following Dark Band)	Equatorial Light Band	19.0	0.181
14.	Dark Band		17.4	0.197
15.	Dark Band		16.2	0.182
16.	Dark Band	N Tropical Dark Band	17.4	0.180

CONTINUATION OF TABLE 1

No.	Characteristics of Details	Identification with "Constant" Formations	$W_b, \text{\AA}$	R_b
17.	Light Band		17.2	0.162
18.	Light Band		13.6	0.168
19.	Dark Sharp Detail		13.0	0.158
20.	Light Band		12.8	0.150
21.	Light Band		11.4	0.141
22.	N-Polar Region		12.5	0.160
23.	N-Polar Region		-	-

February 12-13 UT 16^h38^m ($L_I = 216.7^\circ$, $L_{II} = 205.6^\circ$)

1.	S-Polar Region		18.9	0.193
2.	S-Polar Region		16.6	0.169
3.	Light Band		18.8	0.212
4.	Light Band		21.6	0.206
5.	Light Band		24.2	0.241
6.	Dark Band		24.0	0.252
7.	Light, Clearly Distinguishable Band		24.6	0.245
8.	Same		25.6	0.248
9.	Dark Band	S Tropical Dark Band	24.4	0.245
10.	Dark Band (Center)		23.8	0.251
11.	Dark Band		23.7	0.248
12.	Light Band	Equatorial Light Band	26.5	0.264
13.	Light Band (Overlapping with Following Dark Band)		25.0	0.255
14.	Dark Band	N Tropical Dark Band	26.2	0.255
15.	Dark Band		25.8	0.254
16.	Dark Band (Overlapping with Following Light Band)		22.8	0.238
17.	Light Band		23.1	0.226
18.	Dark Abrupt Band		23.6	0.224
19.	Light Band		22.0	0.218
20.	Overlapping of Preceding Band with Following Dark Band		22.2	0.223
21.	Dark Band		21.6	0.218
22.	Dark Band		22.2	0.212
23.	Light Detail in Polar Region		19.4	0.205
24.	N-Polar Region		17.2	0.184
25.	N-Polar Region		-	-

February 12-13 UT 18^h22^m ($L_I = 280.2^\circ$, $L_{II} = 268.4^\circ$)

1.	S-Polar Region		17.5	0.168
2.	Light Band		14.8	0.160
3.	Light Band		18.0	0.192

CONTINUATION OF TABLE 1

No.	Characteristics of Details	Identification with "Constant" Formations	$W_b, \text{\AA}$	R_b
4.	Dark Band		16.6	0.187
5.	Dark Band		19.2	0.200
6.	Light Band		19.9	0.212
7.	Light Band (Center)		20.4	0.203
8.	Light Band		20.3	0.212
9.	Overlapping of Light and Following Dark Bands		23.8	0.239
10.	Dark Band	S Tropical Dark Band Equatorial Light Band N Tropical Dark Band	22.0	0.226
11.	Dark Band (Slight Overlapping with Following Light Band)		25.2	0.218
12.	Light Band		24.8	0.247
13.	Light Band		24.0	0.236
14.	Overlapping of Light Band and Following Dark Bands		25.2	0.240
15.	Dark Band		21.2	0.221
16.	Light Band		21.7	0.226
17.	Light Band		20.0	0.223
18.	Overlapping of Light Band and Dark Region		21.9	0.221
19.	Dark Region		22.4	0.222
20.	Dark Region		20.0	0.202
21.	N-Polar Region		17.2	0.171
22.	N-Polar Region		16.8	0.186
23.	N-Polar Region		-	-

October 14-15 UT 20^h45^m ($L_I = 176.6^\circ$, $L_{II} = 109.5^\circ$)

1.	S-Polar Region		9.7	0.113
2.	Dark Detail		10.9	0.128
3.	Overlapping of Preceding Detail with Light Band		13.9	0.160
4.	Light Band		13.7	0.188
5.	Light Band		19.7	0.197
6.	Light Band		22.2	0.216
7.	Overlapping of Light and Light Band		25.5	0.245
8.	Dark Band	S Tropical Dark Band	23.8	0.230
9.	Dark Band		25.7	0.258
10.	Dark Band (Overlapping with Following Light Band)		31.9	0.290
11.	Light Band	Equatorial Light Band	28.5	0.266
12.	Superposition of Light Band with Following Dark Band		27.2	0.270
13.	Dark Band	N Tropical Dark Band	28.0	0.252
14.	Dark Band		28.0	0.246

CONTINUATION OF TABLE 1

No.	Characteristics of Details	Identification with "Constant" Formations	$W_b, \text{\AA}$	R_b
15.	Light Band		25.9	0.248
16.	Light Band		23.6	0.190
17.	Light Band		22.4	0.222
18.	Light Band		21.1	0.200
19.	Light Band		17.1	0.183
20.	Light Band (Overlapping with Darker Regions)		16.2	0.171
21.	Dark Regions		15.8	0.167
22.	Dark Region		13.6	0.148
23.	N-Polar Region		9.0	0.107
24.	N-Polar Region		7.5	0.103

November 16-17 UT 00^h20^m ($L_I = 284.8^\circ$, $L_{II} = 317.5^\circ$)

1.	S-Polar Region		17.6	0.183
2.	Dark Band		14.9	0.180
3.	Dark Band		16.7	0.191
4.	Overlapping of Dark and Following Light Band		20.1	0.201
5.	Light Band		18.7	0.217
6.	Dark Detail		19.0	0.210
7.	Light Band		20.7	0.214
8.	Light Band		25.2	0.244
9.	Dark Band	S Tropical Dark Band	23.3	0.230
10.	Light Band	Equatorial Light Band	20.0	0.223
11.	Light Band		21.9	0.240
12.	Light Band (Central Segment)		22.6	0.237
13.	Light Band (Darker Segment)		26.6	0.256
14.	Light Band	N Tropical Dark Band	24.5	0.242
15.	Dark Band		23.5	0.235
16.	Dark Band		20.1	0.216
17.	Dark Band		18.1	0.199
18.	Light Detail in Dark Band		17.0	0.195
19.	Light Band		18.0	0.188
20.	Dark Abrupt Band		14.4	0.160
21.	Light Band		12.4	0.152
22.	Dark Region		14.8	0.164
23.	N-Polar Region		15.4	0.178
24.	N-Polar Region		15.9	0.178

November 16-17 UT 02^h22^m ($L_I = 353.7^\circ$, $L_{II} = 25.8^\circ$)

1.	S-Polar Region		19.6	0.207
2.	Dark Region		21.3	0.208

CONTINUATION OF TABLE 1

No.	Characteristics of Details	Identification with "Constant" Formations	$W_b, \text{\AA}$	R_b
3.	Light Band		16.4	0.178
4.	Light Band		17.8	0.181
5.	Darker Band		17.1	0.181
6.	Light Detail		13.9	0.168
7.	Same		15.4	0.189
8.	Dark Band	S Tropical Dark Band	16.6	0.166
9.	Light Band		17.2	0.174
10.	Light Band		17.1	0.180
11.	Darker Segment of Light Band	Equatorial Light Band	16.7	0.180
12.	Dark Band		16.9	0.194
13.	Light Band		15.2	0.184
14.	Light Band		15.2	0.198
15.	Darker Segment of Light Band		17.5	0.198
16.	Darker Region		19.5	0.208
17.	Darker Region	N Tropical Dark Band	20.1	0.200
18.	(underexposure)		-	-
19.	-	-	-	-
20.	-	-	-	-
21.	-	-	-	-
22.	-	-	-	-
23.	-	-	-	-
24.	-	-	-	-

November 19-20 UT 19^h56^m ($L_I = 232.3^\circ$, $L_{II} = 243.7^\circ$)

1.	S-Polar Region	18.1	0.173
2.	Light Region	13.4	0.168
2.	Light Region	13.4	0.144
4.	Dark Detail of Light Region	13.2	0.166
5.	Same	13.6	0.156
6.	Light Region	15.1	0.177
7.	Light Region	15.6	0.158
8.	Light Region	13.9	0.158
9.	Darker Segment of Light Region	13.9	0.156
10.	Same	13.9	0.156
11.	Dark Band	15.6	0.186
12.	Dark Band	15.7	0.184
13.	Dark Band	16.7	0.191
14.	Dark Band	23.3	0.238
15.	Dark Band	22.5	0.232
16.	Dark Band	18.9	0.218
17.	Dark Band	16.9	0.152
18.	-	-	-
19.	-	-	-

CONTINUATION OF TABLE 1

No.	Characteristics of Details	Identification with "Constant" Formations	$W_{b,A}$	R_b
20.	-		-	-
21.	-		-	-
22.	-		-	-

1966

March 22-23 UT 18^h05^m ($L_I = 147.3^\circ$, $L_{II} = 300.8^\circ$)

1.	S-Polar Region	19.7	0.204
2.	S-Polar Region	18.8	0.205
3.	Light Band	19.1	0.208
4.	Light Band	17.2	0.202
5.	Superposition of Dark and Light Bands	19.6	0.234
6.	Light Band	21.6	0.218
7.	Light Band	23.8	0.235
8.	Dark Band	23.4	0.229
9.	Dark Band	22.5	0.239
10.	Superposition of Dark and Following Light Bands	22.8	0.244
11.	Light Band	22.5	0.230
12.	Light Band (Superposing with Following Dark Band)	23.6	0.236
13.	Dark Band	21.8	0.234
14.	Dark Band	22.8	0.224
15.	Light Band	20.8	0.222
16.	Dark Region	17.8	0.217
17.	N-Polar Region	16.1	0.172

March 22-23 UT 18^h48^m ($L_I = 173.5^\circ$, $L_{II} = 326.8^\circ$)

1.	S-Polar Region	17.5	0.173
2.	Light Detail	18.4	0.188
3.	Dark Band	18.1	0.183
4.	Lighter Region	16.0	0.186
5.	Dark Band	20.6	0.206
6.	Dark Band	21.1	0.202
7.	Light Band	20.7	0.226
8.	Light Band	20.6	0.208
9.	Dark Band (Overlapping with Preceding Light Band)	24.8	0.228
10.	Darkest Site of Dark Band	22.1	0.234
11.	Light Band	22.0	0.230
12.	Light Band	22.8	0.224
13.	Dark Band	21.1	0.221

CONTINUATION OF TABLE 1

No.	Characteristics of Details	Identification with "Constant" Formations	$W_D, \text{\AA}$	R_D
14.	Dark Band		18.2	0.204
15.	Dark Band		21.8	0.207
16.	Dark Band		22.2	0.231
17.	Light Band		23.3	0.218
18.	N-Polar Region		19.6	0.210
19.	N-Polar Region		17.8	0.194

March 22-23 UT (19^h54^m ($L_I = 213.7^\circ$, $L_{II} = 6.7^\circ$)

1.	S-Polar Region		16.4	0.160
2.	S-Polar Region		17.8	0.194
3.	Dark Region		18.1	0.186
4.	Dark Region		18.5	0.203
5.	Light Band		16.1	0.176
6.	Light Band		17.6	0.192
7.	Light Band		16.8	0.175
8.	Light Band		19.4	0.205
9.	Dark Band (Slight Overlapping with Preceding Light Band)		18.9	0.200
10.	Dark Band		19.8	0.210
11.	Overlapping of Dark and Light Bands		20.7	0.222
12.	Light Band		18.9	0.210
13.	Overlapping of Light and Dark Bands		22.1	0.238
14.	Dark Band		21.3	0.240
15.	Light Band		22.2	0.206
16.	Dark Detail		21.1	0.208
17.	N-Polar Region		20.7	0.204
18.	N-Polar Region		15.5	0.154

March 23-24 UT 17^h13^m ($L_I = 273.4^\circ$, $L_{II} = 59.4^\circ$)

1.	S-Polar Region		12.3	0.118
2.	Light Band		16.4	0.160
3.	Overlapping of Light and Dark Bands		14.4	0.175
4.	Light Sharp Band		15.0	0.160
5.	Dark Band (Slight Overlapping with Preceding Light Band)		15.1	0.163
6.	Dark Band		15.7	0.181
7.	Light Band		17.9	0.183
8.	Light Band		16.5	0.195
9.	Dark Band		17.4	0.190
10.	Light Band (Lightest on Disk)		18.4	0.192
11.	Dark Region		21.6	0.222

CONTINUATION OF TABLE 1

No.	Characteristics of Details	Identification with "Constant" Formations	$W_b, \text{\AA}$	R_b
12.	Dark Region		20.6	0.212
13.	Dark Region		21.6	0.201
14.	Dark Region		19.1	0.204
15.	Light Band		20.8	0.212
16.	Light Band		20.1	0.182
17.	Polar Region		19.3	0.171

March 23-24 UT 17^h24^m ($L_I = 280.1^\circ$, $L_{II} = 66.1^\circ$)

1.	S-Polar Region		15.4	0.164
2.	Light Band		14.3	0.176
3.	Light Band		14.7	0.179
4.	Light Band		14.0	0.162
5.	Dark Band		18.4	0.190
6.	Lighter Site in Dark Band		16.8	0.180
7.	Overlapping of Light and Dark Bands		16.4	0.174
8.	Dark Band	} S Tropical Dark Band Equatorial Light Band	19.2	0.196
9.	Dark Band		19.3	0.198
10.	Light Sharp Band		20.2	0.229
11.	Dark Band	} N Tropical Dark Band	21.5	0.215
12.	Dark Band		19.4	0.207
13.	Overlapping of Dark and Following Light Band		17.8	0.208
14.	Light Band		19.7	0.217
15.	Light Band		19.0	0.200
16.	N-Polar Region		18.4	0.202
17.	N-Polar Region		18.8	0.191

March 23-24 UT 17^h38^m ($L_I = 288.6^\circ$, $L_{II} = 74.5^\circ$)

1.	S-Polar Region		18.4	0.172
2.	Light Band		16.8	0.167
3.	Light Band		18.4	0.188
4.	Light Band		19.4	0.174
5.	Dark Band		16.2	0.188
6.	Dark Band		17.1	0.180
7.	Dark Band		16.2	0.175
8.	Dark Band		19.7	0.206
9.	Dark Band (Darkest on Disk)		18.7	0.204
10.	Light Band		21.5	0.229
11.	Light Band		20.9	0.212
12.	Dark Sharp Band		19.7	0.210
13.	Light Band (Overlapping with Preceding Dark Band)		20.4	0.222

CONTINUATION OF TABLE 1

No.	Characteristics of Details	Identification with "Constant" Formations	$W_B, \text{\AA}$	R_B
14.	Dark Band		21.6	0.217
15.	Light Band		18.2	0.207
16.	Light Band		20.1	0.202
17.	N-Polar Region		20.0	0.204

March 23-24 UT 17^h49^m ($L_I = 295.3^\circ$, $L_{II} = 81.2^\circ$)

1.	S-Polar Region		12.0	0.132
2.	Light Band		17.1	0.170
3.	Light Band		18.5	0.182
4.	Light Band		14.4	0.156
5.	Light Band		14.7	0.168
6.	Dark Band		15.4	0.163
7.	Light Band		17.0	0.174
8.	Dark Band		17.3	0.165
9.	Dark Band		16.8	0.177
10.	Light Band		18.5	0.198
11.	Light Band		19.2	0.206
12.	Light Band		19.4	0.210
13.	Overlapping of Light and Dark Bands		22.6	0.229
14.	Overlapping of Dark and Following Light Bands		20.2	0.194
15.	Light Band		19.4	0.196
16.	Light Band		17.8	0.200
17.	N-Polar Region		20.3	0.212

March 23-24 UT 17^h58^m ($L_I = 300.8^\circ$, $L_{II} = 86.6^\circ$)

1.	S-Polar Region		16.9	0.178
2.	Light Band		17.2	0.178
3.	Light Band		15.8	0.178
4.	Light Band		15.6	0.176
5.	Dark Band		18.0	0.184
6.	Dark Band (Overlapping with Light Detail)		17.3	0.177
7.	Overlapping of Light Detail and Following Dark Band		16.0	0.167
8.	Dark Band		18.0	0.192
9.	Light Abrupt Band		15.6	0.167
10.	Overlapping of Dark and Light Bands		18.0	0.192
11.	Light Band		20.0	0.204
12.	Light Band (Darker Site)		20.9	0.204

CONTINUATION OF TABLE 1

No.	Characteristics of Details	Identification with "Constant" Formations	$W_b, \text{\AA}$	R_b
13.	Dark Band (Darkest on Disk)		19.8	0.188
14.	Light Band		18.2	0.194
15.	Dark Region		18.3	0.204
16.	N-Polar Region		18.8	0.178
17.	N-Polar Region		15.7	0.148

March 27-28 UT 18^h15^m ($L_I = 222.0^\circ$, $L_{II} = 337.2^\circ$)

1.	S-Polar Region		16.2	0.168
2.	Light Region		19.9	0.209
3.	Dark Detail in Light Region		13.6	0.171
4.	Light Region		14.7	0.179
5.	Light Region		14.6	0.186
6.	Overlapping of Light Region and Following Dark Band		15.2	0.180
7.	Dark Band		15.5	0.182
8.	Darker Band (Overlapping with Following Light Band)		15.9	0.172
9.	Light Sharp Band		14.9	0.178
10.	Same		16.0	0.180
11.	Same		17.4	0.176
12.	Same		13.8	0.150
13.	Same		20.5	0.222
14.	Dark Region		21.2	0.248
15.	Dark Region		16.5	0.206
16.	N-Polar Region		13.2	0.138

March 27-28 UT 19^h27^m ($L_I = 265.8^\circ$, $L_{II} = 20.7^\circ$)

1.	S-Polar Region		19.4	0.207
2.	Dark Region		14.4	0.156
3.	Light Band		16.5	0.184
4.	Dark Band		17.1	0.211
5.	Light Band		18.6	0.212
6.	Darker Band		19.2	0.212
7.	Light Detail		21.3	0.236
8.	Dark Sharp Band		19.4	0.216
9.	Light Band		20.8	0.232
10.	Light Band		19.7	0.217
11.	Light Band		19.9	0.220
12.	Light Band		20.5	0.214
13.	Dark Sharp Detail		18.1	0.198
14.	Same		18.9	0.199
15.	Light Band		13.8	0.170

CONTINUATION OF TABLE 1

No.	Characteristics of Details	Identification with "Constant" Formations	$W_D, \text{\AA}$	R_D
16.	Dark Region		16.2	0.202
17.	N-Polar Region		16.2	0.194
August 30-31 UT 02 ^h 14 ^m ($L_I = 272.6^\circ$, $L_{II} = 113.1^\circ$)				
1.	S-Polar Region		19.5	0.195
2.	Dark Region		20.5	0.185
3.	Dark Region		17.0	0.185
4.	Light Band		18.9	0.195
5.	Light Band		18.2	0.185
6.	Light Band		20.0	0.186
7.	Overlapping of Light and Following Dark Bands		15.8	0.192
8.	Dark Band		18.3	0.191
9.	Dark Band		20.8	0.185
10.	Dark Band		17.2	0.175
11.	Light Band		18.0	0.202
12.	Overlapping of Light Band and Darker Region		15.4	0.185
13.	Dark Region		18.3	0.205
14.	N-Polar Region		17.1	0.182
15.	N-Polar Region		16.2	0.202
August 30-31 UT 02 ^h 31 ^m ($L_I = 283.0^\circ$, $L_{II} = 102.8^\circ$)				
1.	S-Polar Region		16.2	0.185
2.	Light Band		15.6	0.175
3.	Dark Region		16.3	0.182
4.	Light Band		14.3	0.171
5.	Light Band		15.5	0.180
6.	Light Band		16.9	0.185
7.	Overlapping of Light and Following Dark Bands		16.4	0.192
8.	Dark Band		18.4	0.195
9.	Dark Band		15.2	0.185
10.	Dark Sharp Detail		17.8	0.205
11.	Light Band		18.3	0.210
12.	Light Band		17.0	0.202
13.	Dark Band		18.9	0.205
14.	Dark Band		20.8	0.215
15.	N-Polar Region		13.1	0.160

TABLE 2. DISTRIBUTION OF METHANE ABSORPTION IN THE 6190 Å BAND
ALONG THE EQUATOR

NO.	$W_b, \text{\AA}$ R_b		$W_b, \text{\AA}$ R_b		$W_b, \text{\AA}$ R_b		$W_b, \text{\AA}$ R_b		$W_b, \text{\AA}$ R_b	
	Nov. 29/30 1963 UT 18 ^h 26 ^m ($L_1=166.3$)		Aug. 26/27 1964 UT 0 ^h 37 ^m ($L_1=300.1$)		Aug. 28/29 1964 UT 22 ^h 58 ^m ($L_1=195.6$)		Aug. 29/30 1964 UT 22 ^h 00 ^m ($L_1=323.0$)		Aug. 29/30 1964 UT 22 ^h 00 ^m ($L_1=323.0$)	
1	21.2	0.200	—	—	—	—	18.1	0.198	19.0	0.193
2	21.1	0.198	—	—	14.1	0.185	14.9	0.185	15.1	0.185
3	19.1	0.170	9.6	0.125	13.5	0.195	11.9	0.180	11.0	0.175
4	23.3	0.198	10.6	0.140	17.0	0.171	19.1	0.179	17.6	0.175
5	21.2	0.220	12.6	0.150	18.7	0.206	16.3	0.188	18.4	0.179
6	20.8	0.210	12.6	0.155	19.6	0.208	19.0	0.188	17.8	0.175
7	21.9	0.220	13.5	0.160	19.9	0.210	18.4	0.176	18.7	0.175
8	25.2	0.230	12.8	0.155	19.4	0.201	21.3	0.212	17.2	0.202
9	24.0	0.220	17.0	0.175	17.7	0.208	20.8	0.205	19.4	0.211
10	19.8	0.212	11.1	0.160	18.6	0.211	20.1	0.206	19.8	0.202
11	23.3	0.218	18.3	0.170	18.8	0.205	22.0	0.207	19.1	0.212
12	25.7	0.228	14.6	0.185	19.4	0.226	21.9	0.226	19.6	0.216
13	23.6	0.230	17.0	0.180	18.2	0.219	23.0	0.217	20.9	0.214
14	21.4	0.220	17.0	0.180	17.0	0.212	23.1	0.222	17.8	0.219
15	27.3	0.238	17.6	0.180	18.0	0.212	22.4	0.219	19.3	0.215
16	22.2	0.230	17.5	0.195	18.1	0.210	20.4	0.203	19.1	0.205
17	29.4	0.250	16.7	0.195	18.8	0.216	19.5	0.200	19.2	0.206
18	23.7	0.220	20.0	0.190	18.3	0.202	17.9	0.201	17.2	0.191
19	25.1	0.228	18.6	0.200	15.5	0.199	21.4	0.198	19.6	0.191
20	26.0	0.220	17.8	0.190	18.5	0.186	18.0	0.181	17.7	0.187
21	24.2	0.248	19.2	0.195	18.2	0.188	18.3	0.192	17.5	0.190
22	25.8	0.230	19.4	0.190	15.6	0.168	18.4	0.188	19.1	0.190
23	24.4	0.230	14.9	0.170	17.4	0.172	15.2	0.170	17.6	0.180
24	24.3	0.217	—	—	15.2	0.172	14.1	0.145	—	—
25	22.9	0.207	—	—	12.3	0.159	15.1	0.170	19.7	0.184
26	20.3	0.179	—	—	—	—	—	—	—	—
27	23.8	0.218	—	—	—	—	—	—	—	—
28	23.6	0.178	—	—	—	—	—	—	—	—
29	19.9	0.210	—	—	—	—	—	—	—	—

CONTINUATION OF TABLE 2

No.	$W_b, \text{\AA}$ R_b		$W_b, \text{\AA}$ R_b		$W_b, \text{\AA}$ R_b		$W_b, \text{\AA}$ R_b		$W_b, \text{\AA}$ R_b	
	Sep. 27/28 ¹⁹⁶⁴ UT 21 ^h 26 ^m ($L_1=198.3$)		Jan. 24/25 ¹⁹⁶⁵ UT 20 ^h 46 ^m ($L_1=250.9$)		Jan 25/26 ¹⁹⁶⁵ UT 21 ^h 07 ^m ($L_1=62.2$)		Feb. 12/13 ¹⁹⁶⁵ UT 17 ^h 21 ^m ($L_1=242.9$)		Nov. 16/17 ¹⁹⁶⁵ UT 1 ^h 09 ^m ($L_1=309.2$)	
1	—	—	8.3	0.114	—	—	13.4	0.160	—	—
2	14.1	0.148	10.7	0.114	9.7	0.128	16.4	0.164	—	—
3	17.6	0.157	11.4	0.136	10.7	0.122	18.2	0.191	17.8	0.186
4	18.2	0.171	11.0	0.152	12.3	0.137	12.5	0.190	16.7	0.185
5	18.1	0.180	15.4	0.159	12.7	0.146	20.3	0.209	19.9	0.191
6	18.3	0.198	17.7	0.176	16.5	0.164	22.3	0.218	20.4	0.196
7	19.4	0.206	17.7	0.170	17.5	0.174	21.4	0.208	18.4	0.208
8	22.6	0.220	16.4	0.174	18.6	0.199	22.2	0.214	22.0	0.219
9	19.3	0.204	16.6	0.174	20.9	0.190	22.6	0.222	22.9	0.226
10	19.6	0.223	19.7	0.176	20.2	0.201	21.6	0.210	22.8	0.216
11	20.8	0.215	14.8	0.161	20.3	0.196	21.6	0.215	22.2	0.223
12	20.4	0.214	17.1	0.196	21.0	0.198	19.9	0.206	23.0	0.223
13	19.7	0.209	15.1	0.172	20.4	0.190	21.2	0.202	19.6	0.210
14	19.2	0.196	13.4	0.156	18.2	0.186	18.8	0.196	19.8	0.208
15	17.0	0.194	14.5	0.164	19.0	0.187	17.2	0.176	17.2	0.186
16	19.0	0.186	11.9	0.144	18.9	0.191	17.5	0.205	16.0	0.189
17	18.6	0.187	10.9	0.134	18.8	0.178	20.6	0.200	17.9	0.182
18	15.7	0.174	10.8	0.118	15.7	0.166	25.0	0.257	17.6	0.178
19	15.7	0.182	9.8	0.136	15.8	0.158			16.3	0.184
20	15.5	0.164	9.5	0.120	17.0	0.176			14.6	0.174
21	17.5	0.188	9.5	0.104	15.6	0.156			15.9	0.193
22	22.1	0.222			11.2	0.137			17.6	0.204
23					16.2	0.175			19.2	0.216
24					17.2	0.154				
25					13.2	0.126				

CONTINUATION OF TABLE 2

No.	$W_b, \text{\AA}$		R_b		No.	$W_b, \text{\AA}$		R_b	
	Mar. 27/28 1965 UT 20 ^h 31 ^m ($L_1 = 304.9^\circ$)		Aug. 30/31 1966 UT 2 ^h 49 ^m ($L_1 = 293.9^\circ$)			Mar. 27/28 1965 UT 20 ^h 31 ^m ($L_1 = 304.9^\circ$)		Aug. 30/31 1966 UT 2 ^h 49 ^m ($L_1 = 293.9^\circ$)	
1	16.9	0.180	16.1	0.168	10	18.3	0.188	16.7	0.170
2	14.7	0.137	12.6	0.135	11	19.1	0.197	17.3	0.170
3	13.3	0.138	17.7	0.135	12	18.0	0.201	15.2	0.160
4	15.7	0.170	18.8	0.135	13	17.2	0.191	15.5	0.160
5	18.5	0.207	18.3	0.190	14	17.2	0.200	15.9	0.160
6	17.0	0.190	18.4	0.185	15	18.7	0.201	17.0	0.185
7	19.1	0.208	17.1	0.185	16	19.9	0.215	13.7	0.155
8	19.7	0.210	18.4	0.190	17	18.2	0.211	14.2	0.160
9	19.1	0.208	19.0	0.200	18	16.7	0.180		

Note: The first point of each spectrogram corresponds to the western limb of the planet.

TABLE 3. VALUES OF W_b AND R_b FOR THE 6190 \AA CH_4 BAND FOR THE SOUTH AND NORTH POLAR REGIONS, THE WEST AND EAST LIMBS OF JUPITER

Date	Time of Observation	$W_b, \text{\AA}$	R_b	Longitude of Central Meridian	
				L_I	L_{II}
Nov. 16-17, 1965					
N-Polar Region	1 ^h 45 ^m	19.8	0.186	--	3.5°
Mar. 22-23, 1966					
N-Polar Region	20 ^h 20 ^m	12.9	0.151	--	22.4°
S-Polar Region	21 ^h 09 ^m	15.8	0.174	--	51.7°
Western Limb	18 ^h 26 ^m	16.3	0.164	160.1°	--
Eastern Limb	19 ^h 09 ^m	18.2	0.184	186.3°	--
Mar. 27-28, 1966					
N-Polar Region	18 ^h 44 ^m	12.3	0.155	--	354.7°
S-Polar Region	20 ^h 00 ^m	16.9	0.188	--	40.7°

DISTRIBUTION OF METHANE ABSORPTION IN THE 6190 Å BAND OVER THE DISK OF SATURN IN 1966

V.V. Avramchuk

ABSTRACT: Some results are given of an analysis of five spectrograms of Saturn obtained with the aid of a 70-cm reflector attached to a diffraction spectrograph (dispersion of 30 Å/mm) in August of 1966. It is shown that, during the period of observations, the absorption in the 6190 Å methane band was stable at the center of the Saturn disk, and equal to 25-27 Å. At the same time, the polar regions showed substantial variations. During the observation period, the equivalent width for the 6190 Å band decreased from 32-33 to 25-26 Å.

A number of passages of the Earth and Sun through the plane of the rings of Saturn were observed in 1966. The periods of these passages, as well as the periods of visibility of the "night" side of the rings, are very suitable for studying the disk of Saturn. For this, we obtain the number of spectrograms of Saturn with orientation of the spectrograph slit along the central meridian and along the equator of the planet.

The observations were carried out on a 70-centimeter reflector in a Cassegrainian focus ($F_{\text{eff}} = 30$ m) with the aid of the diffraction spectrograph ASP-21 (dispersion of 30 Å/mm). The spectral width of the slits was 4 Å. Kodak OaF plates were used. The exposures were 100-120 min. The method of analyzing the Saturn spectrograms was the same as for the analysis of the Jupiter spectrograms [1].

This study contains the results of an analysis of 5 Saturn spectrograms obtained in August of 1966 with orientation of the spectrograph slit along the central meridian.

We will give a brief description of the results obtained. The figure (a) gives the distribution of methane absorption in the 6190 Å band for July 31-August 1, 1966. It is clearly seen that the central part of the Saturn disk is characterized by less absorption than are the middle and polar latitudes. The value of the absorption for the S-polar region is somewhat higher than for the N-polar region. During this period, we observed in the southern part of the disk a light formation which showed greater absorption than did the neighboring segments.

The curves for methane absorption on August 1-2 repeat the cited characteristics almost completely.

A somewhat different nature for the methane absorption along the central meridian was observed on August 5-6. During this period, the values for the equivalent widths W_b of the 6190 Å band for the polar regions were the same as for the center of the disk. The light formation in the southern part of the Saturn disk shows the greatest absorption.

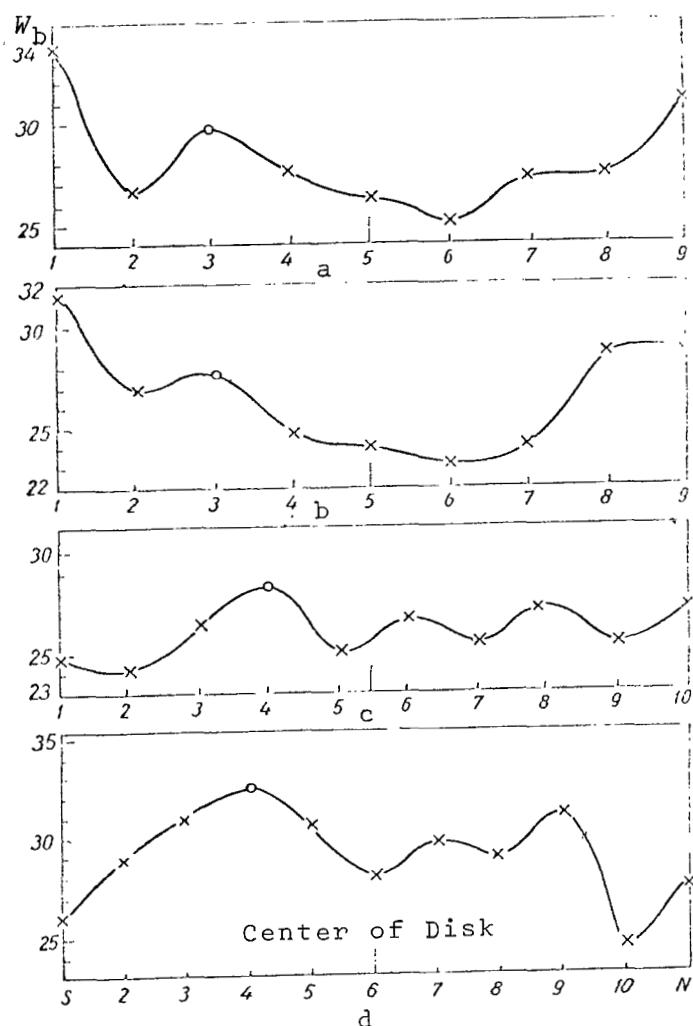


Fig. Distribution of Methane Absorption Along the Central Meridian. (a) July 31-Aug. 1, UT 02^h35^m; (b) Aug. 1-2, UT 00^h45^m; (c) Aug. 5-6, UT 00^h00^m; (d) Aug. 30-31, UT 23^h00^m; (O) Light Formation.

Two spectrograms of Saturn were obtained on August 30-31. The results, averaged over these spectrograms, are given in the figure (d). The distribution of methane absorption is more complex for this period than for the other periods. As on August 5-6, the light formation shows the greatest absorption on the disk.

The following conclusions can be drawn on the basis of the results obtained.

During the entire observation period, the intensity of methane absorption remained almost unchanged at the center of the disk, and was equal to 25-27 Å; the polar regions showed substantial variations. The equivalent width of the 6190 Å band for these regions decreased from 32-33 to 25-26 Å during the observation period. Although a small number of spectrograms was measured, these variations are probable, since they follow from the general nature of the absorption distribution over the central meridian.

One of the possible reasons for the variations in intensity of molecular absorption in the polar regions of Saturn may be a change in extent of the polar "cap", as a result of which the linear thickness of the atmosphere over the clouds changes.

As was already mentioned, a light formation was observed during the entire observation period in the southern part of the Saturn disk, and it was characterized by greater absorption than were the neighboring dark sections. This circumstance can be explained by assuming that the light formation was situated at a lower level than were the neighboring regions. This conclusion agrees with the results of many years of photometric investigations of Saturn carried out at the Khar'kov Astronomical Observatory [2], according to which the light regions are somewhat lower than the dark bands.

REFERENCES

1. Avramchuk, V.V.: This Collection, p. 126.
2. Barabashov, N.P.: Rezul'taty fotometricheskikh issledovaniy Luny i planet na astronomicheskoy observatorii KhGU (Results of Photometric Investigations of the Moon and Planets at the Khar'kov State University Astronomical Observatory). Khar'kov University Press, p. 134, 1957.

THE PROBLEM OF DIFFUSE REFLECTION OF MONOCHROMATIC RADIATION

E.G. Yanovitskiy

ABSTRACT: The problem of the diffuse reflection of monochromatic radiation by a semi-infinite plane layer of a medium, with isotropic scattering, is discussed. A recurrence formula is obtained in order to calculate the terms in the expansion of the Ambartsumyan function $\phi(\eta, \lambda)$ for powers of $z = \sqrt{1-\lambda}$, where λ is the albedo of the particles for single scattering, $\phi(\eta, 1)$ is assumed to be known. The case of the simplest nonspherical indicatrix of scattering is discussed.

In investigating the diffusion of radiation, it is of particular interest to study the case of almost pure scattering, i.e., the case when, after each act of quantum absorption, its re-emission in the medium almost always follows. This interest is due, first of all, to the fact that this case is realized rather frequently during the transfer of radiation in turbid media (for example, in the visible part of the continuous spectrum, the atmospheres of Venus and the giant planets can be considered as almost purely scattering), and, secondly, an examination of almost pure scattering can be reduced, from the mathematical point of view to a study of the pure scattering of light, which greatly simplifies the problem.

A calculation of the intensity of diffusely reflected monochromatic radiation by a semi-infinite plane layer of the medium in isotropic scattering is reduced to the problem of finding the Ambartsumyan function $\phi(\eta, \lambda)$ which satisfies the following nonlinear integral equation [1]:

$$\varphi(\eta, \lambda) = 1 + \frac{\lambda}{2} \eta \varphi(\eta, \lambda) \int_0^1 \frac{\varphi(\eta', \lambda)}{\eta + \eta'} d\eta', \quad (1)$$

where λ is the probability of quantum burn-out in an elementary scattering at, $\arccos \eta$ is the angle of reflection of radiation from the layer. At $(1-\lambda) \ll 1$,

$$\varphi(\eta, \lambda) = [1 - \sqrt{3(1-\lambda)} \eta] \varphi_0(\eta) + o[1-\lambda] \quad (2)$$

where

$$\varphi_0(\eta) = \varphi(\eta, 1), \quad (3)$$

i.e., the solution to the problem of diffuse reflection of light in almost pure scattering is reduced to that of diffuse reflection in pure scattering ($\lambda = 1$). Therefore, it is of interest to solve the following problem.

The function $\phi(\eta, \lambda)$ is given. We must find the expansion of this function into a series by powers of

$$z = (1 - \lambda)^{1/2}, \quad (4)$$

where the function $\phi_0(\eta)$ is considered to be known.¹

PRINCIPAL EQUATIONS

In addition to (1), the function $\phi(\eta, \lambda)$ also satisfies the linear integral equation [2]

$$a(\eta) \varphi(\eta, \lambda) = 1 + \frac{\lambda}{2} \eta \int_0^1 \frac{\varphi(\eta', \lambda)}{\eta' - \eta} d\eta', \quad (5)$$

where

$$a(\eta) = 1 - \frac{\lambda}{2} \eta \ln \frac{1 + \eta}{1 - \eta}. \quad (6)$$

It is well known that

$$\alpha_0(\lambda) = \int_0^1 \varphi(\eta, \lambda) d\eta = \frac{2}{\lambda} (1 - \sqrt{1 - \lambda}) = 2 \sum_{n=0}^{\infty} (-1)^n z^n, \quad (7)$$

while the function $\phi(\eta, \lambda)$ satisfies the following relationships:

$$\frac{\lambda}{2} \int_0^1 \frac{\varphi(\eta, \lambda)}{1 - k\eta} d\eta = 1, \quad (8)$$

where k is the root of the equation, i.e.,

¹ This problem was formulated by V.V. Sobolev.

$$\frac{\lambda}{2k} \ln \frac{1+k}{1-k} = 1. \quad (9)$$

We should mention that, as follows from (7),

$$k = \sqrt{3}z \left[1 - \frac{2}{5}z^2 - o(z^4) \right]. \quad (10)$$

Using (7), Equation (5) can be rewritten in the following way:

$$a(\eta) \varphi(\eta, \lambda) = \sqrt{1-\lambda} + \frac{\lambda}{2} \int_0^1 \frac{\varphi(\eta', \lambda)}{\eta' - \eta} \eta' d\eta'. \quad (11)$$

The precise analytical solution to (11) can be obtained by the method of Carleman [2], while, as follows from the formulas found by V.V. Sobolev [4], this solution has the following form:

$$\varphi(\eta, \lambda) = \frac{2e^{\omega(\eta) - \omega(0)} (1 - k\eta)}{(1 - \eta) R(\eta)}, \quad (12)$$

where

$$R^2(\eta) = 4a^2(\eta) + \pi^2 \lambda^2 \eta^2; \quad (13)$$

$$\omega(\eta) = \frac{1}{\pi} \int_0^1 \arctan \left[\frac{\lambda \pi \eta'}{2a(\eta')} \right] \frac{d\eta'}{\eta' - \eta}. \quad (14)$$

Let us mention a number of relationships of the theory of singular integral equations which we will need in the future.

It was shown in the monograph by F. Tricomi [5, p. 241], that if the function $\phi(\eta, \lambda)$ satisfies (11), then it will also satisfy the following relationship:

$$\frac{a(\eta)(1-\eta)\varphi(\eta, \lambda)}{1-k\eta} e^{-\omega(0)} = \frac{\lambda}{2} \int_0^1 \frac{\varphi(\eta', \lambda)(1-\eta')\eta'}{(1-k\eta')(\eta' - \eta)} d\eta'. \quad (15)$$

In deriving (15), we used (12).

$$e^{-\omega(0)} = \frac{\lambda}{2} \int_0^1 \frac{\varphi(\eta', \lambda)\eta'}{1-k\eta'} d\eta',$$

Thus, using (7) and (8), we find

$$e^{-\omega(0)} = \frac{\sqrt{1-\lambda}}{k}.$$

Consequently, instead of (12), we can write the following expression:

$$\varphi(\eta, \lambda) = \frac{2\sqrt{1-\lambda} e^{\omega(\eta)} (1-k\eta)}{k(1-\eta) R(\eta)}.$$

In particular, considering (10), we find that

$$\varphi_0(\eta) = \frac{2e^{\omega_0(\eta)}}{\sqrt{3} R_0(\eta) (1-\eta)},$$

where the functions $R_0(\eta)$ and $\omega_0(\eta)$ are determined by (13) and (14), respectively at $\lambda = 1$.

An equation of the type

$$a_0(\eta) F(\eta) = f(\eta) + \frac{1}{2} \int_0^1 \frac{F(\eta') \eta' d\eta'}{\eta' - \eta} \quad (16)$$

has the following solution [5, p. 247]:

$$F(\eta) = \frac{4f(\eta) a_0(\eta)}{R_0(\eta)} + \\ + 2\varphi_0(\eta) (1-\eta) \int_0^1 \frac{f(\eta') \eta' d\eta'}{R_0^2(\eta') (1-\eta') (\eta' - \eta) \varphi_0(\eta')} + C \varphi_0(\eta),$$

where

$$a_0(\eta) = 1 - \frac{1}{2} \eta \ln \frac{1+\eta}{1-\eta}, \quad (17)$$

while the value C is an arbitrary integration constant. Moreover, it was found [5, p. 245] that the function $\phi_0(\eta)$ satisfies the relationship

$$\frac{4a_0(\eta)}{R_0^2(\eta)(1-\eta)\varphi_0(\eta)} + 2 \int_0^1 \frac{\eta' d\eta'}{R_0^2(\eta')(1-\eta')(\eta'-\eta)\varphi_0(\eta')} = \sqrt{3}. \quad (18)$$

In the future, we will need the following formula [6, p. 174]:

$$2\eta \int_0^1 \frac{d\eta'}{R_0^2(\eta')(\eta'-\eta)} = 1 - \frac{4a_0(\eta)}{R_0^2(\eta)} - 3\eta^2 + 2\eta \int_0^1 \frac{d\eta'}{R_0^2(\eta')(\eta+\eta')}. \quad (19)$$

CASE OF ISOTROPIC SCATTERING

Let us assume that $0 \leq z < 1$,

$$\varphi(\eta, \lambda) = \sum_{n=0}^{\infty} \varphi_n(\eta) z^n. \quad (20)$$

Substituting (20) into (11) and equalizing the expressions in both sides for identical powers of z , we find that

$$a_0(\eta) \varphi_{2n+1}(\eta) = 1 - \sum_{i=1}^n \varphi_{2i-1}(\eta) + \frac{1}{2} \int_0^1 \frac{\varphi_{2n+1}(\eta') \eta'}{\eta' - \eta} d\eta', \quad (21)$$

$$a_0(\eta) \varphi_{2n}(\eta) = - \sum_{i=1}^n \varphi_{2i-2}(\eta) + \frac{1}{2} \int_0^1 \frac{\varphi_{2n}(\eta') \eta'}{\eta' - \eta} d\eta' \quad (n \geq 1). \quad (22)$$

It follows from (7) and (20) that

$$\frac{1}{2} \int_0^1 \varphi_n(\eta) d\eta = (-1)^n, \quad (23)$$

while it follows from (21) and (22) that

$$a_0(\eta) [\varphi_{n+2}(\eta) - \varphi_n(\eta)] = -\varphi_n(\eta) + \frac{1}{2} \int_0^1 \frac{\varphi_{n+2}(\eta') - \varphi_n(\eta')}{\eta' - \eta} \eta' d\eta', \quad (24)$$

At the same time, we have the following from (23):

$$\int_0^1 [\varphi_{n+2}(\eta) - \varphi_n(\eta)] d\eta = 0. \quad (25)$$

Using (17) and omitting C with the aid of (25), we find from (24) that

$$\begin{aligned} \varphi_{n+2}(\eta) = \varphi_n(\eta) \left[1 - \frac{4\sigma_n(\eta)}{R_0^2(\eta)} \right] - \\ - 2\varphi_0(\eta) \eta \int_0^1 \frac{\varphi_n(\eta')}{R_0^2(\eta')(\eta' - \eta)} \cdot \frac{d\eta'}{\varphi_0(\eta')} \quad (n \geq 0). \end{aligned} \quad (26)$$

Thus, we have found the recurrence formula to obtain any term of the expansion in (20). As for the function $\phi_1(\eta)$, we find from

$$\sigma_0(\eta) \varphi_1(\eta) = 1 + \frac{1}{2} \int_0^1 \frac{\varphi_1(\eta') \eta'}{\eta' - \eta} d\eta', \quad (27)$$

using (17), (23) and (18), that

$$\varphi_1(\eta) = -\sqrt[3]{3} \eta \varphi_0(\eta). \quad (28)$$

In particular, it follows from (26) and (28), considering (19), that

$$\varphi_2(\eta) = \{3\eta - 2\sigma_0(\eta)\} \varphi_0(\eta) \eta, \quad (29)$$

$$\varphi_3(\eta) = \frac{2}{5} \sqrt[3]{3} \varphi_0(\eta) \eta - \sqrt[3]{3} \varphi_2(\eta) \eta, \quad (30)$$

where

$$u(\eta) = \int_0^1 \frac{d\eta'}{R_0^2(\eta')(\eta' - \eta)}. \quad (31)$$

In all appearances, the function $u(\eta)$ is not expressed in terms of the elementary functions. In deriving (30), we use the following, which can be proven:

$$\int_0^1 \frac{d\eta}{R_0^2(\eta)} = \frac{1}{5}. \quad (32)$$

Numerical values of the function $u(\eta)$ are given below:

η	0.05	0.10	0.15	0.20	0.25	0.30	0.35	0.40	0.45	0.50
$\gamma\mu(\eta)$	0.035	0.054	0.068	0.079	0.088	0.095	0.102	0.108	0.113	0.117
η	0.55	0.60	0.65	0.70	0.75	0.80	0.85	0.90	0.95	1.00
$\gamma\mu(\eta)$	0.121	0.125	0.128	0.131	0.134	0.136	0.139	0.141	0.143	0.145

Thus, the following formula is derived from (28), (29) and (30)²:

$$\begin{aligned} \Phi(\eta, \lambda) = & \left\{ 1 - \sqrt{3}\eta(1-\lambda)^{1/2} + [3\eta - 2\mu(\eta)]\gamma_1(1-\lambda) + \right. \\ & \left. + \sqrt{3}\eta \left[\frac{2}{5} - 3\eta^2 + 2\gamma\mu(\eta) \right] (1-\lambda)^{3/2} + o[(1-\lambda)^2] \right\} \Phi_0(\eta). \end{aligned} \quad (33)$$

Obviously, using the recurrence formulas in (26), we can obtain the terms of the expansion of the function $\phi(\eta, \lambda)$ into a series by z and higher orders.

CASE OF THE SIMPLEST NONSPHERICAL INDICATRIX OF SCATTERING

The formulas given above for a spherical indicatrix of scattering can be used in deriving analogous formulas in the case of the simplest nonspherical indicatrix of scattering of the following type:

$$\chi(\gamma) = 1 + x_1 \cos \gamma, \quad (34)$$

where γ is the angle of scatter. This is all the more important in that we have a dependence on one more parameter here, x_1 .

According to S. Chandrasekhar [7], the Ambartsumyan functions $\phi_0(\eta)$ and $\phi_1^0(\eta)$ are expressed in terms of the function $H(\eta)$, which satisfies the following equation:

$$H(\eta) = 1 + \eta H(\eta) \int_0^1 \frac{\Psi(\eta')}{\eta + \eta'} H(\eta') d\eta', \quad (35)$$

where

$$\Psi(\eta) = \frac{1}{2} \lambda [1 + x_1(1-\lambda)\eta^2], \quad (36)$$

² V.V. Ivanov also obtained (33) by another method.

while

$$H(-\eta) = \frac{1}{H(\eta) T(\eta)}. \quad (37)$$

Here

$$T(\eta) = 1 - 2\eta^2 \int_0^1 \frac{\Psi(\eta') d\eta'}{\eta^2 - \eta'^2}. \quad (38)$$

It follows from (35) and (37) that the function $H(\eta)$, in addition to (35), also satisfies the following equation:

$$T(\eta) H(\eta) = 1 + \eta \int_0^1 \frac{\Psi(\eta')}{\eta' - \eta} H(\eta') d\eta'. \quad (39)$$

It follows from (36) and (38) that

$$T(\eta) = \frac{2}{\lambda} \Psi(\eta) a(\eta) - x_1 (1 - \lambda)^2 \eta^2, \quad (40)$$

while, considering moreover that [7]

$$\int_0^1 H(\eta) \Psi(\eta) d\eta = 1 - \left[1 - 2 \int_0^1 \Psi(\eta') d\eta' \right]^{1/2}, \quad (41)$$

instead of (39), we have the following:

$$\begin{aligned} \frac{2}{\lambda} \Psi(\eta) a(\eta) H(\eta) &= \frac{1 - (1 - \lambda)(3 - \lambda x_1)}{\sqrt{3}} + x_1 (1 - \lambda)^2 \eta^2 H(\eta) + \\ &+ \int_0^1 \frac{\Psi(\eta') \eta'}{\eta' - \eta} H(\eta') d\eta'. \end{aligned} \quad (42)$$

Using the same method as in the case of a spherical indicatrix of scattering, we can obtain the recurrence formula in order to find any term of the expansion of the function $H(\eta)$ into a series by powers of z . We will limit ourselves to the expansion terms of power no higher than z^3 . In this case, instead of (42), we have the following:

$$a(\eta)h(\eta) = \sqrt{1-\lambda} + \frac{\lambda}{2} \int_0^1 \frac{h(\eta')\eta'}{\eta' - \eta} d\eta', \quad (43)$$

where

$$h(\eta) = \frac{2}{\lambda} \sqrt{\frac{3}{3-\lambda x_1}} W(\eta) H(\eta). \quad (44)$$

Considering (11) and (43), which coincide completely, we have the following:

$$a(\eta)[h(\eta) - \varphi(\eta)] = \frac{\lambda}{2} \int_0^1 \frac{[h(\eta') - \varphi(\eta')]\eta'}{\eta' - \eta} d\eta', \quad (45)$$

at the same time, it follows from (41) and (44) that

$$\frac{\lambda}{2} \int_0^1 h(\eta) d\eta = \frac{\sqrt{3} - \sqrt{(1-\lambda)(3-\lambda x_1)}}{\sqrt{3-\lambda x_1}}. \quad (46)$$

Considering (7) and (8) and solving (45) by the method of Carleman [3], we find

$$H(\eta) = \frac{\sqrt{3-k}\sqrt{3-\lambda x_1}\eta}{\sqrt{3(1-k\eta)[1+x_1(1-\lambda)\eta^2]}} \varphi(\eta, \lambda). \quad (47)$$

In order to obtain the terms for the expansion of $H(\eta)$ into a series by powers of z , we must expand the right-hand part of (47) into a series by powers of z and limit ourselves to terms of power no greater than z^3 .

As follows from (42) and (43), the relationship in (47) is fulfilled all the more accurately when η is closer to zero, which can be seen from the precise values of $H_T(\eta)$ given below for $\lambda = 0.95$ and $x_1 = 1$, as well as the values calculated according to (47) (it was assumed in the calculations that the function $\phi(\eta, \lambda)$ was known):

η	1	0.5	0.1
H_T	2.1814	1.7195	1.2029
H	2.1879	1.7183	1.2028

Let

$$H(\eta) = \sum_{n=0}^{\infty} H_n(\eta) z^n, \quad (48)$$

Then, considering (10), (28), (29) and (30), after expanding the right-hand part of (47) into a series by powers of z , we have the following:

$$H_0(\eta) = \varphi_0(\eta), \quad (49)$$

$$H_1(\eta) = -\sqrt{3-x_1} \varphi_0(\eta) \eta, \quad (50)$$

$$H_2(\eta) = \{(3-x_1)\eta - 2u(\eta)\} \varphi_0(\eta) \eta, \quad (51)$$

$$H_3(\eta) = -\sqrt{3-x_1} \eta \left[(3-x_1)\eta^2 - \frac{3(4-3x_1)}{10(3-x_1)} - 2u'(\eta) \right] \varphi_0(\eta). \quad (52)$$

As Chandrasekhar showed [7], the functions

$$\varphi_0^0(\eta) = (1 - c\eta) H(\eta), \quad (53)$$

$$\varphi_1^0(\eta) = p \eta H(\eta), \quad (54)$$

where

$$c = \frac{\lambda x_1 (2 - \lambda \bar{\alpha}_0) \bar{\alpha}_1}{4 - \lambda^2 x_1 \bar{\alpha}_1^2}, \quad (55)$$

$$p = \frac{2(2 - \lambda \bar{\alpha}_0)}{4 - \lambda^2 x_1 \bar{\alpha}_1^2}, \quad (56)$$

$$\bar{\alpha}_n = \int_0^1 H(\eta) \eta^n d\eta. \quad (57)$$

It is well known [4] that the functions $\phi_0^0(\eta)$ and $\phi_1^0(\eta)$ determine the component of the intensity of radiation diffusely reflected by a semi-infinite plane layer of the medium for indicatrix of scattering of (34), which does not depend on the azimuth.

In order to find the expansion of the function $\phi_0^0(\eta)$ and $\phi_1^0(\eta)$ into a series by z , we will determine the values for the moments of the function $\phi_0(\eta)$. We will use the following symbols:

$$\alpha_n(\lambda) = \int_0^1 \varphi(\eta, \lambda) \eta^n d\eta, \quad (58)$$

$$\alpha_n^{(0)} = \int_0^1 \varphi_0(\eta) \eta^n d\eta. \quad (59)$$

Considering (1) and using (7), we can obtain the following:

$$\sqrt{1-\lambda} \alpha_{2n}(\lambda) = \frac{1}{2n+1} + \frac{\lambda}{4} \sum_{i=1}^{2n-1} (-1)^i \alpha_i(\lambda) \alpha_{2n-i}(\lambda) \quad (n \geq 1), \quad (60)$$

from which

$$\frac{1}{2n+1} + \frac{\lambda}{4} \sum_{i=1}^{2n-1} \alpha_i^{(0)} \alpha_{2n-i}^{(0)} = 0. \quad (61)$$

As is well known [7,9]

$$\alpha_0^{(0)} = 2, \quad (62)$$

$$\alpha_1^{(0)} = \frac{2}{\sqrt{3}}, \quad (63)$$

$$\alpha_2^{(0)} = \frac{2}{\sqrt{3}} q(\infty), \quad (64)$$

where $q(x)$ is a Hopf function, $q(\infty) = 0.710$, while [8]

$$q(\infty) = \frac{1}{\sqrt{3}} \left[1 + 2 \int_0^1 \frac{d\eta}{R_0^3(\eta) \varphi_0(\eta)} \right]. \quad (65)$$

It follows from (61) and (62) that

$$\alpha_3^{(0)} = \frac{\sqrt{3}}{5} + \frac{1}{\sqrt{3}} q^2(\infty). \quad (66)$$

Using (49)-(52), (62)-(64) and (66), we find that

$$\alpha_0 = 2 - 2 \frac{\sqrt{3-x_1}}{\sqrt{3}} z + \left(1 - \frac{x_1}{\sqrt{3}} q(\infty) \right) z^2 - \frac{\sqrt{3-x_1}}{\sqrt{3}} \times$$

$$\times \left[\frac{30 - 14x_1 + 3x_1^2}{5(3 - x_1)} - x_1 q^2(\infty) \right] z^3 + o(z^4), \quad (67)$$

$$\bar{a}_1 = \frac{2}{\sqrt{3}} \left\{ 1 - \sqrt{3 - x_1} q(\infty) z + \frac{1}{10} [14 - (3 + 5q^2(\infty)) x_1] z^2 + o(z^3) \right\}, \quad (68)$$

Then,

$$p = \sqrt{\frac{3}{3 - x_1}} \left\{ 1 - \frac{x_1 q(\infty)}{\sqrt{3 - x_1}} z + \frac{x_1}{10(3 - x_1)} [4 + 15q^2(\infty) - (3 - 5q^2(\infty)) x_1] z^2 \right\} z + o(z^4), \quad (69)$$

$$c = \sqrt{\frac{x_1}{3 - x_1}} \left\{ 1 - \frac{3q(\infty)}{\sqrt{3 - x_1}} z + \left[\frac{2}{5} + \frac{(6q^2(\infty) - 1)x_1}{2(3 - x_1)} \right] z^2 \right\} z + o(z^4). \quad (70)$$

Consequently,

$$\begin{aligned} \Phi_0^0(\eta) = & \left\{ 1 - \frac{3\eta}{\sqrt{3 - x_1}} z + \left[3\eta + \frac{3x_1 q(\infty)}{3 - x_1} - 2u(\eta) \right] \eta z^2 - \right. \\ & - \frac{3\eta}{\sqrt{3 - x_1}} \left[3\eta^2 + \left(\frac{13}{30} + q(\infty)\eta - \eta^2 \right) x_1 + \frac{(6q^2(\infty) - 1)x_1^2}{6(3 - x_1)} - \right. \\ & \left. \left. - \frac{2}{5} - 2\eta u(\eta) \right] z^3 + o(z^4) \right\} \Phi_0(\eta), \end{aligned} \quad (71)$$

$$\begin{aligned} \Phi_1^0(\eta) = & \sqrt{\frac{3}{3 - x_1}} z \left\{ 1 - \frac{(3 - x_1)\eta + x_1 q(\infty)}{\sqrt{3 - x_1}} z + \right. \\ & + \frac{1}{10} [(3 - x_1)\eta + x_1 q(\infty) - 2u(\eta)] \eta z^2 + \\ & + \frac{x_1}{10(3 - x_1)} [4 + 15q^2(\infty) - (3 - 5q^2(\infty)) x_1] z^2 + \\ & \left. + o(z^3) \right\} \Phi_0(\eta) \eta. \end{aligned} \quad (72)$$

The spherical albedo of the planet surrounded by a semi-infinite atmosphere is determined by the following formula [3] for an indicatrix of scattering of the type in (34):

$$A_c = 1 - 2 \int_0^1 q_1^n(\eta) \eta d\eta = 1 - \frac{4c}{\lambda x_1} \quad (73)$$

Substituting (69) into it, we find that

$$A_c = 1 - \frac{4z}{\sqrt{3-x_1}} \left\{ 1 - \frac{3q(\infty)}{\sqrt{3-x_1}} z + \right. \\ \left. + \left[\frac{7}{6} + \frac{6q^2(\infty)-1}{2(3-x_1)} x_1 \right] z^2 \right\} + o(z^4). \quad (74)$$

If we eliminate the terms greater than first order relative to z in (71) and (72), we will obtain the formulas found by V.V. Sobolev [10].

REFERENCES

1. Ambartsumyan, V.A.: Doklady Akad. Nauk S.S.S.R., Vol. 38, No. 8, p. 257, 1943.
2. Sobolev, V.V.: Doklady Akad. Nauk S.S.S.R., Vol. 69, No. 3, p. 353, 1949.
3. Carleman, T.: Arkiv Mat., Astr. och Fysik, Vol. 16, p. 26, 1922.
4. Sobolev, V.V.: Perenos luchistoy energii v atmosferakh zvezd i planet (Transfer of Radiant Energy in the Atmospheres of Stars and Planets). Moscow, "GITTL", 1956.
5. Tricconi, F.: Integral'nyye uravneniya (Integral Equations). Moscow, Foreign Literature Publishing House, 1960.
6. Case, K.M., F.de. Hoffmann and G. Placzek: Introduction to the Theory of Neutron Diffusion, U.S. Government Printing office, Los-Alamos - Washington, 1953.
7. Chandrasekhar, S.: Perenos luchistoy energii (Transfer of Radiant Energy). Moscow, Foreign Literature Publishing House, 1950.
8. Minin, I.N.: Doklady Akad. Nauk S.S.S.R., Vol. 120, No. 1, p. 63, 1958.
9. Kourganoff, V.: Basic methods in Transfer Problems. Oxford, 1952.
10. Sobolev, V.V.: Astron. Zhur., Vol. 41, No. 1, p. 97, 1964.

BRIGHTNESS COEFFICIENTS OF A HOMOGENEOUS PLANE LAYER OF A TURBID MEDIUM

E.G. Yanovitskiy

ABSTRACT: Three types of equations determining the Ambartsumyan ϕ and ψ functions are obtained for the case when the indicatrix of scattering proves to be a finite number of terms in an expansion into a series by Legendre polynomials. Linear relationships connecting the cited functions are obtained.

Using his probability of quantum yield from a medium, V.V. Sobolev [1] obtained three types of equations determining the Ambartsumyan ϕ and ψ - ϕ functions for isotropic scattering. V.A. Ambartsumyan [2,3] found two types of these equations.

In this study, these equations are obtained for the case when the indicatrix of scattering $\chi(\gamma)$ can be represented in the form of a finite number of terms in an expansion into a series by Legendre polynomials. In this case, we will base our arguments on the more general relationships obtained by the author of [4] for a plane layer of a heterogeneous medium, in which the indicatrix of scattering and the probability of quantum release λ are arbitrary preset functions of the optical depth τ . Moreover, we will find linear relationships which connect the Ambartsumyan functions ϕ_K and ψ_K .

PRINCIPAL EQUATIONS FOR THE HETEROGENEOUS MEDIUM

Let us have a plane layer of optical thickness τ , the upper limit ($\tau = 0$) to which is illuminated by parallel rays falling at an angle of arc $\cos \zeta$ to the normal at an azimuth of ϕ_0 ; πS is the illuminence of the area perpendicular to the incident rays at the upper boundary of the atmosphere; the probability of quantum release $\lambda(\tau)$ and the scattering indicatrix $\chi(\gamma, \tau)$, which are arbitrary functions of the optical depth (γ is the angle of scatter), are given.

We will assume that the characteristic scattering curves can be represented with a sufficient degree of accuracy in the following form:

$$\chi(\gamma, \tau) = \sum_{m=0}^n x_m(\tau) P_m(\cos \gamma), \quad (1)$$

where

$$x_n(\tau) = \frac{2n+1}{2} \int_0^\pi \chi(\gamma, \tau) P_n(\cos \gamma) \sin \gamma d\gamma, \quad (2)$$

$P_n(\cos \gamma)$ is the Legendre polynomial of n order.

The brightness coefficients for diffusely reflected and diffusely admitted radiation passing from the layer at an angle of arc η to the normal at azimuth of ϕ are then determined by the following formulas [4], respectively:

$$\rho(\eta, \zeta, \varphi) = \sum_{m=0}^n r_m(\eta, \zeta, \tau_0) \cos m(\varphi - \varphi_0), \quad (3)$$

$$\sigma(\eta, \zeta, \varphi) = \sum_{m=0}^n s_m(\eta, \zeta, \tau_0) \cos m(\varphi - \varphi_0), \quad (4)$$

where the components r_m and s_m of the brightness coefficients are determined by the relationships below

$$r_m(\eta, \zeta, \tau_0) = \frac{1}{\delta_m} \sum_{l=m}^n (-1)^{l+m} \int_0^{\tau_0} \mu_l^m(t) \psi_l^m(\zeta, t) \psi_l^m(\eta, t) \frac{dt}{\eta}, \quad (5)$$

$$s_m(\eta, \zeta, \tau_0) = \frac{1}{\delta_m} \sum_{l=m}^n \int_0^{\tau_0} \mu_l^m(t) \psi_l^m(\zeta, t) \tilde{\varphi}_l^m(\eta, t) e^{-\frac{\tau_0-t}{\eta}} \frac{dt}{d\zeta}, \quad (6)$$

$$\tilde{r}_m(\eta, \zeta, \tau_0) = \frac{1}{\delta_m} \sum_{l=m}^n (-1)^{l+m} \int_0^{\tau_0} \mu_l^m(t) \tilde{\varphi}_l^m(\zeta, t) \tilde{\varphi}_l^m(\eta, t) e^{-\frac{\tau_0-t}{\eta} \left(\frac{1}{\eta} + \frac{1}{\zeta} \right)} \frac{dt}{\eta \zeta}, \quad (7)$$

$$\tilde{s}_m(\eta, \zeta, \tau_0) = \frac{1}{\delta_m} \sum_{l=m}^n \int_0^{\tau_0} \mu_l^m(t) \tilde{\varphi}_l^m(\zeta, t) \psi_l^m(\eta, t) e^{-\frac{\tau_0-t}{\zeta}} \frac{dt}{d\zeta}, \quad (8)$$

while

$$\delta_m = \begin{cases} 2, & m=0, \\ 1, & m>0, \end{cases} \quad (9)$$

$$\mu_k^m(\tau) = \frac{1}{2} \lambda(\tau) x_k(\tau) \frac{(k-m)!}{(k+m)!}. \quad (10)$$

The values \tilde{r}_m and \tilde{s}_m are components of the brightness coefficients for the medium under investigation, which is illuminated

from below. Moreover, the functions $r_m(\eta, \zeta, \tau_0)$, $s_m(\eta, \zeta, \tau_0)$, $\tilde{r}_m(\eta, \zeta, \tau_0)$ and $\tilde{s}_m(\eta, \zeta, \tau_0)$ also satisfy the following system of integral-differential equations:

$$\frac{\partial r_m}{\partial \tau_0} \eta \zeta = \frac{1}{\delta_m} \sum_{i=m}^n (-1)^{i+m} \mu_i^m(\tau_0) \psi_i^m(\zeta, \tau_0) \psi_i^m(\eta, \tau_0), \quad (11)$$

$$\frac{\partial s_m}{\partial \tau_0} \eta \zeta = -s_m(\eta, \zeta, \tau_0) \zeta + \frac{1}{\delta_m} \sum_{i=m}^n \mu_i^m(\tau_0) \psi_i^m(\zeta, \tau_0) \tilde{\varphi}_i^m(\eta, \tau_0), \quad (12)$$

$$\begin{aligned} \frac{\partial \tilde{r}_m}{\partial \tau_0} \eta \zeta = & -\tilde{r}_m(\eta, \zeta, \tau_0) (\eta + \zeta) + \\ & + \frac{1}{\delta_m} \sum_{i=m}^n (-1)^{i+m} \mu_i^m(\tau_0) \tilde{\varphi}_i^m(\zeta, \tau_0) \tilde{\varphi}_i^m(\eta, \tau_0), \end{aligned} \quad (13)$$

$$\frac{\partial \tilde{s}_m}{\partial \tau_0} \eta \zeta = -\tilde{s}_m(\eta, \zeta, \tau_0) \eta + \frac{1}{\delta_m} \sum_{i=m}^n \mu_i^m(\tau_0) \tilde{\varphi}_i^m(\zeta, \tau_0) \psi_i^m(\eta, \tau_0), \quad (14)$$

where

$$\varphi_k^m(\zeta, \tau_0) = P_k^m(\zeta) + \delta_m (-1)^{k+m} \zeta \int_0^1 r_m(\eta', \zeta, \tau_0) P_k^m(\eta') d\eta', \quad (15)$$

$$\psi_k^m(\zeta, \tau_0) = P_k^m(\zeta) e^{-\frac{\tau_0}{\zeta}} + \delta_m \zeta \int_0^1 s_m(\eta', \zeta, \tau_0) P_k^m(\eta') d\eta', \quad (16)$$

$$\tilde{\varphi}_k^m(\zeta, \tau_0) = P_k^m(\zeta) + (-1)^{k+m} \delta_m \zeta \int_0^1 \tilde{r}_m(\eta', \zeta, \tau_0) P_k^m(\eta') d\eta', \quad (17)$$

$$\tilde{\psi}_k^m(\zeta, \tau_0) = P_k^m(\zeta) e^{-\frac{\tau_0}{\zeta}} + \delta_m \zeta \int_0^1 \tilde{s}_m(\eta', \zeta, \tau_0) P_k^m(\eta') d\eta'. \quad (18)$$

A substitution of the values for (5)-(8) into (15)-(18), respectively, gives four systems of integral equations to find the auxiliary functions $\tilde{\varphi}_k^m$, ψ_k^m , $\tilde{\varphi}_k^m$ and $\tilde{\psi}_k^m$, by which the brightness coefficients are also determined.

FINDING THE BRIGHTNESS COEFFICIENTS OF THE HOMOGENEOUS PLANE LAYER

Let us have a homogeneous plane layer in a turbid medium. Then, instead of (10), we have the following:

$$\mu_k^m(\tau) = \mu_k^m = \frac{1}{2} \lambda x_k \frac{(k-m)!}{(k+m)!}. \quad (19)$$

Obviously, if the layer is homogeneous, then the intensity of diffusely reflected radiation does not depend on the direction for illumination of the layer. In this case,

$$\begin{aligned} \rho(\eta, \zeta, \varphi) &= \rho(\eta, \zeta, \varphi) \quad \text{and} \quad \sigma(\eta, \zeta, \varphi) = \sigma(\eta, \zeta, \varphi), \\ \varphi &= \sigma(\eta, \zeta, \varphi), \quad \text{as well as} \quad r_m(\eta, \zeta, \tau_0) = \tilde{r}(\eta, \zeta, \tau_0), \quad s_m(\eta, \zeta, \tau_0) = \tilde{s}(\eta, \zeta, \tau_0), \\ \zeta, \tau_0, \quad \varphi_k^m(\eta, \tau_0) &= \tilde{\varphi}_k^m(\eta, \tau_0) \quad \text{and} \quad \psi_k^m(\eta, \tau_0) = \tilde{\psi}_k^m(\eta, \tau_0). \end{aligned}$$

Equations (11)-(14) are then rewritten in the following way:

$$\frac{\partial r_m}{\partial \tau_0} \eta \zeta = \frac{1}{\delta_m} \sum_{i=m}^n (-1)^{i+m} \mu_i^m \psi_i^m(\zeta, \tau_0) \varphi_i^m(\eta, \tau_0), \quad (20)$$

$$\frac{\partial s_m}{\partial \tau_0} \eta \zeta = -s_m(\eta, \zeta, \tau_0) \zeta + \frac{1}{\delta_m} \sum_{i=m}^n \mu_i^m \psi_i^m(\zeta, \tau_0) \varphi_i^m(\eta, \tau_0), \quad (21)$$

$$\frac{\partial r_m}{\partial \tau_0} \eta \zeta = -r_m(\eta, \zeta, \tau_0) (\eta + \zeta) + \frac{1}{\delta_m} \sum_{i=m}^n (-1)^{i+m} \mu_i^m \varphi_i^m(\zeta, \tau_0) \varphi_i^m(\eta, \tau_0), \quad (22)$$

$$\frac{\partial s_m}{\partial \tau_0} \eta \zeta = -s_m(\eta, \zeta, \tau_0) \eta + \frac{1}{\delta_m} \sum_{i=m}^n \mu_i^m \varphi_i^m(\zeta, \tau_0) \psi_i^m(\eta, \tau_0), \quad (23)$$

while instead of the four relationships of (15)-(18), we will have only two:

$$\varphi_k^m(\zeta, \tau_0) = P_k^m(\zeta) + (-1)^{k+m} \delta_m \int_0^1 r_m(\eta', \zeta, \tau_0) P_k^m(\eta') d\eta', \quad (24)$$

$$\psi_k^m(\zeta, \tau_0) = P_k^m(\zeta) e^{-\tau_0} + \delta_m \int_0^1 s_m(\eta', \zeta, \tau_0) P_k^m(\eta') d\eta'. \quad (25)$$

1. Let us equalize the right-hand parts of (20) and (22), (21) and (23). As a result, we find that

$$r_m(\eta, \zeta, \tau_0) = \frac{1}{\delta_m} \sum_{i=m}^n (-1)^{i+m} \mu_i^m \frac{\varphi_i^m(\eta, \tau_0) \varphi_i^m(\zeta, \tau_0) - \psi_i^m(\eta, \tau_0) \psi_i^m(\zeta, \tau_0)}{\eta - \zeta}, \quad (26)$$

$$s_m(\eta, \zeta, \tau_0) = \frac{1}{\delta_m} \sum_{i=m}^n \mu_i^m \frac{\varphi_i^m(\zeta, \tau_0) \psi_i^m(\eta, \tau_0) - \varphi_i^m(\eta, \tau_0) \psi_i^m(\zeta, \tau_0)}{\eta - \zeta}. \quad (27)$$

Substituting (26) and (27) into (24) and (25), respectively, we will obtain a system of integral equations in order to find the functions $\varphi_k^m(\zeta, \tau_0)$ and $\psi_k^m(\zeta, \tau_0)$:

$$\begin{aligned} \varphi_k^m(\zeta, \tau_0) &= P_k^m(\zeta) + \zeta \sum_{i=m}^n (-1)^{i+k} \mu_i^m \times \\ &\times \int_0^1 \frac{\varphi_i^m(\eta', \tau_0) \varphi_i^m(\zeta, \tau_0) - \psi_i^m(\eta', \tau_0) \psi_i^m(\zeta, \tau_0)}{\eta' + \zeta} P_k^m(\eta') d\eta', \end{aligned} \quad (28)$$

$$\begin{aligned} \psi_k^m(\zeta, \tau_0) &= P_k^m(\zeta) e^{-\frac{\tau_0}{\zeta}} + \zeta \sum_{i=m}^n \mu_i^m \times \\ &\times \int_0^1 \frac{\varphi_i^m(\zeta, \tau_0) \psi_i^m(\eta', \tau_0) - \varphi_i^m(\eta', \tau_0) \psi_i^m(\zeta, \tau_0)}{\eta' - \zeta} P_k^m(\eta') d\eta'. \end{aligned} \quad (29)$$

2. We find from (5) and (6) that, in the homogeneous case,

$$r_m(\eta, \zeta, \tau_0) = \frac{1}{\delta_m} \sum_{i=m}^n (-1)^{i+m} \mu_i^m \int_0^{\tau_0} \psi_i^m(\zeta, t) \psi_i^m(\eta, t) \frac{dt}{\zeta}, \quad (30)$$

$$s_m(\eta, \zeta, \tau_0) = \frac{1}{\delta_m} \sum_{i=m}^n \mu_i^m \int_0^{\tau_0} \psi_i^m(\zeta, t) \varphi_i^m(\eta, t) e^{-\frac{\tau_0-t}{\zeta}} \frac{dt}{\eta \zeta}. \quad (31)$$

Substituting (30) and (31) into (24) and (25), we obtain the following:

$$\begin{aligned} \varphi_k^m(\zeta, \tau_0) &= P_k^m(\zeta) + \\ &+ \sum_{i=m}^n (-1)^{i+k} \mu_i^m \int_0^{\tau_0} \psi_i^m(\zeta, t) dt \int_0^1 \psi_i^m(\eta', t) P_k^m(\eta') \frac{d\eta'}{\eta'}, \end{aligned} \quad (32)$$

$$\begin{aligned} \psi_k^m(\zeta, \tau_0) &= P_k^m(\zeta) e^{-\frac{\tau_0}{\zeta}} + \\ &+ \sum_{i=m}^n \mu_i^m \int_0^{\tau_0} \psi_i^m(\zeta, t) e^{-\frac{\tau_0-t}{\zeta}} dt \int_0^1 \varphi_i^m(\eta', t) P_k^m(\eta') \frac{d\eta'}{\eta'}. \end{aligned} \quad (33)$$

3. Equations (7) and (8) are written in the following way for the homogeneous medium:

$$r_m(\eta, \zeta, \tau_0) = \frac{1}{\delta_m} \sum_{i=m}^n (-1)^{i+m} \mu_i^m \int_0^{\tau_0} \varphi_i^m(\zeta, t) \varphi_i^m(\eta, t) e^{-(\tau_0-t) \left(\frac{1}{\eta} + \frac{1}{\zeta} \right)} \frac{dt}{\eta \zeta}. \quad (34)$$

$$s_m(\eta, \zeta, \tau_0) = \frac{1}{\delta_m} \sum_{i=m}^n \mu_i^m \int_0^{\tau_0} \varphi_i^m(\zeta, t) \psi_i^m(\eta, t) e^{-\frac{\tau_0-t}{\zeta}} \frac{dt}{\eta \zeta}. \quad (35)$$

A substitution of (34) into (25) and (35) into (26) results in the following equations:

$$\begin{aligned} \varphi_k^m(\zeta, \tau_0) &= P_k^m(\zeta) + \\ &+ \sum_{i=m}^n (-1)^{i+m} \mu_i^m \int_0^{\tau_0} \varphi_i^m(\zeta, t) e^{-\frac{\tau_0-t}{\zeta}} dt \int_0^1 \varphi_i^m(\eta', t) P_k^m(\eta') e^{-\frac{\tau_0-t}{\eta'}} \frac{d\eta'}{\eta'}, \end{aligned} \quad (36)$$

$$\begin{aligned} \phi_k^m(\zeta, \tau_0) = e^{-\frac{\tau_0}{\zeta}} & \left[P_k^m(\zeta) + \sum_{i=m}^n \mu_i^m \int_0^{\tau_0} \varphi_i^m(\zeta, t) e^{\frac{t}{\zeta}} dt \times \right. \\ & \left. \times \int_0^1 \psi_i^m(\eta', t) P_k^m(\eta') \frac{d\eta'}{\eta'} \right]. \end{aligned} \quad (37)$$

Expressions (26)-(29) were first obtained by Ambartsumyan [5] for a semi-infinite medium in anisotropic scattering, and by Chandrasekhar [6] in the case of a medium of finite optical thickness. Ambartsumyan [2,3] obtained Equations (26)-(29) and (30)-(33) for isotropic scattering, while Sobolev [1] derived Equations (34)-(37); as was already mentioned, Sobolev obtained all the equations (26)-(37) very simply (for isotropic scattering) on the basis of his probability of quantum yields from the medium.

Here, we have found all three types of equations for the functions ϕ_k^m and ψ_k^m , for the arbitrary indicatrix of scattering represented in the form of (1), as a particular case of the more general equations obtained for the heterogeneous medium.

LINEAR EQUATIONS CONNECTING THE FUNCTIONS ϕ_k^m AND ψ_k^m

It is easy to show that useful relationships connecting the functions ϕ_k^m and ψ_k^m follow from (28) and (29). Let us use a recurrence formula for the associated Legendre functions

$$P_k^m(\eta) \eta = \frac{k-m+1}{2k+1} P_{k+1}^m(\eta) + \frac{k+m}{2k+1} P_{k-1}^m(\eta). \quad (38)$$

Considering that

$$\frac{\zeta}{\eta' + \zeta} = 1 - \frac{\eta'}{\eta' + \zeta},$$

and substituting (38) into the integrand of (28), as well as introducing the symbols below

$$\alpha_{ik}^m = \int_0^1 \varphi_i^m(\eta) P_k^m(\eta) d\eta, \quad (39)$$

$$\beta_{ik}^m = \int_0^1 \psi_i^m(\eta) P_k^m(\eta) d\eta, \quad (40)$$

we find the following

$$\begin{aligned}
\varphi_k^m(\zeta) &= P_k^m(\zeta) + \sum_{i=m}^n (-1)^{i+k} \mu_i^m [\varphi_i^m(\zeta) \alpha_{ik}^m - \psi_i^m(\zeta) \beta_{ik}^m] - \\
&- \sum_{i=m}^n (-1)^{i+k} \mu_i^m \int_0^1 \frac{\varphi_i^m(\eta') \varphi_i^m(\zeta) - \psi_i^m(\eta') \psi_i^m(\zeta)}{\eta' + \zeta} P_k^m(\eta') \eta' d\eta' = \\
&= P_k^m(\zeta) + \sum_{i=m}^n (-1)^{i+k} \mu_i^m [\alpha_{ik}^m \varphi_i^m(\zeta) - \beta_{ik}^m \psi_i^m(\zeta)] + \\
&+ \frac{1}{\zeta} \sum_{i=m}^n (-1)^{i+k+1} \mu_i^m \frac{k-m+1}{2k+1} \zeta \times \\
&\times \int_0^1 \frac{\varphi_i^m(\eta') \varphi_i^m(\zeta) - \psi_i^m(\eta') \psi_i^m(\zeta)}{\eta' + \zeta} P_{k+1}^m(\eta') d\eta' + \\
&+ \frac{1}{\zeta} \sum_{i=m}^n (-1)^{i+k-1} \mu_i^m \frac{k+m}{2k+1} \zeta \times \\
&\times \int_0^1 \frac{\varphi_i^m(\eta') \varphi_i^m(\zeta) - \psi_i^m(\eta') \psi_i^m(\zeta)}{\eta' + \zeta} P_{k-1}^m(\eta') d\eta'. \quad (41)
\end{aligned}$$

Using (28), we ultimately obtain the following, instead of (41):

$$\begin{aligned}
&\frac{k-m+1}{2k+1} \varphi_{k+1}^m(\zeta) - \varphi_k^m(\zeta) \zeta + \frac{k+m}{2k+1} \varphi_{k-1}^m(\zeta) = \\
&= \zeta \sum_{i=m}^n (-1)^{i+k} \mu_i^m [\beta_{ik}^m \psi_i^m(\zeta) - \alpha_{ik}^m \varphi_i^m(\zeta)]. \quad (42)
\end{aligned}$$

In a similar way, we find from (29) and (38) that

$$\begin{aligned}
&\frac{k-m+1}{2k+1} \psi_{k+1}^m(\zeta) - \psi_k^m(\zeta) \zeta + \frac{k+m}{2k+1} \psi_{k-1}^m(\zeta) = \\
&= \zeta \sum_{i=m}^n (-1)^{i+k} \mu_i^m [\beta_{ik}^m \varphi_i^m(\zeta) - \alpha_{ik}^m \psi_i^m(\zeta)]. \quad (43)
\end{aligned}$$

We should mention that the values α_{ik}^m and β_{ik}^m are connected by the following relationships:

$$\alpha_{kk}^m = \int_0^1 P_k^m(\eta) P_k^m(\eta) d\eta + \frac{1}{2} \sum_{i=m}^n (-1)^{i+k} \mu_i^m [(\gamma_{ik}^m)^2 - (\beta_{ik}^m)^2], \quad (44)$$

This follows from (28), considering (39).

In a particular case when $k = m = 0$, $n = 1$ and $\tau_0 = \infty$, we have the following from (42):

$$\varphi_1^0(\zeta) = \frac{\left(1 - \frac{\lambda}{2} \sigma_{00}^0\right)}{1 - \frac{\lambda}{2} x_1 \zeta z_{10}^0} \varphi_0^0(\zeta) \zeta, \quad (45)$$

i.e., we obtain the formula which Ambartsumyan found [5].

It follows from (44) that

$$\alpha_{10}^0 = \frac{2}{\sqrt{\lambda x_1}} \left[1 - \sigma_{00}^0 + \frac{\lambda}{4} (\gamma_{00}^0)^2 \right]^{1/2}. \quad (46)$$

Substituting (46) into (45), we find that

$$\varphi_1^0(\zeta) = \frac{\left(1 - \frac{\lambda}{2} \sigma_{00}^0\right) \varphi_0^0(\zeta) \zeta}{1 - \sqrt{\lambda x_1} \left[1 - \sigma_{00}^0 + \frac{\lambda}{4} (\gamma_{00}^0)^2 \right]^{1/2} \zeta}. \quad (47)$$

Consequently, the function $\phi_1^0(\zeta)$ is completely determined by knowing the function $\phi_0^0(\zeta)$, and the inverse. The function $\phi_0^0(\zeta)$ can be found regardless of the function $\phi_1^0(\zeta)$ by solving the linear integral equation obtained by Sobolev [3, p. 148].

In the general case, for any fixed m and n , as follows from (42) and (43), any of the functions for $\phi_k^m(\zeta)$ (there will be $n - m + 1$ in all) can be represented as a linear combination of the remaining $(n - m)$ functions. Obviously, this also holds for the function $\phi_k^m(\zeta)$.

In using (42) and (43), we must keep in mind that $m \leq k \leq n - 1$ and $\phi_{k-1}^k(\eta) \equiv 0$, $\phi_{k-1}^k(\eta) \equiv 0$. These identities follow from (38) and from the fact that

$$P_{k+1}^k(\eta) = (2k + 1) \eta P_k^k(\eta).$$

Thus, the relationships obtained (42), (43) and (44) may prove to be useful for a numerical solution to the system of integral equations determining the functions ϕ_k^m and ψ_k^m .

REFERENCES

1. Sobolev, V.V.: Astron. Zhur., Vol. 34, p. 336, 1957.
2. Ambartsumyan, V.A.: Doklady Akad. Nauk S.S.S.R., Vol. 37, p. 257, 1943.
3. Sobolev, V.V.: Perenos luchistoy energii v atmosferakh zvezd i planet (Transfer of Radiant Energy in the Atmospheres of Stars and Planets). Moscow, "GITTL", 1956.
4. Yanovitskiy, E.G.: Astron. Zhur., Vol. 38, p. 912, 1961.
5. Ambartsumyan, V.A.: Zhur. Eksp. i Teoret. Fiz., Vol. 13, No. 9-10, p. 224, 1943.
6. Chandrasekhar, S.: Perenos luchistoy energii (Transfer of Radiant Energy). Moscow, Foreign Literature Publishing House, 1953.

COUNT RATE METER (CRM)

O.I. Bugayenko

ABSTRACT: The schematic diagram of a count rate meter which measures the statistical frequency of signals admitted per unit input of the trigger, with Poisson distribution of the intervals between pulses, is described in this study.

When working with a photon counter, there must be preliminary information on the intensity of the measured signal. An industrial CRM of the "Tyul'pan" type (ISS-3) is usually used in order to determine the requisite storage time and to select the scaling factor of the channels. Unfortunately, this instrument operates rather reliably only under laboratory conditions, while it must be rejected when used in a device intended for operation in open air.

The schematic diagram of a CRM (figure) measuring the statistical frequency of signals n per unit input of the figure, with Poisson distribution of the integrals between pulses, is proposed in this study. A periodic signal f_0 is admitted in the zero input. The on-off time ratio $\bar{\xi}$ is determined as the ratio between the time the trigger is found in space "1" and the total observation time:

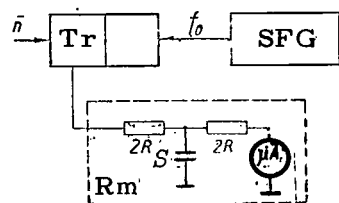
$$\bar{\xi} = \frac{T^{(1)}}{T^{(0)} + T^{(1)}}. \quad (1)$$

Obviously, at $\frac{\bar{n}}{f_0} = 0$ $\xi = 0$ (the trigger is in the "0" state the entire time), while for $\frac{\bar{n}}{f_0} \rightarrow \infty \rightarrow 1$. Consequently, the function $\xi \frac{\bar{n}}{f_0}$ is of a sharply defined nonlinear nature and, as will be seen below, has a form close to logarithmic in the operative range of measured frequencies. The latter circumstance is very convenient, since it allows us to carry out measurements in different parts of the scale of the output device with identical relative error.

In order to determine the appearance of the function $\xi(\bar{n}, T)$ where $T = \frac{1}{f_0}$, we must find the distribution function $F(\xi)$ of the random value ξ , i.e., we must find the probability of an event where the on-off time ratio is ξ in an arbitrary interval $[0, T]$.

Considering the principle of stationarity of the process

(Poisson) under investigation, we can limit ourselves to a determination of the function $F(\xi)$ per unit interval T . In this case, we have two mutually exclusive situations:



(1) No pulse arrives in the time interval T ; the probability of this situation is equal to $e^{-\bar{n}T}$. Then $\xi = 0$ and

$$F(0) = e^{-\bar{n}T}. \quad (2)$$

Fig. Block Diagram of CRM. (T_r) Trigger; (SFG) Standard-Frequency Pulse Generator; (RM) Device Measuring the On-Off Time Ratio of the Trigger Signal; (S) Smoothing Capacitor; (μA) Output Device.

(2) One or several pulses are admitted in the interval T , while only the first pulse changes the state of the trigger. For a particular case, let us determine the probability of admittance of the first pulse in the interval $[t, t + dt]$, where $0 \leq t \leq T$. The probability of absence of a pulse in the interval $[0, t]$ is equal to $e^{-\bar{n}t}$.

The probability of appearance of a pulse in the interval dt is equal to $\bar{n}dt$. The unknown probability

$$dF(\xi) = \bar{n}e^{-\bar{n}t} dt, \quad (3)$$

while by definition

$$\bar{\xi} = \frac{T-t}{T} = 1 - \frac{t}{T}, \quad (4)$$

so that

$$dF(\xi) = -T\bar{n}e^{-(1-\xi)\bar{n}T} d\xi. \quad (5)$$

Thus, the distribution function $F(\xi)$ is determined completely by (2) and (5).

Let us introduce the function

$$f(x) = \int e^{-i\xi x} dF(\xi). \quad (6)$$

It is well known from the theory of Fourier transforms that

$$\bar{\xi} = \frac{1}{T} f'(0), \quad (7)$$

$$\bar{\xi}^2 = [f'(0)]^2 - f''(0), \quad (8)$$

where $\bar{\xi}$ and $\bar{\xi}^2$ are the mathematical expectations and deviance of the random value ξ , respectively.

Substituting (2) and (5) into (6), we obtain the following:

$$f_T(x) = \int_0^1 n T e^{-(1-\bar{\xi})\bar{n}T + i\bar{\xi}x} d\bar{\xi} + e^{\bar{n}T + ix0} = \bar{n} T e^{-\bar{n}T} (e^{\bar{n}T + ix} - 1) + e^{-\bar{n}T}. \quad (9)$$

Equation (9) corresponds to the function of ξ per unit interval of T .

If ξ is assigned to an interval of mT , and considering that the values of ξ are independent in each unit integral, then we find the following according to the theorem of the characteristic function for the sum m of independent values:

$$f_{mT}(x) = f_T^{(m)}(x) = [\bar{n} T e^{-\bar{n}T} (e^{\bar{n}T + ix} - 1) + e^{-\bar{n}T}]^m. \quad (10)$$

Substituting (10) into (7) and (8), and considering that $0 \leq \xi \leq 1$, we find that

$$\bar{\xi} = 1 - \frac{1}{T\bar{n}} (1 - e^{-\bar{n}T}), \quad (11)$$

$$\sqrt{\bar{\xi}^2} = \frac{\sqrt{1 - e^{-2\bar{n}T} - 2\bar{n}T e^{-\bar{n}T}}}{\sqrt{m\bar{n}T}}. \quad (12)$$

Graduation of the scale of the output device is carried out according to (11), while the root-mean-square measurement error is estimated according to (12). Differentiating (11), we obtain the following:

$$\frac{d\bar{n}}{\bar{n}d\bar{\xi}} = \frac{\bar{n}T}{1 - e^{-\bar{n}T} (1 + \bar{n}T)} \quad (13)$$

Assuming that $\sqrt{\bar{\xi}^2} \rightarrow d\xi$, for $m \rightarrow \infty$ we find that

$$V_{\xi^2 \rightarrow d\xi}, \text{ при } m \rightarrow \infty \text{ имеем } ,$$

$$\frac{\Delta \bar{n}}{\bar{n}} \simeq \frac{V_{1 - e^{-2\bar{n}T} - 2\bar{n}Te^{-\bar{n}T}}}{(1 - e^{-\bar{n}T} - \bar{n}Te^{-\bar{n}T})}. \quad (14)$$

If ϵ is the error in reading the output device, due to the degree of accuracy and the parallax for reading the indices, the total relative error in measuring the values \bar{n} is equal to the following:

$$V_{\delta^2} = \sqrt{\left(\frac{\Delta \bar{n}}{\bar{n}}\right)^2 + \left(\epsilon \frac{d\bar{n}}{\bar{n}d\xi}\right)^2} = \frac{V_{1 - e^{-\bar{n}T} - 2\bar{n}Te^{-\bar{n}T} + m\epsilon T\bar{n}}}{(1 - e^{-\bar{n}T} - \bar{n}Te^{-\bar{n}T}) V_{\bar{m}}}.$$

Values of $\bar{\xi}$, $\sqrt{\bar{\xi}^2}$, $\sqrt{\bar{m}} \frac{d\bar{n}}{\bar{n}d\xi}$, and $\sqrt{\bar{m}} \frac{\Delta \bar{n}}{\bar{n}}$ calculated according to (11)-(14) are given in the table. For an example, the table also contains values of $\sqrt{\bar{\delta}^2}$ for the case when $\epsilon = 10^{-2}$ and $m = 10^3$ (the value of ϵ corresponds to the degree of accuracy of 1.0 usually assumed for the instruments; at $m = 10^3$ both components of the total error are of one order), as well as the relative root-mean-square fluctuations in flux with intensity of \bar{n} for a time $\frac{1}{m\bar{n}T}$ of $10^3 T$. For lower m , the difference in errors for $\sqrt{\bar{\delta}^2}$ and $\sqrt{\frac{1}{m\bar{n}T}}$

is less, although the errors themselves naturally increase. Considering the purpose of the instrument, an error of 5-10% may be admissible. Relative frequencies $\bar{n}T$ from 0.4 to 10 can be measured with this accuracy in a single range of the output scale. Thus, the interval of measured frequencies from 40 Hz to 100 kHz can be spanned by three ranges with reference frequencies of $f_0 = 100$ Hz, 1 and 10 kHz. The stability of the frequency of the reference generator SFG should be no less than 1%, which is easily realized in practice. The time for averaging mT in the CRM is given by the time constant RC of the integration circuits of the on-off time ratio meter. The optimal value (from the point of view of obtaining the greatest accuracy for a minimal averaging time) is $m = 1000$, i.e., for the cited standard frequencies the value RC is equal to 10, 1 and 0.1 sec, respectively.

$\bar{n}T$	$\bar{\xi}$	$V_{\bar{\xi}^2}$	$\frac{d\bar{n}}{\bar{n}d\xi}$	$\sqrt{\bar{m}} \frac{\Delta \bar{n}}{\bar{n}}$	$V_{\bar{\delta}^2}$	$1/\sqrt{10^3 \bar{n}T}, \%$
0.1	0.049	0.17	21.2	3.66	24	10.0
0.25	0.116	0.25	9.46	2.40	13	6.3
0.5	0.213	0.32	5.54	1.77	8	4.5
1.0	0.368	0.36	3.78	1.36	5	3.2
2.0	0.568	0.33	3.37	1.12	5	2.2
4.0	0.755	0.23	4.40	1.02	5	1.6
10.0	0.900	0.10	10.0	1.00	10	1.0

In deriving (11), it was assumed that the trigger has no time lag. Actually, the speed of response of the trigger is limited to a certain limit frequency $f_{\text{lim}} = \frac{1}{\tau}$. In this case, instead of (11) we have the following:

$$\bar{\xi}_\tau = \left(1 - \frac{\tau}{T}\right) e^{-\bar{n}\tau} - \frac{1}{nT} (e^{-\bar{n}\tau} - e^{-\bar{n}T}) \quad (16)$$

For $\bar{n}\tau < 0.1$, we have the following:

$$\bar{\xi} - \bar{\xi}_\tau = n\tau \left(1 - \frac{\tau}{T}\right) = a\bar{n},$$

where a is the constant for the given measurement limit. The correction for the time lag of the trigger can be disregarded if the condition $\bar{n}\tau < 0.01$ is satisfied.

AN ELECTROPHOTOMETER FOR LOW LUMINOUS FLUXES

L.A. Bugayenko, O.I. Bugayenko, V.D. Krugov
and V.G. Parusimov

ABSTRACT: A device intended for automatic determination of polarization components with a two-channelled instrument investigating low luminous fluxes according to pulse counts is described. The device is made of transistors.

The instrument intended for polarimetric and photometric investigations of low luminous fluxes by the method of photoncounting operates on two regimes: the regime for measurement of the polarization (polarimeter) and the regime of a two-channelled photometer. It consists of two principal measurement channels I and II, of one auxiliary channel *I*, which is used for automatic determination of the polarization components, and a time-reading channel operating on a quartz-crystal oscillator. Interaction of the channels is accomplished through the control units of the instrument. The maximum speed for counting pulses distributed randomly in time is about 200 kHz. The resolving time of the input instruments is no less than 10^{-7} sec. The sensitivity of the amplifiers is about 10^{-2} V. The electronic clock allows discrete assignment of the time for storage of information from 1 to 900 sec with accuracy of 0.01 sec. The information stored in the counters and the indices of the time meter are transferred to the number printer and duplicated in binary-decimal code with neon lamps. Moreover, preliminary information on the measured flux can be obtained from the count rate meter [3], which is connected to either of the principal channels. The entire instrument is made completely of semiconducting elements. The radiation receivers are photomultipliers which are sensitive in the spectral range of 0.35-0.8 μ .

Let us present some general concepts which determine the principal characteristics and structural features of the instrument under description.

Let a luminous flux with intensity of m photons per second be admitted on the cathode of the photomultiplier with quantum effectiveness of γ . The average number of photoelectrons (mathematical expectation) recorded in the form of pulses of the photomultiplier current in a time of t is then equal to the following:

$$N = m\gamma t = \bar{n}t, \quad (1)$$

where \bar{n} is the statistical frequency of the pulse signal.

Since the pulse signal sent from the photomultiplier has a time distribution similar to the Poisson distribution¹, the variance in $\bar{\delta}^2$ is equal to the number of recorded pulses N . The relative root-mean-square error of a single measurement is

$$\bar{\sigma} = \frac{\sqrt{\bar{\delta}^2}}{N} = \frac{1}{\sqrt{N}}. \quad (2)$$

It follows from (1) and (2) that, to measure a luminous flux with intensity of \bar{n} , we must record no fewer than $1/\bar{\sigma}^2$ pulses, while the time for accumulation of the pulses is

$$t \geq \frac{1}{\bar{n} \bar{\sigma}^2}.$$

The above relationships are valid only for recording systems with no time lag. For the actual systems, a short recovery time after the effect of each recorded pulse on them is characteristic.

Let τ be the resolving time of the input systems in the counter. The expressions for the mathematical expectation and variance are then determined in the following way [1]:

$$N_{\tau} = \frac{\bar{n}t}{1 + \bar{n}\tau}, \quad (3)$$

$$\bar{\delta}_{\tau}^2 = \frac{\bar{n}t}{(1 + \bar{n}\tau)^3}, \quad (4)$$

where N_{τ} is the number of pulses recorded, from the total number of pulses $\bar{n}t$. Expressions (3) and (4) determine the measured number

¹ The Poisson distribution is described by the expression

$P(n, t) = \frac{(\bar{n}t)^n e^{-\bar{n}t}}{n!}$, where $P(n, t)$ is the probability of incidence of n pulses in the time interval t . For the Poisson distribution, the dispersion is equal to the mathematical expectation. $\sum_{n=0}^{\infty} n^2 P(n, t) = \sum_{n=0}^{\infty} n P(n, t) = \bar{n}t$.

For the photomultiplier signal, the dispersions in the Poisson distribution are caused mainly by two factors: variation in the transit time of the electrons during multiplication in the dynode system and, as a result, impossibility of recording pulses with a short interval and feedback into the photomultiplier in the counting regime (optical and ion). The first factor imposes a fundamental limit on using the photomultiplier in the regime of photon counting; the latter are the results of the structural and technological imperfections of the photomultiplier and appear in substantial amplifications of the dynode system.

of pulses and its variation. In practice, we must know the true intensity of the signal \bar{n} and its relative root-mean-square error $\bar{\sigma}$.

$$\bar{n} = \frac{N_{\tau}}{t - N_{\tau}} \quad (5)$$

Differentiating $\ln \bar{n}$ by N_{τ} , and assuming that $\sqrt{\sigma^2} = \Delta N_{\tau}$ at $\sqrt{N_{\tau}} \gg 1$, we find that

$$\bar{\sigma} = \frac{1}{\sqrt{N_{\tau}}} \quad (6)$$

Thus, the relative root-mean-square error in the value \bar{n} depends only on the number of pulses recorded by the system, and does not depend on the resolving time.

An important case in practice is that when a noise signal with intensity of \bar{n}_n acts together with the measured signals (background of the sky, dark current of the photomultiplier, etc.). Since both signals have a Poisson distribution, their mathematical expectation and variance are summed up:

$$N_{\Sigma} = N + N_n$$

$$\bar{\sigma} = \frac{\sqrt{1 + \frac{\bar{n}_n}{\bar{n}}}}{\sqrt{N}} \quad (7)$$

The requisite observation time is

$$t \geq \frac{1 + \frac{\bar{n}_n}{\bar{n}}}{\bar{n} \bar{\sigma}^2} \quad (8)$$

The errors examined above are due to the statistically random nature of the measured signal, and do not include errors connected with the experimental condition (instability of the atmosphere, guiding accuracy, change in amplification of the photomultiplier).

Let there be a polaroid-analyzer rotating at an optical angular frequency of $\omega = 2\pi f$ in front of the photomultiplier. We are examining a luminous flux with average intensity of n_0 , magnitude of polarization of P and plane of polarization of α , starting with the conditional zero. Since the probability of penetration of a quantum with orientation of γ to the polarization plane of the

analyzer is equal to \cos^2 according to the Malus law, the intensity of the pulse signal is a function of the time:

$$n_t = n_0 [1 + P \cos(\omega t + \alpha)]. \quad (9)$$

Let the time for accumulation of the signal be equal to T and a multiple of the value $\frac{1}{f}$, i.e.,

$$T = \frac{m}{f} = mT_0,$$

where m is the number of revolutions of the analyzer (at $m > 100$, the condition of multiplicity is not essential). The following number of pulses, on the average, is then admitted in a time of T into the measuring system:

$$\bar{N}_0 = Tn_0 \quad (10)$$

If the system has time selection, and for time intervals of $[(k-1)T_0, \frac{2k-1}{2}T_0]$ (first halves of the periods), where k is an interger and $1 \leq k \leq m$, the admitted pulses are added, while for the intervals of $[\frac{2k-1}{2}T_0, kT_0]$ (second halves of the periods), the system operates on subtraction, then as a result the following statistically mean value is recorded:

$$\bar{N}_1 = -\frac{2Tn_0}{\pi} P \sin \alpha, \quad \bar{N}_2 = -\frac{2}{\pi} P \sin \alpha. \quad (11)$$

Similarly, adding the pulses for intervals of $[\frac{2k-1}{4}T_0, \frac{2k+1}{4}T_0]$ (the same as for \bar{N}_1 , but with a shift by $\frac{\pi}{2}$) and subtracting for the intervals of $[\frac{2k+1}{4}T_0, \frac{4k+1}{4}T_0]$, we obtain the following:

$$\frac{\bar{N}_3}{\bar{N}_0} = -\frac{2}{\pi} P \cos \alpha. \quad (12)$$

The signs of the values \bar{N}_1 and \bar{N}_2 characterize only the quadrant in which the angle α is found, and are determined by the selection of the initial plane of reference. Therefore, when it is not fundamentally important, we will disregard the signs of \bar{N}_1 and \bar{N}_2 . Expressions (10), (11) and (12) were obtained by integration over t of (9) within the corresponding limits.

Actually, we have substituted (9) into (1), assuming that

the time t in (1) is differentially short. The validity of this substitution will be proven when we calculate the variance in the values $\bar{N}_0, \bar{N}_1, \bar{N}_2$.

Let us divide the interval T_0 (the time of one optical revolution of the analyzer) into l equal intervals θ . The number of divisions can always be selected as sufficiently great for the $n\theta$ in the interval θ to be independent of t .

Let $f(y)$ be the characteristic function of the Poisson distribution and

$$f(y) = \sum_{n=0}^{\infty} e^{iy n} P(n, \theta) = e^{\bar{n} \theta (e^{iy} - 1)}$$

Then for the k -th interval ($0 \leq k \leq l - 1$)

$$f_k(y) = e^{n_0 [1 + P \cos(\omega k \theta + \alpha)] (e^{iy} - 1)} \quad (13)$$

Considering the mutual independence of the arrival of pulses in the integrals of θ and the property of the characteristic function for the sum of independent events, we will find $f(y)$ for the interval T_0 :

$$f_{T_0}(y) = \prod_{k=0}^{l-1} e^{n_0 [1 + P \cos(\omega k \theta + \alpha)] (e^{iy} - 1)} \quad (14)$$

Let m be the number of revolutions of the analyzer. Using the same property of the characteristic function again for the interval T , we find the following:

$$f_T(y) = e^{m n_0 T (e^{iy} - 1)} \quad (15)$$

The mathematical expectation of \bar{N} (average significance of the random value) and the variance $\bar{\sigma}^2$ are connected with the characteristic function by the following relationships:

$$N = \frac{1}{i} f'(0), \quad (16)$$

$$\bar{\sigma}^2 = [f'(0)]^2 - f''(0). \quad (17)$$

Differentiating (14) twice and substituting the results into (15) and (16), we ultimately find the following at $y = 0$:

$$\bar{N}_0 = n_0 T,$$

This coincides with (10). We also find the root-mean-square deviation, i.e.,

$$\sqrt{\bar{\delta}^2} = \sqrt{n_0 T}. \quad (18)$$

Thus, the harmonically modulated signal in the interval T behaves in the same way as a signal with intensity of n_0 distributed according to the Poisson law, which also follows from a comparison of (12) and (15).

Carrying out analogous operations for the first and second half-periods in m intervals, subtracting the mathematical expectations and adding the dispersions (the signals are independent and distributed according to the Poisson law), we have the following for \bar{N}_1 :

$$\begin{aligned} \bar{N}_1 &= n_0 \Theta P \sin \left(\alpha - \frac{\omega \Theta}{2} \right) \operatorname{cosec} \frac{\omega \Theta}{2}, \\ \sqrt{\bar{\delta}^2} &= \sqrt{n_0 T}. \end{aligned} \quad (19)$$

At $\Theta \ll \frac{1}{\omega}$

$$\bar{N}_1 = \frac{2}{\pi} \bar{N}_0 P \sin \alpha,$$

which coincides with (11).

It follows from (19) that the absolute root-mean-square error in measurement of the polarization component does not depend on the magnitude of polarization or the angle α .

Let us examine the problem of the effect of the resolving time of the circuit on a determination of the polarization components $P \sin \alpha$ and $P \cos \alpha$. For this, we will substitute (9) into (3), on the assumption that $T \gg \tau$, and integrating from 0 to 2π , we obtain the following

$$\bar{N}_{0\tau} = \frac{T}{\tau} \left(1 - \frac{1}{\sqrt{(1 + n_0 \tau)^2 - (n_0 \tau P)^2}} \right). \quad (20)$$

We will find $\bar{N}_{1\tau}$ as the difference in integrals with limits of $[0, \pi]$ and $[\pi, 2\pi]$:

$$\bar{N}_{1\tau} = \frac{2}{\pi} \cdot \frac{T_0 \arctan \frac{n_0 \tau P \sin \alpha}{\tau \sqrt{(1+n_0 \tau)^2 - (n_0 \tau I)^2}}}{\tau \sqrt{(1+n_0 \tau)^2 - (n_0 \tau I)^2}}.$$

Disregarding orders of magnitudes of $(n_0 \tau)^3$, we find that

$$\frac{\bar{N}_{1\tau}}{\bar{N}_{0\tau}} \simeq \frac{2}{\pi} \cdot \frac{P \sin \alpha}{1 + n_0 \tau \left(1 - \frac{P^2}{2}\right)}. \quad (21)$$

For values of $P < 0.3$, the term $\frac{P^2}{2}$ can almost always be disregarded.

Similarly, we have the following for the component $P \cos \alpha$:

$$\frac{\bar{N}_{2\tau}}{\bar{N}_{0\tau}} \simeq \frac{2}{\pi} \cdot \frac{P \cos \alpha}{1 + n_0 \tau \left(1 - \frac{P^2}{2}\right)}. \quad (22)$$

In measuring low luminous fluxes, the magnitude of the dark current and the stability of the noise level of the photomultiplier are substantial. This problem, as well as the problem of the amplitude distribution of the photomultiplier pulses, are examined in detail in [2]. We will merely mention that the best examples of photomultipliers are those with clearly pronounced computing-characteristic panels and with a ratio between the magnitude of dark current in the direct-current measurement regime and the number of pulses recorded in the regime of photon counting during measurements under comparable conditions which is close to unity.

The initial photomultiplier regime is selected at the middle of the computing-characteristic panel. Obviously, the photomultiplier should operate with least possible amplification, and the latter should be compensated in the recording part of the photometer. The pulse amplitude at the photomultiplier anode U depends on the amplification of the dynode system M and the total capacitance C acting in the anode circuit, i.e.,

$$U = \frac{e \Delta I}{C}. \quad (23)$$

Here e is the electron charge.

Expression (23) is valid if the time constant of the anode circuit is much greater than the duration of the pulse of the anode current.

The sensitivity of the signal amplifier of the photomultiplier should be such that pulses with amplitude a factor of 2-3 less than that calculated according to (23) can be recorded reliably. Modern multipliers allow us to obtain amplification up to $5 \cdot 10^6$. The capacitance acting in the anode circuit usually does not exceed $10^{-11} F$. The average signal amplitude is then obtained according to (23) as about 0.1 V. The discrimination threshold of the input amplifiers is less than 0.01 V in the instrument being described.

As has been shown [(2), (6) and (19)], the relative root-mean-square deviation in a unit measurement both in the photometric and the polarimetric regimes depends only on the number of pulses accumulated in the counter. For most polarimetric problems and in some cases of photometry (for example, when the noise-to-signal ratio is $\bar{n}_n/\bar{n} > 1$), the measurement error should not exceed 0.1%. Therefore, we can determine the requisite capacitance of the counter from (2). In our instruments, the total capacitance of channels I and II is equal to $1.024 \cdot 10^6$, while the three high-order decimal digits, which are also transferred to the printing device, bear the useful information. On the other hand, using the lowest luminous fluxes in a measurement with statistical error of 6%, we can find from (2) the requisite number of recorded pulses as 2^8 and, assuming that the absolute root-mean-square error (2^4) is equal to the scale of the digits not recorded, we can find the minimum capacitance of the channels as $1.6 \cdot 10^4$.

An important advantage of the method of photon counting is the fact that the method itself does not impose any fundamental limitations during measurements of arbitrarily low fluxes. The sensitivity threshold is due to the magnitude of the noise signal and the admissible time for accumulation of the signal, which should not exceed 15 min according to different theories. On the other hand, in measuring relatively high fluxes the threshold becomes the resolving time of the input devices of the instrument. In designing the instrument, we took a limit capacitance for reading statistical signals at a frequency of 200 kHz for resolving time of 100 nsec. Thus, considering a measurement of signals with intensity of 10 pulse/sec to be possible under advantageous conditions, we will mention that the instrument allows us to carry out photometric studies of luminous fluxes in a range greater than 10 stellar magnitudes

The transition from the photometer regime to the polarimeter regime is carried out with the aid of a tumbler switch which generates the corresponding potentials. The latter carry out the structural rearrangement of the flow chart.

It is more convenient to begin the description of the block diagram with an examination of the function of the design of the instrument in the regime of the two-channel photometer, (Fig. 1). Channels I and II, and the "clock" channel are used in this regime. The first two are completely identical and are intended for synchronous measurement of the intensity of luminous fluxes admitted from the two photomultipliers PM-1 and PM-2. The PM signals are amplified by the pulse amplifiers, formed in terms of duration and amplitude, and sent through the control gates G_1 and G_2 to the counting channels, each of which consists of three groups of counters (FM, OC, C) and the overflow bit. The counters C-I and C-II are the principal ones and are transferred, together with the overflow bit, onto the printer. The third channel carries out the function of the electronic clock assigning the time for storage of the measured signals. The reference frequency of the timer is produced by a thermostated quartz-crystal oscillator with pulse frequency of 72 kHz. This signal is sent to the frequency divider with overfill coefficient of 720. The frequency divider has outputs of the following frequencies: 24, 12, 2.4 kHz; 800, 400, 200 and 100 kHz, which are used in different parts of the instrument. A frequency of 100 Hz is sent through the controlled gate to a 5-bit decade counter (timer unit), the three high-order decades of which are the principal ones and are transferred to the printer. The frequency sent to the input of the principal decades depends on the position of the three-position switch (100, 10, 1 Hz). Moreover, the coincidence circuit which generates the output pulse for the count stop upon realization of a code in the decade which coincides with the code of the key-actuated time selector (from 0 to 9), operates together with the high-order decade of the timer. To obtain preliminary information on the measured fluxes, the instrument design includes an RCM, which is connected to any measuring channel (with the aid of the switch). The reference frequency, in units of which the RCM is graduated, is sent through the band selector from the frequency-divider unit.

The instrumental circuit operating in the photometer regime is phased in the following way. In initial state, gates G_1 , G_2 , and G_3 are closed. The "start" pulse changes the state of the stop trigger, which opens the gates to the counting channels and the timer gates. A reset pulse is generated at the same time, and the C-I, C-II and timer units are reset to their original state. The counting in the channels is carried out until the arrival of the stop pulse, which is produced when the preset surge time is reached (the signal is sent from the timer unit) and there is overflow of one of the counters (the signal is developed according to the sign "1" of the overflow bit of the corresponding counter). The halt can be accomplished manually with the "Stp" button. The stop pulse resets the stop trigger in its initial state and develops the pulse which turns on the printer. In the instrument being described, there is a printer of the BZ-15 type,

which records eleven-bit decimal codes with parallel input.

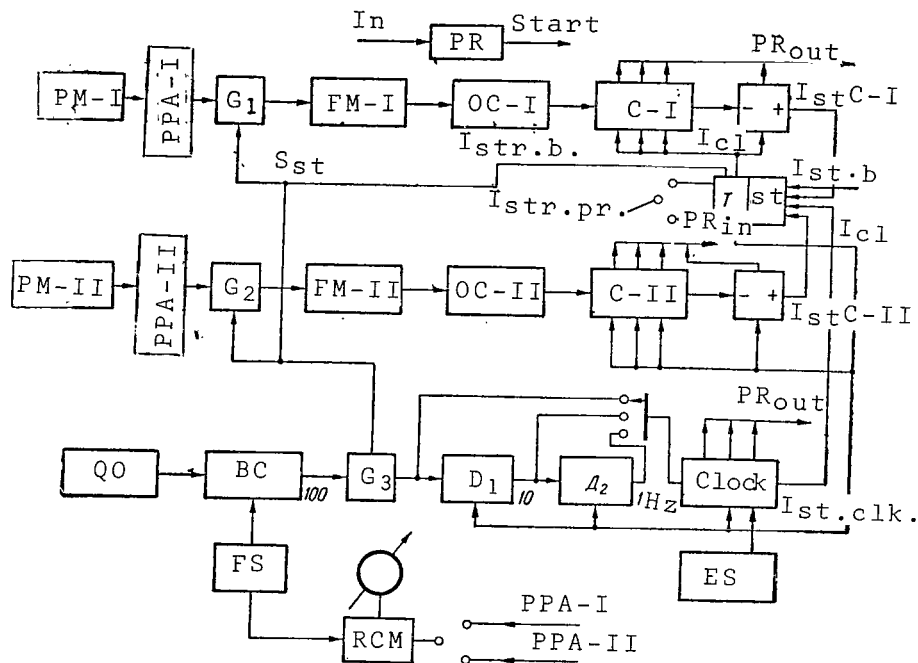


Fig. 1. Schematic Diagram of Instrument Operating in Photometer Regime (PM-Photomultipliers; PPA-Photomultiplier Pulse Amplifier; FM-Flow Meters; C-Decimal Counters; Tst-Stop Trigger; PR-Printer; QO-Quantizing Crystal Oscillator; 72 kHz; FD-Frequency Divider; RCM-Rate Count Meter; FS-Standard-Frequency Selector of the RCM; ES-Exposure Selector; I-Pulse; P-Potential; D₁-II and D₂-I-Preliminary Timer Decade).

The timer indices corresponding to the selected storage time are recorded in the 11-th, 10-th and 9-th bits if the stop takes place according to the signal of the timer unit, or the time interval before overflow if the halt occurs with overflow. The state of the overflow bits is recorded in the 8-th and 4-th bits. The indices of units C-I and C-II are recorded in the 7-th, 6-th, 5-th, 3-rd, 2-nd and 1-st bits, respectively.

During operation in the regime of information read-out, 10 pre-count pulses generated synchronously with the rotation of the digit drum are sent from the PR, while the digits pass under the printing hammers in reverse order. The pre-count pulses are sent simultaneously to all of the bits of the units C-I, C-II

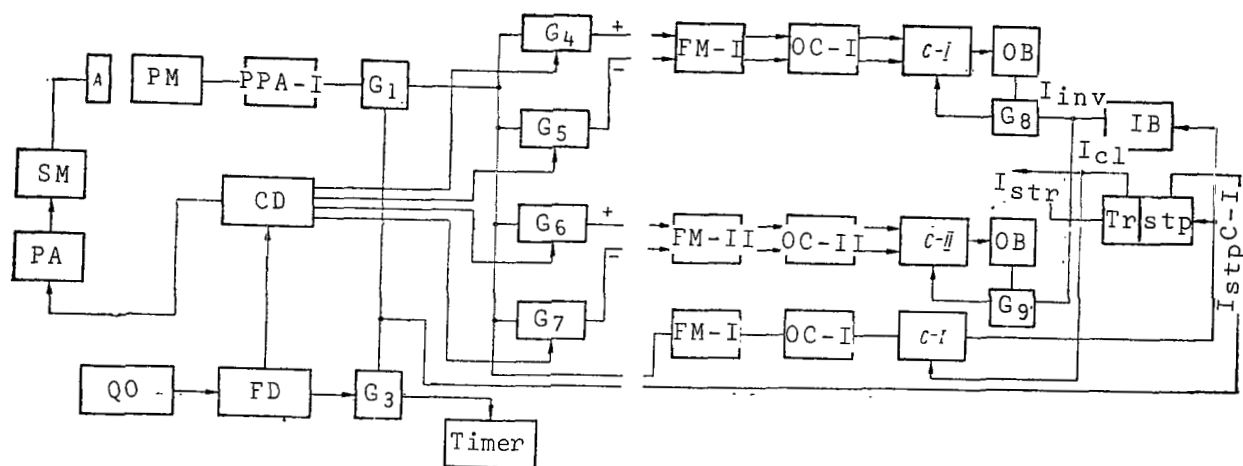


Fig. 2. Block-Diagram of the Instrument Operating on the Polarimeter Regime. (A) Polaroid; (SM) Synchronous Motor; (PA) Power Amplifier; (G) Gates; (OB) Overflow Bit; (IB) Inversion Block; (FM-I), (OC-I), (C-I) Auxiliary Polarization Channels.

and the timer, and are printed. The connections between decades are blocked by the stop trigger. The output pulses of the decades and overflow bits control the corresponding PR-hammers. If the number a is written in a given bit, then the output pulse appears in the k -th pre-count pulse where $a + k = 10$. Since the k -th pre-count pulse corresponds to the $(10-k)$ -th digit of the drum, the number a is written out in the given bit. After read-out of the information from the PR, a pulse is sent for termination of the printing. This pulse generates the "start" pulse through the tumbler switch for the regime of "Automatic-Single" measurements. For single measurements, the "start" pulse is sent to the stop trigger through the "start" button.

The principle of harmonic modulation by the analyzer of the polarization component of the emitted luminous flux and subsequent synchronous two half-period detection of the signal with arbitrary initial phase underlies the method of measuring polarization in the instrument being described. In this case, the orthogonal components of the polarization vector are determined directly. A block diagram of the instrument operating on the polarimeter regime is given in Figure 2. The polaroid analyzer is put into rotation by a synchronous motor, the voltage on which is supplied through the power amplifier from the synchronous detector. The amplified PM signal is sent directly through gate G_1 to the input of Channel I and through gates $G_4 - G_7$, which are controlled by the synchronous detector, to channels I and II. Channels I and II operate in reverse phase. A direct count is made when the gates G_4 and G_6 are open, and a reverse count when the gates G_5 and G_7 are open. The time diagram represented in Figure 3 illustrates the operation of the synchronous detector.

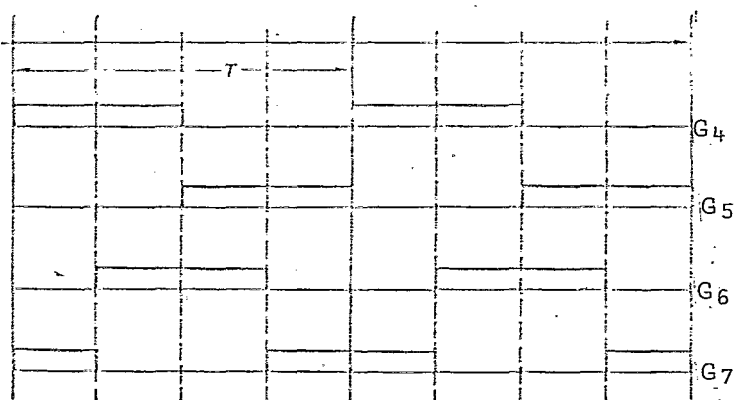


Fig. 3. Time Diagram of the Operation of the Synchronous Detector. (T - Period of Optical Modulation of the Signal; the Rectangles Correspond to Time Intervals When the Corresponding Gate is Open).

As can be seen from Figure 3, the gates to each channel are antiphased. The time shift between channels is equal to $\pi/2$.

Let us examine the spacing of the instrument operating on the polarimeter regime. We should mention that, to simplify reading Figure 2, we do not show the circuits for start, reset and information read-out on the PR. Their effect is identical in both instrumental regimes.

The counting is stopped by the sign of loading of Channel I, in which the entire signal sent from the photomultiplier is stored. The timer channel records the time interval during which the signal was stored in Channel I. The scaling factor of Channel I is closely connected with the scaling factors of Channels I and II and selected so that the polarization vector components stored in Channels I and II are expressed in units of the average signal intensity. In the polarimeter regime, the overflow bits fulfill the function of sign bits of the corresponding polarization vector components. The negative numbers in the binary-decimal counters are recorded in a supplementary code. Therefore, before printing out the negative number, it must be converted into direct code. The conversion is made along the following scheme: "supplementary-reverse-direct" code. To convert the number from the supplementary to the reverse code, it is necessary to add one to each bit of the counter, except the low-order one, on the condition that zero is not in the preceding bit. The connections between bits should be blocked. Conversion from the reverse to the direct code is accomplished by replacing the code of each bit by its complement up to ten. The numbers 0 and 5, which have identical representation in the reverse and direct codes, are not inverted (for example, a negative number in the complimentary code of 940, in the reverse 040, in the direct 060). The inversion operations are carried out after the dark pulse and are terminated before the arrival of the first pre-count pulse of the PR.

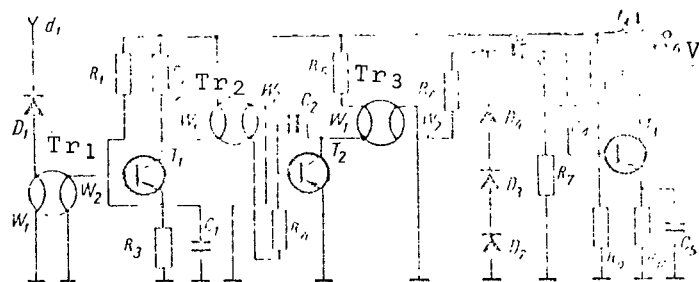


Fig. 4. Photomultiplier Pulse Amplifier. ($T_1 - T_3$) Triodes P416-B; (D_1) Tunnel Diode ZI301-V; (D_2) Diode D-12; (a_1, Z_1) Input; (b_1) Output; (PC) Pulse Converters, $R_1, R_9, R_{12}, R_{14}, R_{16}, R_{22} = 51 \text{ k}\Omega$; $R_2 = 110 \text{ k}\Omega$; $R_3, R_{19} = 510 \text{ }\Omega$, $R_4 = 160 \text{ k}\Omega$; $R_5, R_7 = 390 \text{ }\Omega$; $R_8 = 22 \text{ k}\Omega$; $R_{10} = 1 \text{ k}\Omega$, $R_{11}, R_{13} = 10 \text{ k}\Omega$, $R_{15} = 1.2 \text{ k}\Omega$, $R_{17} = 3 \text{ k}\Omega$, $R_{18} = 470 \text{ }\Omega$, $R_{20}, R_{24}, R_{25} = 91 \text{ }\Omega$, $R_{23} = 4.7 \text{ k}\Omega$, $C_1, C_3, C_4, C_8 = 1000 \text{ pf}$, $C_2 = 510 \text{ f}$, $C_5, C_6, C_7 = 360 \text{ f}$, $C_9 = 330 \text{ f}$, $C_{10}, C_{11} = 220 \text{ f}$.

The instrumental design includes a special device by which tests are carried out both for the entire instrument on the whole and for separate parts. The test-problems are divided into two groups: the first group is intended for checking the correct operation of the instrument, and the second group is intended for operative localization of the break-down site. Formation of the pulses for the test-problems is accomplished by a triple-pulse shaper, the schematic diagram of which is given in Figure 4.

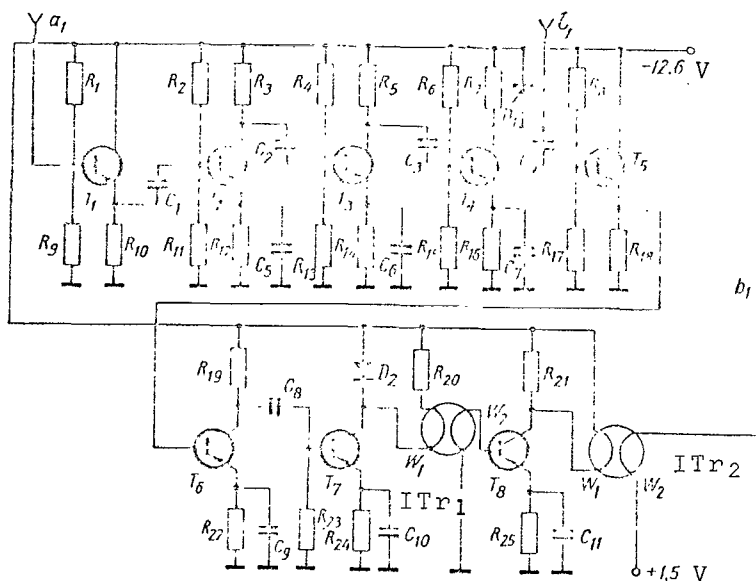


Fig. 5. Triple-Pulse Shaper. (T_1 - T_3) Triodes P416-B; (D_1) Diode D-9I; (D_2 - D_4) Tunnel Diodes ZI301V; $R_1 = 3.6$ kOhm, $R_2 = 680$ Ohm, $R_3 = 91$ Ohm, $R_4 = 820$ Ohm, $R_5, R_{10} = 51$ Ohm, $R_6, R_7 = 470$ Ohm, $R_8 = 91$ kOhm, $R_9 = 1.2$ kOhm, $C_2, C_4 = 1000$ f, $C_3 = 24$, $C_5 = 360$ f, d_1 -Input Pulse.

The pulse amplifier of the PM signal, the schematic diagram of which is given in Figure 5, is made of eight transistors of the P416-B type. The first three amplification cascades (triodes T_1 - T_3) make up the preliminary amplifier and are assembled together with the photomultiplier. In the principal loop, together with amplification, there is shaping of the standard pulse. The shaping begins with recovery of the front in the fourth cascade and is accomplished with the aid of the tunnel diode, shunting the collector load of the triode T_4 . The signal is limited in amplitude at the same time. The ultimate shaping is accomplished in the output cascades of T_7, T_8 on the pulse converters. The principal parameters of the amplifier are the following: amplification over the circuit no less than 10^3 ; transmission band of 25 mHz; outpulse amplitude for load of 100 Ohm equal to 9 V; rectangular

shape of the pulse; duration of the pulse fronts of 10 nsec, duration of the pulse on the 0.1 levels no longer than 40 nsec. The revolving time of the amplifier is determined by the parameters of the pulse converters and selected as equal to 100 nsec. The principal input of the amplifier a_1 is blocked in solving the test-problems, while the signal of the triple-pulse shaper is sent to the input l_1 .

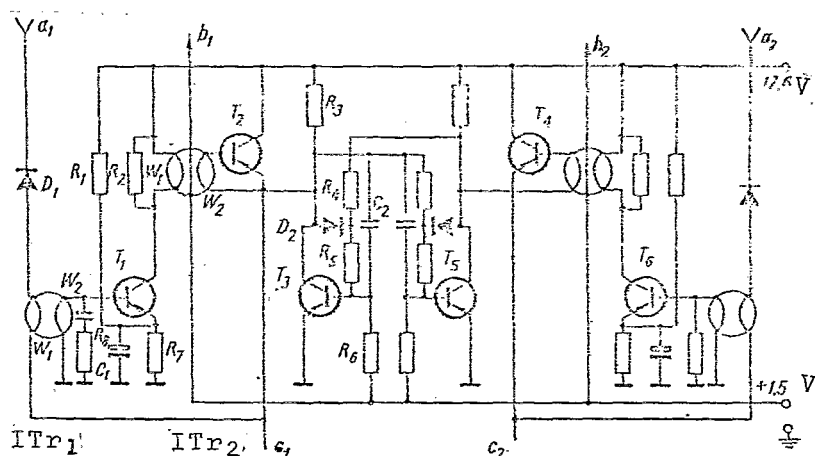


Fig. 6. Trigger ($T_1 - T_6$) Triodes P416-B; (D_1) Diode D-18; (D_2) Diode D-9I, (a_1, a_2) Pulse Input; (b_1, b_2) Pulse Output; $R_1, R_6 = 3.6 \text{ k}\Omega$, $R_2 = 510 \text{ k}\Omega$, $R_3 = 1.2 \text{ k}\Omega$, $R_5 = 1.6 \text{ k}\Omega$, $R_7 = 91 \text{ }\Omega$, $R_8 = 360 \text{ }\Omega$, $C_1 = 3.0 \text{ }\mu\text{f}$, $C_2 = 15-20 \text{ }\mu\text{f}$.

The operational principle of the shaper is the following. In the second cascade of T_2 , a pulse is generated with a linearly rising leading edge. This pulse is sent through a buffer resistor R_6 to the tunnel diodes (D_2, D_3, D_4), which shape the step signal. This signal is differentiated by the R_7C_3 circuit and sent in the form of a packet of three pulses through the amplifying cascade of T_3 to the PPA. The interval between pulses is fixed by the integrating circuit R_4C_2 . The cascade T_1 is intended for standardization of the input pulses.

The principal unit of a counter of the FM type is the high-speed trigger (Fig. 6) made in the design of an unsaturated trigger, started on a collector. In order to speed up the switching time, there are triodes on the trigger which shunt the collector loads at the moment of a change in state of the trigger. The resolving time of the trigger is about 100 nsec. The trigger is started by pulses with amplitude of 6-12 V and duration of 30-50 nsec. To control the following circuits, the trigger has pulse outputs b_1 and b_2 . The capacity of counters of the FM type is three binary bits. The counters FM-I and FM-II were designed according to the reverse diagram.

The change in total capacity of channels I, II and I is

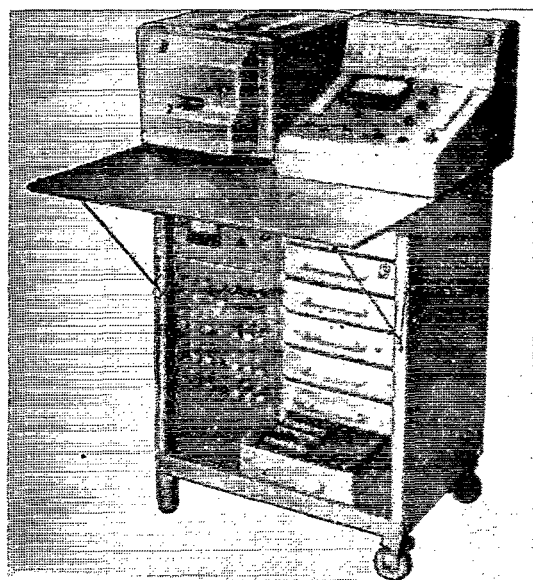


Fig. 7. Low-Flux Electrometer. (1) Sub-Unit Frame; (2) Control Panel; (3) Printer; (4) Supply Unit.

accomplished in counters of the OC type. Counters of the OC type operate in binary code and have a variable scaling factor of 2, 4, 32 and 128. In the polarimeter regime, the scaling factor of all the channels is fixed at the same time with the aid of a single switch. In the photometer regime, the capacity of the OC-I and OC-II counters is fixed separately.

The counters C-I and C-II are designed on a binary decimal code with weighting factors of 5211. The scaling factor of the counter is 10^3 . The counter CI is made in binary code and has scaling factor of 2048. However, to express the polarization vector components in units of the average intensity, it is necessary that the scaling factor of the counter CI be $\pi/2$ times greater than the capacity of the counters C-I and C-II, i.e., equal to 1571 (with accuracy up to 0.01%). This requirement follows from (11) and (12). The requisite scaling factor is attained by introducing a reset pulse of code 477 into the counter CI.

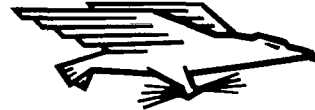
The entire instrument, except for counters of the FM type, is made of standard cells designed at the Cybernetics Institute of the Academy of Sciences of the Ukrainian SSR (Fig. 7).

REFERENCES

1. Ritov, S.M.: Vvedeniye v statisticheskuyu radiofiziku (Introduction to Statistical Radiophysics). Moscow, "Nauka", 1966.
2. Kovaleva, T.A. et al.: Pribory i Tekhnika Eksperimenta, Vol. 5, No. 5, 1966.
3. Bugayenko, O.I.: This Collection, p. (178).

Translated for the National Aeronautics and Space Administration by:
Aztec School of Languages, Inc.,
Research Translation Division (454)
Maynard, Massachusetts.
NASw-1692.

FIRST CLASS MAIL



POSTAGE AND FEES PAID
NATIONAL AERONAUTICS AND
SPACE ADMINISTRATION

POSTMASTER: If Undeliverable (Section 158
Postal Manual) Do Not Return

"The aeronautical and space activities of the United States shall be conducted so as to contribute . . . to the expansion of human knowledge of phenomena in the atmosphere and space. The Administration shall provide for the widest practicable and appropriate dissemination of information concerning its activities and the results thereof."

— NATIONAL AERONAUTICS AND SPACE ACT OF 1958

NASA SCIENTIFIC AND TECHNICAL PUBLICATIONS

TECHNICAL REPORTS: Scientific and technical information considered important, complete, and a lasting contribution to existing knowledge.

TECHNICAL NOTES: Information less broad in scope but nevertheless of importance as a contribution to existing knowledge.

TECHNICAL MEMORANDUMS:
Information receiving limited distribution because of preliminary data, security classification, or other reasons.

CONTRACTOR REPORTS: Scientific and technical information generated under a NASA contract or grant and considered an important contribution to existing knowledge.

TECHNICAL TRANSLATIONS: Information published in a foreign language considered to merit NASA distribution in English.

SPECIAL PUBLICATIONS: Information derived from or of value to NASA activities. Publications include conference proceedings, monographs, data compilations, handbooks, sourcebooks, and special bibliographies.

TECHNOLOGY UTILIZATION PUBLICATIONS: Information on technology used by NASA that may be of particular interest in commercial and other non-aerospace applications. Publications include Tech Briefs, Technology Utilization Reports and Technology Surveys.

Details on the availability of these publications may be obtained from:

SCIENTIFIC AND TECHNICAL INFORMATION DIVISION
NATIONAL AERONAUTICS AND SPACE ADMINISTRATION
Washington, D.C. 20546